HEMODYNAMIC REGULATION OF CARDIAC OUTFLOW MORPHOGENESIS

A Dissertation

Presented to the Faculty of the Graduate School

of Cornell University

In Partial Fulfillment of the Requirements for the Degree of

Doctor of Philosophy

by

Stephanie Elaine Lindsey

February 2016

HEMODYNAMIC REGULATION OF CARDIAC OUTFLOW MORPHOGENESIS

Stephanie Elaine Lindsey, Ph.D.

Cornell University 2016

ABSTRACT

Throughout development, blood flow guides cardiac morphogenesis, sculpting tissue by promoting growth in response to increased mechanical demands. Alterations in flow patterns during critical stages of development may therefore lead to adverse tissue remodeling and subsequent functional cardiac defects. Distinguishing the specific effects due to hemodynamics and genetic mutations is a current challenge, as the role of hemodynamics in outflow tract and pharyngeal arch artery morphogenesis is poorly understood. There exists a need for more clinically relevant animal models that allow for the study of disease pathogenesis both structurally and molecularly. My work begins to delineate the effects of structural changes resulting from abnormal hemodynamic patterning and elucidate their effects in the creation of congenital heart defects through a combination of experimental interventions and computational modeling.

Two- photon microscopy guided femtosecond laser pulses were used to nucleate and control the growth of cavitation bubbles within developing outflow vessels without disturbing surrounding tissues. These cavitation bubbles temporarily occluded the vessel, while a more stable occlusion while a more stable occlusion was formed by ablating the circulating thrombocytes that accumulated behind the bubble. Using this approach, I examined the effects of PAA vessel occlusions on embryonic viability,

hemodynamic rearrangement, and downstream outflow tract morphogenesis (Chapter 3).

A zero-dimensional (0D) electric analog model that allows for global tuning of the embryo's vasculature relative to the arches was developed (Chapter 4). A 3D-0D model was used to characterize natural variation in day3, day4, and day 5 arch artery pressure, flow, and shape changes. These 0D bounds served as a basis for prediction of flow distribution to the cranial and caudal outlets when switching between normal and aberrant flow (Chapter 5).

Results revealed distinct morphology dynamics for day3, day4, and day 5 geometries, as well as natural shifts in arch artery dominance at different stages and across individual days. Immediate remodeling of the arch artery vasculature took place following day 3 experimental occlusions. In some embryos, that remodeling worked to lessen the severity of increased pressure magnitude in the cranial part of the aortic sac. My findings contribute a more detailed picture of arch artery growth and adaptation across a critical window of development.

BIOGRAPHICAL SKETCH

Stephanie graduated in 2010 from Washington University in St. Louis with a B.S. in Biomedical Engineering. As a freshman, she became a research assistant in the Department of Anesthesiology at Washington University School of Medicine. She quickly switched to the biomechanics lab of Dr. Larry Taber, where she was first introduced to the powerful interplay between experiments and computational modeling. Stephanie rose to the level of an independent researcher and was awarded the NIH Undergraduate Transition to Advanced Research (U-STAR) Award for her work investigating the mechanics of head-fold morphogenesis in the gastrulating chick embryo. Stephanie spent the summers after her sophomore and junior year surveying foreign medical systems in Senegal and France respectively. Outside of academics, Stephanie dabbled in water polo, Latin dance, Indian dance and break dancing, joining various teams and performing throughout her undergraduate career.

Stephanie studied as a Ph.D. candidate in the Cardiovascular Developmental Bioengineering Laboratory of Dr. Jonathan Butcher at Cornell University. During her tenure at Cornell, Stephanie was awarded the Alfred P. Sloan Fellowship, the NSF GRFP (Graduate Research Fellowship Program) Fellowship and the NSF GROW (Graduate Research Opportunities Worldwide) Fellowship. Stephanie has mentored multiple students and authored four first-author original research papers, as well as two review papers. She has presented her work at six conferences across the globe as well as an international seminar. Her research focuses on understanding the role hemodynamics plays in creation of cardiac outflow abnormalities.

Dedicated to my family

In loving memory of Jacob Bryan Lindsey

ACKNOWLEDGMENTS

Above all, I would like to acknowledge and thank my mother whose constant support and encouragement have made me the person I am today. Her intellectual curiosity and ambitious nature inspired me to not only nourish my passions for math, engineering, and medicine, but to believe that I could become anything that I wanted to be. To my brother and sister, thank you for reminding me that the world goes round even in the most difficult of times. To my aunt and uncle, thank you for the late night or early morning phone calls and advice you have given me over the years. To Jeremy, thank you for being my best friend.

I would like to thank my advisor Dr. Jonathan Butcher for his guidance and support throughout this process. Without him, I would undoubtedly not be the researcher I am today. I would also like to thank my committee members, Drs Chris Schaffer, Drew Noden and Irene Vignon-Clementel. The Schaffer-Nishimura Lab was a second home for me, serving as the base for my experimental work for the first three years of my Cornell tenure. Dr. Vignon-Clementel welcomed me to her numerical simulation group in France and helped me to develop the computational tool sets used throughout this thesis. Together, you have expanded the idea of what is possible and guided me to become a dynamic researcher and engineer. Thank you for your patience, availability, and advice during my research challenges.

To my undergraduate mentors Dr. Larry Taber and Dr. Mary Sansalone, although you did not contribute directly to this work, you have both inspired me in more ways than you know and I am truly grateful.

I must also acknowledge the body of people who have aided me along the way these past five years. Thank you to my lab families: Jennifer Richards, Phil Buskohl, Emily Farrar, Laura Hockaday, and Russ Gould, in the Butcher Lab; Liz Wayne and

Amanda Barres in the Schaffer Lab; Chloe Audebert, Benoit Fabreges, and Sanjay Pant at INRIA. You have shared your knowledge and brightened my days.

Finally, I would like to thank my entire family for your unwavering support and encouragement.

Funding for this work was provided by the Alfred P. Sloan Fellowship and the NSF- GRFP Fellowship.

TABLE OF CONTENTS

LIST OF FIGURES

LIST OF TABLES

LIST OF ABBREVIATIONS

α-SMA : α –Smooth muscle actin

AV: Atrioventricular

AVJ: atrioventricular junction

BAV: Bicuspid aortic valve

CFD: Computational fluid dynamics

CHD: Congenital heart defects

CTB: Conotruncal banding

ECE : Endothelin converting enzyme

ECM: Extracellular matrix

EMT: Endocardial to mesenchymal transformation

ET: Endothelin

HH: Hamburger-Hamilton

HLHS: Hypoplastic left heart

KLF-2: Kruppel-like factor-2

LAL: Left atrial ligation

LV: Left ventrical

NOS: Nitric oxide synthase

OT: Outflow tract

PE: Proepicardium

RCR: Resistor capacitor resistor

RV: Right ventrical

TGFβ: Transforming growth factor-β

TOF: Tetralogy of fallot

VIC: Valvular interstitial cell

VEGF: Vascular endothelial growth factor

VMTK: Vascular modeling toolkit

WSS: Wall shear stress

PREFACE

The etiology of many congenital heart defects, or cardiac abnormalities resulting from improper or incomplete development, is poorly understood. Traditionally, biologists have pioneered work in the field, studying these abnormalities from a molecular or genetic perspective. The role of hemodynamics is often ignored and poorly quantified. Here, I examine abnormal cardiac morphogenesis through an engineering lens, by quantifying hemodynamic forces and isolating the effects of hemodynamics alone in abnormal patterning of the outflow tract. Chapters 1 through 2 review relevant literature and highlight key events in cardiac morphogenesis. In Chapter 3, I present the minimally invasive targeted microsurgery I use to create cardiac defects and examine the effects of vessel occlusions on embryonic viability, hemodynamic rearrangement, and downstream outflow tract morphogenesis. In Chapter 4, I introduce a multiscale modeling approach that utilizes zero-dimensional (0D) electric analog components to render computational studies more clinically relevant. The multiscale modeling is used to establish a natural framework for day 3, day 4 and day 5 cardiac outflow morphogenesis in Chapter 4. The same model is subsequently used to understand the effects of abnormal cardiac morphogenesis, resulting from vessel occlusion, in Chapter 5. Establishing a framework for normal and aberrant cardiac morphogenesis leads to the creation of informed interventions with the possibility of restoring function or reverse the formation of a diseased state.

CHAPTER 1

INTRODUCTION: THE CYCLE OF FORM AND FUNCTION IN CARDIAC VALVULOGENESIS[1]

1.1 Abstract

The formation and remodeling of the embryonic valves is a complex and dynamic process that occurs within a constantly changing hemodynamic environment. Defects in embryonic and fetal valve remodeling are the leading cause of congenital heart defects, yet very little is known about how fibrous leaflet tissue is created from amorphous gelatinous masses called cushions. Microenvironmental cues such as mechanical forces and extracellular matrix composition play major roles in cell differentiation, but almost all research efforts in valvulogenesis center around genetics and molecular approaches. This review summarizes what is known about the dynamic mechanical and extracellular matrix microenvironment of the atrioventricular and semilunar valves during embryonic development and their possible guidance roles. A variety of new computational tools and sophisticated experimental techniques are progressing that enable precise microenvironmental alterations that are critical to complement genetic gain and loss of function approaches. Studies at the interface of mechanical and genetic signaling in embryonic valvulogenesis will likely pay significant dividends, not only in terms of increasing our mechanistic understanding, but also lead to the development of novel therapeutic strategies for patients with congenital valve abnormalities.

---

[1] This chapter, with modifications, was previously published as: Lindsey, S.E., and Butcher, J. (2011). The cycle of form and function in cardiac valvulogenesis. *Aswan Heart Centre Science & Practice Series*, 1-17.

1.2 Introduction

Congenital heart defects are among the most severe congenital abnormalities [1], accounting for over 29 percent of deaths from developmental abnormalities and 1 percent of infant mortality [2]. Advances in diagnostic technology and perinatal/neonatal intervention techniques facilitated a 33.3 percent decline in deaths from congenital heart defects between 1999 and 2006. If all patients with congenital heart defects born in the United States in the year 2000 underwent full treatment, the American Heart Association estimated 750,000 survivors for those suffering from simple lesions, 400,000 for those suffering for moderate lesions and 180,000 for those suffering from complex lesions. Without treatment these numbers would decline to 400,000, 220,000, and 30,000 respectively [2]. While technology and access to health care facilities are prevalent in the United States, most developing countries are not afforded the same luxuries. In impoverished countries, where 80 percent of all cardiovascular disease occurs, there is a lack of research and applicable therapies for cardiovascular disease [3]. Overshadowed by the trials of infectious disease, the large burden of cardiovascular disease is often overlooked in these countries [4].

Complementing advancements in surgical techniques has been a steady increase in our understanding of how the heart and valves develop and malform [5-7]. The classical approach was to observe morphological changes developed as a result of experimental manipulations in animal models, but over the past thirty years tools from the genetic revolution have dominated learning in this field [8-11]. Very recently, however, the joining of classical experimental and genetic approaches has revealed vast potential for understanding that can be applied directly to clinical experience [12, 13]. It is becoming increasingly clear that the proper formation of the heart is intimately tied to its proper function at each stage of development. While these responses at a cellular

level are driven by gene expression changes, it is networks of genes rather than single genes that are coordinated to bring about cardiac tissue assembly and remodeling [14]. Therefore, the role of the cellular microenvironment, particularly mechanical forces [15] and the heterogeneous extracellular matrix [16, 17], have moved center stage in this pursuit. Advancing this frontier does not require the latest in first world research technology, but rather a focused synergy of biological and engineering disciplines. In this review, we summarize what is known about the morphogenesis of heart valves from the perspective of microenvironmental signaling, animal models and experimental techniques. We then conclude with some comments regarding microenvironmental regulation of key congenital heart defects.

1.3 Morphogenesis of valves

Prevalvular Cushions. The early embryonic heart originates from bilaterally symmetric fields of mesoendodermal cells that migrate and fuse medially to form a linear tube with an outer sheath of myocardial progenitor cells and an inner layer of endocardial cells. Separating these two layers is a gelatinous acellular hyaline matrix called the cardiac jelly. Initially, the cardiac jelly is present throughout the heart tube, but becomes restricted to the atrioventricular (AV) canal and outflow tract (OT) segments [18]. Recent studies suggest that TBX3 [19] and Notch1 [20] act in these regions to localize the myocardial-endocardial signals that initiate valve formation. In the first stage of this process, a subset of endocardial cells lining these two zones transform into a mesenchymal phenotype and invade the cardiac jelly [21, 22]. The molecular process of endocardial to mesenchymal transformation (EMT) has been studied for over thirty years, with over 100 regulatory genes identified [23-29]. This invasive, proliferating mesenchyme progressively remodels the hyaluronan matrix, replacing it with proteoglycans, matricellular proteins, and eventually structural

proteins such as collagen I [16, 30, 31]. These amorphous, compliant, cellularized masses, now dubbed cushions, continue to grow and extend into the lumen space [32]. Two cushions (superior and inferior) form initially in the AV canal at HH16 (E9.5 in mouse), followed by the appearance of two mural/lateral cushions on the left and right side of the AV canal at HH19 [33] (Figure 1A). The superior and inferior AV cushions fuse together by HH26 (E12 in mouse) forming a septation of the AV canal that joins with the ventricular septum and the protruding atrial cap. The lateral portions of this fused mass undergo continued remodeling to valves, as do the left and right mural cushions.

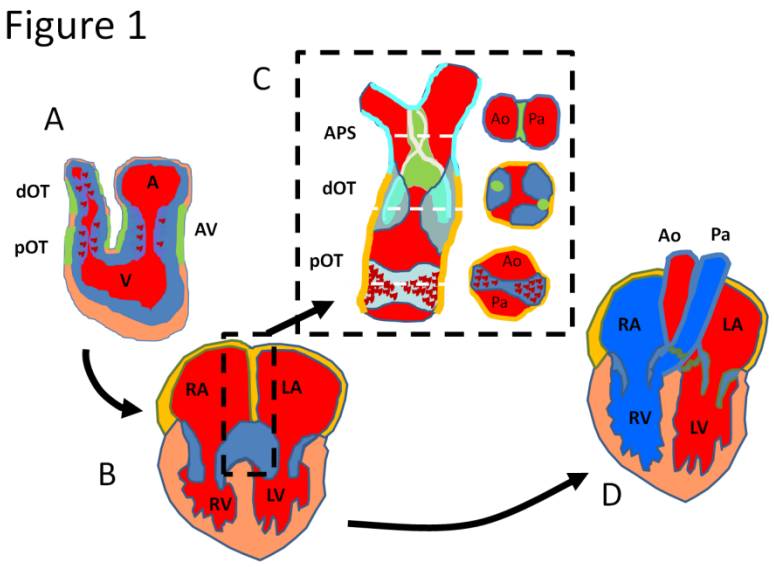

Figure 1.1: Cardiac and valvular morphogenesis.
After the heart loops, endocardially derived mesenchyme (blue) invades the cardiac jelly (blue) in the atrioventricular (AV) junction and distal and proximal outflow tract (dOT and pOT respectively) segments (red cells) (A). These primitive structures, dubbed cushions, grow into the early atrioventricular (B) and semilunar valves (C) of the now septated four chambered fetal heart. Note the invading aorticopulmonary septum (APS, green) that spirals through the outflow tract to create separate pulmonic (Pa) and aortic (Ao) outlet arteries, each with their own valve primordia at the dOT site, while at the pOT site the cushions become myocardialized to form the pulmonary infundibulum. The valves become fully condensed into thin fibrous tissues in the mature heart (D). A, atrium; V, ventricle; R, right; L, left.

Outflow tract. The outflow tract is somewhat different in that endocardial cells along nearly the whole tubular lumen undergo EMT. Paired bulges emanating in proximal (just outside the right ventricle) and distal zones (just after a 'dogleg' bend in the OT) become cushions around HH22/E10, while the rest of the cardiac jelly regresses. A third distal cushion ridge forms later (HH25/E11). The proximal/conal cushions are alternatively referred to as the septal/sinistroventral and parietal/dorsodextral ridges [34, 35]. These growing cushions also fuse in the midline, creating two tortuous lumens. Between HH26/E11.5 and HH30/E13, the distal dorsal cushion of the OT aligns with the proximal left cushion along the inner heart curvature, continuous with the superior cushion of the AV canal. Simultaneously, a wishbone shaped ridge of mesenchyme invades the outflow tract in a spiraling pattern, separating it into left and right portions and dividing the outflow cushions into two groups of three. While the fused proximal cushions myocardialize and form a muscular infundibulum separating the right and left ventricular outlets, the distal cushions become the rudiments of the pulmonary and aortic outlet valves [35] (Figure 1C). Comparative animal staging is presented in Table 1.

Table 1

Human (days) [weeks]	Mouse (E)	Chick (HH)	zebrafish (hpf)	Major events in heart development
22 [3 wks]	7 - 8	7-10		Fusion of paired heart tubes
22 [3 wks]	7. 5 - 8.5	10	24-36	|First appearance of myofibrils in myocytes
				| First myocardial contractions
				| Cardiac looping (mouse E 8.5)
24 [3.5 wks]	8 -8.5	9-12+	22	First blood flow through heart
26 [3.5+ wks]	9-11	11-12		First ventricular trabeculations
28 [4 wks]	10-12	13-22	60	First definable endocardial cushions (chick 28)
29 [4 wks]	11-13.5	15-23		First appearance atrial septum prium
31 [4.5 wks]	12	24-28		First appearance primordia semilunar valves, start AV septation
33 [4.5+ wks]	12-13	25-28	96	|Completion AP septum
35 [5 wks]	13-15	26-31		| completion intraventricular septation
37 - 43 [5+wks to 6wks]		27-34	105	| maturation semilunar valves

Table 1.1: Comparative cardiovascular development across animal models.[2]

1.4 Remodeling into fibrous leaflets

Atrioventricular Valves. The AV myocardium forms a fold at its junction with the ventricular myocardium creating a substrate on which the AV cushions can extend. The cushions extend along their substrate through the expansion of a proliferation zone in the subepithelial portion of the AV cushions [36]. Fenestrations develop as a result of the elongating cushions and the ventricular tissue underneath the cushion tissue delaminates, resulting in primitive leaflets that are continuous with developing papillary muscles [37] and the simultaneous expansion of the ventricular OT [38].

[2] Adapted from [109-111]

The myocardial tissue of the AV valves disappears and they condense into fibrous leaflets (Figure 2) [39]. Thin strands of elongated muscle remain tethered to the valve tissue with thickened trabecular aspects on the ventricular myocardial wall. These structures become the tendinous chords and papillary muscles of the mature valve [40].

Figure 2

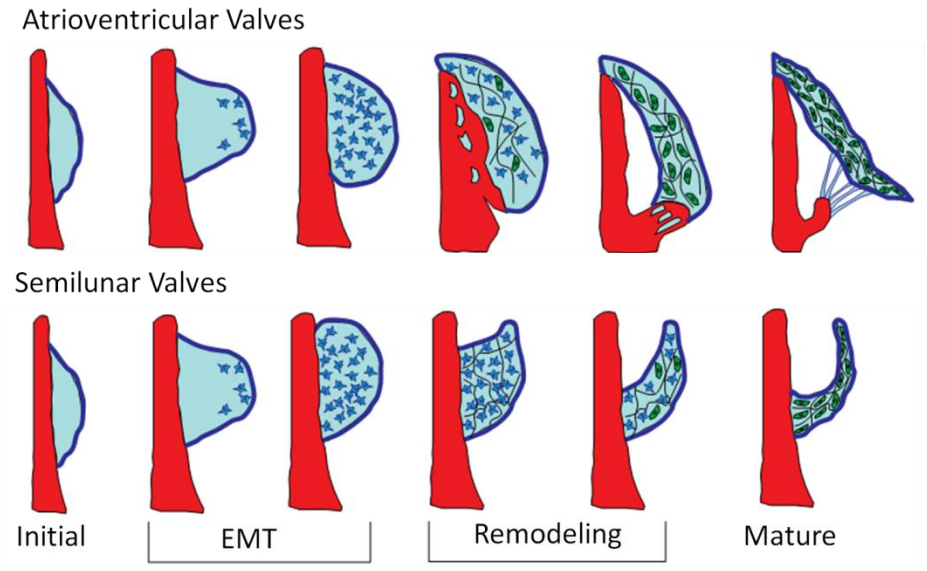

Figure 1.2: Schematic of the morphogenic transition from globular cardiac jelly to fibrous cusps/leaflets of the semilunar and atrioventricular valves.[3]

Outflow Tract. Unlike the AV valves, which formed through delamination from the muscular walls, valves of the OT form through a process of excavation or hollowing of the cushion's aortic side. Cushion excavation begins at HH29/ED13 with a small depression in the arterial face of the cusps. The endothelium lining the aortic surface

[3] Taken from [42]

of the valves becomes thickened with rounded cells that flake and undergo apoptosis, while the ventricular epithelium remains flat and elongated [41]. The deepening furrow condenses the fibrous matrix around it [42], creating thin cusps of tissue that are attached in an arc pattern called the commissures (Figure 2).

1.5 Valve tissue maturation

Extracellular matrix striation. Throughout the formation of the prevalvular complexes, endocardial cushions undergo a transition from more pliable structures (HH 17) to rigid structures (HH21) capable of successfully fusing and opposing flow [17]. This increase in rigidity is accompanied by a change from a hyaluronan rich cushion to a more collagen filled cushion. As the valves mature the extracellular matrix (ECM) transforms into three overlapping layers known as the fibrosa, spongiosa and ventricularis. The fibrosa, or arterial aspect of the cusp, is composed primarily of collagen fibers aligned in the parallel orientation providing stiffness and strength to the valve [43, 44]. The central spongiosa zone is composed of loosely arranged proteoglycans, presenting a compressible matrix that allows for shape change during the cardiac cycle [44]. The ventral side of the ventricularis contains elastin fibers interspersed with short radially aligned collagen fibers [45]. In the human fetus, the homogenous structure of 14 week post gestation valves becomes a bilaminar structure with sparse, loose, unorganized collagen by week 20. This period of ECM stratification corresponds with valvular interstitial cell (VIC) compartmentalization. Between the 14 and 20 week gestation period, VICs showed significantly higher proliferation indices and expressed the α –smooth muscle actin (α-SMA) positive phenotype attributed to myofibroblasts [46]. Trilaminar structure doesn't become apparent until 36 weeks of gestation and still differs from the normal adult valve structure. During tissue elongation both aggregan, a chondroitin sulfate proteoglycan,

and collagen III, a collagen found abundantly in cartilage, are expressed. Aggregan and collagen can also be seen in the fibrosa during cusp remodeling, with aggregan appearing in the spongiosa as well. Tenascin, a large elastic glycoprotein is localized to the annulus, on which the valves anchor, during cushion elongation and extends into the fibrosa and ventricular endothelium during cusp remodeling. It has been shown to mediate cell adhesion and migration functions [47]. Elastin, a vascular matrix protein, is present in the proximal ventricularis during cusp remodeling and exhibits increased expression throughout development.

Versican is a chondroitin sulfate proteoglycan with a high affinity for binding to hyaluronan [48]. It is encoded by the versican (PG-M) gene and can be found in the crest of the developing atrial and ventricular septa throughout cushion and valve development. Versican expression is detected in the AV canal as cells undergo EMT and migrate into the cardiac jelly. At E10.5 versican is highly expressed in both the AV cushions and the newly developing cushions of the OT. Versican protein expression in the AV and OT cushions increases as the cushions transition into more rigid structures and continues to be highly expressed throughout development [49]. Gaussin et al. suggest that the late embryonic and early neonatal valves undergo a process of condensation, elongation, formation of nodular thickenings, and ECM remodeling. Condensation begins at the atrial cusp side (mouse E15.5) and expands toward the ventricular side (Mouse E18.5), resulting in a 1.3 fold increase in cellular density. Increased expression of α-SMA, fibronectin, N-cadherin, and proliferating cell nuclear antigen indicate underlying mechanisms of interstitial collagen bridging, cellular adhesion and proliferation. At E18.5, the length of the papillary muscle side of the leaflets elongates past its once continuous position with the free edge. Both edges continue to increase in length postnatally, with the papillary muscle level remaining

significantly longer than the free edge. Proliferation is shown to be restricted to the distal tip of the leaflet and the point anchoring the papillary muscle [50]. A second phase of elongation occurs after neonatal day (N) 4.5, when rapid growth of the heart is thought to pull the leaflets at the papillary level. Elongation is accompanied by decreased cell density and decreased interstitial collagen cell bridging. This is followed by postnatal ECM remodeling. At E15.5 and 18.5 both hyaluronan and versican are present in the mitral mural leaflet except in the area of condensation. These proteins become restricted to the arterial side of the leaflet beginning at N6.5. Similarly, collagen I expression is seen throughout the entire leaflet between E15.5 and E18.5 before being restricted to the ventricular side after birth. The triscupid leaflet also exhibits these patterns of homologous expression followed by restriction (Figure 3). Hyaluronan and versican become restricted to the atrial side of the tricuspid leaflet at 8 weeks of age; collagen I is restricted to the ventricular side of the leaflet at 8 weeks of age [50]. Nodular thickenings, marked by collagen IV expression, develop at the closure points of the AV valve [51].

Figure 3

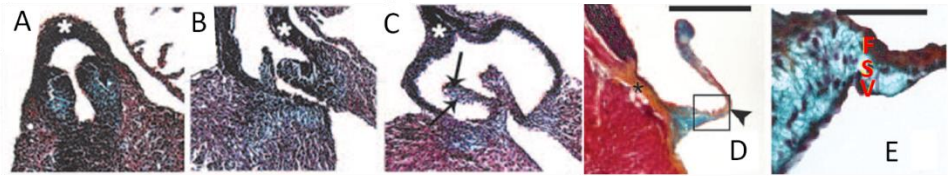

Early	Late	Postnatal
Hyaluronan +++	Hyaluronan ++	Hyaluronan + (S)
Versican +	Versican ++	Versican +
Fibrillin 2 +	Tenascin ++	Tenascin ++
Fibronectin +	Collagen I +	Collagen I +++
Collagen I –	Collagen II, V, VI ++	Collagen III ++ (F)
Elastin –	Elastin +/-	Elastin ++ (V)

Figure 1.3: Protein expression in extracellular matrix remodeling.
Adapted from [46,50,54,55], (+) and (-) indicate degrees of expression. S, Spongia; V, ventricularias; F, Fibrosa. Pictures examine Movat's pentachrome stain of extracellular matrix (ECM) organization and valvular interstitial cell (VIC) compartmentalization within mouse semilunar valves as seen in the (A) cushion, (B) elongation, and (C) remodeling period. The white asterisk indicates the aorta; arrows highlight cusp and leaflet remodeling. (D) Showa mature valve cusps, the black asterisk marks the annulus, the arrow marks the leading edge ventricularis. The boxed area is magnified in (E). Elastin fibers are black, collagen yellow, proteogylcans blue, cell nuclei purple, and muscle red.

Cellularity and differentiation. Many of the structural changes that occur throughout development are facilitated by phenotypical changes at the cellular level. Along with ECM stratification, valve maturation is accompanied by a valvular interstitial cell transition from an activated myofibroblastic-like phenotype to a quiescent fibroblast phenotype. VICs exhibit an activated myofibroblast-like phenotype abundant in matrix metalloproteinase-collagenases thoughout development [46]. These cells later regress into a quiescent state for much of adulthood. Aikawa et al. hypothesize that changes are a result of the valvular tissue adapting to its environmental conditions. When VICs

are stimulated by mechanical loading they become activated to mediate connective tissue remodeling. The cells then return to quiescence after equilibrium is restored [46]. Endocardial cell activation is accompanied by a change from a polygonal quiescent epithelial phenotype to spindle shaped migratory cells capable of invading the hyaluronan-rich cardiac jelly matrix. Endocardial cell transformation into a mesenchymal phenotype is characterized by expression of α-SMA [52]. α-SMA-positive cells are thought to play an important role in initiating or enforcing fusion of the OT cushions, as their expression persists until valve leaflets formation [34]. Cellular remodeling into a differentiated fibroblastic phenotype is responsible for the cushion condensation seen in the remodeling of the AV valves [53]. Throughout the whole process of valve maturation and remodeling, a progressive decrease in cell density is observed and continues throughout life; the total number of cells decreases substantially [54, 55]. While it has already been established that cardiac neural crest cells play a critical role in septation [56], recent studies have suggested that neural crest cells also orchestrate changes in ECM and apoptosis during valve remodeling [57]. Cardiac neural crest cells greatly contribute to the mesenchyme of the outflow tract [58]. Depleting the heart and aortic arch arteries of neural crest derived cells can result in hemodynamic changes that precede structural defects [59]. Semilunar valve leaflet remodeling is thought to be dependent upon interactions of the second heart field, neural crest and valve mesenchyme [57].

1.6 Hemodynamic changes during valvulogenesis

Growth and morphogenesis of the early embryonic heart are accompanied by changing hemodynamic function. Tables 2 and 3 evaluate changes in heart rate and blood pressure in humans and common animal models of cardiovascular development. In general, the embryonic heart rate increases as development progresses, though there are variations in species. Systolic and diastolic function follow a similar pattern, increasing as the embryo grows to accommodate increasing needs. As early as 43 hours after incubation, two blood streams are apparent in the heart. Incongruities in the size of the streams leads to spiraling, as the force of the larger stream pulls the smaller stream around it [60]. Movement of the spiraling site plays a large role in heart formation. The rapid growth of the endothelial tube inside the primitive heart is a result of the increase in blood pressure [61]. It is after this proliferation that cardiac jelly swellings appear in the AV canal and OT. In this manner, blood flow guides cardiac morphogenesis, sculpting tissue by promoting growth in response to increased demands. As the heart continues to grow, the energy extended in pulsatile flow increases from one-third to two-thirds of total energy between HH 18 and 29 [62]. Theoretical models of growth suggest the duration of vessel growth and their morphological characteristics are related to blood flow, shear stress and stretching forces [63]. Along with tissue sculpting, shear stress has been shown to regulate gene expression [13]. The magnitude of wall shear stress (WSS) is dependent on flow, pressure gradient and vessel wall motion [64]; WSS regulates events from cushion formation to leaflet maturation. As the heart forms, shear stress is greatest in the inner curvature and sites of lumen constrictions, corresponding to the AV canal and OT where the endocardial cushions form and develop into functioning valves. The lowest values of shear stress are found in the outer curvature and intertrabecular sinuses [65]. Shear stress patterns in the transvalvular region are summarized in Figure 4C.

Differences in wall shear stress are thought to affect valve formation. The formation of the muscular flap of a chick embryo develops in the presence of peak wall shear stress, while it's left mural counterpart differentiates into a fibrous leaflet under low shear stress [15]. High unidirectional shear stress has been suggested to promote cushion extension in the direction of flow in contrast to low recirculating flows, which encourage a prevalvular sculpting process [15]. Blood viscosity is defined by shear rate, the relationship of shear stress to the gradient of velocity [66]. The shear rate is determined both by the velocity of flow and the size of the vessel [67].

Table 2

Human :	Days or Weeks	bpm	Zebrafish:	dpf	bpm
	37days	101-109		2	141
	41 days	120-134		3	147.2
	45 days	130-158		4	165.9
	50-52 days	120-175		5	171.5
	8+ wks	150-176			
	9+ wks	150-172			
	10+ wks	140			
Chick:	**Stage (HH)**	**HR, bpm**	**Mouse:**	**Emb day**	**HR mean**
	16	110		10.5	124.7
	18	147.5		11.5	135.6
	21	145		12.5	147.3
	24	155		13.5	173.6
	27	155		14.5	194.3
	29	194			209
				15.5	
	31	221			
	35	230			

Table 1.2: Heart rate across developmental animal models.[4]

[4] Adapted from [62,110,112,113].

Table 3

Human:	weeks	Right Ventricular Systolic Pressure (mmHg)	Right Ventricular Diastolic Pressure (mmHg)	Zebrafish:	Body mass (mg)	Systolic Pressure (mmHg)	Diastolic Pressure (mmHg)
	14	30.996	8.4518		.5	0.061	0.3575
	16	35.424	9.6592		1.25	0.1045	0.84575
	18	39.852	10.8666		2.25	0.1625	1.49675
	20	44.28	12.074		3.25	0.2205	2.14775
	22	48.708	13.2814		3.75	0.2495	2.47325
	24	53.136	14.4888				
	26	57.564	15.6962				
Chick:	Stage (HH)	Ventricular Systolic Pressure (mmHg)	Vantricular Diastolic Pressure (mmHg)	Mouse:	Emb Day	Systolic Pressure (mmHg)	Diastolic Pressure (mmHg)
	16	1.15	0.25		10.5	3.44	.52
	18	1.31	0.33		11.5	5.01	.50
	21	1.61	0.34		12.5	6.43	.90
	24	1.96	0.4		13.5	9.0	.86
	27	2.35	0.56		14.5	11.15	.88
	29	3.45	0.82				

Table 1.3: Blood Pressure across developmental animal models.[5]

As shown in Figure 4A, the velocity profile of flow through the valves begins as a laminar parabola (HH 17), before resembling plug flow; wall shear stress follows a similar pattern (Figure 4B). Cushions form in areas of turbulent vortices, which arise shortly after peak inflow velocity and extend perpendicularly to the direction of flow [15]. The presence of cardiac cushions changes the geometry of the OT lumen cross-section, which plays a role in reducing blood flow [64]. Retrograde flow in these vortices creates a downward lip in the cushions at HH23 which become more pronounced throughout development [15]. Flow patterns as described in this section

[5] Adapted from [114-117].

are necessary for normal development. Changes in blood flow, and subsequent WSS patterns, are associated with many diseased conditions. While arterial flow may be altered to compensate for changing environmental conditions, maintenance of circulatory energy efficiency and pressure are critical for development [68].

Figure 4

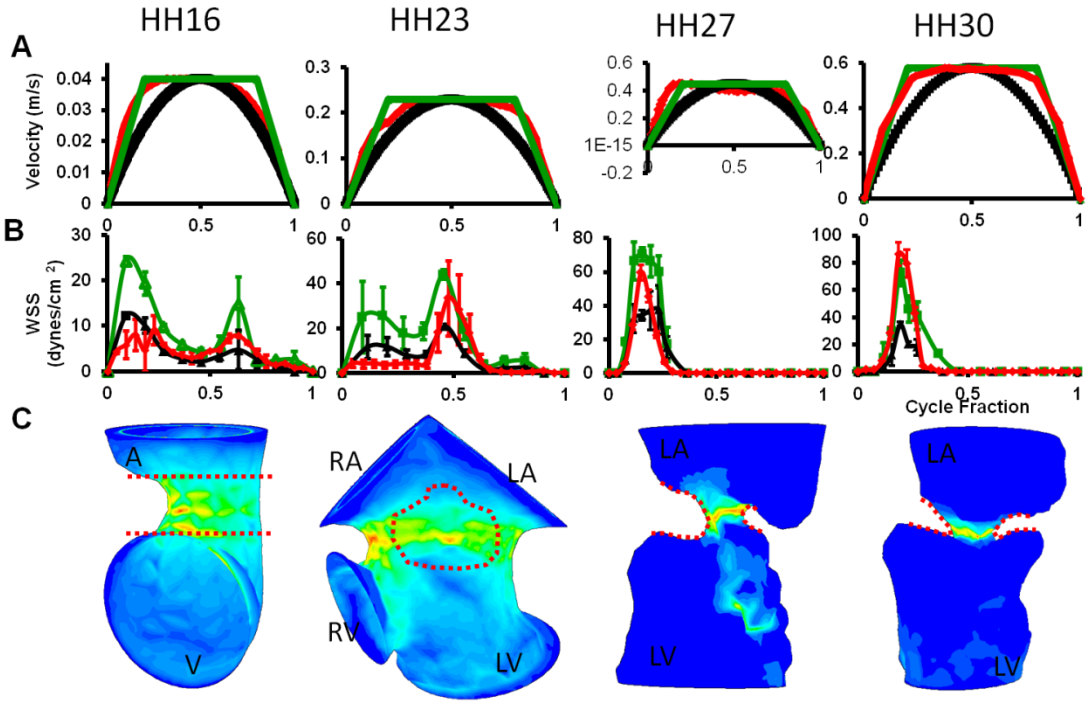

Figure 1.4: Hemodynamic changes in valvulogenesis.
Adapted from [108]. (A) peak velocity profiles (B) spatially averaged wall shear stress profiles. Red profiles correspond to flow and wall shear stress as calculated by computational fluid dynamics, black refers to the poiseuille profile and green plug flow (boundary layer is taken to be one-fifth diameter). (C) transvalvular shear stress quantifications calculated by computational fluid dynamics. High magnitudes of shear stress correspond to red; low magnitudes, blue.

Hemodynamics and gene regulation

Shear stress and shear stress-induced or repressed gene expression are important factors in remodeling of the cardiovascular system[13, 65]. While it is well known

that looping of the primitive heart can progress in the absence of hemodynamic forces [69], the role of hemodynamic signaling in valve formation is less understood and somewhat controversial. While many highlight shear stress development of cardiac malformations [5,6,12,70], other studies claim myocardial function trumps shear stress as a major epigenetic factor [9]. The close association of changes in flow pattern with genetic knockout models strongly supports the notion of shear stress as a major epigenetic factor. Hove et al. found the collapse of inflow and outflow tracts after blockage of flow to the atrium or from the heart to the aorta closely resembles that of jekyll mutatants, who exhibit abnormal flow due to a missing AV valve [5]. Hogers et al. show the divergence of blood from the yolk sac region to a more ventral course along the outer curvature of the conotruncus results in a host of cardiac malformations paralleling that of endothelin-1 knockout mice and neural crest ablated embryos [70]. While the exact mechanism is unknown, endocardial cells lining the luminal surface of cushions may play a role in regulating cushion and valvular morphogenesis through the integration of hemodynamic stimuli and signaling of the underlying mesenchyme [17].

A number of studies have demonstrated shear sensitivity of valvular morphogens *in vivo*. Endothelin-1 (ET-1) and endothelial nitric oxide synthase (NOS-3) are shear stress response genes thought to be involved in cardiovascular development, as knockout mice for these genes display a spectrum of cardiovascular defects [10, 11]. Groenendijk et al. investigated their expression throughout cardiovascular development in conjunction with kruppel-like factor-2 (KLF2), which has been shown to produce AV valve dysgenesis in zebrafish knockouts [65]. Results were consistent with the hypothesis that changes in blood flow result in morphologic changes by way of shear stress induced alterations in gene expression. Periods of intense

cardiovascular remodeling (HH20-HH30) were marked by ET-1 and KLF2/NOS-3 restriction to narrow sites [65]. ET-1 was negatively correlated to shear stress, while KLF2 and NOS-3 were positively correlated to shear stress. Changes in flow patterns due to vitelline vein obstruction resulted in altered shear stress and gene expression which, in turn, lead to cardiovascular malformations [13]. Following venous clipping and the induction of increased shear stress, KLF2 and NOS-3 levels were augmented, while ET-1 was downregulated. Areas of high shear stress in normal development, such as the upstream slope of outflow cushions, exhibited prominent changes in gene expression [13]. Both the magnitude and the retrograde nature of flow have been shown to influence valve patterning [15, 71]. During valvulogenesis, retrograde flow is thought to trigger flow responsive genes in the AV canal and initiate valve formation. Expression of Notch1b, KLF2a, and BMP4 become restricted to a region of high reversing flow in the AV canal [71].

In addition to the above genes, the expression patterns of potent vavular morphogens transforming growth factor-β (TGFβ), bone morphogenetic protein (BMP) and vascular endothelial growth factor (VEGF) are spatially and temporally restricted in a manner that suggests hemodynamic regulation [14, 72]. In situ hybridization shows TGFβ appearing in the endocardium of the valve forming regions around HH20, as flow transitions from laminar Poiseuille flow to more plug-like flow and rapidly increases in velocity [15]. Low levels of VEGFA gene expression are also found in the endocardium of the AV cushions at this time. By HH25 retrograde flow vortices are present throughout the cushion region, sculpting a downward pointing lip in the cushions [15]. TGFβ can be seen across cushion endocardium and mesenchyme and BMP is rapidly restricted to the boundary between the AV cushion and junctional myocardium. Following cushion fusion (HH28-29), a period coincident with increased

flow velocity and increased peak vorticity of the transvalvular region [15], TGFβ expression becomes restricted to remodeling regions of the valves, while VEGFA expression remains endocardial-specific [14]. The pronounced curvature of the septal leaflets causes inflowing blood to strike the left free wall of the left ventricle and spiral back towards the top of the ventricle. After peak velocity, spiraling flow along the outflow surface of the cushions results in a negative shear stress with respect to the inflow direction [15]. From HH33-36, TGFβ expression increases in the endocardium of the AV valves with greater expression on the atrial inflow side [14] (Figure 5). By this time, BMP2 expression is no longer detectable in the AV region.

Figure 5

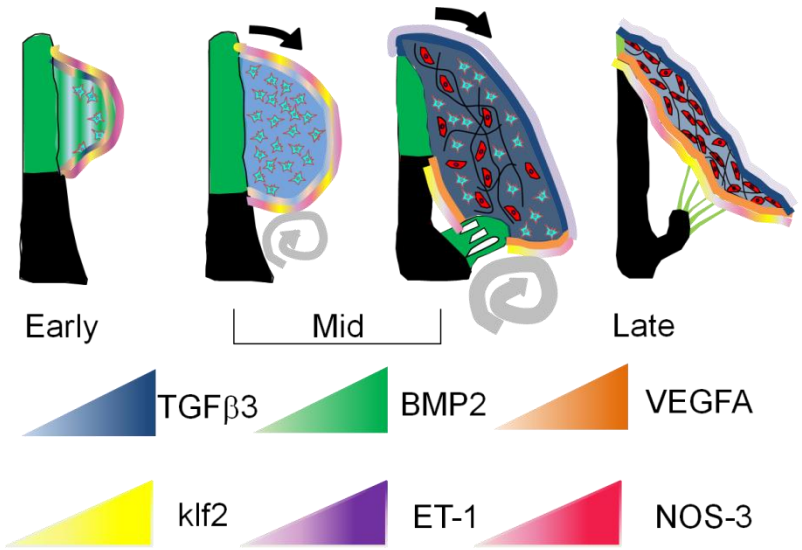

Figure 1.5: Summary of flow and gene expression in early, late and mid valvular cusps.

Adapted from [14, 65]. ET-1 is the only gene still expressed on both sides of the leaflet at late valvulogenesis. The increasing force of unidirectional flow in the atrial, inflow, surface corresponds with TGFβ and ET-1 expression, while the increase in magnitude of retrograde flow vortices on the ventricular side corresponds with VEGFA, NOS-3, KLF2, and ET-1 expression. BMP is restricted to the boundary between the cushions and junctional myocardium. Black arrows indicate inflow, gray spiral retrograde flow vortices.

1.7 Animal models of valve formation and maturation

The heart is already four chambered by the time human hearts are visible via ultrasound (8 weeks). Therefore, almost all of what we know about valve development has been obtained through animal models, including zebrafish, chick and mouse. Each model provides genetic or experimental advantages, with varying degrees of anatomical and morphogenetic similarities to that of humans (Table 4). The zebrafish embryo is virtually transparent, which permits the imaging of its internal structure using standard light microscopy [73]. The zebrafish's heart is the first organ to develop, resembling a three-week old human heart at 24 hours post fertilization (hpf) [74]. A large advantage of the zebrafish is that the embryo itself is not dependent on the cardiovascular system for at least 5 days post fertilization (dpf); sufficient oxygen is obtained by diffusion [75]. This allows for easy genetic manipulation of the heart. Large numbers of genetically identical offspring can be generated in the zebrafish. While heart formation of the zebrafish does parallel that of the human, the zebrafish only possesses a two-chambered heart. In addition, zebrafish do not undergo EMT, rather their valves emerge from the endothelium through cell rearrangements and shape changes [76].

Table 4

Summary of advantages and disadvantages of different animal models in the study of valve development

Organism:	Easy to Manipulate genetically ?	Easy access to embryos?	Extensive staging system ?	Easily facilitated observation of organogenesis?	Major anatomical /formation differences
Chick	yes	yes	yes	no	Muscular flap valve in AVJ
Mouse	yes	no	no	no	Less extensive striation Less pronounced chorda tendinae
Zebrafish	yes	yes	no	Yes	No EMT

Table 1.4: Summary of advantages and disadvantages of animal models in the study of cardiac development

The chick model is traditionally the most used model in the study of cardiac morphogenesis. The embryos are large, sustainable and develop externally to the mother. The chick embryo has been extensively study and its course of development universally staged. The anatomy of the chick heart closely parallels that of the human heart. A small difference is that, while the initial development of the AV leaflet resembles that of the human heart, the mesenchymal tissue is replaced by myocardium tissue resulting in the formation of a muscular flap valve in the right atrioventricular junction (AVJ) [77]. Constructs cannot be routinely injected into the chick embryo, as the cells are too small for the direct injection of constructs [78]. Genetic mutation is therefore performed through the use of electropolaration, where an electric field induces the direct opening of pores in the cell membrane, lipofection, microparticle bombardment, and viral vector transmission [79-81]. Transient or long-term gene

expression or repression is possible, as well as the tracing of affected cell lineages [80]. Recent advances have even allowed electroporation of expression vectors and morpholino oligonucleotides soon after laying with precise spatial and temporal control [82].

The mouse is the standard model for genetic manipulation as it is easy to genetically manipulate and provides a stable mammalian model of development. The mammalian cardiovascular system differs from that of the vertebrates and amphibians in that it couples to both yolk sac and placental circulations. Mouse embryos are harder to access as they develop inside their mother. While the mouse is a mammal, its heart still contains structural differences from that of the human heart. The mouse chordae are far less prominent than the pronounced tendinous chords of the human heart valves [77]. The arrangement of the atrioventricular septal structures is different in mice. The membraneous septum found in the human heart is seen as a less extensive thick structure in the fetal mouse, possibly as a result of incomplete delamination of the septal leaflet of the tricuspid valve [83].

1.8 Experimental techniques

Quantification of hemodynamic performance throughout development is a challenging task as the vessels are still forming and are very delicate. The use of imaging provides a noninvasive way to evaluate cardiac performance in normal and abnormal development. Jones et al. used confocal laser-scanning microscopy, a technique in which a laser is used to repetitively scan along a single line positioned perpendicularly to the targeted vessel [84]. The erythroblasts are tagged with green fluorescent protein (GFP) and a measurement of velocity is calculated based on the number of times a cell is seen crossing the same line. The minimum velocity detected can be adjusted

through the number of line scans performed, while the maximum velocity is a limit of instrumentation speed. Jones et al. were able to calculate speeds well above those detected in the embryonic mouse, highlighting confocal microscopy as a valuable tool. The method is limited in that it cannot determine the level of oscillatory stress. Unlike laminar stress, continuous particle tracking is needed to measure forces exerted by particles with circular or irregular trajectories [84]. Hove et al. used high speed fluorescent confocal imaging to visualize flow patterns inside the heart chambers of zebrafish [5]. Their study was limited in that digital particle velocimetry requires 3D movements be projected into a 2D plane, thereby collapsing and underestimating distances traveled by a given cell. Despite dealing with the underestimation of distance traveled, Hove et al. were able to quantify relative changes between a normal and developmentally perturbed heart. Beads were implanted into GFP embryos either in front of the sinus venous, to block blood influx into the atrium, or in the back of the ventricle to block blood efflux from heart to aorta. They noted an accumulation of erythrocytes in front of the atrium and inside the heart chamber respectively. In both cases the embryos showed severe regurgitation of blood inside the heart and reduced blood flows, resulting in dramatically reduced shear forces [5].

India ink is another method researchers use to visualize flow patterns in the developing embryo. Hogers et al. used India ink to study flow patterns in the normal and abnormal chick heart [70]. In their 1997 study, abnormal development was induced through the ligation of vitelline veins. Following unilateral ligation of the vein, blood immediately re-routed itself [70] producing a range of cardiac defects. Observed malformations included subaortic ventricular septal defects, semilunar valve anomalities, atrioventricular anomalies, and paryngeal arch artery malformations [70]. Ligations of the right and left vitelline veins produced a similar array of abnormalities.

Irrespective of the ligated veins, the shift in blood flow was predominantly to the ventral side of the outflow tract. This shift in force is thought to play a role in improper looping [6]. Perturbed embryos did not form a third chamber, lacked heart looping and possessed weak inflow and outflow tract walls which were collapsed and fused. Similar to vitelline vein ligation, venous clippings in which a microclip is inserted into the right lateral vein, induce a spectrum of outflow abnormalities. In the venous clip model, the load on the embryonic myocardium is temporarily reduced resulting in less developed ventricles and delayed cardiac looping [70]. In addition to ligating veins, left atrial ligations and conotruncal banding, in which a suture is passed over the conotruncus but not pulled tightly enough to arrest blood flow, have been performed [85]. In conotruncal banding, ventricular dilation was observed along with changes in the trabeculae. Interestingly, the right AV valve no longer consisted of a muscular flap but rather resembled a bicuspid structure. Left atrial ligations resulted in hypoplasia of the left ventricle. In all the above studies, surgically manipulated embryos developed abnormal cardiovascular phenotypes. The problem with ligations and clippings is that remodeling may be the result of mechanical interferences in addition to disruption of hemodynamic properties. There exists a need for more clinically relevant models.

Photoablation within an embryo is a powerful tool that can be used to study the underlying mechanisms of morphogenesis and as well as aid in the restoration of properties required for normal morphogenesis. Männer et al. demonstrated the use of photoablation as an alternative to ligation in their study of photoablation of the proepicardium (PE) in chick embryos [86]. Loss of PE function was induced by photoablation of the PE which led to long lasting loss of PE function. Previous experiments involving the blocking of normal PE behavior by means of physical

barriers did not permanently prevent the colonization of the developing heart with PE derived cells, instead it caused a delay in the formation of some PE derived tissues. Photoablation facilitated the complete elimination of the PE without damaging adjacent structures [86]. The authors were able to conclude that a subpopulation of PE-derived cells invading the mesenchyme of the AV cushions does not contribute any substantial number of cells to the mature AV valves. Yalcin et al. used photoablation as a way to disrupt AV cushion mechanics, instigating cardiac remodeling in a way similar to mechanical ligations. Results suggested a promising new minimally invasive technique for the study of disease formation in the embryonic heart [7].

1.9 Hemodynamics and congenital heart defects

The embryonic heart grows and develops to adapt ventricular geometry and function to optimize mechanical efficiency [87]. It is therefore unsurprising that many defects arise from alterations in the normal embryonic environment. Goerttlet suggested that deviations in normal heart development resulting from genetic or exogenous factors lead to alterations in embryonic tissue, while abnormal cardiac structure is the result of displaced blood-streams [88]. Distinctions between gene and hemodynamic-related abnormalities are not that well defined. Chromosomes linked to particular defects have been identified but do not provide the full picture, with roughly 10-15 percent of left ventricular outflow malformations linked to a chromosomal abnormality [89]. While underlying genetic mutations are associated with congenital heart defects, one cannot simply mutate a gene to induce a congenital heart defect. Alternatively, the mechanical perturbation of blood flow can induce diseased phenotypes, as altered flow patterns are the mark of many congenital heart defects. In this section the pathology of three major defects associated with valvular abnormalities are explored. These are

bicuspid aortic valve, hypoplastic left heart syndrome, and tetralogy of fallot. Abnormal hemodynamic patterning is associated with the development of all three defects.

Bicuspid aortic valve. Bicuspid aortic valve (BAV) disease is the most frequent congenital anomaly of the heart. It is commonly associated with aortic valve stenosis, regurgitation and endocarditis, though these symptoms develop much later despite the formation of irregular valves during development. In bicuspid aortic valve, the patient possesses a valve of limited mobility, as the free edges of the bicuspid valve are more straight than rounded. The leaflets are usually of unequal size with a raphe, or seam-like union, apparent in the larger leaflet [90]. Excessive length of one or both cusps results in abnormal contact which in turn leads to fibrous thickening that will later become diffuse and calcified. The strong correlation between a deficiency in the shear stress induced NOS gene and the development of BAV supports a role for hemodynamics in disease formation [8].

Stenosis usually develops in bicuspid valves containing no redundant cusp tissue, while valve incompetence is associated with redundancy and endocarditis. The valve likely becomes stenotic as its cusps become fibrotic and calcified. The large calcific deposits associated with BAV are unusual before the age of thirty and very prevalent thereafter [91]. In a 2003 study of 44 bicuspid aortic valves, BAV patients without significant stenosis or regurgitation were found to have a larger aortic annulus, aortic sinus and proximal ascending aorta when compared to normal tricuspid valves. The peak aortic velocity [92] and peak systolic wall velocity in the anterolateral region of the ascending aorta [93] were higher in BAV patients than controls, implying these regions are subjected to great levels of stress.

*Hypoplastic left hear*t. Hypoplastic left heart syndrome (HLHS) is marked by severe underdevelopment of the left ventricle. Patients born with HLHS continue to have some of the highest mortality rates within the first year of life among all infants with congenital heart defects [94]. No strong genetic correlation exists. In a study of 83 HLHS patients, nine had underlying chromosomal abnormalities, four had single gene defects, ten had one or more extracardiac anomaly and two were patients of insulin-dependent mothers [95]. Cardiac defects associated with HLHS include mitral valve hypoplasia or mitral stenosis coincident with a left heart obstruction of a hypoplastic left ventricle and aortic atresia, hypoplastic aorta, or coarctation of the aorta. The ascending aorta and aortic arch in patients with HLHS are thought to become hypoplastic as a result of diminished flow to the left ventricle and aortic outflow tract throughout development. Retrograde aortic flow may be responsible for impaired development of the aortic root and ascending aorta [96]. Out of 96 HLHS patients, 37.5 percent were found to have malfunctioning aortic and mitral valves, 50 percent had malformed AV valves and 12.5 percent exhibited dysplastic aortic valvular stenosis [97].

Harh et al. were among the first to investigate the hypothesis that alterations in the site of the primordial mitral valve may induce the HLHS phenotype. They accomplished this by placing a nylon device in the left AV canal. This resulted in greatly reduced or eliminated ejection of blood flow from the left ventricle into the ascending aorta, which limited the range of rhythmic aortic expansion. Failure of the cushion differentiation into a thin fibrous tissue resulted in a thickened hypoplastic valve and a subsequent hemodynamically induced hypoplasia. Narrowing or closure of the mitral valve resulted in an obligatory reversed atrial shunt [98]. Other mechanically induced

HLHS embryos have been shown to display altered ventricular filling patterns and altered epicardial strain patterns [99], though variations in heart rate and AV inflow velocity were acute to non-existent [100]. All of these studies add credence to the paradigm that altered ventricular filling in development results in altered ventricular function and geometry.

Tetralogy of fallot. Tetralogy of fallot (TOF) is a combination of a large ventricular septal defect, pulmonary stenosis, right ventricular hypertrophy, and an overriding aorta. As a result of anterocephaled deviation of a malaligned oulet septum, in combination with hypertrophy of septoparietal trabeculations, there is narrowing of the subpulmonary infundibulum [101]. This narrowing of the infundibulum facilitates greater right to left shunting via the malaligned ventricular septal defect and overriding aorta [102]. Aortic dilation has been shown to vary inversely with the degree of right ventricular outflow tract dilation [103]. In addition, there is a positive correlation between histological changes and the degrees of aortic dilation. Histological abnormalities are present in the media of the aortic root and ascending aorta. These abnormalities include focal loss of smooth muscle cells, fibrosis, elastic fragmentation, and disruption of elastic lamellae [104]. Among TOF patients, aortic dilation is greatest when coupled with pulmonary atresia, or malformation of the pulmonary valve, as aortic volume overloading is maximal. Hemodynamic stress from volume overloading is thought to play an important role in the initiation of aortic dilation, as aortic root dilation and regurgitation are commonly seen in congenital defects where there is volume overloading of the aortic root and ascending aorta [103]. Aortic regurgitation may occur as a direct result of dilation of the aortic annulus, which results in incomplete coaption of the aortic cusps or as a result of infective endocarditis [102].

1.10 Conclusion

In 2008 the infant mortality rate was 49 per 1000 live births worldwide, 6 per 1000 in developed nations and 85 per 1000 in severely underdeveloped countries [105]. Congenital heart defects account for 5 to 31 percent of these deaths [106]. Undoubtedly, much remains to be done to guarantee the appropriate medical care to children born across the world with cardiac abnormalities. The surgical treatment of congenital heart defects requires complex infrastructures and highly skilled professionals. Many developing countries are just now starting to build structures capable of delivering the appropriate care [106]; others lack the appropriate resources. In Africa, the ratio of congenital heart surgeons to individuals is 1:38,000,000 compared to the 1:3,500,000 seen in North American and Europe [107]. More accessible strategies are required to address the needs of children with congenital heart defects in developing countries. Researchers have a responsibility to focus on creating new solutions to tackle the clinical problems affecting children of developing countries using economically attainable strategies. These problems can begin to be addressed in animal models of clinically relevant congenital heart defects which are used to elucidate mechanisms of impaired remodeling. Understanding the underlying mechanisms of hemodynamics is essential to understanding valve development and congenital heart defect formation. The sequelae of genetic defects associated with congenital heart defects are suspected to be the result of upstream hemodynamic changes that are either poorly adapted to or caused by mechanics itself. New experimental and computational techniques can further this understanding and enable direct prediction of mechanical environmental consequences on heart and valve development. Regenerative strategies should utilize developmental signaling paradigms to accelerate and control tissue remodeling in valve disease.

1.11 Acknowledgements

This research was supported by funding from the American Heart Association, the National Science Foundation, the LeDucq Foundation, and The Hartwell Foundation. The authors have no financial interests to disclose.

References

1. Pradat, P. et al. The epidemiology of cardiovascular defects, part I: a study based on data from three large registries of congenital malformations. *Pediatric cardiology* **24**, 195-221(2003).

2. Lloyd-Jones, D. et al. Heart disease and stroke statistics--2010 update: a report from the American Heart Association. *Circulation* **121**, e46-e215(2010).

3. Yusuf, S. et al. Global Burden of Cardiovascular Diseases: Part I: General Considerations, the Epidemiologic Transition, Risk Factors, and Impact of Urbanization. *Circulation* **104**, 2746-2753(2001).

4. Yusef, S., Vaz, M. & Pais, P. Tackling the challenge of cardiovascular disease burden in developing countries. *The American heart journal* **148**, 1-4

5. Hove, J.R. et al. Intracardiac fluid forces are an essential epigenetic factor for embryonic cardiogenesis. *Nature* **421**, 172-7(2003).

6. Hogers, B. et al. Extraembryonic venous obstructions lead to cardiovascular malformations and can be embryolethal. *Cardiovascular research* **41**, 87-99(1999).

7. Yalcin, H.C. et al. Two-photon microscopy-guided femtosecond-laser photoablation of avian cardiogenesis: noninvasive creation of localized heart defects. *American journal of physiology. Heart and circulatory physiology* **299**, H1728-35(2010).

8. Lee, T.C. et al. Abnormal aortic valve development in mice lacking endothelial nitric oxide synthase. *Circulation* **101**, 2345-8(2000).

9. Bartman, T. et al. Early myocardial function affects endocardial cushion development in zebrafish. *PLoS biology* **2**, E129(2004).

10. Yanagisawa, H. et al. Dual genetic pathways of endothelin-mediated intercellular signaling revealed by targeted disruption of endothelin converting enzyme-1 gene. *Development* **125**, 825-836(1998).

11. Kurihara, Y. et al. Aortic arch malformations and ventricular septal defect in mice deficient in endothelin-1. *The Journal of clinical investigation* **96**, 293-300(1995).

12. Yashiro, K., Shiratori, H. & Hamada, H. Haemodynamics determined by a genetic programme govern asymmetric development of the aortic arch. *Nature* **450**, 285-8(2007).

13. Groenendijk, B.C.W. et al. Changes in shear stress-related gene expression after experimentally altered venous return in the chicken embryo. *Circulation research* **96**, 1291-8(2005).

14. Chiu, Y.-N. et al. Transforming Growth Factor beta, Bone Morphogenetic Protein, and Vascular Endothelial Growth Factor Mediate Phenotype Maturation and Tissue Remodeling by Embryonic Valve Progenitor Cells: Relevance for Heart Valve Tissue Engineering. *Tissue engineering. Part A* **00**, 1-10(2010).

15. Yalcin, H.C. et al. Hemodynamic patterning of the avian atrioventricular valve. *Developmental dynamics : an official publication of the American Association of Anatomists* **240**, 23-35(2011).

16. Person, A.D., Klewer, S.E. & Runyan, R.B. Cell biology of cardiac cushion development. *International review of cytology* **243**, 287-335(2005).

17. Butcher, J.T. et al. Transitions in early embryonic atrioventricular valvular function correspond with changes in cushion biomechanics that are predictable by tissue composition. *Circulation research* **100**, 1503-11(2007).

18. Markwald, R.R., Fitzharris, T.P. & Manasek, F.J. Structural development of endocardial cushions. *The American journal of anatomy* **148**, 85-119(1977).

19. Moorman, A.F.M. et al. Development of the building plan of the heart. *Annals of the New York Academy of Sciences* **1015**, 171-81(2004).

20. Luna-Zurita, L. et al. Integration of a Notch-dependent mesenchymal gene program and Bmp2-driven cell invasiveness regulates murine cardiac valve formation. *The Journal of clinical investigation* **120**, 3493-507(2010).

21. Zhou, B. et al. Characterization of Nfatc1 regulation identifies an enhancer required for gene expression that is specific to pro-valve endocardial cells in the developing heart. *Development (Cambridge, England)* **132**, 1137-46(2005).

22. Krug, E.L., Runyan, R.B. & Markwald, R.R. Protein extracts from early embryonic hearts initiate cardiac endothelial cytodifferentiation. *Developmental biology* **112**, 414-26(1985).

23. Eisenberg, L.M. & Markwald, R.R. Molecular Regulation of Atrioventricular Valvuloseptal Morphogenesis. *Circ. Res.* **77**, 1-6(1995).

24. Camenisch, T.D. et al. Temporal and Distinct TGFβ Ligand Requirements during Mouse and Avian Endocardial Cushion Morphogenesis. *Developmental Biology* **248**, 170-181(2002).

25. Butcher, J.T. et al. Periostin promotes atrioventricular mesenchyme matrix invasion and remodeling mediated by integrin signaling through Rho/PI 3-kinase. *Developmental biology* **302**, 256-66(2007).

26. Armstrong, E.J. & Bischoff, J. Heart valve development: endothelial cell signaling and differentiation. *Circulation research* **95**, 459-70(2004).

27. Tavares, A.L.P. et al. TGF beta-mediated RhoA expression is necessary for epithelial-mesenchymal transition in the embryonic chick heart. *Developmental dynamics : an official publication of the American Association of Anatomists* **235**, 1589-98(2006).

28. Runyan, R.B. & Markwald, R.R. Invasion of mesenchyme into three-dimensional collagen gels: a regional and temporal analysis of interaction in embryonic heart tissue. *Developmental biology* **95**, 108-14(1983).

29. Combs, M.D. & Yutzey, K.E. Heart valve development: regulatory networks in development and disease. *Circulation research* **105**, 408-21(2009).

30. Norris, R. a et al. Identification and detection of the periostin gene in cardiac development. *The anatomical record. Part A, Discoveries in molecular, cellular, and evolutionary biology* **281**, 1227-33(2004).

31. Bernanke, D. Hyaluronidase activity in embryonic chick heart muscle and cushion tissues and cells*1. *Developmental Biology* **106**, 351-359(1984).

32. Schroeder, J. a et al. Form and function of developing heart valves: coordination by extracellular matrix and growth factor signaling. *Journal of molecular medicine (Berlin, Germany)* **81**, 392-403(2003).

33. Snarr, B.S., Kern, C.B. & Wessels, A. Origin and fate of cardiac mesenchyme. *Developmental dynamics : an official publication of the American Association of Anatomists* **237**, 2804-19(2008).

34. Ya, J. et al. Normal development of the outflow tract in the rat. *Circulation research* **82**, 464-72(1998).

35. Qayyum, S.R. et al. Septation and valvar formation in the outflow tract of the embryonic chick heart. *The Anatomical record* **264**, 273-83(2001).

36. Sugi, Y. et al. Fibroblast growth factor (FGF)-4 can induce proliferation of cardiac cushion mesenchymal cells during early valve leaflet formation. *Developmental Biology* **258**, 252-263(2003).

37. Oosthoek, P.W. et al. Development of the atrioventricular valve tension apparatus in the human heart. *Anatomy and embryology* **198**, 317-29(1998).

38. Wenink, a C. & Gittenberger-de Groot, a C. Embryology of the mitral valve. *International journal of cardiology* **11**, 75-84(1986).

39. Lange, F.J. de et al. Lineage and morphogenetic analysis of the cardiac valves. *Circulation research* **95**, 645-54(2004).

40. Icardo, J.M. & Colvee, E. Atrioventricular valves of the mouse: III. Collagenous skeleton and myotendinous junction. *The Anatomical record* **243**, 367-75(1995).

41. Garcia-Martinez, V., Sanchez-Quintana, D. & Hurle, J.M. Histochemical and Ultrastructural Changes in the Extracellular Matrix of the Developing Chick Semilunar Heart Valves. *Cells Tissues Organs* **142**, 87-96(1991).

42. Butcher, J.T. & Markwald, R.R. Valvulogenesis: the moving target. *Philosophical transactions of the Royal Society of London. Series B, Biological sciences* **362**, 1489-503(2007).

43. Tan, H. et al. Expression and deposition of fibrous extracellular matrix proteins in cardiac valves during chick development. *Microscopy and microanalysis : the official journal of Microscopy Society of America, Microbeam Analysis Society, Microscopical Society of Canada* **17**, 91-100(2011).

44. Rabkin-Aikawa, E. et al. Dynamic and reversible changes of interstitial cell phenotype during remodeling of cardiac valves. *The Journal of heart valve disease* **13**, 841-7(2004).

45. Schoen, F.J. Aortic valve structure-function correlations: role of elastic fibers no longer a stretch of the imagination. *The Journal of heart valve disease* **6**, 1-6(1997).

46. Aikawa, E. et al. Human semilunar cardiac valve remodeling by activated cells from fetus to adult: implications for postnatal adaptation, pathology, and tissue engineering. *Circulation* **113**, 1344-52(2006).

47. Schellings, M.W.M., Pinto, Y.M. & Heymans, S. Matricellular proteins in the heart: possible role during stress and remodeling. *Cardiovascular research* **64**, 24-31(2004).

48. LeBaron, R.G., Zimmermann, D.R. & Ruoslahti, E. Hyaluronate binding properties of versican. *The Journal of biological chemistry* **267**, 10003-10(1992).

49. Henderson, D.J. & Copp, A.J. Specification , Septation , and Valvulogenesis in the Developing Mouse Heart. *Circulation Research* (1998).

50. Kruithof, B.P.T., Krawitz, S. a & Gaussin, V. Atrioventricular valve development during late embryonic and postnatal stages involves condensation and extracellular matrix remodeling. *Developmental biology* **302**, 208-17(2007).

51. Ho, S.Y. Anatomy of the mitral valve. *Heart* **88**, 5iv-10(2002).

52. Nakajima, Y. et al. Expression of smooth muscle alpha-actin in mesenchymal cells during formation of avian endocardial cushion tissue: a role for transforming growth factor beta3. *Developmental dynamics : an official publication of the American Association of Anatomists* **209**, 296-309(1997).

53. De la Cruz, M.V. & Markwald, R.R. Embryological development of the ventricular inlets. Septation and atrioventricular valve apparatus. *Living morphogenesis of the heart* (2000).

54. Hinton, R.B. et al. Extracellular matrix remodeling and organization in developing and diseased aortic valves. *Circulation research* **98**, 1431-8(2006).

55. Lincoln, J., Alfieri, C.M. & Yutzey, K.E. Development of heart valve leaflets and supporting apparatus in chicken and mouse embryos. *Developmental dynamics : an official publication of the American Association of Anatomists* **230**, 239-50(2004).

56. Kirby, M.L., Turnage, K.L. & Hays, B.M. Characterization of conotruncal malformations following ablation of "cardiac" neural crest. *The Anatomical record* **213**, 87-93(1985).

57. Jain, R. et al. Cardiac neural crest orchestrates remodeling and functional maturation of mouse semilunar valves. **121**, (2011).

58. Jiang, X. et al. Fate of the mammalian cardiac neural crest. *Development (Cambridge, England)* **127**, 1607-16(2000).

59. Stewart, D.E. et al. Hemodynamic changes in chick embryos precede heart defects after cardiac neural crest ablation DE Stewart, ML Kirby and KK Sulik Circ. Res. 1986;59;545-550. *Circulation Research* (1986).

60. Jaffee, O.C. Hemodynamic Factors in the Development of the Chick Embryo Heart. *The Anatomical record* **151**, 69-75(1965).

61. Chang, C. On the reaction of the endocardium to the blood stream in the embryonic heart, with special reference to the endocardial thickenings in the atrioventricular canal and the bulbus cordis. *The Anatomical Record* **51**, 253-265(1932).

62. Hu, N. & Clark, E. Hemodynamics of the stage 12 to stage 29 chick embryo. *Circ. Res.* **65**, 1665-1670(1989).

63. Taber, L. a & Eggers, D.W. Theoretical study of stress-modulated growth in the aorta. *Journal of theoretical biology* **180**, 343-57(1996).

64. Liu, A. et al. Finite element modeling of blood flow-induced mechanical forces in the outflow tract of chick embryonic hearts. *Computers & Structures* **85**, 727-738(2007).

65. Groenendijk, B.C.W. et al. Development-related changes in the expression of shear stress responsive genes KLF-2, ET-1, and NOS-3 in the developing cardiovascular system of chicken embryos. *Developmental dynamics : an official publication of the American Association of Anatomists* **230**, 57-68(2004).

66. Wells, R.E. & Merrill, E. Influence of flow properties of blood upon viscosity-hematocrit relationships. *Journal of Clinical Investigation* (1962).

67. Eckmann, D. & Bowers, S. Hematocrit, volume expander, temperature, and shear rate effects on blood viscosity. *Anesthesia & Analgesia* (2000).at <http://www.anesthesia-analgesia.org/content/91/3/539.full>

68. Lucitti, J.L., Tobita, K. & Keller, B.B. Arterial hemodynamics and mechanical properties after circulatory intervention in the chick embryo. *The Journal of experimental biology* **208**, 1877-85(2005).

69. Manning, A. & McLachlan, J.C. Looping of chick embryo hearts in vitro. *Journal of anatomy* **168**, 257-63(1990).

70. Hogers, B. et al. Unilateral Vitelline Vein Ligation Alters Intracardiac Blood Flow Patterns and Morphogenesis in the Chick Embryo. *Circ. Res.* **80**, 473-481(1997).

71. Vermot, J. et al. Reversing blood flows act through klf2a to ensure normal valvulogenesis in the developing heart. *PLoS biology* **7**, e1000246(2009).

72. Butcher, J.T. & Nerem, R.M. Valvular endothelial cells and the mechanoregulation of valvular pathology. *Philosophical transactions of the Royal Society of London. Series B, Biological sciences* **362**, 1445-57(2007).

73. Denvir, M.A., Tucker, C.S. & Mullins, J.J. Systolic and diastolic ventricular function in zebrafish embryos: influence of norepenephrine, MS-222 and temperature. *BMC biotechnology* **8**, 21(2008).

74. Glickman, N.S. & Yelon, D. Short survey Cardiac development in zebrafish : coordination of form and function. *Online* **13**, 507-513(2002).

75. Sehnert, A.J. et al. Cardiac troponin T is essential in sarcomere assembly and cardiac contractility. *Nature genetics* **31**, 106-10(2002).

76. Scherz, P.J. et al. High-speed imaging of developing heart valves reveals interplay of morphogenesis and function. *Development (Cambridge, England)* **135**, 1179-87(2008).

77. Wessels, A. & Sedmera, D. Developmental anatomy of the heart: a tale of mice and man. *Physiological genomics* **15**, 165-76(2003).

78. Stern, C.D. The chick; a great model system becomes even greater. *Developmental cell* **8**, 9-17(2005).

79. Muramatsu, T. et al. Comparison of three nonviral transfection methods for foreign gene expression in early chicken embryos in ovo. *Biochemical and biophysical research communications* **230**, 376-80(1997).

80. Nakamura, H. et al. Gain- and loss-of-function in chick embryos by electroporation. *Mechanisms of development* **121**, 1137-43(2004).

81. Chesnutt, C. & Niswander, L. Plasmid-based short-hairpin RNA interference in the chicken embryo. *Genesis (New York, N.Y. : 2000)* **39**, 73-8(2004).

82. Voiculescu, O., Papanayotou, C. & Stern, C.D. Spatially and temporally controlled electroporation of early chick embryos. *Nature protocols* **3**, 419-26(2008).

83. Webb, S. et al. Septation and separation within the outflow tract of the developing heart. *Journal of anatomy* **202**, 327-42(2003).

84. Jones, E. a V. et al. Measuring hemodynamic changes during mammalian development. *American journal of physiology. Heart and circulatory physiology* **287**, H1561-9(2004).

85. Sedmera, D. et al. Remodeling of chick embryonic ventricular myoarchitecture under experimentally changed loading conditions. *The Anatomical record* **254**, 238-52(1999).

86. Männer, J., Schlueter, J. & Brand, T. Experimental analyses of the function of the proepicardium using a new microsurgical procedure to induce loss-of-proepicardial-function in chick embryos. *Developmental dynamics : an official publication of the American Association of Anatomists* **233**, 1454-63(2005).

87. Lin, I.E. & Taber, L.A. A model for stress-induced growth in the developing heart. *Journal of biomechanical engineering* (1995).

88. Goerttler, K. Normale aud pathologische Entwicklung des menschlichen Herzens. (1958).

89. McBride, K.L. et al. Linkage analysis of left ventricular outflow tract malformations (aortic valve stenosis, coarctation of the aorta, and hypoplastic left heart syndrome). *European journal of human genetics : EJHG* **17**, 811-9(2009).

90. Yener, N. et al. Bicuspid aortic valve. *Annals of thoracic and cardiovascular surgery : official journal of the Association of Thoracic and Cardiovascular Surgeons of Asia* **8**, 264-7(2002).

91. Roberts, W.C. The congenitally bicuspid aortic valveA study of 85 autopsy cases. *The American Journal of Cardiology* **26**, 72-83(1970).

92. Nkomo, V.T. Bicuspid Aortic Valve Associated With Aortic Dilatation: A Community-Based Study. *Arteriosclerosis, Thrombosis, and Vascular Biology* **23**, 351-356(2003).

93. Bauer, M. et al. Different hemodynamic stress of the ascending aorta wall in patients with bicuspid and tricuspid aortic valve. *Journal of cardiac surgery* **21**, 218-20(2010).

94. Jenkins, K. et al. Consensus-based method for risk adjustment for surgery for congenital heart disease1. *Journal of Thoracic and Cardiovascular Surgery* **123**, 110-118(2002).

95. Natowicz, M. et al. Genetic Disorders and Major Extracardiac Anomalies Associated With the Hypoplastic Left Heart Syndrome The online version of this article , along with updated information and services , is located on the World Wide Web at : Genetic Disorders and Major Ext. *Pediatrics* (1988).

96. Simpson, J.M. & Sharland, G.K. Natural history and outcome of aortic stenosis diagnosed prenatally. *Heart (British Cardiac Society)* **77**, 205-10(1997).

97. Ilbawi, A.M. et al. Morphologic study of the ascending aorta and aortic arch in hypoplastic left hearts: surgical implications. *The Journal of thoracic and cardiovascular surgery* **134**, 99-105(2007).

98. Harh, J.Y. et al. Experimental production of hypoplastic left heart syndrome in the chick embryo. *The American journal of cardiology* **31**, 51-6(1973).

99. Tobita, K. & Keller, B.B. Right and left ventricular wall deformation patterns in normal and left heart hypoplasia chick embryos. *American journal of physiology. Heart and circulatory physiology* **279**, H959-69(2000).

100. Tobita, K. et al. Regional passive ventricular stress-strain relations during development of altered loads in chick embryo. *American journal of physiology. Heart and circulatory physiology* **282**, H2386-96(2002).

101. Gatzoulis, M. a et al. Echocardiographic and morphological correlations in tetralogy of Fallot. *European heart journal* **20**, 221-31(1999).

102. Tan, J.L., Gatzoulis, M. a & Ho, S.Y. Aortic root disease in tetralogy of Fallot. *Current opinion in cardiology* **21**, 569-72(2006).

103. Niwa, K. et al. Structural Abnormalities of Great Arterial Walls in Aorta : Biopsy Specimens. *Journal of Pathology, The* (2001).

104. Tan, J.L. et al. Intrinsic histological abnormalities of aortic root and ascending aorta in tetralogy of Fallot: evidence of causative mechanism for aortic dilatation and aortopathy. *Circulation* **112**, 961-8(2005).

105. Bureau, P.R. 2008 WORLD POPULATION Data Sheet. *Population (English Edition)* (2008).

106. Rosano, a et al. Infant mortality and congenital anomalies from 1950 to 1994: an international perspective. *Journal of epidemiology and community health* **54**, 660-6(2000).

107. Bernier, P.-L. et al. The challenge of congenital heart disease worldwide: epidemiologic and demographic facts. *Seminars in thoracic and cardiovascular surgery. Pediatric cardiac surgery annual* **13**, 26-34(2010).

108. Yalcin, H.C. et al. Hemodynamic patterning of the avian atrioventricular valve. *Developmental dynamics : an official publication of the American Association of Anatomists* **240**, 23-35(2011).

109. Stainier, D.Y. & Fishman, M.C. The zebrafish as a model system to study cardiovascular development. *Trends in cardiovascular medicine* **4**, 207-12(1994).

110. Phoon, C. Circulatory physiology in the developing embryo. *Current Opinion in Pediatrics* (2001).

111. Sissman, N.J. Developmental landmarks in cardiac morphogenesis: comparative chronology. *The American journal of cardiology* **25**, 141-8(1970).

112. Yu, Q. & Leatherbury, L. Cardiovascular assessment of fetal mice by in utero echocardiography. *Ultrasound in medicine & biology* (2008).

113. Keller, B. & MacLennan, M. In vivo assessment of embryonic cardiovascular dimensions and function in day-10.5 to-14.5 mouse embryos. *Circulation ...* (1996).

114. Ishiwata, T. et al. Developmental changes in ventricular diastolic function correlate with changes in ventricular myoarchitecture in normal mouse embryos. *Circulation research* **93**, 857-65(2003).

115. Hu, N. et al. Diastolic filling characteristics in the stage 12 to 27 chick embryo ventricle. *Pediatric research* **29**, 334-7(1991).

116. Hu, N. et al. Structure and Function of the Developing Zebrafish Heart. **157**, 148 -157(2000).

117. Johnson, P. et al. Intracardiac pressures in the human fetus. *Heart (British Cardiac Society)* **84**, 59-63(2000).

CHAPTER 2: REGULATION OF HEART DEVELOPMENT BY MECHANICAL FORCES[6]

2.1 Experimental Flow Alteration Techniques

Animal models of abnormal cardiac morphogenesis following experimental manipulation of flow champion hemodynamics as a driving force throughout development. Of note are conotruncal banding (CTB) and left atrial ligation (LAL) experiments performed in the early chick animal model. In CTB, a knot is tied around the conotruncus region of the outflow tract in an HH18 chick embryo, but not pulled tightly enough to arrest flow (Clark et al., 1984). This resulted in an immediate increase in ventricular pressure, subsequent ventricular dilation and abnormal trabeculae patterning. An increase in the blood velocity was observed in the banded section of the OFT (Rugonyi et al., 2008). Strain patterns emphasized the need for banded hearts to exert more energy to adequately support the embryo. Following CTB, there was a dilatation as well as thickening of the compact myocardium and trabeculae in LV (Sedmera et al., 1999).

In LALs, a suture is tied around the left atria and pulled tightly enough to disrupt flow in HH20-21 chick embryos (Sedmera et al., 1999). Following a left-atrial ligation, flow is shifted to the right side of the heart causing increased preload on the right ventricle and a decrease in preload on the left ventricle (Sedmera et al., 1999). Subsquent wall deformation patterns were observed in the right ventricle (RV) and left ventricle (LV) following LAL (Tobita and Keller, 2000). Both maximum and average AV canal velocities decreased immediately after LAL (at HH21, pre-septation) with

[6] This chapter, with modifications, was previously published as portions from: Lindsey, S.E., Butcher, J.T., Yalcin, H.C. (2014). Mechanical regulation of cardiac development. *Frontiers in Physiology,* 5, 1-15

respect to control embryos. At HH31 (post septation), average RV inflow velocity was higher in LAL embryos while maximum LV inflow velocity was lower in LAL embryos, consistent with flow redirection to the right side of the heart following LAL. A subsequent increase in RV flow in LAL embryos accelerated the onset of RV circumferential strain patterns observed in controls, while decreased flow in LV abolished these patterns. Through the use of computational fluid dynamics, Kowalski et.al were able to determine flow alterations immediately following a LAL, led to a decrease in WSS at the left atrioventricular canal as well as at the left side of the common ventricle in LAL embryos compared to controls (Kowalski et al., 2014).

LAL resulted in hypoplasia of the left heart structures with compensatory overdevelopment on the right side (Sedmera et al., 1999). Myocyte proliferation rate was decreased in the LV (Sedmera et al., 2002). Interesting, partial clipping of the right atrial appendage reversed these symptoms, immediately increasing flow to the left ventricle and subsequently increasing chamber volume and myocardial mass (deAlmeida et al., 2007). Similarly, addition of fibroblast growth factor-2, a factor previously shown to stimulate division of the embryonic myocytes, to the left ventricular myocardium in LAL and normal embryos, was also shown to attenuate phenotypic severity by increasing cellular proliferation (deAlmedia and Sedmera, 2009)

Abnormal development following CTB and LAL, also affected maturation of the conduction system (Reckova et al., 2003). CTB resulted in the early emergence of the mature apex-to-base activation sequence whereas LAL resulted in a delayed transition to the mature sequence. Following LAL, endothelin converting enzyme (ECE) protein, which is involved in the inductive recruitment of Purkinje fibers in embryonic chick conduction systems, was down regulated in the under-loaded LVs and up regulated in the over-loaded RV (Sedmera et al., 2008). Sankova et al. tested the effects of

hemodynamic unloading on the conduction system maturation using whole embryonic heart cultures (Sankova et al., 2010). In hearts cultured without hemodynamic loading, a significant decrease in the percentage activated through the primary ring conduction pathway was observed, suggesting primitive development of the conduction system. This phenotype was completely rescued with the artificial loading of the ventricles with a droplet of silicone oil suggesting that the appropriate loading is required during the early phases of the conduction system formation and maturation.

2.2 Hemodynamics and outflow vessel formation:

Outflow vessels are derived from the pharyngeal arch arteries. A total of six paired arches form successively from anterior to posterior throughout outflow tract development. Some of these vessels remodel into major arteries while others disappear. Third arch pair forms the mature brachiocephalic arteries while sixth arch pair forms pulmonary artery and ductus arteriosus. Aortic arch is derived from the right fourth arch in in the vertebrate model and from the left fourth arch in mammals (Hiruma et al, 1995). Truncus arteriosus and aortic sac septate cranially to caudally, triggering the separation of the pulmonary artery and right ventricular outflow tract anteriorly from the aorta and left ventricular outflow tract posteriorly (Qayyum et al., 2001, Hu et al., 2009)

Hemodynamic forces play a major role in extensive remodeling of the symmetric pairwise aortic arch system into a highly asymmetric system. Yashiro et.al. investigated mechanisms behind the regression of right sixth aortic arch and persistence of left sixth arch in mice (Yashiro et al., 2007). Using a variety of experimental and genetic mutant models, they found that, the genetic program, including the expression of Pitx2, induces a dynamic morphological change in the

OFT, which in turn generates a differential distribution of blood flow. Increased blood flow in the left sixth arch is sufficient to stimulate PDGFR and VEGFR2 signaling and the consequent maintenance of arterial structure, whereas the decreased blood flow in the right sixth arch results in its regression. Hemodynamics and arch morphology were studied for HH18 and HH24 chick embryos using computational modeling (Wang et al., 2009). Across stage comparisons revealed that, increased wall shear stress levels correspond with increased arch diameters, suggesting shear stress might be a stimulus for cell proliferation. In a follow up study, aortic arch flow dynamics in the intermediate stage HH21 was investigated (Kowalski et al., 2013). CFD analysis showed that WSS is substantially elevated compared to both the previous (stage 18) and subsequent (stage 24) developmental time-points, suggestive that acute increases in WSS are followed by a period of vascular remodeling to restore normative hemodynamic loading. Effects of altered hemodynamics on aortic arch morphogenesis was investigated by Hu et.al. (2009). LAL resulted in an immediate redistribution of blood flows through arch vessels, which eventually resulted in the askew and distorted formation of these vessels compared to controls. Overall, these results suggest that hemodynamic forces play a significant role in asymmetric remodeling of aortic arch network. Alterations in normal hemodynamic forces might be important sources for CHD related to outflow tract and arch network abnormalities, which include 50% of infants with a CHD (Roger et al., 2011).

2.3 Hemodynamics and congenital heart defects

The embryonic heart grows and develops to adapt ventricular geometry and function to optimize mechanical efficiency (Lin and Taber, 1995). Distinctions between gene and hemodynamic-related abnormalities are not that well defined. Chromosomes

linked to particular defects have been identified but do not provide the full picture, with roughly 10-15 percent of left ventricular outflow malformations linked to a chromosomal abnormality (McBride et al., 2009). While underlying genetic mutations are associated with congenital heart defects, genes cannot be mutated to produce congenital heart defects in the way that flow can be perturbed to induce diseased phenotypes. The use of computational modeling in the study of abnormal development has led to more detailed analyses of disease etiology and the mechanisms required for proper formation. In this section, the pathology of two major defects associated with abnormal hemodynamic pattering and valve formation is explored: bicuspid aortic valve and hypoplastic left heart syndrome.

Bicuspid aortic valve (BAV) disease is the most common congenital anomaly of the heart, wherein the patient is born with two aortic valve leaflets rather than three. This two cusped configuration constrains the patient, as the free edges of the bicuspid valve are more straight than rounded and offer limited mobility. The leaflets are usually of unequal size with a raphe, or seam-like union, apparent in the larger leaflet (Yener et al., 2002). BAV is frequently associated with aortic valve stenosis, regurgitation and endocarditis, though these symptoms develop well after valve formation. Excessive length of one or both cusps results in abnormal contact which in turn leads to fibrous thickening that will later become diffuse and calcified. Stenosis usually develops in bicuspid valves containing no redundant cusp tissue, while valve incompetence is associated with redundancy and endocarditis. The large calcific deposits associated with BAV are unusual before the age of thirty and very prevalent thereafter (Roberts, 1970). In a 2003 study of 44 bicuspid aortic valves, BAV patients without significant stenosis or regurgitation were found to have a larger aortic annulus, aortic sinus and proximal ascending aorta when compared to normal tricuspid valves. The peak aortic

velocity (Nkomo et al., 2003) and peak systolic wall velocity in the anterolateral region of the ascending aorta (Bauer et al., 2006) were also found to be higher in BAV patients than controls. This flow has been classified as helical or flow composed of a forward component along the long axis of the aorta and a rotational component rotating around the long axis in a circumferential direction (Bissell et al., 2013, Lorenz et al., 2014). A significant increase in absolute peak relative helicity is present during systole of BAV patients, with a considerably greater heterogeneous distribution of mean helicity in the aorta (Lorenz et al., 2014).

Recent advances in technology, particularly cardiovascular magnetic resonance imaging, have allowed scientists to map these regions and collect 3D spatial visualizations of flow patterns over time (Bissell et al., 2013, Lorenz et al., 2014). In this way, temporal evolution of complex flow patterns over time can be studied and linked to aortic function. Bissel et. al. found that patients with BAV had predominantly abnormal right-handed helical flow in the ascending aorta, larger ascending aortas, higher helical flow, elevated systolic angle and elevated systolic wall shear stress. In their study of 69 BAV patients, right-handed helical flow, occurred in 72% of patients, normal flow patterns were observed in 11%, complex flow in 13%, and left-handed helical flow in 4%. Distensibility, aortic strain, and pulse wave velocity of the aorta were similar across all groups, supporting the hypothesis that flow abnormalities initiate the aortopathy as a potential compensatory response to maintain constant WSS (Bissell et al., 2013). Chandra et al, 2012 used fluid-structure interaction models to quantify regional BAV leaflet wall-shear stress over the course of aortic valve disease and link the degree of leaflet calcification to orifice area, oscillatory shear index and temporal shear magnitude. While the regular tricuspid and non-coronary BAV leaflets shared similar shear stress characteristics, the base of the fused BAV leaflet fibrosa exhibited showed that the temporal shear magnitude was

heavily modulated by the degree of calcification, with 6-fold, 10-fold and16-fold increases seen over BAV ranging gtom normal to severely calcified. Results for Chandra et al support the existence of a mechano-sensored progression of calcified aortic valve disease in the BAV patients (Chandra et al., 2012)

Hypoplastic left heart syndrome (HLHS) consists of a severely underdeveloped left ventricle. No strong genetic correlation exists. In a study of 83 HLHS patients, nine had underlying chromosomal abnormalities, four had single gene defects, ten had one or more extracardiac anomaly and two were patients of insulin-dependent mothers (Natowicz et al., 1988). Disease formation is thought to result from diminished flow to the left ventricle and aortic outflow tract throughout development. Retrograde aortic flow may play a role in impaired development of the aortic root and ascending aorta (Simpson and Sharland, 1997). Cardiac defects associated with HLHS include mitral valve hypoplasia or mitral stenosis coincident with a left heart obstruction of a hypoplastic left ventricle and aortic atresia, hypoplastic aorta, or coarctation of the aorta. Out of 96 HLHS patients, 37.5 percent were found to have malfunctioning aortic and mitral valves, 50 percent had malformed AV valves and 12.5 percent exhibited dysplastic aortic valvular stenosis (Ilbawi et al., 2007). The closest experimental animal recapitulation of HLHS comes from the left atrial ligation in which a suture is made to repress left atrium volume in HH21 chicken embryos. Changes in longitudinal and circumferential strain were highlighted as disease formation drivers (Tobita and Keller, 2000). Kowalski et.al. recently studied the immediate blood flow alterations following LAL using an in-silico CFD model. They found that intracardiac flow patterns change immediately following LAL. Wall shear stress was reduced at the left atrioventricular canal and left side of the common ventricle. These changes in shear stress may be responsible for the underdevelopment of left heart structures previously seen in literature (Kowalski et al., 2013). Variations

in heart rate and AV inflow velocity were acute to non-existent in these models (Tobita et al., 2002). Mechanical manipulation of ventricular filling began with Harh et. al. (Harh et al., 1973) They investigated importance of mitral valve placement by inserting a nylon device in the left AV canal, thereby greatly reducing ejection volume from the left ventricle into the ascending aorta. Failure of the cushion differentiation into a thin fibrous tissue resulted in a thickened hypoplastic valve and a subsequent hemodynamically induced hypoplasia. Narrowing or closure of the mitral valve resulted in an obligatory reversed atrial shunt. These studies all support the role of hemodynamics in abnormal cardiac and valve formation, though many questions remain about the channels through which hemodynamics works. Combining experimental results with computation models is a promising way to connect and understand the mechanisms through which this change may come about.

2.4 Conclusions and future directions

Mechanical forces are essential coordinators of growth and remodeling of the embryonic tubular heart into a multi-chambered, valved pump capable of functioning a lifetime. Late embryonic and fetal morphogenesis and remodeling are clinically relevant periods of CHD formation, and there is a need for understanding the mechanobiological mechanisms guiding heart development at these periods. Specifically, most CHD result from either improper alignment of the chambers and the outflow tract, abnormal remodeling of cushions into valves or incomplete remodeling of the aortic arches into great vessels. In order to investigate the biomechanics of embryonic CHD formation, there is a need for quantitative imaging modalities capable of visualizing morphogenesis at these later stages and quantifying hemodynamic changes. For the experimental animal studies, micro-computed tomography, optical

coherence tomography and other similar imaging modalities can be integrated with computational fluid dynamics analysis and growth modeling. Utilizing minimally invasive surgical techniques such as laser ablation, to induce in vivo hemodynamic/mechanical manipulation of embryonic development will enable scientists to separate hemodynamic and genetic contributions to disease phenotype. In vitro 3D culture and bioreactor studies will help to understand how specific mechanical forces influence multi-scale biological responses. A better understanding of normal and abnormal cardiac morphogenesis will lead to more targeted pharmacological interventions and restorative care. Likewise, surgical intervention, whether in utero or postnatal, can become more advanced and better informed (Foker et al., 2013).

1. Bauer, M., Siniawski, H., Pasic, M., Schaumann, B., & Hetzer, R. (2010). Different hemodynamic stress of the ascending aorta wall in patients with bicuspid and tricuspid aortic valve. *Journal of cardiac surgery*, *21*(3), 218–20.

2. Bissell, M. M., Hess, A. T., Biasiolli, L., Glaze, S. J., Loudon, M., Pitcher, A., … Myerson, S. G. (2013). Aortic dilation in bicuspid aortic valve disease: flow pattern is a major contributor and differs with valve fusion type. *Circulation. Cardiovascular imaging*, *6*(4), 499–507.

3. Chandra, S., Rajamannan, N. M., & Sucosky, P. (2012). Computational assessment of bicuspid aortic valve wall-shear stress: implications for calcific aortic valve disease. *Biomechanics and modeling in mechanobiology*, *11*(7), 1085–96.

4. Harh, J. Y., Paul, M. H., Gallen, W. J., Friedberg, D. Z., & Kaplan, S. (1973). Experimental production of hypoplastic left heart syndrome in the chick embryo. *The American journal of cardiology*, *31*(1), 51–6.

5. Ilbawi, A. M., Spicer, D. E., Bharati, S., Cook, A., & Anderson, R. H. (2007). Morphologic study of the ascending aorta and aortic arch in hypoplastic left hearts: surgical implications. *The Journal of thoracic and cardiovascular surgery*, *134*(1), 99–105.

6. Kowalski, W. J., Teslovich, N. C., Menon, P. G., Tinney, J. P., Keller, B. B., & Pekkan, K. (2014). Left Atrial Ligation Alters Intracardiac Flow Patterns and the Biomechanical Landscape in the Chick Embryo, 1–11.

7. Lin, I. E., & Taber, L. A. (1995). A model for stress-induced growth in the developing heart. *Journal of biomechanical engineering*.

8. Lorenz, R., Bock, J., Barker, a J., von Knobelsdorff-Brenkenhoff, F., Wallis, W., Korvink, J. G., … Markl, M. (2014). 4D flow magnetic resonance imaging in bicuspid aortic valve disease demonstrates altered distribution of aortic blood flow helicity. *Magnetic resonance in medicine : official journal of the Society of Magnetic Resonance in Medicine / Society of Magnetic Resonance in Medicine*, *71*(4), 1542–53.

9. McBride, K. L., Zender, G. a, Fitzgerald-Butt, S. M., Koehler, D., Menesses-Diaz, A., Fernbach, S., … Belmont, J. W. (2009). Linkage analysis of left ventricular outflow tract malformations (aortic valve stenosis, coarctation of the aorta, and hypoplastic left heart syndrome). *European journal of human genetics : EJHG*, *17*(6), 811–9.

10. Natowicz, M., Chatten, J., Clancy, R., Conard, K., Glauser, T., Huff, D., … Kelley, R. I. (1988). Genetic Disorders and Major Extracardiac Anomalies Associated With the Hypoplastic Left Heart Syndrome The online version of this

article , along with updated information and services , is located on the World Wide Web at : Genetic Disorders and Major Ext. *Pediatrics*.

11. Nkomo, V. T. (2003). Bicuspid Aortic Valve Associated With Aortic Dilatation: A Community-Based Study. *Arteriosclerosis, Thrombosis, and Vascular Biology*, *23*(2), 351–356.

12. Roberts, W. C. (1970). The congenitally bicuspid aortic valve. A study of 85 autopsy cases. *The American journal of cardiology*, *26*(1), 72–83.

13. Sankova, B., Machalek, J., & Sedmera, D. (2010). Effects of mechanical loading on early conduction system differentiation in the chick. *American journal of physiology. Heart and circulatory physiology*, *298*(5), H1571–6.

14. Sedmera, D, Pexieder, T., Rychterova, V., Hu, N., & Clark, E. B. (1999). Remodeling of chick embryonic ventricular myoarchitecture under experimentally changed loading conditions. *The Anatomical record*, *254*(2), 238–52.

15. Sedmera, David, Harris, B. S., Grant, E., Zhang, N., Jourdan, J., Kurkova, D., & Gourdie, R. G. (2008). Cardiac expression patterns of endothelin-converting enzyme (ECE): implications for conduction system development. *Developmental dynamics : an official publication of the American Association of Anatomists*, *237*(6), 1746–53.

16. Simpson, J. M., & Sharland, G. K. (1997). Natural history and outcome of aortic stenosis diagnosed prenatally. *Heart (British Cardiac Society)*, *77*(3), 205–10.

17. Tobita, K., & Keller, B. B. (2000). Right and left ventricular wall deformation patterns in normal and left heart hypoplasia chick embryos. *American journal of physiology. Heart and circulatory physiology*, *279*(3), H959–69.

18. Yener, N., Oktar, G. L., Erer, D., Yardimci, M. M., & Yener, A. (2002). Bicuspid aortic valve. *Annals of thoracic and cardiovascular surgery : official journal of the Association of Thoracic and Cardiovascular Surgeons of Asia*, *8*(5), 264–7.

CHAPTER 3

GROWTH AND HEMODYNAMICS AFTER EARLY EMBRYONIC AORTIC ARCH OCCLUSION[7]

3.1 Abstract

The majority of severe clinically significant forms of congenital heart disease (CHD) is associated with great artery lesions, including hypoplastic, double, right or interrupted aortic arch morphologies. While fetal and neonatal interventions are advancing, their potential ability to restore cardiac function, optimal timing, location, and intensity required for intervention remain largely unknown. We here combine computational fluid dynamics (CFD) simulations with *in vivo* experiments to test how individual pharyngeal arch artery hemodynamics alters as a result of local interventions to obstruct individual arch artery flow. Simulated isolated occlusions within each pharyngeal arch artery were created with image derived three-dimensional (3D) reconstructions of normal chick pharyngeal arch anatomy at Hamburger-Hamilton (HH) developmental stages HH18 and HH24. Acute flow redistributions were then computed using *in vivo* measured subject-specific aortic sinus inflow velocity profiles. A kinematic vascular growth-rendering algorithm was then developed and implemented to test the role of changing local wall shear stress patterns in downstream 3D morphogenesis of arch arteries. CFD simulations predicted that altered pressure gradients and flow redistributions were most sensitive to occlusion of the IVth arches. To evaluate these simulations experimentally, a novel *in vivo* experimental model of pharyngeal arch occlusion was developed and implemented using two-photon microscopy guided femtosecond laser based photodisruption surgery. The right IVth arch was occluded at HH18, and resulting diameter changes were followed for up to 24 hours. Pharyngeal arch diameter responses to acute

[7] This chapter, with modifications, was previously published as: Lindsey, S.E., Menon, P.G., Kowalski, W.J., Shekhar, A., Yalcin,H.C., Nishimura, N., Schaffer, C.B., Butcher, J.T., Pekkan, K. (2014). Growth and hemody94namics after early embryonic aortic arch occlusion. *Biomechanics and Modeling in Mechanobiology*, 14(4), 735-751.

hemodynamic changes were predicted qualitatively but poorly quantitatively. Chronic growth and adaptation to hemodynamic changes however were predicted in a subset of arches. Our findings suggest that this complex biodynamic process is governed through more complex forms of mechanobiological vascular growth rules. Other factors in addition to wall shear stress, or more complex WSS rules are likely important in the long-term arterial growth and patterning. Combination *in-silico*/experimental platforms are essential for accelerating our understanding and prediction of consequences from embryonic/fetal cardiovascular occlusions, and lay the foundation for non-invasive methods to guide CHD diagnosis and fetal intervention.

3.2 Introduction

Pharyngeal arch artery (PAA) morphogenesis involves complex transformations of the generalized vertebrate template of six symmetric pairs of embryonic PAA into species-specific patterns that include the mature and asymmetric aortic arch, pulmonary arteries and great vessels. Concurrent with PAA morphogenesis, outflow tract (OT) morphogenesis transforms the common outlet of the embryonic heart into the separate great vessels and semilunar valves. This delicate sequence of vascular and cushion/primitive valve remodeling takes place within an active biomechanical environment that includes changes in ventricular function, vascular impedance and vessel geometry, as well as finely orchestrated changes in cellular and matrix biology. The regulation of such outflow (PAA and OT) morphogenesis has been an area of intense interest for nearly a century (Bremer, 1928; Elzenga and Gittenberger-de-Groot, 1985; Kirby, 2002; Yashiro et al, 2007). Errors in PAA and OT morphogenesis occur in more than 50% of infants with congenital heart disease (CHD) (Go et al. 2013). Defects associated with malformation of the OT and PAA include hypoplastic left heart syndrome with arch atresia, aorticopulmonary septation defects with arch

anomalies such as tetralogy of Fallot (25% with right pharyngeal arch), double outlet right ventricle with arch interruption, transposition of the great vessels and vascular rings.

Although the etiologies of congenital heart defects are not yet fully understood, they are thought to result in part from changes in hemodynamics (Culver and Dickinson, 2010; Hove et al., 2003; Jaffee, 1965; Kamiya and Togawa, 1980; Langille, 1996; le Noble et al., 2005; Thoma, 1893), with wall shear stress (WSS), being a major extrinsic mechanical stimulus for vascular remodeling (Culver and Dickinson, 2010; Rodbard, 1975). Changes in WSS patterns are detected through endothelial cells, which convert mechanical stimuli into intracellular signals, leading to an increase or decrease in vessel diameter (Bayer et al., 1999; Girerd et al., 1996; Langille and O'Donnell, 1986). Recent studies of the Hamburger-Hamilton (HH) stage 18, 21, and 24 PAA have revealed clear relationships between PAA flow, WSS, and luminal growth (Kowalski et al., 2013; Wang et al., 2009). While the asymmetric PAA regression pattern has been shown to occur by differential apoptosis (Molin et al., 2002), the expression of genes that normally orchestrate left/right asymmetry has not been observed in the PAA (Liu et al., 2002; Yashiro et al., 2007). Whereas the right lateral PAA IV diameter increases significantly ($p<0.05$) from stage 18 to 21 to 24, the left lateral diameter remains the same from stage 21 to 24 (Kowalski et al., 2013). This asymmetric growth correlates with the asymmetric flow distribution, in which the right lateral consistently receives >65% of all flow directed to PAA pair IV – the largest imbalance among all PAA pairs.

The vertebrate chick embryo undergoes PAA and OT morphogenesis similar to humans and is amenable to imaging and manipulation (Clark et al., 1989; Hu et al., 2009;

Pexieder, 1986). It has been extensively used to study the role of hemodynamics in embryonic cardiovascular development, where acute and chronic perturbations in blood flow have produced a spectrum of cardiovascular defects (deAlmeida et al., 2007; Gessner, 1966b; Hogers et al., 1999; Lucitti et al., 2005; Reckova et al., 2003; Sedmera et al., 1999; Tobita et al., 2005). Vascular interventions such as chronic left atrial ligation (LAL) and unilateral vitelline vein ligation (VVL) result in a redistribution of blood flow to the individual PAAs, generating a variety of abnormalities (Hogers et al., 1999; Hu et al., 2009; Rychter and Lemez, 1965). Distinct PAA perfusion patterns were demonstrated by Rychter and Lemez, who further showed that these patterns were disrupted by transection or ligation of vitelline veins. The VVL model was extended by Hogers et al. (Hogers et al., 1999), revealing a change in intra-cardiac flow patterns as well. Fully hatched embryos displayed multiple defects in PAA development, including hypoplastic right brachiocephalic artery, interrupted aortic arch, double aortic arch, and hypoplastic pulmonary artery. The LAL model also produced changes in PAA flow, which was significantly reduced in all PAA, as measured by laser Doppler velocimetry (Hu et al., 2009). Defects such as absent PAA III and IV and PAA hypoplasia were present in stage 27 LAL embryos. More recently, we developed and applied a femtosecond laser ablation technique to the embryonic heart to perturb prevalvular cushion and ventricular development (Yalcin et al., 2010a; Yalcin et al., 2010b). Compared to LAL and VVL that alter the "upstream" intra-cardiac flow streams, these contemporary embryonic vascular interventions have been shown to generate more drastic effects in blood flow and hemodynamics, primarily due to the low Reynolds number flow regimes of the early embryo damping the upstream differences in intra-cardiac flow streams (Kowalski et al., 2013).

In this manuscript, the femtosecond pulsed laser photoablation technique has been extended to occlusion of the PAA of the early chick embryo, together with a detailed comparative PAA-by-PAA computational hemodynamic analysis of its consequences at multiple developmental time-points. We explore the alteration of neighboring arch hemodynamics due to targeted arch occlusion. Using the WSS field computed from computational fluid dynamics (CFD) analysis, we implement a simple proportionality model to test its ability to forecast downstream shear-mediated three-dimensional PAA growth. As experimental tools and simulation strategies improve and integrate, this combinatorial strategy will inform how PAA development may progress under clinically relevant structural abnormalities.

3.3 Materials and Methods

In silico pharyngeal arch occlusion and flow modeling

Subject-specific 3D geometries of the HH18 and HH24 PAA are generated using microinjected polymerizing resin (diluted MICROFIL® Silicone Rubber Injection Compounds MV-blue, Flow Tech Inc., Carver, MA) and micro computed tomography (micro-CT) as previously described (Butcher et al., 2007; Wang et al., 2009). PAA geometries extended from the distal outflow tract to the dorsal aorta and paired cranial aortae. Occlusion of a single PAA was modeled *in silico* by creating a geometric discontinuity with flat cut surfaces at two locations symmetrically positioned from a central plane bisecting the PAA. *In silico* occlusion and preparation of 3D geometries for CFD was performed in Geomagics Studio 10 (Geomagic Inc., Durham, NC). For comparison with our *in vivo* experiment, we modeled occlusion of the right lateral

PAA IV (denoted "PAA^{IV}-R" and similar hereafter) in the HH18 model. We further modeled occlusions of the PAA^{III}-R in the HH18 model and each of the six PAA present in the HH24 model (right and left laterals of PAA pairs III, IV, and VI), totaling eight *in silico* occlusion test cases (Figure 1).

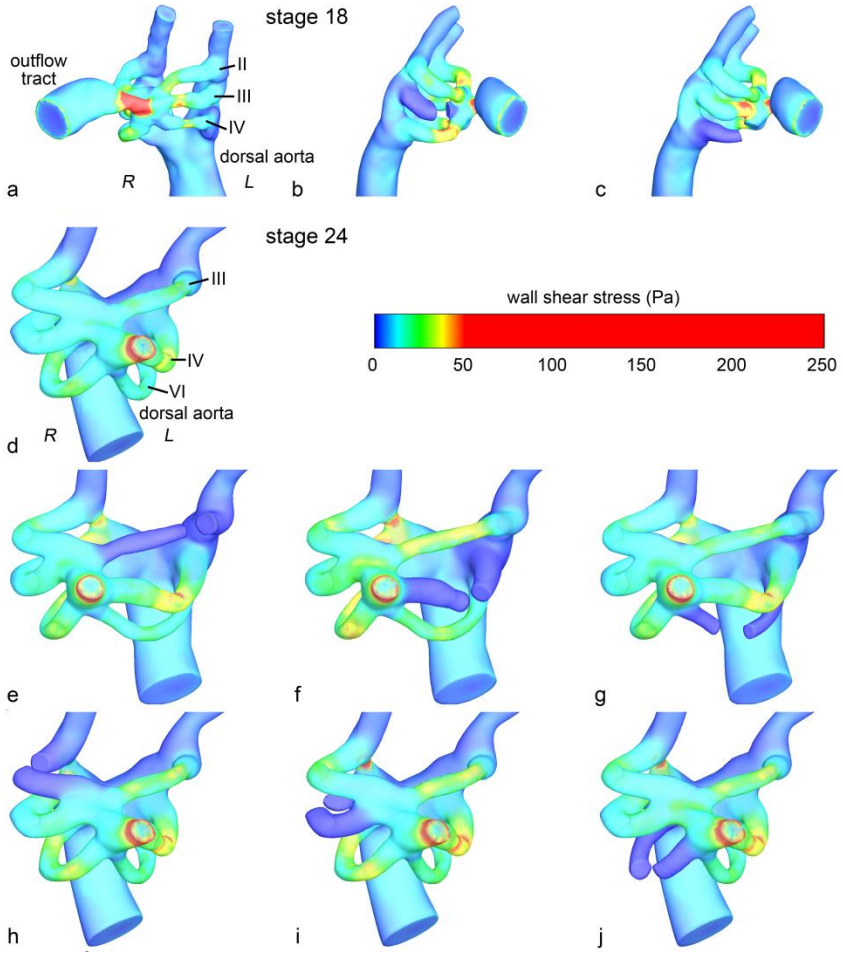

Figure 3.1. Control and occluded HH18 (a-c) and HH24 (d-j) PAA models. The peak WSS indicated by surface color. In the control models (a and d), the PAA and relevant vascular structures are labeled. *R* – right, *L* – left.

For each PAA occlusion and the control HH18 and HH24 geometries, we modeled 3D blood flow using an in-house pulsatile cardiovascular flow solver incorporating a validated 2^{nd} order accurate multi-grid artificial compressibility numerical method (Menon et al., 2013). Blood was treated as a Newtonian fluid with constant hemodynamic properties (ρ = 1060 kg/m^3, μ = 3.71 $\times$ 10^{-3} Pa.s) and rigid, impermeable vessel walls were assumed with no slip boundary conditions. Flow was simulated in terms of inlet normalized spatio-temporal units, on a high-resolution unstructured Cartesian immersed boundary grid with finite-difference numerical treatment. Grid sensitivity analysis was conducted in the control PAA models in order to ensure consistency and reliability of the numerical solutions and also identify an appropriate spatial resolution (0.01 mm, 500,000 fluid nodes) for all simulations presented in this study, beyond which resulting mass-flow redistributions were insensitive to further Cartesian grid refinements.

As per recent studies, (Bharadwaj et al., 2012), Poiseuille flow inlet boundary profiles were applied in the HH18 model, while plug flow profiles were applied in the HH24 model. A fixed mass flow-split type outflow boundary condition was imposed in each model in order to maintain distribution of the total cardiac output to dorsal aorta and cranial vessels in the ratio of 90/10. Pulsatile flow was simulated based on outflow tract cardiac output waveforms selected from our previously published studies (Wang et al., 2009; Yoshigi et al., 2000). Pulsatile flow was modeled in order to more realistically account for the inertial effects of the accelerating flow fields on pressure and velocity, but for practical purposes hemodynamic parameters were reported only for peak systole.

CFD simulations were conducted at Pittsburgh Supercomputing Center's Blacklight supercomputing cyber-infrastructure. Each simulation was terminated after 5 cardiac cycles and cost an average of 22 hours at 32 core parallelism. Convergence of the transient CFD solution was monitored using the time-evolution of mass-flow split distributions between the PAA at the instant of peak systole. Simulation data from the 5^{th} cardiac cycle was analyzed in order to ensure damping of initial transients.

Computational model of shear driven pharyngeal arch growth

We developed a WSS driven three-dimensional luminal growth kinematics model of the short-term response to altered hemodynamics after PAA occlusion. This numerical model was applied to the control and right lateral PAA IV (PAA^{IV}-R) occluded HH18 models, corresponding to our experiment. WSS at the immersed boundary nodes of the mesh was computed at the instant of peak systole flow from the CFD solution. Kriging interpolation (Davis, 1986) was then used to sample WSS on the PAA wall surface (Tecplot, Bellevue, WA). For each wall surface node, a vector comprising the principal diagonal elements of the shear stress tensor was calculated based on the local growth rule. A simple local growth rule is specified where the wall displacement ($\Delta \boldsymbol{x}$) was computed by offsetting the wall surface along the vector direction indicated by the principal diagonal shear stress vector ($\boldsymbol{\tau}$), assuming a linear relation between shear stress and displacement. The basic growth law is defined in Eq 1, where α is the proportionality constant, valued at 8.1×10^{-6} μm/Pa·s for all PAA. The proportionality between shear-stress and displacement was calibrated based on relationships approximated from our previous study, which monitored natural PAA growth between HH18 and HH21(Kowalski et al., 2013).

$$d\boldsymbol{x}/dt = \alpha\boldsymbol{\tau} \quad (1)$$

In order to avoid effects of artificial peaks and plateaus in the WSS field as well as to smooth the region of influence predicting wall displacements, the peak systole WSS field was smoothed using a function solving an iterative solution to the Laplace equation. The smoothed WSS was arrived at from the solution to a difference equation for WSS, using generalized coordinates (Anderson et al., 1984), defining a diffusive smoothing parameter, D, set between 0 and 0.95 to determine the extent of smoothing. The number of point-Jacobi iterations used to solve this equation for WSS (i.e. smoothed WSS) was an additional input variable, which smoothed the region of influence of the WSS field. Each pass of smoothing (i.e. each iteration) shifted the value of the variable at a data point towards an average of the values at its neighboring data points. In this study, we examine the likely displacement effects of WSS using D=0.90 and 100 smoothing iterations. The choice of these smoothing parameters and their effects in light of true shear-mediated response is a subject of presently ongoing studies.

We computed wall displacement for eight time points from HH18 to HH24 (a 24 hour period) in both a normal and PAA^{IV}-R occluded model. Wall displacement at each time point was based on the WSS computed from the initial CFD solution. As a first approximation and to limit computational expense, we did not re-solve the flow-growth algorithm between growth steps after the initial step. Therefore, in our growth model, the WSS field was independent of time, and Eq 1 was simplified to $\Delta \boldsymbol{x} = \alpha \boldsymbol{\tau} \Delta t$. The hydraulic diameter of the PAA at every time point was computed based on the cross sectional area at the PAA midpoint to assess net luminal growth and compare with the experiment.

Experimental pharyngeal arch occlusion

Embryo culture and preparation

Fertile white Leghorn chicken eggs were incubated blunt-side up for three days in a continuous rocking incubator at 37.5^{o}C. Embryos were then open cultured as previously described (Yalcin et al., 2010a; Yalcin et al., 2010b). Briefly, HH18 embryos were transferred onto a polyurethane (Saran Wrap) membrane and placed atop a plastic cup partially filled with water. Injection micro-needles were fashioned from pulled capillary tubes (0.75 mm ID) cut to 20 µm inner diameter via a microforge (Glassworx, St. Louis, MO). A micromanipulator (model M3301L, World Precision Instruments, Sarasota FL) positioned the needle into a vitelline vein (usually >100 µm in diameter), and 1-1.5 µl of Texas red dextran (70,000 MW, neutral Sigma-Aldrich D1830) diluted in Earle balanced salt solution (5% w/v) was slowly injected. The embryos were returned to the incubator and monitored until the dye could be seen throughout the vasculature.

Two-photon microscopy and femtosecond pulsed laser ablation

A custom built two-photon excited fluorescence (2PEF) microscope was modified to include a path for a femtosecond pulsed photoablation laser, as described previously (Nishimura et al. 2006; Yalcin et al., 2010a). Laser pulses from a 1040-nm fiber laser (µJewel-FCPA, IMRA America, Inc, 1MHz, 350-fs pulses) or a Ti:Sapphire laser tuned to 900 nm (Chameleon, Coherent, 80 MHz, 75-fs pulses) were used for two-photon excitation. Pulses were scanned by galvonometric scanners (3 frames per second) and focused into the sample using a 1.0 numerical aperture, 20x water immersion objective (Zeiss). Fluorescence emission from the Texas red dextran was reflected by a dichroic mirror, collected through a 645 nm bandpass filter, and relayed

to photomultiplier tubes. Laser scanning and data acquisition were controlled by ScanImage (Pologruto et al, 2003).

A 1-kHz high-pulse-energy Ti:Sapphire amplified laser system with 50-fs pulse duration (Legend-USP, Coherent, Santa Clara, CA, 800-nm central wavelength) was used to perform the targeted vessel disruption. This laser beam was focused into the center of the imaging plane to induce clotting in vessels (see (Yalcin et al., 2010a) for experimental set-up). Incident laser energy and exposure time was controlled through the use of neutral density filters and a fast mechanical shutter (2-ms minimum opening time, Uniblitz Rochester, NY).

Targeted vessel occlusion

The PAA^{IV}-R was identified and occluded in HH18 (Day 3) embryos. HH18 embryos with smaller PAA^{IV}-R were specifically chosen to facilitate faster occlusion experiments, as it is easier to occlude arteries with smaller cross sectional areas. Femtosecond pulses were tightly focused into the center of the PAA lumen causing nonlinear absorption of laser energy that drives photodisruptive damage. This absorption separates positively and negatively charged ions, which quickly recombine to form a gas bubble that expands and contracts in size based on an equilibrium between the laser energy input and its external environment (Vogel and Venugopalan 2003; Nishimura et al. 2006). Photodisruption was confined to the volume focused by the two-photon microscopy optics. Laser pulse energies of 3-4.5 µJ were required to grow and maintain a cavitation bubble that temporarily stopped flow in vessels ranging from 30-70 µm in diameter (Figure 2D). HH18 embryos (Day 3) with smaller PAA^{IV}-R were therefore specifically chosen to facilitate faster occlusion experiments. Occlusion was further facilitated by pre-cooling embryos in an ice bath in order to

slow the heart rate ~50% (and thereby the blood flow rate), resulting in greater persistence of cavitation bubbles that mark the beginning of the occlusion process. Following the creation of this cavitation bubble, laser energy was directed to the increasingly more stagnant flow directly behind the cavitation bubble, accumulating damage and cohesion in the lumen (Figure 2B). This process was adjusted and/or repeated as needed until a stable occlusion was formed. Stable occlusions were taken to be those that persisted for 5 minutes without laser perturbation. Figure 2C illustrates the process as observed with the two-photon microscopy. Embryos were imaged in their ice bath no longer than one hour, and then promptly returned to the incubator. Embryos quickly returned to 37.5^{o}C and normal heart rate was restored within 20 minutes. Previous studies demonstrated no adverse effects of this temporary hypothermia (Yalcin et al., 2010a). Sham control embryos were placed in a similarly cooled water bath outside of any beam path for the duration of an occlusion cycle. The location and degree of vessel occlusions were confirmed through intravital microscopy, India ink and/or thin section histology. Occlusions were created either at the base or head of the arch artery (Figure 3).

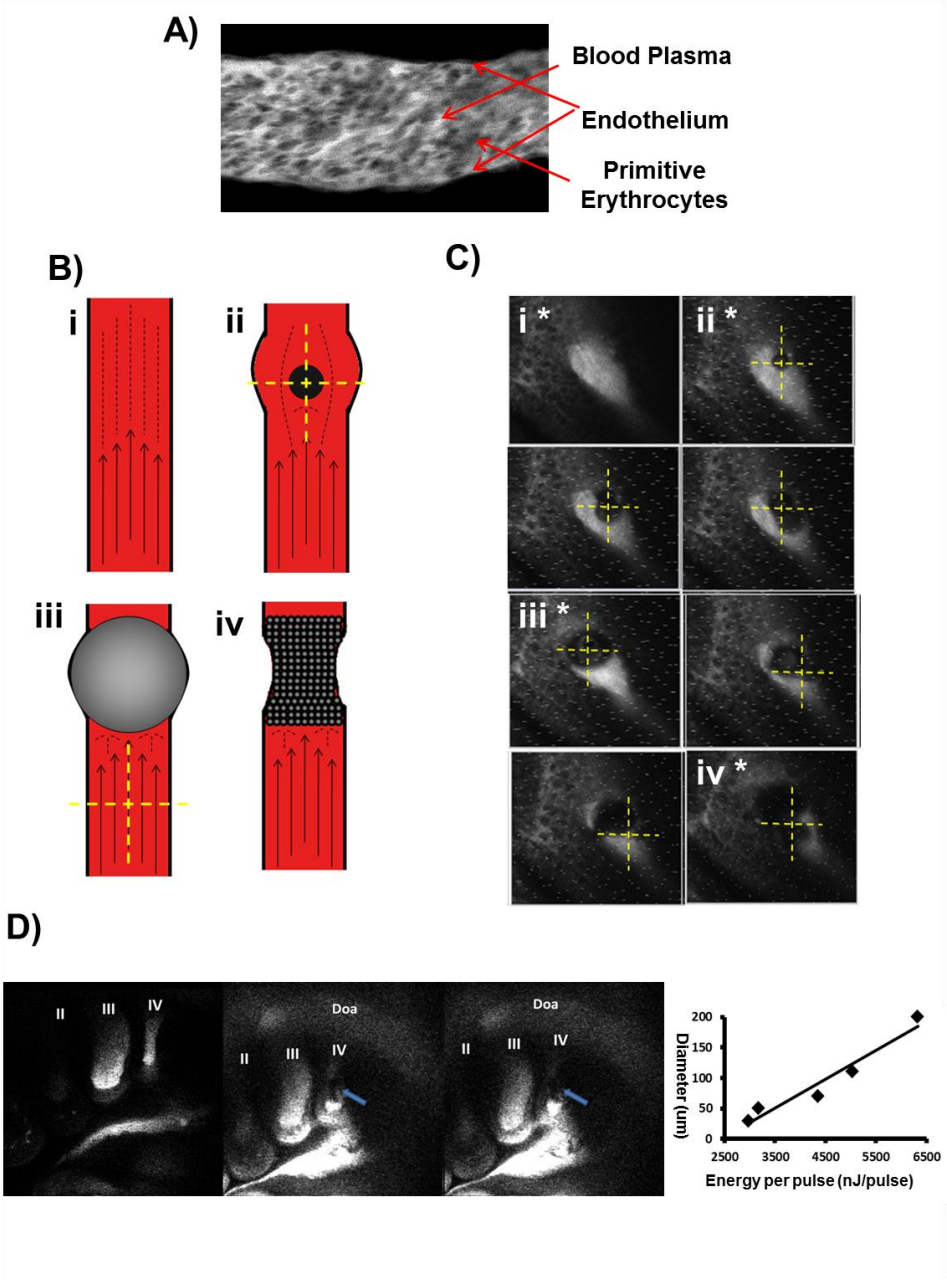

Figure 3.2. A) Two-photon image of flow inside of an HH18 vessel. Blood plasma is visible as bright fluorescence while primitive erythrocytes remain dark spheres. B) Schematics representing occlusion process. Identification of vessel in question (i), creation of cavitation bubble (ii), temporary blockage of vessel flow via a large cavitation bubble (iii) and formation of permanent vessel occlusion (iv). C) Two photon fluorescent images of vessel occlusion process with roman numerals and asterisks marking occlusion process as defined by schematic. Yellow crosshairs mark ablation laser focal point. D) Full vessel view at baseline (left) during (middle) and after (right) the occlusion process as seen through two-photon fluorescence. Blue

arrows indicate occluded vessel. On right is a plot of cavitation bubble diameter as a function of laser energy.

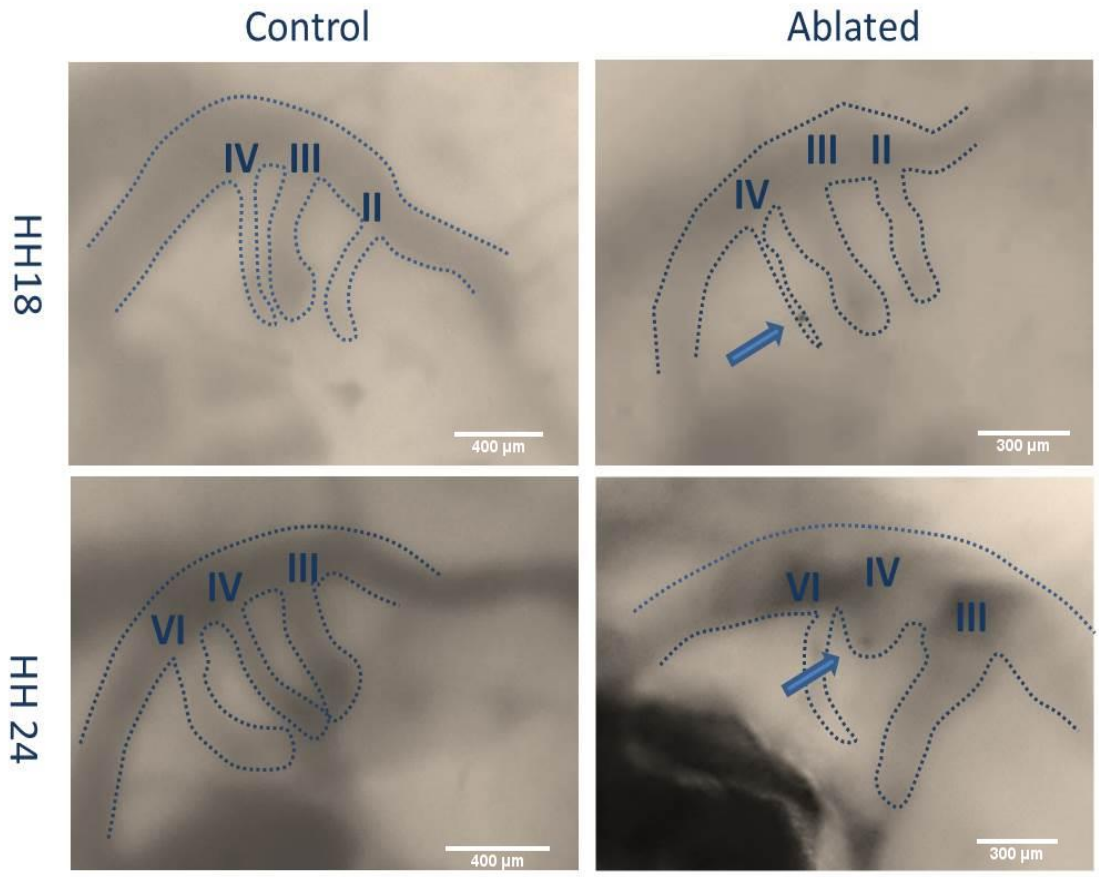

Figure 3.3. Stereoscope images of H18 and HH24 PAAs for a control and ablated embryo.

Dashed lines mark vessel diameters. Roman numerals identify PAA branches. Arrows point to vessel occlusion.

Measurement of vessel diameter

Embryonic pharyngeal arch artery diameters were visualized using India ink injections, and measured at their midpoints with a calibrated stereomicroscope (Zeiss stereo Discovery) immediately following occlusion (HH18), 3 hours post occlusion (HH19), and 24 hours following occlusion (HH22/23). Additional embryos were maintained for 48 hours after vessel occlusion (HH28), then fixed in 4% paraformaldehyde. These embryos were then paraffin processed, cut into 10μm sections, and stained with hematoxylin and eosin (H&E). Experimental results are based off a set of 3 occlusion embryos and 4 control embryos.

Statistics

Statistical comparisons were made through the use of GraphPad Prism (GraphPad Software, Inc San Diego, CA) statistical software. Linear regressions were performed on experimental and simulation control and occlusion subsets for the diameter of each of the three arch pairs (II, III, IV) as a function of time. Two-tailed analysis of covariance (ANCOVA) was then performed comparing experimental control to experimental occlusion curves, experimental control to simulation control curves, and experimental occlusion curves to simulation occlusion curves. These analyses tested the null hypothesis that the curves were identical, comparing slopes first and then the curve as a whole, using $P<0.05$ to assign significance.

3.4 Results

Wall shear stress based PAA vessel 3D growth simulation

As expected, the highest values for WSS were noted at sites of narrowest PAA diameters, which in-turn were the locations which experienced the maximum displacement as per our short-term PAA growth prediction model. The WSS based growth model was expected to reduce peak WSS by dilating such narrowed regions. However, since our first-approximation WSS-based growth model does not anticipate the naturally occurring disappearance of the PAA^{II} arches or the generation of the PAA^{VI} arches, the proposed predictive kinematics approach is focused on ascertaining short-term growth effects attributable only to current hemodynamic and anatomical conditions, but doesn't account for ongoing biological programs.

WSS created wall-displacement model results for the control HH18 models are presented in Figure 4. Cross-sectional ovalization of each PAA was predicted correctly using the WSS dependent growth model, supporting local WSS based PAA remodeling. Simulated incremental changes in PAA diameter were then plotted over eight equally-spaced developmental time intervals from HH18 to HH24 (Figure 7). Diameters are normalized to the initial value at HH18. Videos of the growth of PAA are available in the supplementary material.

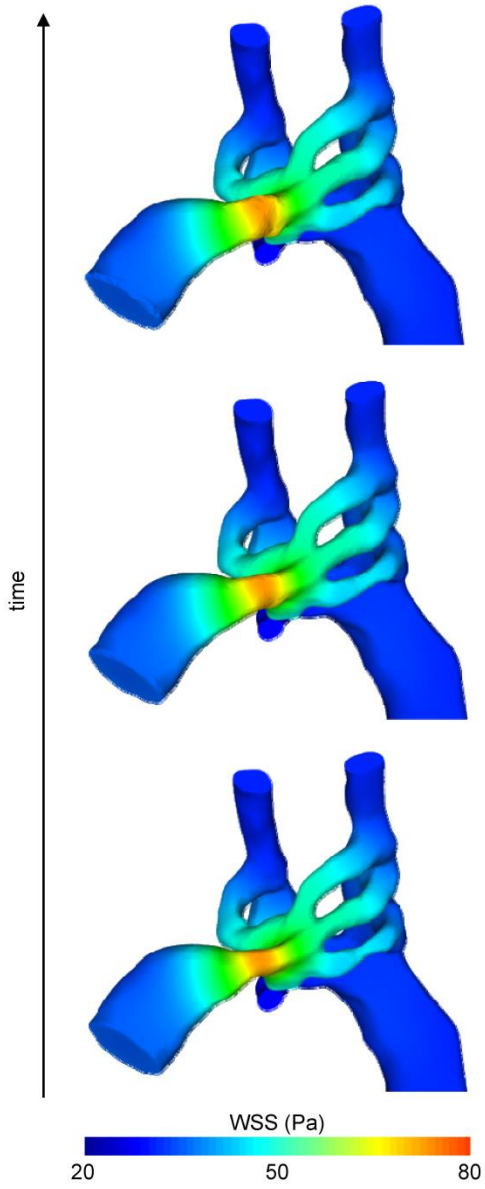

Figure 3.4.WSS-based short term growth prediction in the normal HH18 model.

Given that our inflow boundary condition (total cardiac output waveform) remained constant, the flow into an occluded PAA must be re-distributed among the remaining vessels. This effect is shown in Table 1, which presents the peak flow in each PAA at HH18. In the control geometry, the flow distribution aligns well with the hydraulic resistances of the PAA vessels, i.e. PAA^{III}-R is the largest diameter and receives the

highest flow and PAA^{IV}-L is the smallest diameter and receives the least flow. In the case of simulated PAA^{IV}-R occlusion at HH18, the flow distribution pattern is retained (Table 1). Following PAA^{III}-R occlusion, PAA^{II}-R emerges as the vessel with the greatest flow (.22 mm^3/s), followed closely by PAA^{III}-L and PAA^{IV}-R (Table 1). In the case of a III-R occlusion, PAA^{II}-R is positioned to become the dominant arch of the aorta. Though the right lateral PAA^{IV}-R is predetermined to become the aorta, at HH18 the PAA^{IV} pair has only recently formed and is nearly 40% smaller than PAA^{III}. By HH24, however, PAA^{IV} pair enlarge significantly (especially the right lateral) and eclipses PAA^{III} in diameter (Wang et al., 2009). Therefore, occluding the presumptive aorta at this early stage is likely to result in a variety of PAA defects. Our simulations suggest that the PAA^{III}-R would then become the dominant PAA and may compete to become the mature great vessel during later stages of development.

	flow (mm^3/s)		% change from occlusion		% cardiac output	
	R	L	R	L	R	L
	No Occlusion					
PAA II	0.14	0.14	0.00%	0.00%	16%	16%
PAA III	0.26	0.16	0.00%	0.00%	30%	18%
PAA IV	0.14	0.045	0.00%	0.00%	16%	5.1%
	Right Lateral PAA IV Occluded					
PAA II	0.17	0.16	21%	14%	19%	18%
PAA III	0.31	0.18	19%	13%	35%	21%
PAA IV	0.00	0.051	-100%	13%	0.00%	5.8%
	Right Lateral PAA III Occluded					
PAA II	0.22	0.18	57%	29%	25%	21%
PAA III	0.00	0.21	-100%	31%	0.00%	24%
PAA IV	0.20	0.062	43%	38%	23%	7.1%

Table 3.1. Flow rate, cardiac output, and percent change of occluded HH18 subsets with respect to the control or non-occluded HH18 model.
Note how PAA^{II}-R received the largest percent increase with PAA^{III}-R occlusion (57% increase) and PAA^{IV}-R occlusion (21% increase). In both cases PAA^{II}-R and PAA^{III}-L are brought to be within 0.1 mm^3/s from each other.

HH24 PAA in silico occlusion cases

The flow changes after *in silico* PAA occlusions at HH24, shown in Table 2, further demonstrate the importance of the PAA^{IV}-R. Similar to the HH18 occlusion cases, all but two HH24 PAA occlusions result in the PAA^{IV}-R experiencing the largest relative increase in blood flow. In the cases of PAA^{VI}-L occlusion and right lateral PAA^{IV}-R occlusion, flow to the PAA^{III}-R increased the most. Although PAA^{IV}-R is the largest

in diameter at HH24, the occlusion based re-distribution pattern is not always as simple as the geometry may suggest. In particular, we expected left sided occlusions to shift flow toward the remaining left sided vessels in order to maintain equal distribution between the paired cranial aortae. However, as each cranial aorta receives just 5% of the total cardiac output, maintaining equal right and left sided PAA ratio may not be a strong requirement. Our previous CFD model suggested that the PAA^{IV}-R is placed in an optimal position due to outflow tract orientation, which may be a reason for its preference during flow re-distribution after PAA occlusion (Kowalski et al., 2012). However, as in the HH18 model, simulated occlusion of the PAA^{IV}-R at HH24 resulted in the largest flow increase to PAA^{III}-R. This pattern suggests that PAA^{III}-R is positioned to take on the role of the mature aorta after such occlusion.

Table 3.2. Flow rate, cardiac output, and percent change of HH24 occluded subsets.

	flow (mm^3/s)		% cardiac output		% change from occlusion		flow (mm^3/s)		% cardiac output		% change from occlusion	
	R	L	R	L	R	L	R	L	R	L	R	L
	Right Lateral PAA III Occluded						Left Lateral PAA III Occluded					
PAA III	0.00	0.18	0.00%	12%	-100%	20%	0.25	0.00	17%	0.00%	8.7%	-100%
PAA IV	0.42	0.47	29%	32%	24%	15%	0.38	0.45	26%	31%	12%	9.8%
PAA VI	0.28	0.11	19%	7.6%	17%	11%	0.27	0.11	19%	7.6%	13%	11%
	Right Lateral PAA IV Occluded						Left Lateral PAA IV Occluded					
PAA III	0.31	0.19	21%	13%	35%	27%	0.31	0.21	21%	14%	35%	40%
PAA IV	0.00	0.52	0.00%	36%	-100%	27%	0.47	0.00	32%	0.00%	38%	-100%
PAA VI	0.31	0.12	21%	8.2%	29%	21%	0.34	0.14	23%	9.6%	42%	41%
	Right Lateral PAA VI Occluded						Left Lateral PAA VI Occluded					
PAA III	0.27	0.18	19%	12%	17%	20%	0.25	0.16	17%	11%	8.7%	6.7%
PAA IV	0.41	0.49	28%	34%	21%	20%	0.36	0.43	25%	30%	5.9%	4.9%
PAA VI	0.00	0.12	0.00%	8.2%	-100%	21%	0.26	0.00	18%	0.00%	8.3%	-100%
	No Occlusion											
PAA III	0.23	0.15	16%	10%	0.00%	0.00%						
PAA IV	0.34	0.41	23%	28%	0.00%	0.00%						
PAA VI	0.24	0.099	16%	6.8%	0.00%	0.00%						

Table 3.2. Flow rate, cardiac output, and percent change of HH24 occluded subsets with respect to the control or non-occluded HH24 model.
Note how PAA^{IV}-R occlusion leads to the largest percent increase in PAA^{III}-R (35% increase), the most cranial right arch artery at this stage, while PAA^{III}-R occlusion leads to the largest percent increase in PAA^{IV}-R, the most cranial right arch artery available at this stage.

In vivo PAA photo-occlusion

Live multi-photon microscopy was used to visualize the vasculature of embryos injected with fluorescent dye. The pharyngeal arch arteries (PAA) were located and the imaging plane was adjusted so that the entire profile of the selected arch was clearly visible. Blood plasma was fluorescent and circulating cells appeared as dark disks against the fluorescent background (Figure 2A). Tightly-focused femtosecond laser pulses were used to cause targeted damage inside the vessel lumen, forming a transient cavitation and upstream aggregation of circulating cells that blocked blood flow. The minimum energy per pulse required to produce a stable occlusion increased linearly with vessel diameter from 3 μJ at 30 μm to 6.5 μJ at 200 μm (Figure 2D). The time required to form a stable occlusion (5-20 minutes) varied in part based on embryo size, vessel size, and the initial flow rate through the vessel. Permanent vessel occlusion was confirmed post photoablation acutely via two photon microscopy and long-term via histological sections. Figure 5 depicts a sagittal view of a control and ablated embryo in their natural orientation, right side up, with the arches and dorsal aorta visible upstream of the heart.

Acute diameter changes after PAA occlusion

A comparison between experimental results and computational model predictions of PAA diameters at HH19 is shown in Figure 6. Bars represent percent change in "occluded" diameters (meaning embryos whose PAA^{IV}-R arch was occluded) with respect to control diameters. Because overall embryo size varies at HH19, initial diameters have been normalized to the PAA^{II}-R mean HH19 value within their respective experimental and simulation subsets. However, notable differences between simulations and experimental conditions were found. Simulated PAA^{IV}-R arch occlusion predicted nearly homogeneous changes in diameter across the other arch arteries, while the actual experimental changes in vessel diameter varied considerably between arch arteries. Four of the six arch artery diameters increase or decrease in the same direction as that predicted by simulations, though the magnitude of that change differs greater than 75%.

While our simplified, linear WSS-driven growth model was able to capture some qualitative trends in PAA growth in control and PAA^{IV}-R occluded embryos, more rigorous quantitative agreement between the experimental and model-predicted PAA diameters is desired.. Quantitative disparity was particularly large in the short-term period (<12 hours) following occlusion (Figure 7). We examine several sources of this disagreement, including limitations of the CFD model, the role of additional mechanical factors, developmental trends not incorporated in our growth prediction, and biological alterations and responses ignored by our model. The latter is addressed in the Discussion of this manuscript, while the remaining three points are considered here.

Most importantly, the present CFD model makes several assumptions related to the flow boundary conditions. We specify a 90/10 flow split between the trunk and cranial vessels, which is consistent across the investigated timeframe (Hu and Clark, 1989). We maintain this 90/10 trunk/cranial ratio in the occluded model as well, however we did not measure flow in any occluded experiments, and therefore cannot determine if the flow split is maintained post-intervention. Furthermore a 50/50 right/left cranial aorta flow split was assumed in the occluded model. As occlusion of an entire PAA vessel changes the left/right lumped resistances and impedances of the PAA network, it is possible that the cranial aortae flow split changes after occlusion. Growth of the PAA may restore the flow distribution, but in the short term, the cranial boundary condition may be inaccurate. Experiments to measure flow distributions after PAA occlusion would provide better data for the outflow conditions of our model, which may improve agreement with experimental trends. The above reasoning is supported since the disparity between our model and experiment is larger in the short term. Occlusion of the PAAIV-R increases afterload on the embryonic ventricle. We do not incorporate this type of feedback into our model, instead maintaining a constant outflow tract waveform. Coupling a lumped-parameter ventricle model to our 3D PAA CFD model would allow incorporation of cardiac responses (such as change in CO and heart rate), and may improve the predictive capabilities of our growth model. Finally, our model specifies no-slip, rigid walls. This assumption is made to simplify the CFD solution, but ignores importance mechanical aspects of the PAA. These are discussed further in the next paragraph.

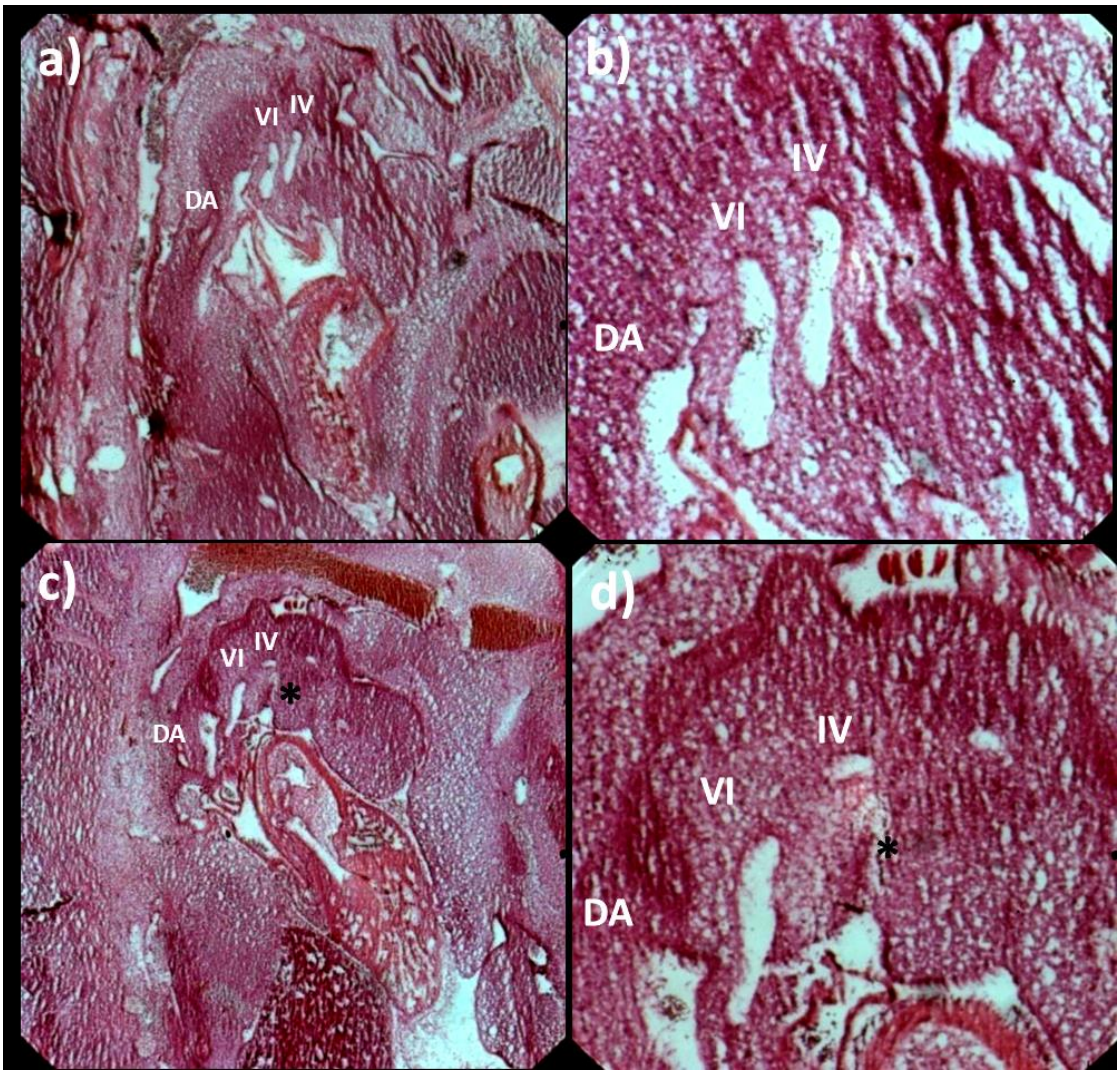

Figure 3.5. H&E section of HH28.

Control embryo (a) and ablated embryo (HH18 R IV occluded) (c) with roman numerals marking PAA branches in plane. Note PAA III is out of the plane slice. (b) and (d) show close up of PAA. Asterisks marks occluded embryo. DA – dorsal aorta.

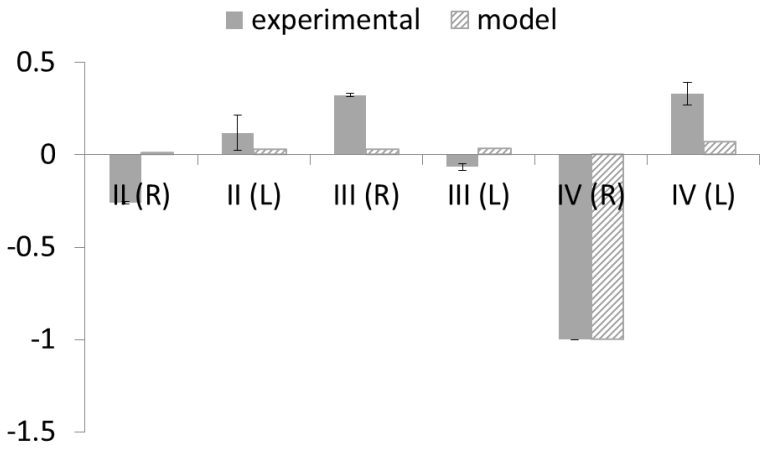

Figure 3.6. Change in diameter upon occlusion.
Graphs for experimental PAA diameters (solid) and WSS-based model embryos (hashed). Diameters are normalized to an initial HH19 PAA IIR value within each subset.

During the HH18-24 timeline of this study, the walls of the PAA are comprised of a single endothelium surrounded by 1-2 cell layers of mesenchyme and externally constrained by the surrounding mesoderm-derived pharyngeal arches. (Waldo et al., 2005; Waldo et al., 1996). While the material properties are unknown at these early stages, these soft tissues are likely able to elastically deform under pressure, generating impedance to flow. For simplicity and due to the lack of appropriate material models, we applied a rigid wall assumption to our model. This boundary condition can over-estimate WSS values as it ignores vascular compliance. Since our proportionality constant was based on similar rigid-wall models, we feel that this assumption has little effect on the predicted WSS-growth response. Without a PAA wall model, however, we are unable to compute transmural stresses and thus had to exclude them from our growth model. Growth and remodeling of blood vessels requires both WSS at the endothelium and stress within the vascular wall (Culver and

Dickinson, 2010; Huang et al., 2003; Lucitti et al., 2007; May et al., 2004). The inclusion of only one of these biomechanical factors (WSS) as the sole driver of PAA growth limits our ability to simulate the *in vivo* environment, leading to the quantitative disparity between our model and the experimental results. Incorporating an arterial wall component and formulating more sophisticated growth laws would enhance our model and its predictive capacity. Structural models of adult arteries have been combined with integrative growth laws to examine growth and remodeling in cardiovascular disease (Figueroa et al., 2009; Humphrey and Rajagopal, 2002; Valentin et al., 2011). Modeling the development of embryonic vessels is more challenging, as the properties and composition of the vascular wall change as differentiation, proliferation, and genetic state progress. Growth and remodeling of the embryonic and postnatal aorta has, to date, only been performed on cylindrical, axisymmetric geometries (Taber, 1998; Taber and Eggers, 1996; Wagenseil, 2010). The extension to complex networks such as the PAA will require more sophisticated computational strategies as well as greater data on the structural properties of embryonic blood vessels.

The initial geometry of our model is a representative HH18 PAA network, which we based on micro-CT scans and verified by comparing PAA diameter and length to experimentally measured values (Wang et al., 2009). However, by HH24, which acts as the endpoint of our model timeline in this study, the PAA geometry changes dramatically, including the regression of PAA^{II} and emergence of PAA^{VI}, elongation of the PAA, migration of the outflow tract, and localized enlargements and reductions in dorsal and cranial aortae diameters (Wang et al 2009). We previously performed a parametric study of 2D PAA models to investigate the effects of PAA length and curvature on flow and WSS, and found that WSS was maintained within 20% when

PAA length increased 50% and varied 10% when PAA tortuosity increased 10% (Kowalski et al., 2013). Therefore, we may be able to ignore small changes in PAA length in our model. However, the importance of outflow tract migration and rotation in the asymmetric morphogenesis of the PAA has been demonstrated by several studies (Bajolle et al., 2006; Bremer, 1928; Dor and Corone, 1985; Gessner, 1966a; Liu et al., 2002; Yashiro et al., 2007). Additionally, cardiac function is changing rapidly during this period; in particular, cardiac output increases exponentially (Broekhuizen et al., 1993; Ursem et al., 2001). These morphologic and hemodynamic trends create a dynamic biomechanical environment within the PAA, and adaptation to new mechanical loads, in part, drives their growth. For simplicity, our model does not include these developmental trends, and instead assumes a constant WSS field throughout the 24 hour timeline. Applying time-dependent morphological changes to the outflow tract and cranial and dorsal aortae, as well as the inflow waveform, is required to fully simulate the biomechanical environment over a long-term period. The quantitative disparity between our model and the experimental results demonstrates the importance of these developmental trends in shaping the PAA.

Chronic vessel growth data comparisons

Simulation predictions and occlusion experiments both confirmed significant overall PAA growth over 24 hours for both the right and left side ($P < 0.0002$ for control embryos and $P < 0.0038$ for occlusion embryos). Growth rate differences in individual arches between occlusion and control conditions occurred *within* the experimental and simulation datasets (Figure 7).

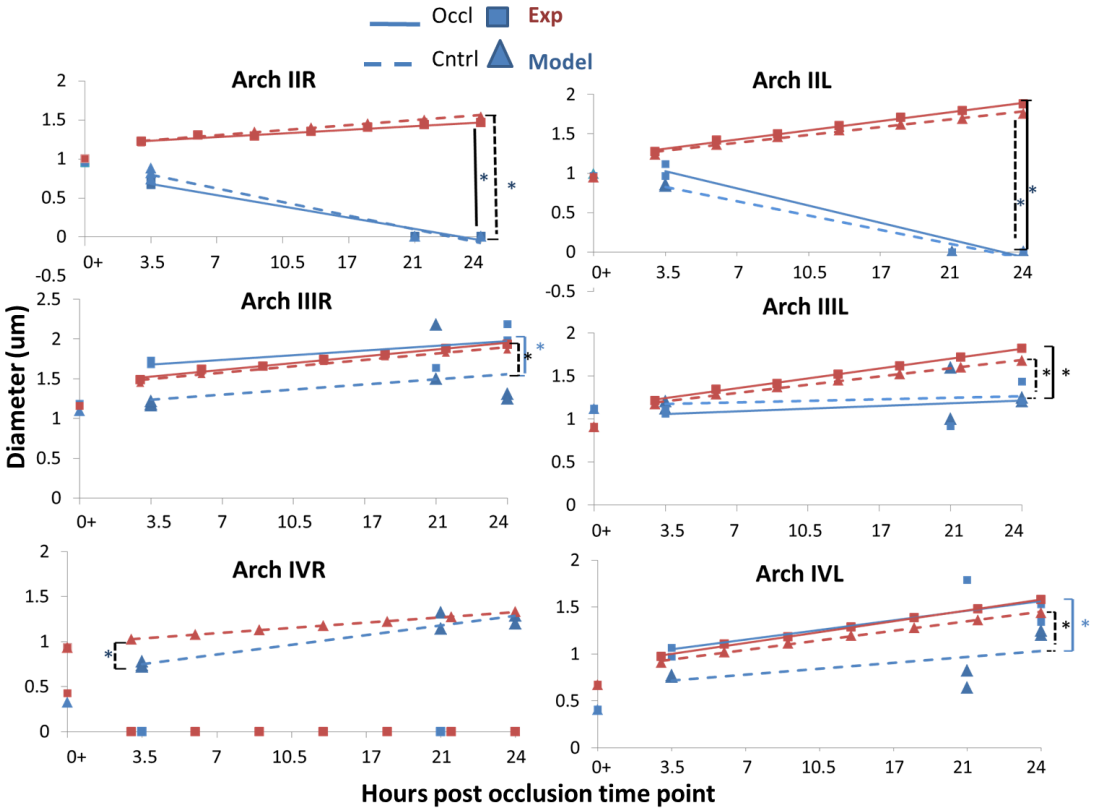

Figure 3.7. Graphs representing diameter changes as a result of HH18 right IV vessel occlusion imposed flow redistributions for both experimental and computational data over a 24 hour period.

Each data set has been fit with linear trend lines. A) PAA II right B) PAA III right C) PAA IV right. D) PAA II left E) PAA III left F) PAA IV left. Both control (dashed line, triangles) and occluded (solid line, squares) trends are shown for experimental (blue) and computational (red) data. Brackets with asterisks couple significantly different trends. Black lines indicate comparison of simulation and model subsets, dashed lines indicate comparison between control subsets. Blue brackets indicate a comparison between model subsets. Diameters are normalized to an initial HH18 PAA IIR value within each subset.

Experimental comparisons

PAA^{II}-L and PAA^{II}-R both regress completely in the experimental embryos (occlusion and control, $P<0.004$), while no significant growth trend was measured in PAA^{III}-R and PAA^{III}-L under control conditions. PAA^{IV}-R grew at a rate of 13.5% per hour (P

= 0.007; R^2 = 0.9168) in control conditions, while PAA^{IV}-L displayed no significant change in growth over time (occlusion or control conditions).

Computational comparisons

In contrast, our simple wall shear stress based PAA growth simulations predicted that with the exception of the occluded PAA^{IV}-R, all vessels would increase significantly in diameter in both control and "occlusion" (meaning PAA^{IV}-R occlusion) subsets. Specifically, simulated PAA^{II}-R increased 6.7% per hour (P<0.0001, R^2 = 0.9=7) within the control subset but only increased 4.7% per hour (P = 0.0002, R^2 = 0.95) in the occlusion subset. Likewise, simulated PAA^{III}-R control and occlusion subsets increased by 8.3 % and 8.8% respectively, (P= 0.002, R^2 = 0.95; P < 0.0001, R^2 = 0. 89). PAA^{IV}-R was predicted to increase by 6% per hour in control conditions. PAA^{II}-L was predicted to increase by 10.3% per hour (P < 0.0001, R^2 = 0.98) in the control case and 12% (P< 0.0001, R^2 = 0.98) per hour in the occlusion case. Similarly, PAA^{III}-L increased 10% (R^2 = 0.98, P < 0.0001) in the control case and 12% (R^2 = 0.99) in the occluded case. PAA^{IV}-L was predicted to increase by 12% per hour in the occlusion case (R^2 = 0.99, P < 0.0001), and only 10.6% per hour (R^2 = 0.99, P < 0.0001) in the control case. Table 3 summarizes the equations of each arch artery growth curve, it's R^2 value and significance in terms of slope.

exp (occl)	equation	R^2 value	slope significatly non-zero?	P-Value	Model (occl)	equation	R^2 value	slope signifantly non-zero?	P-value
II	Y = -0.1804*X + 4.099	0.9576	Yes	0.0038	II	Y = 0.04720*X + 0.3375	0.9496	Yes	0.0002
III	Y = 0.07810*X + 0.1867	0.4725	No	0.1997	III	Y = 0.08796*X - 0.1481	0.9716	Yes	< 0.0001
IV	----------				IV	----------			
IIL	Y = -0.2727*X + 6.198	0.9518	Yes	0.0046	IIL	Y = 0.1197*X - 0.9651	0.9852	Yes	< 0.0001
IIIL	Y = 0.04138*X + 0.2681	0.1949	No	0.4567	IIIL	Y = 0.1197*X - 1.039	0.9932	Yes	< 0.0001
IVL	Y = 0.1259*X - 1.331	0.5945	No	0.1269	IVL	Y = 0.1208*X - 1.300	0.9933	Yes	< 0.0001

exp (cntrl)	equation	R^2 value	slope significatly non-zero?	P-value	Model (cntrl)	equation	R^2 value	slope signifantly non-zero?	P-value
II	Y = -0.2207*X + 4.981	0.9458	Yes	0.0002	II	Y = 0.06731*X - 0.04047	0.9664	Yes	< 0.0001
III	Y = 0.07535*X - 0.1823	0.1591	No	0.3753	III	Y = 0.08326*X - 0.08899	0.9538	Yes	0.0002
IV	Y = 0.1350*X - 1.809	0.9168	Yes	0.0007	IV	Y = 0.06117*X - 0.1315	0.9973	Yes	< 0.0001
IIL	Y = -0.2280*X + 5.147	0.9421	Yes	0.0013	IIL	Y = 0.1033*X - 0.6809	0.9779	Yes	< 0.0001
IIIL	Y = 0.02256*X + 0.7484	0.04341	No	0.692	IIIL	Y = 0.09950*X - 0.6854	0.9885	Yes	< 0.0001
IVL	Y = 0.08583*X - 0.9238	0.3944	No	0.1818	IVL	Y = 0.1058*X - 1.073	0.989	Yes	< 0.0001

Table 3.3. Summary Arch Artery Equations

Statistics for the lines made to fit arch artery trends. The equation of the curve, R^2 value, significance of the slope and P-value are displayed. Note how not all the experimental curves are significantly non-zero while the model curves are all significantly non-zero. Exp- experiment, Occl- Occluded, Cntrl – control

Computational vs experimental growth

We employed Analysis of covariance (ANCOVA) to compare the differences *between* control and PAA^{IV}-R occlusion ("occlusion") growth trends for both experimental and simulation conditions. As expected, the experimental occlusion and the control PAA^{II} changes were significantly different from their simulation counterparts. Vessel diameter growth for the PAA^{IV}-R experimental control condition differed significantly from its simulation ($P = 0.016$). Interestingly, there were no other differences in growth rate (slope) between the simulations and experimental conditions for any other vessels, but we did find significant differences in elevations between the growth curves. These results support that after the initial adaptation to the occlusion, follow on vessel growth was generally predictable by proportionality to wall shear stress.

Our simulations also predicted that growth of the left arch arteries would be significantly different from that of their right-sided pair for the majority of cases. In control conditions, PAA^{II} and PAA^{IV} were predicted to grow significantly from their side-matched counterpart, ($P = 0.002$ and $P = 0.04$ respectively). Simulations predicted all three pairs within the occlusion subgroup to exhibit different growth patterns when compared to their side-matched counterpart ($P = 0.0003$). The experimental results, however, showed that growth of the left arch arteries were statistically similar to their respective vessel on the right side regardless of whether the PAA^{IV}-R arch was occluded. Apart from the obvious difference PAA^{IV}-R and PAA^{IV}-L arch in occluded conditions, only PAA^{II}-R and PAA^{II}-L of the experimental occlusion subgroup also grew differently from each other over time ($P = 0.04$).

Together, these findings suggest that PAA^{IV}-R occlusion causes significant acute changes in initial vessel diameters that are poorly predicted by simple shear stress driven growth simulations. Apart from the PAA^{II} however, post-occlusion vessel growth trends were predicted well by the simulations, which suggests follow-on PAA growth is largely proportional to wall shear stress. Interestingly, in two cases (PAA^{III}-R and PAA^{IV}-L) the predicted vessel growth post-occlusion converges over time with the experimental data. This limited agreement supports a morphogenetic role for wall shear stress in PAA vessel remodeling. Our results also reveal the necessity of a highly influential but yet unaccounted programming that helps drive PAA morphogenesis and hemodynamic adaptation.

3.5 Discussion

Arch artery malformations underlie many clinically significant heart defects, but the dysmorphogenetic mechanisms are poorly understood. This study expands upon our previous intra-cardiac hemodynamic investigations while at the same time highlighting the need for a better understanding of the biological programming that underlies PAA growth and morphogenesis. These strides are necessary in order to begin to reconstruct continuous series of three-dimensional vascular anatomies for abnormal flow and pressure distributions. With this knowledge, scientists could begin to tackle cardiac malformations not directly linked to particular genetic dispositions. We examine the results of abnormal arch artery flow in contrast with those obtained in normal (healthy) 3D PAA morphologies during critical periods of development and highlight the impact of altered arch artery geometry on PAA perfusion. Analysis of redistributed flows indicates that some PAA occlusion can lead to configurations where PAA^{IV} no longer carries the dominant proportion of the flow, leading to

possibly altered PAA growth or regression. The present study predicted that PAA^{IV}-R occlusion would create the greatest flow alteration across the entire network. This finding is notable since this vessel matures to become the adult aortic arch in the chick.

The poor accordance of acute diameter changes with that predicted from our simple linear WSS growth model suggests that these vessel growth and adaptation likely follow more complex fluid dynamics principles, at least at this stage in development. Their growth can only be partially predicted by simple proportionality to wall shear stress. This discrepancy may also be related to the fact that these primitive vessels are completely surrounded by stiff pharyngeal mesenchyme. The best-fit computational to experimental models were that of PAA^{III}-R and PAA^{IV}-L occluded subsets, which converge to similar values over the course of the 24 hour post occlusion time period. Significant changes in flow distribution revealed the importance of local hydrodynamic resistance of the PAA manifold over the peripheral vascular resistance. Intriguingly, flow redistribution after occlusion did not align well with hydraulic resistances of the PAA vessels, which meant that the largest diameter vessel did not receive the largest amount of flow. The fact that flow redistribution and subsequent vessel remodeling again highlights the existence of additional hemodynamic and biological factors in PAA remodeling. Cardiac output and upstream OT morphology can drastically alter the initial hemodynamic conditions of the PAA network (Hu et al., 2009; Wang et al., 2009).

It is well known that morphogenesis of the pharyngeal arches and their corresponding arch arteries is a complex system of events involving precise timing and integration of multiple progenitor infiltrations and biological signaling networks (Graham, 2003;

Macatee et al., 2003; Waldo and Kirby, 1993; Waldo et al., 1996). The present *in silico* computations were unable to account for the regression of PAA^{II} or the appearance of PAA^{VI}, as these features are not solely determined by hemodynamics. Indeed, by HH24 PAA^{II} has completely regressed, while PAA^{IV} is now patent. Arch arteries III, IV and VI persist throughout the rest of development. As Waldo et al have stipulated, a difference between a vessel which regresses and one that persists may be in the associated mesenchyme (Waldo et al., 1996). Indeed in their 1997 paper Kirby, et al. showed that antisense targeted to a paralogous group of Hox messages caused PAA^{III} to regress in a manner similar to PAA^{II}, while antisense targeted to another paralogous group Hox message caused the appearance of an additional pharyngeal arch containing a novel and completely independent pharyngeal arch artery (Kirby et al., 1997). At this stage in their development (HH18/19), the PAA are comprised of endothelium and surrounded by an externally supportive mesenchyme which separates the primitive vessels from the ectodermal and endodermal epithelium (Le Lièvre and Le Douarin 1975; Bockman, Redmond, and Kirby 1989). Subsequent stages (HH18+) are characterized by a gradual increase in medial cell layers and maturation of the tunica media (Bergwerff et al. 1996). The stiffness of the surrounding mesenchyme may therefore be a key parameter regulating acute vessel expansion, as it represents the primitive vessel's first mechanical support. Indeed, the pharyngeal arches don't begin to express soluble tropoelastin until day 5 or 6 (Rosenquist et al. 1990; Rosenquist et al. 1988), indicating a stiffer phenotype may be possible prior to this time period. The onset of elastogenesis corresponds with a period of rapid cardiac growth and morphogenesis (Hu and Clark 1989) and coincides with loss of actin expression from the proximal part of the arterial tree (Bergwerff et al. 1996).

The development of the pharyngeal arches and their corresponding arch arteries is a complex system of events that also involves neural crest migration as well as endoderm signaling (Macatee et al. 2003; Graham 2003; Waldo and Kirby 1993; Waldo, Kumiski, and Kirby 1996). Local hemodynamic forces likely affect early differentiation of smooth muscle cells (SMCs) through changes in endothelium characteristics (Bergwerff et al. 1996). Around the onset of our study, at HH17/18, early markers of SMC differentiation are present in the form of actin positive myoblasts in the aortic sac. By HH21 (roughly 12 hours post the occlusion time point) actin expression has spread further and completely surrounds the dorsal aorta, pharyngeal arteries and aortic sac. At HH24 (24 hours post occlusion time point) the pulmonary arteries acquire actin expression at their junction with the sixth arch arteries, a time point that coincides with the initiation of flow through these vessels. Throughout this time (HH18-HH24 time period), the ability for the arch arteries to functionally communicate with their environment is increasing. Vinculin, a representative component of cellular adherens juctions, was found to be present in actin-positive cells of the dorsal aorta at HH18. At HH21, the aortic sac, pharyngeal arch arteries, and dorsal aorta all express high levels of vinculin, suggesting the existence of an early functional relationship between the cell's cytoskeleton and its environment (Bergwerff et al. 1996). Through the use of our targeted vessel occlusions, future studies may examine the role of hemodynamics in maintaining this functional relationship and the timing of SMC differentiation in response to controlled changes in flow and WSS levels.

Through our analysis of redistributed flow it was possible to model pathological situations where the left and right PAA^{IV} no longer transport the dominant proportion of PAA flow. In an earlier work Rychter experimentally ligated each individual PAA

at HH24 (Rychter, 1962). Ligations were performed through the insertion of a silver microclip into the branchial clefts. Unlike the occlusion experiments presented in this paper, Rychter's ligation also disrupted local tissue mesenchyme, so the effects are not flow specific. Upon PAA^{IV}-R ligation, a variety of mature great vessels patterns were produced. In the majority of Rychter's PAA^{IV}-R arch ligations (performed at HH24) cases (~75%), the PAA^{III}-R became the dominant arch artery or "main substitute channel", taking part in formation of the definitive arch of aorta alone or in combination with others. Our CFD and *in vivo* results agree with Rychter's observations in that the PAAIII-R received the largest flow redistribution and the largest change in diameter. However, our PAA^{IV}-R occlusions at HH18 were highly lethal (100% lethality before HH30), while Rychter's HH24 occlusions were able to grow to hatching. These findings suggest that PAA^{IV}-R flow disruptions between HH18 and HH24 highly influence outflow tract and great vessel morphogenesis and gestational viability. Stage specific flow distribution and downstream morphogenetic consequences remain unclear, but at least between those stages PAA^{IV}-R occlusion appears to favor PAA^{III}-R dominance.

The results of CFD flow changes, following PAA occlusion, can inform Rychter's observations. With Rychter's PAA^{III}-L ligation, the portion of the left carotid artery normally formed by the left lateral PAA^{III}-L is instead derived from the persistence of the ventral portion of PAA^{IV}-L. There is no left brachiocephalic artery, but rather the left subclavian and left carotid arteries have separate origins. This result can be explained in part using our CFD simulations: if the net gain of flow in each PAA is examined after PAA^{III}-R occlusion, then PAA^{IV}-L received the most of the occluded PAA's flow and caused a portion of PAA^{IV}-L to persist when the entire vessel normally degenerates. Similarly, in Rychter's PAA^{VI}-R ligation experiment, the right

ductus arteriosus doesn't form. In some cases, a short thin cord, a persistent remnant of PAA^{IV}-L was present. Our CFD occlusion of PAA^{VI}-L showed PAA^{IV}-R had the greatest percentage increase in flow. PAA^{IV}-L received the most of the occluded PAA's flow, which may explain why a portion of PAA^{IV}-L persists when the entire vessel normally degenerates. These occlusion experiments highlight the importance of unobstructed flow through the right lateral fourth arch artery.

In the embryo, PAA^{IV}-R carries the greatest amount of flow and has unique histogenesis as well as neurological innervation (Molin et al., 2002). Experimental models in which PAA fail to persist are often associated with valvular abnormalities (Molin et al., 2004). The increase in afterload and altered morphology caused by PAA occlusion may also have upstream effects, disrupting flow across the OT cushions, leading to valve defects. Based on our *in-silico* results, a hypoplastic or atretic PAA^{IV} in the embryo may be a critical factor in the development of congenital heart disease (Ilbawi et al. 2007). Complex molecular mechanisms and pathways have been identified to support embryonic endothelial mechanosensitivity (Molin et al., 2002). In vascular development, according to the flow-dependency principle, low WSS is empirically known to lead to chronic vessel regression; whereas, the physiological WSS inhibits apoptosis, contributing to vessel enlargement after flow increase (Roman and Pekkan, 2012).

Our *In silico* analysis of WSS based growth in HH18 controls may serve as a reference for surgical guidance to counteract the progression of arch artery malformations. Our study suggests that if a patient-specific PAA model is reported to have peak flow in an arch artery other than the predetermined dominate right IV, restorative interventions may include PAA flow alterations, either directly (using WSS fields as a guide) or

indirectly (through changes in OT orientation. To our knowledge, this study presents the first 3D growth kinematics predictions of a complex vascular system. We also present here, for the first time, experiments in which PAA flow is obstructed at a specified time point without disrupting the containing vessel or surrounding tissue. Such experiments allow us to differentiate the effects of altered flow from that of local tissue deformation and delineate the effects of disease formation. With the use of this targeted femtosecond laser ablation technology, we can begin to understand how altered hemodynamics initiates changes on both the whole tissue and molecular scale. Once comparable quantitative data in human great vessel development is established the same technology can be applied to predict and plan surgical cardiac interventions of congenital heart patients *in utero*.

During the recent decade, the clinical experience in fetal surgical cardiac interventions in human patients has steadily advanced (McElhinney et al., 2010), however the extremely complex vascular morphodynamics processes require new tools so that these advanced surgical interventions can be timed and planned precisely for the best outcome. Fundamental studies that define key regulatory mechanisms and the limits for *in vivo* adaptation to altered cardiovascular loading conditions is relevant to optimizing fetal management for CHD including the timing of fetal cardiac intervention for critical aortic stenosis and left heart hypoplasia (Emery et al., 2007) as well as other forms of CHD associated with altered biomechanics. The embryo's response to altered flow patterns during critical periods of development is one which scientists have been working to characterize for decades. This study invigorates this investigation by combining a minimally invasive technique to produce occlusions with new computational fluid dynamics mechanisms. While we are not yet able to fully capture and account for in vivo results, we have begun to capture key players and

highlight areas that necessitate further exploration. A precise understanding of the factors involved in abnormal hemodynamics perturbations will prove to be powerful tool in clinical diagnosis and intervention of congenital heart defects.

3.6 Acknowledgements

This research was supported by the National Institutes of Health (HL110328 to JTB), National Science Foundation (CBET-0955712 to JTB, graduate research fellowship to SEL) and European Research Council ERC STR Grant - Vascular Growth project # 307460 to KP.

References

1. Anderson, D.A., Tannehill, J.C., Pletcher, R.H., 1984. Computational Fluid Mechanics and Heat Hemisphere Publishing Corporation.

2. Bajolle, F., Zaffran, S., Kelly, R.G., Hadchouel, J., Bonnet, D., Brown, N.A., Buckingham, M.E.,

3. 2006. Rotation of the myocardial wall of the outflow tract is implicated in the normal
positioning of the great arteries. Circ Res 98, 421-428.

4. Bayer, I.M., Adamson, S.L., Langille, B.L., 1999. Atrophic remodeling of the artery-cuffed artery. Arterioscler Thromb Vasc Biol 19, 1499-1505.

5. Bergwerff, M. et al., 1996. Onset of elastogenesis and downregulation of smooth muscle actin as distinguishing phenomena in artery differentiation in the chick embryo. *Anatomy and embryology*, 194(6), pp.545–57.

6. Bharadwaj, K.N., Spitz, C., Shekhar, A., Yalcin, H.C., Butcher, J.T., 2012. Computational fluid dynamics of developing avian outflow tract heart valves. Ann Biomed Eng 40, 2212- 2227.

7. Bremer, J.L., 1928. Experiments on the aortic arches in the chick. Anat Rec (Hoboken) 37, 225-254.

8. Broekhuizen, M.L., Mast, F., Struijk, P.C., van der Bie, W., Mulder, P.G., Gittenberger-de Groot, A.C., Wladimiroff, J.W., 1993. Hemodynamic parameters of stage 20 to stage 35 chick embryo. Pediatr Res 34, 44-46.

9. Butcher, J.T., Sedmera, D., Guldberg, R.E., Markwald, R.R., 2007. Quantitative volumetric analysis of cardiac morphogenesis assessed through micro-computed tomography. Dev Dyn 236, 802-809.

10. Clark, E.B., Hu, N., Frommelt, P., Vandekieft, G.K., Dummett, J.L., Tomanek, R.J., 1989. Effect of increased pressure on ventricular growth in stage 21 chick embryos. Am J Physiol 257, H55-61.

11. Culver, J.C., Dickinson, M.E., 2010. The effects of hemodynamic force on embryonic development. Microcirculation 17, 164-178.

12. Davis, J.C., 1986. Statistics and Data Analysis in Geology, Second Edition ed. John Wiley, , New York.

13. deAlmeida, A., McQuinn, T., Sedmera, D., 2007. Increased ventricular preload is compensated by myocyte proliferation in normal and hypoplastic fetal chick left ventricle. Circ Res 100, 1363-1370.
14. Dor, X., Corone, P., 1985. Migration and torsions of the conotruncus in the chick embryo heart: observational evidence and conclusions drawn from experimental intervention. Heart Vessels 1, 195-211.

15. Emery, S.P., Kreutzer, J., Sherman, F.R., Fujimoto, K.L., Jaramaz, B., Nikou, C., Tobita, K., Keller, B.B., 2007. Computer-assisted navigation applied to fetal cardiac intervention. Int J Med Robot 3, 187-198.

16. Figueroa, C.A., Baek, S., Taylor, C.A., Humphrey, J.D., 2009. A Computational Framework for Fluid-Solid-Growth Modeling in Cardiovascular Simulations. Comput Methods Appl Mech Eng 198, 3583-3602.

17. Gessner, I.H., 1966a. Spectrum of congenital cardiac anomalies produced in chick embryos by mechanical interference with cardiogenesis. Circ Res 18, 625-633.

18. Gessner, I.H., 1966b. Spectrum of congenital cardiac anomalies produced in chick embryos by mechanical interference with cardiogenesis. Circ Res 18, 625-633.

19. Girerd, X., London, G., Boutouyrie, P., Mourad, J.J., Safar, M., Laurent, S., 1996. Remodeling of the radial artery in response to a chronic increase in shear stress. Hypertension 27, 799-803.

20. Go, A.S. et al., 2013. Executive summary: heart disease and stroke statistics--2013 update: a report from the American Heart Association. *Circulation*, 127(1), pp.143–52.

21. Graham, A., 2003. Development of the pharyngeal arches. Am J Med Genet A 119A, 251-256.

22. Hogers, B., DeRuiter, M.C., Gittenberger-de Groot, A.C., Poelmann, R.E., 1999. Extraembryonic venous obstructions lead to cardiovascular malformations and can be embryolethal. Cardiovasc Res 41, 87-99.

23. Hove, J.R., Koster, R.W., Forouhar, A.S., Acevedo-Bolton, G., Fraser, S.E., Gharib, M., 2003. Intracardiac fluid forces are an essential epigenetic factor for embryonic cardiogenesis. Nature 421, 172-177.

24. Hu, N., Christensen, D.A., Agrawal, A.K., Beaumont, C., Clark, E.B., Hawkins, J.A., 2009. Dependence of aortic arch morphogenesis on intracardiac

blood flow in the left atrial ligated chick embryo. Anatomical record 292, 652-660.

25. Hu, N., Clark, E.B., 1989. Hemodynamics of the stage 12 to stage 29 chick embryo. Circulation Research 65, 1665-1670.

26. Huang, C., Sheikh, F., Hollander, M., Cai, C., Becker, D., Chu, P.H., Evans, S., Chen, J., 2003. Embryonic atrial function is essential for mouse embryogenesis, cardiac morphogenesis and angiogenesis. Development 130, 6111-6119.
27. Humphrey, J.D., Rajagopal, K.R., 2002. A constrained mixture model for growth and remodeling of soft tissues. Math Mod Meth Appl S 12, 407-430.

28. Ilbawi, A.M. et al., 2007. Morphologic study of the ascending aorta and aortic arch in hypoplastic left hearts: surgical implications. *The Journal of thoracic and cardiovascular surgery*, 134(1), pp.99–105.

29. Jaffee, O.C., 1965. Hemodynamic Factors in the Development of the Chick Embryo Heart. Anat Rec 151, 69-75.

30. Kamiya, A., Togawa, T., 1980. Adaptive regulation of wall shear stress to flow change in the canine carotid artery. Am J Physiol 239, H14-21.

31. Kirby, M.L., Hunt, P., Wallis, K., Thorogood, P., 1997. Abnormal patterning of the aortic arch arteries does not evoke cardiac malformations. Dev Dyn 208, 34-47.

32. Kowalski, W.J., Dur, O., Wang, Y., Patrick, M.J., Tinney, J.P., Keller, B.B., Pekkan, K., 2013. Critical transitions in early embryonic aortic arch patterning and hemodynamics. PloS one 8, e60271.

33. Kowalski, W.J., Teslovich, N.C., Dur, O., Keller, B.B., Pekkan, K., 2012. Computational hemodynamic optimization predicts dominant aortic arch selection is driven by embryonic outflow tract orientation in the chick embryo. Biomechanics and modeling in mechanobiology 11, 1057-1073.

34. Langille, B.L., 1996. Arterial remodeling: relation to hemodynamics. Can J Physiol Pharmacol 74, 834-841.

35. Langille, B.L., O'Donnell, F., 1986. Reductions in arterial diameter produced by chronic decreases in blood flow are endothelium-dependent. Science 231, 405-407.

36. le Noble, F., Fleury, V., Pries, A., Corvol, P., Eichmann, A., Reneman, R.S., 2005. Control of arterial branching morphogenesis in embryogenesis: go with the flow. Cardiovasc Res 65, 619-628.

37. Liu, C., Liu, W., Palie, J., Lu, M.F., Brown, N.A., Martin, J.F., 2002. Pitx2c patterns anterior myocardium and aortic arch vessels and is required for local cell movement into atrioventricular cushions. Development 129, 5081-5091.

38. Lucitti, J.L., Jones, E.A., Huang, C., Chen, J., Fraser, S.E., Dickinson, M.E., 2007. Vascular remodeling of the mouse yolk sac requires hemodynamic force. Development 134, 3317-3326.

39. Lucitti, J.L., Tobita, K., Keller, B.B., 2005. Arterial hemodynamics and mechanical properties after circulatory intervention in the chick embryo. J Exp Biol 208, 1877-1885.

40. Macatee, T.L., Hammond, B.P., Arenkiel, B.R., Francis, L., Frank, D.U., Moon, A.M., 2003. Ablation of specific expression domains reveals discrete functions of ectoderm- and endoderm-derived FGF8 during cardiovascular and pharyngeal development. Development 130, 6361-6374.

41. May, S.R., Stewart, N.J., Chang, W., Peterson, A.S., 2004. A Titin mutation defines roles for circulation in endothelial morphogenesis. Dev Biol 270, 31-46.

42. McElhinney, D.B., Tworetzky, W., Lock, J.E., 2010. Current status of fetal cardiac intervention. Circulation 121, 1256-1263.

43. Menon, P.G., Teslovich, N., Chen, C.Y., Undar, A., Pekkan, K., 2013. Characterization of neonatal aortic cannula jet flow regimes for improved cardiopulmonary bypass. J Biomech 46, 362-372.

44. Molin, D.G., DeRuiter, M.C., Wisse, L.J., Azhar, M., Doetschman, T., Poelmann, R.E., Gittenberger-de Groot, A.C., 2002. Altered apoptosis pattern during pharyngeal arch artery remodelling is associated with aortic arch malformations in Tgfbeta2 knock-out mice. Cardiovasc Res 56, 312-322.

45. Molin, D.G., Poelmann, R.E., DeRuiter, M.C., Azhar, M., Doetschman, T., Gittenberger-de Groot, A.C., 2004. Transforming growth factor beta-SMAD2 signaling regulates aortic arch innervation and development. Circ Res 95, 1109-1117.

46. Nishimura, N. et al., 2006. Targeted insult to subsurface cortical blood vessels using ultrashort laser pulses: three models of stroke. *Nature methods*, 3(2), pp.99–108.

47. Pexieder, T., 1986. Standardized Method for Study of Normal and Abnormal Cardiac Development in Chick, Rat, Mouse, Dog and Human Embryos. Teratology 33, 91C-92C.

48. Reckova, M., Rosengarten, C., deAlmeida, A., Stanley, C.P., Wessels, A., Gourdie, R.G., Thompson, R.P., Sedmera, D., 2003. Hemodynamics is a key epigenetic factor in development of the cardiac conduction system. Circ Res 93, 77-85.

49. Rodbard, S., 1975. Vascular caliber. Cardiology 60, 4-49.

50. Roman, B.L., Pekkan, K., 2012. Mechanotransduction in embryonic vascular development. Biomech Model Mechanobiol 11, 1149-1168.

51. Rychter, Z., 1962. Experimental Morphology of the Aortic Arches and the Heart Loop in Chick Embryos, in: Abercrombie, M., Brachet, J. (Eds.), Advances in Morphogenesis. Academic Press, New York, pp. 333-371.

52. Rychter, Z., Lemez, L., 1965. Changes in localization in aortic arches of laminar blood streams of main venous trunks to heart after exclusion of vitelline vessels on second day of incubation. Fed Proc Transl Suppl 24, 815-820.

53. Sedmera, D., Pexieder, T., Rychterova, V., Hu, N., Clark, E.B., 1999. Remodeling of chick embryonic ventricular myoarchitecture under experimentally changed loading conditions. Anat Rec 254, 238-252.

54. Taber, L.A., 1998. A model for aortic growth based on fluid shear and fiber stresses. J Biomech Eng 120, 348-354.

55. Taber, L.A., Eggers, D.W., 1996. Theoretical study of stress-modulated growth in the aorta. J Theor Biol 180, 343-357.

56. Thoma, R., 1893. Untersuchungen über die Histogenese und Histomechanik des Gefässsystems. Verlag von Ferdinand Enke, Stuttgart.

57. Tobita, K., Garrison, J.B., Liu, L.J., Tinney, J.P., Keller, B.B., 2005. Three-dimensional myofiber architecture of the embryonic left ventricle during normal development and altered mechanical loads. Anat Rec A Discov Mol Cell Evol Biol 283, 193-201.

58. Ursem, N.T., Struijk, P.C., Poelmann, R.E., Gittenberger-de Groot, A.C., Wladimiroff, J.W., 2001. Dorsal aortic flow velocity in chick embryos of stage 16 to 28. Ultrasound in medicine & biology 27, 919-924.

59. Valentin, A., Humphrey, J.D., Holzapfel, G.A., 2011. A multi-layered computational model of coupled elastin degradation, vasoactive dysfunction, and collagenous stiffening in aortic aging. Ann Biomed Eng 39, 2027-2045.

60. Vogel, A. & Venugopalan, V., 2003. Mechanisms of pulsed laser ablation of biological tissues. *Chemical reviews*, 103(2), pp.577–644.

61. Wagenseil, J.E., 2010. A constrained mixture model for developing mouse aorta. Biomech Model Mechanobiol.

62. Waldo, K.L., Hutson, M.R., Ward, C.C., Zdanowicz, M., Stadt, H.A., Kumiski, D., Abu-Issa, R., Kirby, M.L., 2005. Secondary heart field contributes myocardium and smooth muscle to the arterial pole of the developing heart. Dev Biol 281, 78-90.

63. Waldo, K.L., Kirby, M.L., 1993. Cardiac neural crest contribution to the pulmonary artery and sixth aortic arch artery complex in chick embryos aged 6 to 18 days. Anat Rec 237, 385-399.

64. Waldo, K.L., Kumiski, D., Kirby, M.L., 1996. Cardiac neural crest is essential for the persistence rather than the formation of an arch artery. Dev Dyn 205, 281-292.

65. Wang, Y., Dur, O., Patrick, M.J., Tinney, J.P., Tobita, K., Keller, B.B., Pekkan, K., 2009. Aortic arch morphogenesis and flow modeling in the chick embryo. Ann Biomed Eng 37, 1069-1081.

66. Yalcin, H.C., Shekhar, A., Nishimura, N., Rane, A.A., Schaffer, C.B., Butcher, J.T., 2010a. Two-photon microscopy-guided femtosecond-laser photoablation of avian cardiogenesis: noninvasive creation of localized heart defects. American journal of physiology. Heart and circulatory physiology 299, H1728-1735.

67. Yalcin, H.C., Shekhar, A., Rane, A.A., Butcher, J.T., 2010b. An ex-ovo chicken embryo culture system suitable for imaging and microsurgery applications. Journal of visualized experiments : JoVE.

68. Yashiro, K., Shiratori, H., Hamada, H., 2007. Haemodynamics determined by a genetic programme govern asymmetric development of the aortic arch. Nature 450, 285-288.

69. Yoshigi, M., Knott, G.D., Keller, B.B., 2000. Lumped parameter estimation for the embryonic chick vascular system: a time-domain approach using MLAB. Comput Methods Programs Biomed 63, 29-41.

CHAPTER 4

CHARACTERIZATION OF AVIAN PHARYNGEAL ARCH ARTERY GROWTH AND HEMODYNAMICS THROUGH MUTLI-SCALE MODELING

4.1 Abstract

Early pharyngeal arch artery growth and morphogenesis are critical events in embryonic development. Remodeling of the primitive paired arch arteries into the great vessels of the heart involves a delicate sequence of events that remains poorly understood. While early studies have examined the cellular make-up of the arches and populations that seed it, examination of their hemodynamic properties is a relatively recent event. Here we work to establish natural variations in arch artery morphology during a critical window of development. We examine day 3, day 4, and day 5 arch artery morphogenesis and the relationship between geometrical, functional and hemodynamic changes across days and arches. Our findings show that the arch arteries possess distinct shape characteristics across days that affect functional parameters and correlate with movement of the outflow tract relative to the arch arteries.

4.2 Introduction

Before formation of the pulmonary artery and aortic arch, blood exits the developing chick embryo through six bilaterally paired pharyngeal arch arteries. Growth and remodeling of these vessels consists of a complex sequence of events that involves the emerging, disappearing, elongating, rotating and twisting of the arch pairs, as they remodel into their mature adult forms. In the chick embryo, the process of growth to maturation of the arch pairs largely occurs over the course of seven days. The mature pulmonary artery and aortic arch are present by HH36 (day 10). Throughout maturation of the arch arteries, three of the six

arch pairs persist: PAA III, PAA IV and PAA VI. PAA III contributes to the brachiocephalic and common carotid arteries. The right lateral PAA IV contributes to the adult aortic arch. The left lateral PAA IV regresses. PAA VI contributes to the ductus arteriosus and parts of the central pulmonary arteries. Of the transitory arch pairs, PAA I and II remodel into capillary beds, while PAA V is fleetingly seen as a segment PAA VI(T Hiruma and Hirakow 1995; Tamiko Hiruma, Nakajima, and Nakamura 2002). This sequence of growth and remodeling is conserved across species, though in mammals, the dominant side is reversed, with the left lateral PAA IV contributing to the mature aortic arch and the right lateral PAA IV forming part of the subclavian artery. Perturbations to this programmed sequence of events, can lead to severe cardiac abnormalities. Abnormal PAA morphogenesis is associated with over 50% of clinically presented congenital heart defects (Go et al. 2013). Despite the high prevalence of cardiac outflow abnormalities, the etiology of such defects continues to elude scientists and doctors alike.

Recent advances in imaging technology have allowed new high resolution studies of cardiac morphogenesis (Yalcin et al. 2010; Liu et al. 2012). Use of these technologies may bring us closer to understanding the mechanics of growth and development in the developing outflow tract, particularly the PAAs whose location within the stiff pharyngeal arch mesenchyme renders the developing vessels difficult to access and study. To date, quantitative studies of the PAAs are few, with no report of individual arch artery flow and velocity measurements, or pressure measurements present for the early remodeling window (Kowalski et al. 2014). Analysis of the natural variation at these stages only exists in the form of idealized composite(or averaged) geometries. Establishing a natural

framework of hemodynamic indices that regulate growth will lead to a better understanding of abnormal development and possible interventions.

Hemodynamics serve as a major epigenetic factor in vascular growth and remodeling. Wall shear stress (WSS) is sensed by endothelial cells and believed to be a major player in vascular remodeling (Fisher 2001, Hove, 2003). Pressure has been shown to modulate vessel shape and stretch (Banerjee et al. 2015; Taber 1995). Epigenetic perturbations in blood flow lead to congenital defects affecting the great vessels (Hogers et al. 1999; Hogers et al. 1997; Hu et al. 2009; Rychter 1962; Rychter and Lemez).

Previous computational and experimental examinations of the arch arteries (Wang et al. 2009; Kowalski et al. 2013; Lindsey et al. 2014; Kowalski et al. 2012) have quantified blood flow and spatial variations in WSS. While we were able to correlate changes in WSS with vessel growth, and provide quantitative evidence for flow-dependent growth in the embryonic arch arteries, we were unable to recapitulate changes occurring on the experimental level.

Here, we provide a more in depth stage-specific and embryo-specific analysis of the PAAs during a critical window of development HH18 (day 3) through HH26 (day 5), looking specifically at the natural variation present at each day. We perform a parallel study, using detailed renderings of fifteen stage-specific arch artery systems (five per day) obtained from nano-computed tomography. Scans were achieved using a contrast agent that penetrates the surrounding tissue and vessel lumens, rather than a resin within the vessels themselves that could expand and possibly deform the primitive vessels. While much has been gained

from studies such as Hiruma et al, these qualitative studies expand the vessel lumen producing diameters that are larger than expected, and perhaps influencing the shape of the vessel itself.

Obtained geometries were subsequently connected to a lumped parameter, electric analog, network of downstream resistance that puts the arch arteries back in the context of embryonic circulation and further facilitates a highly detailed, clinically relevant simulation (Vignon-Clementel et al, 2006). Ultimately, establishing norms for critical windows of development, when the heart is undergoing a number of functionality and shape changes required for normal development, will help identify the origins of congenital malformations and provide insights into the optimal timing for restorative interventions.

4.3 Materials and Methods

Embryo culture and preparation

Fertile white Leghorn chicken eggs were incubated blunt-side up for three, four, and five days in a continuous rocking incubator at 37.5^{o}C. Embryos were removed from the incubator at the appropriate stage and subsequently dissected away from their yolk sac. Injection micro-needles were fashioned from pulled capillary tubes (0.75 mm ID) cut to 20-35 μm inner diameter via a microforge (Glassworx, St. Louis, MO). A micromanipulator (model M3301L, World Precision Instruments, Sarasota FL) was used to position the needle into the apex of heart. The embryo's vascular system was flushed with phosphate buffer solution followed by 4% paraformaldehyde to preserve inner vascular volumetric integrity. The embryos were then left in 4% paraformaldehyde for 24-48 hours before being transferred to a 70% ethanol solution, and stored until needed. Embryos were brought up to a 30% ethanol solution before

being transferred to a diluted form of Lugol solution, aqueous potassium iodide and iodine, (Sigma-Aldrich, L6146). The embryos soaked in Lugol's and the solution was changed over several days until the embryos no longer took up any iodine. Embryos were then dehydrated down to 100% ethanol placed in polymerase chain reaction tubes and sent to undergo 3-4µm nano-computed tomography scans (nano-CT).

Ultrasound Processing and generation of Inlet flow curves

Outflow tract (OFT) velocity and that of the three paired pharyngeal arch arteries were measured using B-mode guided Doppler Ultrasound (Vevo770 and Vevo 2100, Visualsonics, Inc.). Warm Earle's balanced salt solution was used as an aqueous conduit between the embryo and the ultrasound scanhead. Embryos were kept at 37.5^{o}C during imaging by being placed in a heated water bath as previously noted (Yalcin et al. 2010).After imaging, the embryos were transferred back to the incubator and allowed to recover. For each analyzed stage, 11-15 Doppler recordings were averaged to obtain a summary velocity curve.

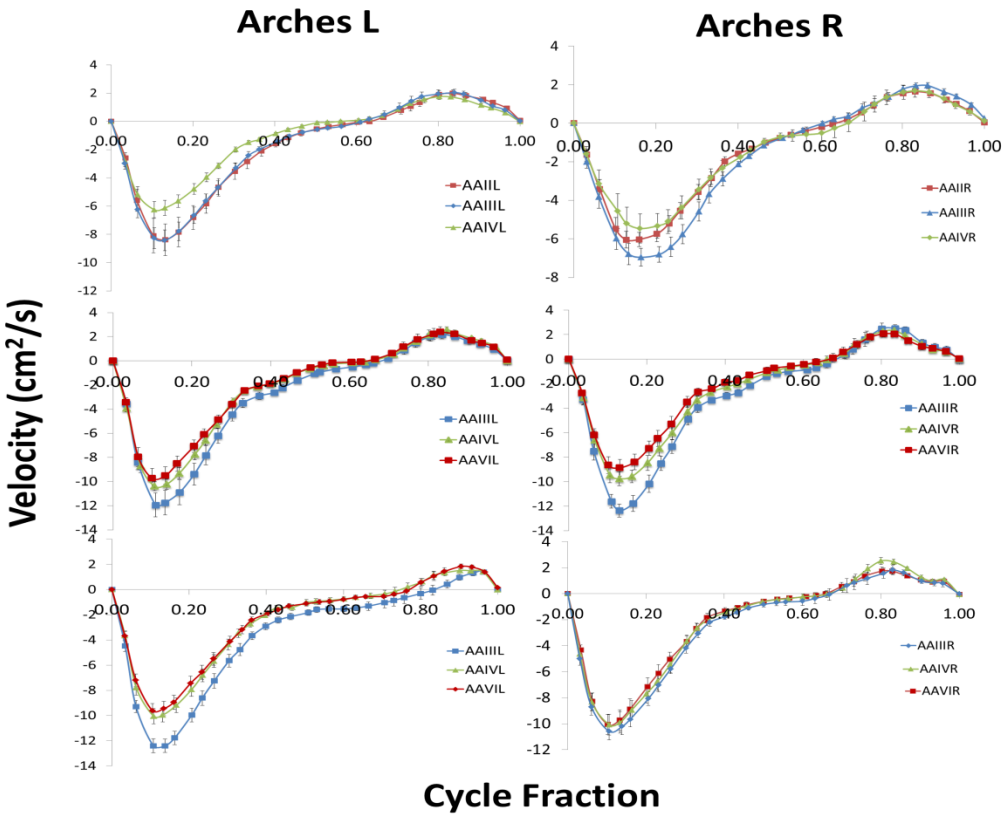

Figure 4.1. Pulse wave Doppler Velocity Measurements of Day 3, Day 4, Day 5 Embryos

Pulse wave measurements were obtained for experimental control day 3 (A) day 4 (B) and day (5) embryos. Summary curves represent 11 – 15 embryos. Of note are the side –specific, day-specific similarities in both shape and velocity. Standard error bars are shown.

A Poiseuille profile was assumed for days 3 (HH18) and day 4 (HH24) OFT flow Bharadwaj et al. 2012). Peak outflow velocity was converted to flow using equation 1.1.

$$Q = \frac{1}{2} Area * Vmax \qquad (1.1)$$

Plug flow was assumed the for the day 5 embryos (HH26) (Bharadwaj et al. 2012) and the peak velocity converted to flow using equation 1.2.

$$Q = Area * Vmax \qquad (1.2)$$

Because the shape of the inlet flow curves differed greatly from that of the individual arches, for each of the measurements taken for day 3, day 4 and day 5, it was assumed to be the result of fluid-structure interactions within the OFT itself. To compensate for the lack of fluid-structure interaction in our CFD inlet, a new inlet curve was calculated. Mean flow, calculated from Doppler ultrasound, was fed to each embryo via a steady-state simulation and the ratio between flow and velocity calculated in each of the individual arches. A new Qinlet was then calculated to be the sum of flow in each of the individual arches via the following equation:

$$Q_{inlet} = \sum_{i=0}^{6} Vi_{max}(t) * \frac{Q_i(ref)}{Vi_{max}} \quad (1.3)$$

where Vi_{max} is the Dopper pulse –wave velocity profile for that arch, ref refers to values measured in the steady state simulation with Doppler imposed flow, and $Qi(ref)/Vi_{max}$ is an estimation of the profile contribution from each arch. In this way the velocity profile for individual arches could be recovered during post-processing and compared to that of experimental curves.

Zero-dimensional lumped parameter estimation model

0D circuit representations of arch artery morphology, in the form of a system of ordinary differential equations, were created for day 3, day 4, and day 5 geometries. Sundials initial value problem solver, Implicit Differential-Algebraic solver, IDA, (Lawerence Livermore National Laboratory, Livermore, CA) was used to obtain solutions to the 0D circuit. This 0D model was used to tune the RCR or Windkessel outlet boundary conditions of day 3, day4 and day5 embryos. Presented models (Figure 4.2) were adapted from Yoshigi et al's single compartment 0D model of HH18 and HH24 embryo circulation as seen from the PAAs (Yoshigi, Knott, and Keller 2000). Yoshigi's lumped parameter model, which was created to match the entirety of embryonic circulation outside the arch arteries, is split into three (Figure 4.2b) and scaled to represent cranial-caudal flow conditions. As a 90-10, cranial-caudal flow

split is maintained over the course of a cardiac cycle, this is achieved by sending 5% of flow to the two cranial branches (respectively) and 90% to the caudal branch. After testing flow and pressure curves, the inductor was found to have a negligent value and removed from the circuits. The three compartment system was then placed back into the context of the arches by connecting it to 0D representations of the arches (Figure 4.2c and Figure4.2d) as well as 3D arch artery reconstructions (Figure 4.2e). Each vessel that flow traveled through in order to reach the outlets was represented by a resistor, as pressure is dissipated across a vessel. Resistance values were updated after 3D simulations according to Ohms law. In the case of vascular structures this takes the form of equation 1.4.

$$P_{in} - P_{out} = Q * R \qquad (1.4)$$

Where P_{in} is pressure at the start of a vessel, P_{out} presents pressure at the end of a vessel and Q is taken midway along the arch diameter. In the event that a pressure drop was not accounted for in the lumped parameter model, a new resistor was added, as was the case with pressure drop seen in the aortic sac for the day3/day 4 circuit model. Final lumped parameter estimation of the day 3 and day 4 geometry is shown in Figure 4.2c. Figure 4.2d represents day 5 morphology. Lumped parameter abstraction of the 3D domain is represented in black; the Windkesssel boundary conditions are outlined with dotted lines.

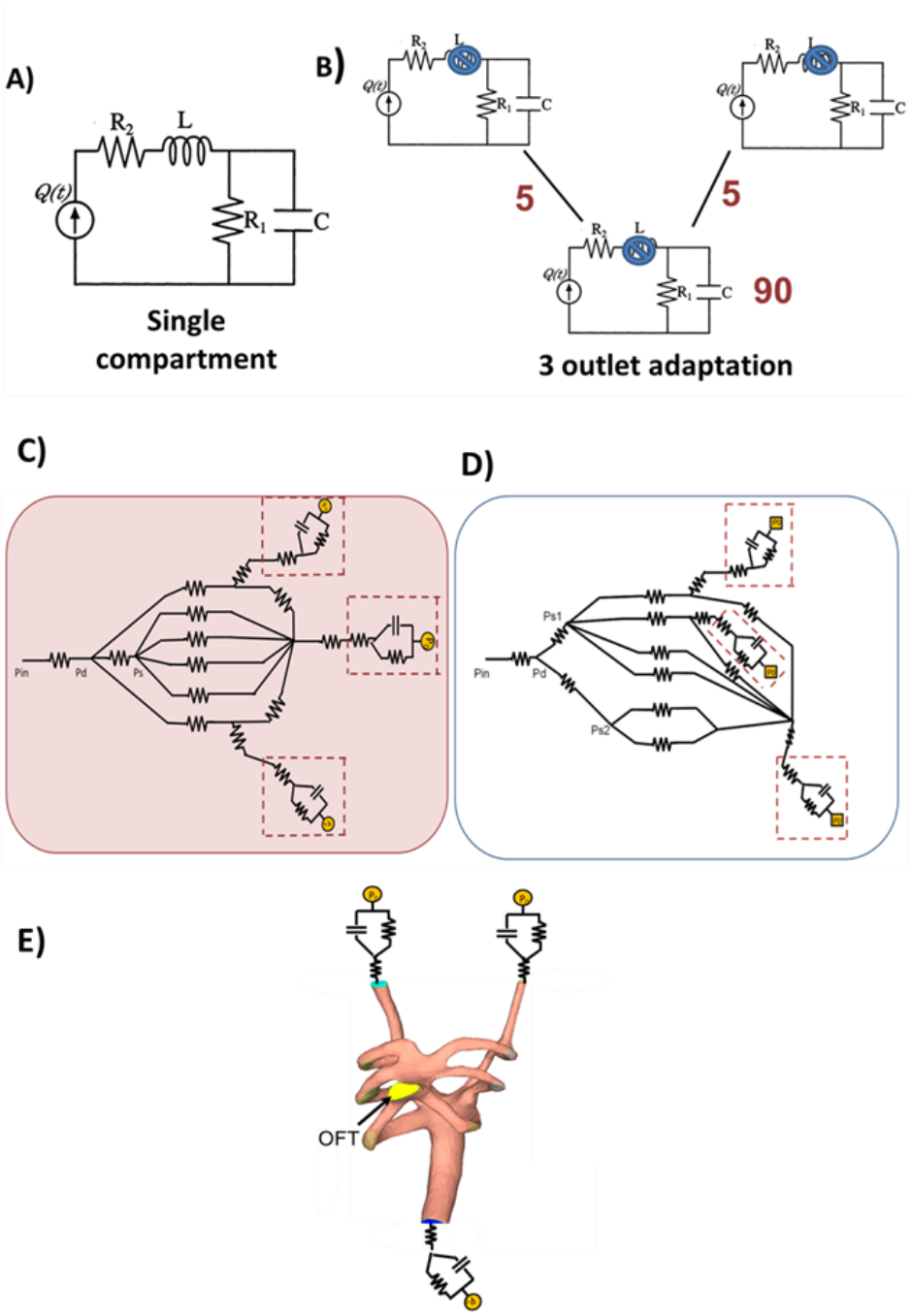

Figure 4.2. 0D Electric Analogs of Day3 and Day4 PAA Systems

Yoshigi lumped parameter model as seen from arches (A), Modifications to account for 3 outlets and 90-10 cranial caudal flow split (B). Day3 and day 4 circuit geometries (C). Only the numbering of the arch arteries themselves will change between the days/stages. (D) Day 5 circuit. Notice how the arches are now split between two junctions. Dashes lines (red) outline 0D bounds.

In-silico geometry preparation and flow modeling

Embryo-specific 3D geometries of the HH18 (day3), HH24 (day 4), and HH26 (day 5) pharyngeal arch artery (PAA) were generated by importing nano-CT images into MIMICS (Materialise, Louvain, Belgium) and 3MATICs (Materialise, Louvain, Belgium) (Figure 4.3). PAA geometries extended from the distal outflow tract to the dorsal aorta and paired cranial aortae. Geomagics Studio 10 (Geomagic Inc., Durham, NC) was also used for the preparation of 3D geometries for CFD. All embryos were scaled by a factor of three to account for the difference between dehydrated and native vessel size. India ink and Texas Red Dextran were used to obtain native vessel size across stages, results compared to that of 3D reconstructions and a scaling factor was generated.

For 3D mesh generation and adaptation, *ghs3d* and *feflo* (Loseille and Rainald 2010) were used. Grid sensitivity analysis was conducted on a control PAA model for each day in order to ensure consistency and reliability of the numerical solutions for all simulations presented in this study, beyond which resulting mass-flow redistributions were insensitive to further Cartesian grid refinements.

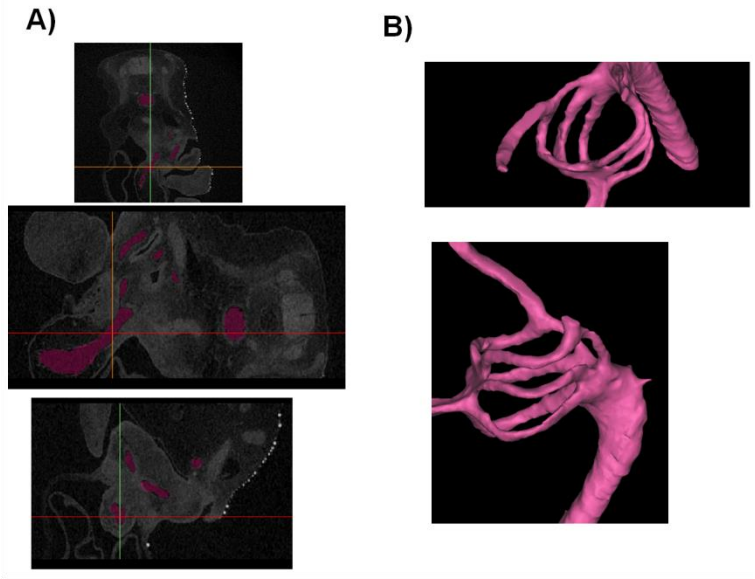

Figure 4.3. Creation of 3D geometries from Nano-CT images.
Nano-Ct computed tissue stack of the arches, outflow tract and dorsal aorta shown from three different cutting planes. B) Corresponding 3D rendering before smoothing and post-processing in MIMICS and 3MATIC.

Boundary Conditions:

A natural flow profile was imposed at the inlet. To obtain this an auxiliary steady Stokes equation, with natural boundary conditions at the outlets, is solved first (Pant, 2013). The resulting outlet velocity profile subsequently scaled at each time-point to match the measured flow-rate,in this case the flow resulting from equation 1.3. RCR Windkessel models are imposed at the outlet, the parrameters tuned to assure the distribution of the total cardiac output to dorsal aorta and cranial vessels maintains a 90-10 flowsplit over the course of one cycle. CFD simulations were conducted at INRIA Paris-Rocquencourt. Day 3 and day 4 simulations cost an average of 20 hours

at 16 core parallelism (2 nodes each) while day 5 simulations cost an average of 27 hours at 16 core parallelism. Pressure values from the 0D model were used as initial estimates of the caudual and cranial pressures, helping the flow to become periodic in one flow cycle. Blood was treated as a Newtonian fluid with constant hemodynamic properties ($\rho = 1060$ kg/m^3, $\mu = 3.71 \times 10^{-3}$ Pa.s) and rigid, impermeable vessel walls were assumed with no slip boundary conditions. Flow was simulated in cgs units, on a high-resolution unstructured Cartesian grid with finite-element numerical treatment through FELiScE (http://felisce.gforge.inria.fr).

For the **outlet boundary conditions** RCR Windkessel models are imposed. These boundary conditions are non-homogeneous Neumann boundary conditions. The differential equation representing the RCR circuit is

$$P + R_5 C \frac{dP}{dt} = (R_4 + R_5)Q + R_5 R_4 C \frac{dQ}{dt} \quad (1.5)$$

Where R_4 is the proximal resistance, R_5 is the distal resistance C represents capacitance P is pressure and Q is flow. This equation was solved for each of the three outlets, via IDA; calculated constants were fed to FELiScE.

Morphology post- processing

The Vascular Modeling Toolkit (vmtk),supported by Orobix, sri, was used to obtain cross-sectional areas, corresponding diameters, and shape functions for evenly spaced cuts taken along the centerline of each geometry. Ensight (Computational Engineering International, Inc, Apex, NC), was used for all post-processing visualization and measurement of hemodynamic properties.

Statistical Analysis

Morphological and hemodynamic changes were compared qualitatively and quantified when possible. Results were summarized in the form of mean and standard deviation

values over the course of one cardiac cycle. Paired T-tests were used where appropriate with $P < 0.05$ denoting significance.

4.4 Results

Pharyngeal arch morphology

For day 3 controls, peak pressure varies between 5100 dyne·cm^{-2} (3.83 mmHg) and 2900 dyne·cm^{-2} (2.17 mmHg) at peak flow (Figure 4.4). Pressure begins to dissipate cranially as flow rises up the aortic sac and laterally as the flow enters the arches. Spikes in WSS can be seen at the inlet in the aortic sac near the third arch artery entrance as well as laterally along the length of the arch.

The right and left lateral third arch consistently received the largest amount of flow in the developing day 3 embryo, receiving between 79% and 92% of flow through the arches over the course of one cardiac cycle. The right side received more flow in two of the five embryos presented, while the left side received an average of 15% more flow in the three other cases.

WSS, pressure distribution

Day 3

	CK26		CK72		CK75		CK76		CK85	
	Right	**Left**	**Right**	**Left**	**Right**	**Left**	**Right**	**Left**	**Right**	**Left**
II	**0.6±0.1%**	**1.5±0.4%**	**3.2±1.3%**	**3.7±2.0%**	**3.5±0.2%**	**4.1±0.4%**	**0.9±0.03%**	**0.2±0.1%**	**3.4±0.7%**	**4.3±0.2%**
III	**47.0±1.4%**	**36.0±1.1%**	**47.1±1.2%**	**38±1.6%**	**35.5±0.3%**	**46.5±0.2%**	**33.3±0.2%**	**59.2±0.2%**	**35.1±0.2%**	**43.3±0.3%**
IV	**6.8±0.04%**	**8.1±0.1%**	**3.0±0.2%**	**4.3±0.3%**	**5.7±0.1%**	**4.7±0.1%**	**2.1±0.04%**	**4.3±0.1%**	**5±0.1%**	**8.7±0.2%**

Table 4.1. Mean Flow distributions across the arches of day 3 embryos

In day 4 controls, the right fourth received over 25% of the flow in three out of five embryos. Surprisingly the right fourth received relatively little flow (8%) and the left fourth received over 25% of the the flow in the remaining two embryos. In the embryos where the left fourth received over 25% of the flow through the arches, flow dominance was shifted to the left side with the left receiving 55% in once instance and 75% in the other.

WSS, pressure distribution

Day 4 peak pressure varies between 7500 dyne·cm^{-2} (5.626 mmHg) and 4650 dyne·cm^{-2} (3.49 mmHg) at peak flow (Figure 4.5A), up 36% and 60 % respectively. Pressure dissipation follows a similar pattern to that of day 3 controls. WSS spikes have increased dramatically with the increase in flow throughout the arches (Figure 4.5B).

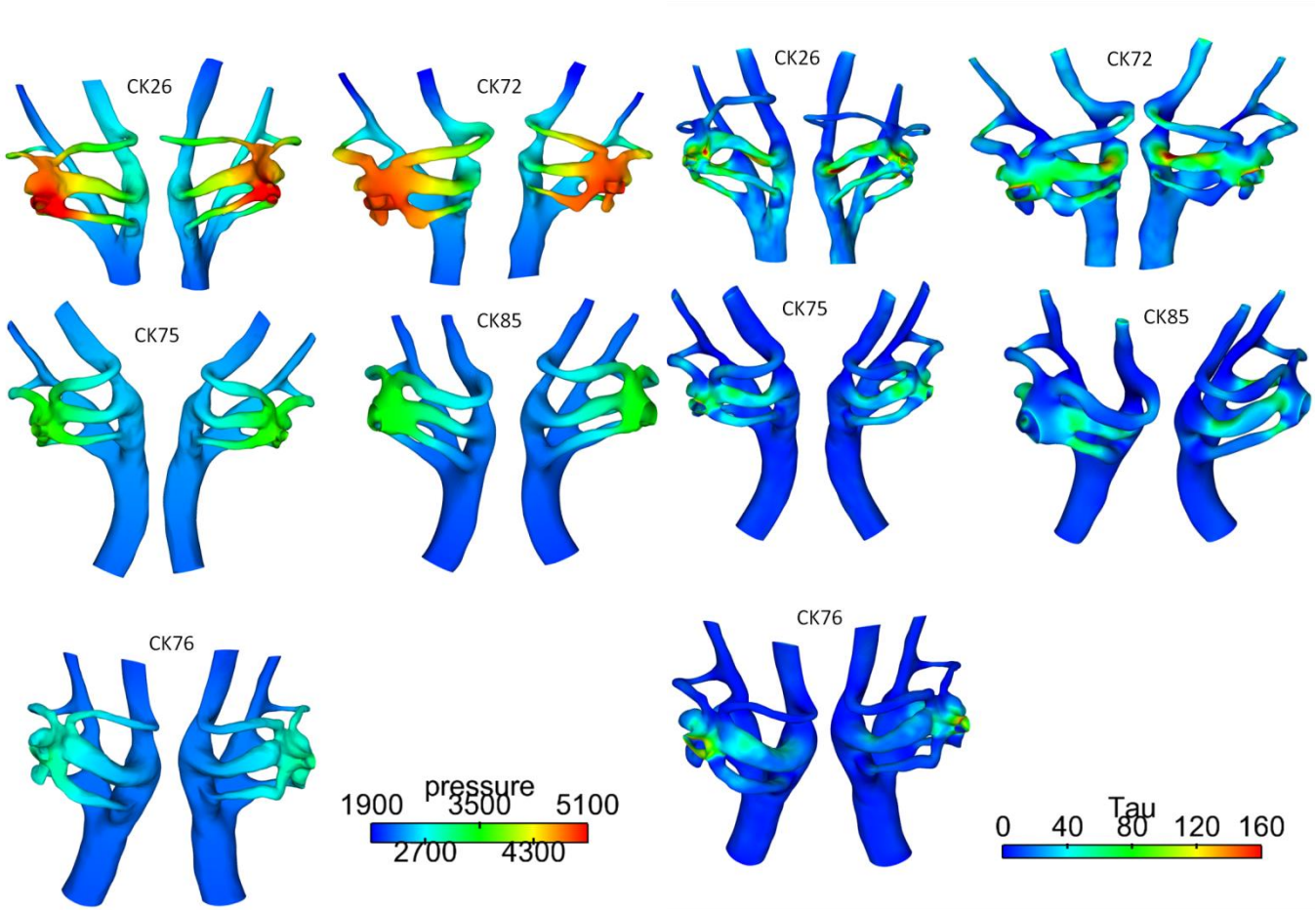

Figure 4.4 Pressure and Wall Shear Stress Distributions Across Day 3 Embryos

Figure 4.4. Pressure distributions (dyne·cm^{-2}) across day 3 embryos at peak flow (A) and the corresponding WSS maps (dyne·cm^{-2}) (B). Though the magnitude of the pressure changes, it is greatest at the inlet and through the aortic sac, before being disbursed through the arches. Peaks in WSS can be found at the inlet junction and large PAAIII in certain embryos.

Day 4

	CK27		**CK68**		**CK69**		**CK73**		**CK74**	
	Right	**Left**	**Right**	**Left**	**Right**	**Left**	**Right**	**Left**	**Right**	**Left**
III	**13.7±7.4%**	**8.7±0.6%**	**18.0±3.7%**	**18.4±2.6%**	**33.7±0.7%**	**17.3±0.2%**	**13.0±6.0%**	**38.8±6.4%**	**31.2±1.0%**	**7.8±1.5%**
IV	**33.5±3.2%**	**10±0.8%**	**7.5±8.6%**	**25.4±4.4%**	**28.4±0.3%**	**13.8±0.4%**	**8.8±5.7%**	**29.3±4.5%**	**25.0±1.1%**	**7.9±0.4%**
VI	**25.6±1.6%**	**8.6±0.5%**	**19.6±2.4%**	**11.1±0.5%**	**5.2±0.3%**	**1.6±0.1%**	**3.6±0.6%**	**6.5±1.5%**	**21.0±0.3%**	**7.2±0.3%**

Table 4.2. Mean Flow distributions across the arches of day 4 embryos.

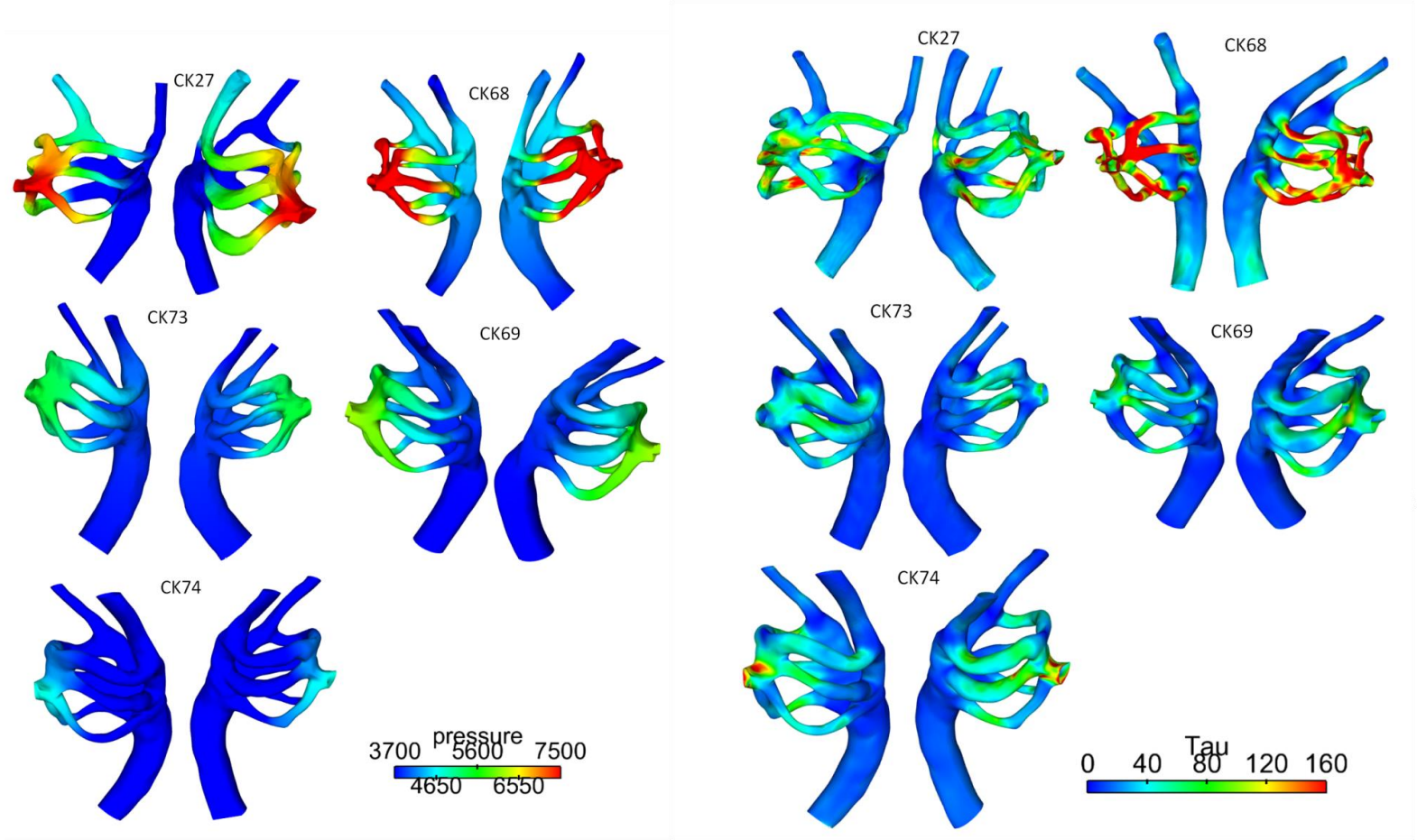

Figure 4.5 Pressure and Wall Shear Stress Distributions Across Day 4 Embryos

Pressure distributions across day 4 embryos (dyne·cm^{-2}) at peak flow (A) and the corresponding WSS maps(dyne·cm^{-2}) (B). Similarly to day 3 embryos, pressure is greatest at the inlet and aortic sac, before being disbursed through the arches. Peaks in WSS are growing at the inlet junction and start to appear in several arches

Day 5

	CK29		CK64		CK70		CK77		CK78	
	Right	**Left**	**Right**	**Left**	**Right**	**Left**	**Right**	**Left**	**Right**	**Left**
III	**7.1±0.9%**	**8.8±1.2%**	**7.2±2.2%**	**13.7±0.6%**	**7.5±1.2%**	**7.4±1.3%**	**9.6±1.0%**	**19.5±1.1%**	**26.8±2.5%**	**16.8±0.1%**
IV	**5.5±0.7%**	**19.4±1.1%**	**5.5±1.1%**	**10.9±1.1%**	**5.1±1.0%**	**8.5±1.6%**	**7.3±0.8%**	**9.5±0.9%**	**21.4±0.8%**	**10.4±1.1%**
VI	**46.4±5.1%**	**12.8±1.1%**	**31.9±2.7%**	**30.8±2.2%**	**53.4±6.5%**	**18.8±1.4%**	**35.6±2.7%**	**19.0±0.4%**	**15.0±0.8%**	**9.8±9.8%**

Table 4. 3. Mean Flow distributions across the arches of day 5 embryos

The right and left lateral six arch begin to receive the majority of flow in day 5 embryos, receiving between 55 % and 72% of the flow in 4 of the five day 5 embryos, and 25% of the flow in the younger day 5 embryo. At this point in development, there is a clear division between the upper four arch arteries (PAA IIIR, PAA IVR, PAA IIIL, PAA IVL) and the bottom PAA VIL and PAA VIR.

WSS, pressure distribution

For day 5 controls, peak pressure varies between 9350 dyne·cm^{-2} (7 mmHg) and 15000 dyne·cm^{-2} (11.25 mmHg) at peak flow (Figure 4.6), double that of day 4 control embryos. Flow is no longer required to progress through the aortic sac in order to distribute to the more cranial arches. Pressure is dissipated almost equally along OFT junctions and dissipates in a uniform fashion along the bilaterally paired arch arteries. WSS takes on 3 distinct patterns among the five embryos presented (Figure 4.6B). CK70 and CK77 possess a segment of elevated WSS along their narrowed IVR arch arteries, as well as small spike in other narrowings along the length of the arch. CK78 and CK64 have elevated levels of WSS as the outflow tract junctions diffuse into the arch arteries. CK29 shows levels of elevated WSS all along its elongated, elevated arches.

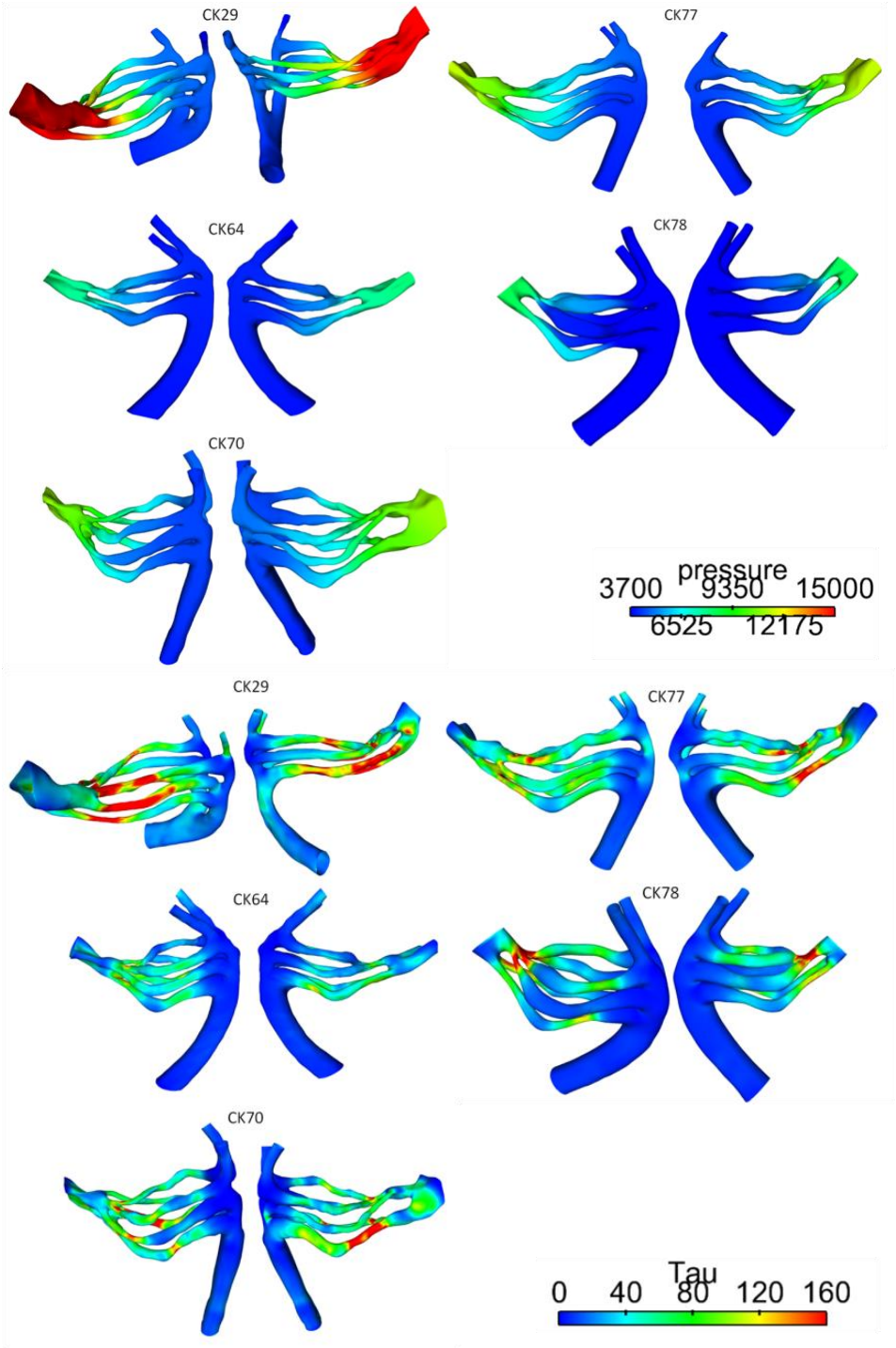

Figure 4.6. Pressure and Wall Shear Stress Distributions Across Day 5 Embryos Pressure distributions (dyne·cm^{-2}) across day 5 embryos at peak flow (A) and the corresponding WSS maps (dyne·cm^{-2}) (B). Following the d3,d4 embryo trend, pressure is greatest at the inlet and aortic sac, before being disbursed through the arches. Three distinct WSS patterns can be seen within the five embryos presented.

Vessel morphology across stages

Vessel cross-sectional area and shape play a large role in the functionality of a vessel. Cross-sectional area has been shown to correlate with flow distribution (Wang et al. 2009; Lindsey 2014), with the "dominant" arch possessing the largest diameter and greatest percentage of flow over one cardiac cycle. When arch diameters vary largely over the course of an arch, it can be uncertain which diameters or cross-sectional areas hold the most meaning. Figure 4.8 illustrates cross-sectional area variation across each embryo for day 3, day 4 and day 5 controls. In addition to the cross-sectional area changes, distinct patterns can be seen in horizontal versus vertical diameter changes across the days. For each cross-section the horizontal diameter is taken to be the left-right diameter, while the vertical diameter is taken to be the cranial caudal diameter as shown in Figure 4.7.

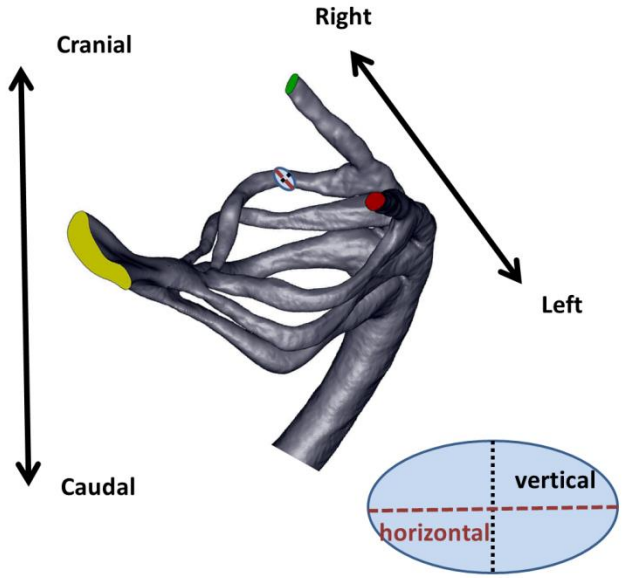

Figure 4.7. Horizontal Vertical Axes of Arch Artery Cross-Sections.

Figure 4.7 Arrows show directionality along the arch arteries. A blue section is taken from the top right arch and expanded in the bottom right corner. The Red line shows the horizontal axis which corresponds to left right, and the black line shows the vertical axis which corresponds to cranial caudal.

Figure 4.9 summarizes these shape changes across the arches for day 3, day 4 and day 5 control embryos. These changes are further characterized in Figure 4.10 which relates the specific arch diameter axes variations with changes in functionality. Though resistance, as measured here, is a hemodynamic parameter that represents a pressure drop to flow ratio, it is also a functional parameter. A three dimensional vessel is reduced to a single resistor in our lumped parameter models and is able to capture its flow curve as seen in the 3D simulation. Resistance values indicate how easy or difficult it is for flow to travel through the vessel. Figure 4.10 F –H shows arch artery electric analog values across the days. Although arch artery values generally decreased in resistance between day 3 and day 4 before subsequently increasing in magnitude between day 4 and day 5, statistically relevant changes only exist between day 3 and day 4 arch IVL ($P = .0385$) and day 4 and day 5 arch VIR ($P = .045$).

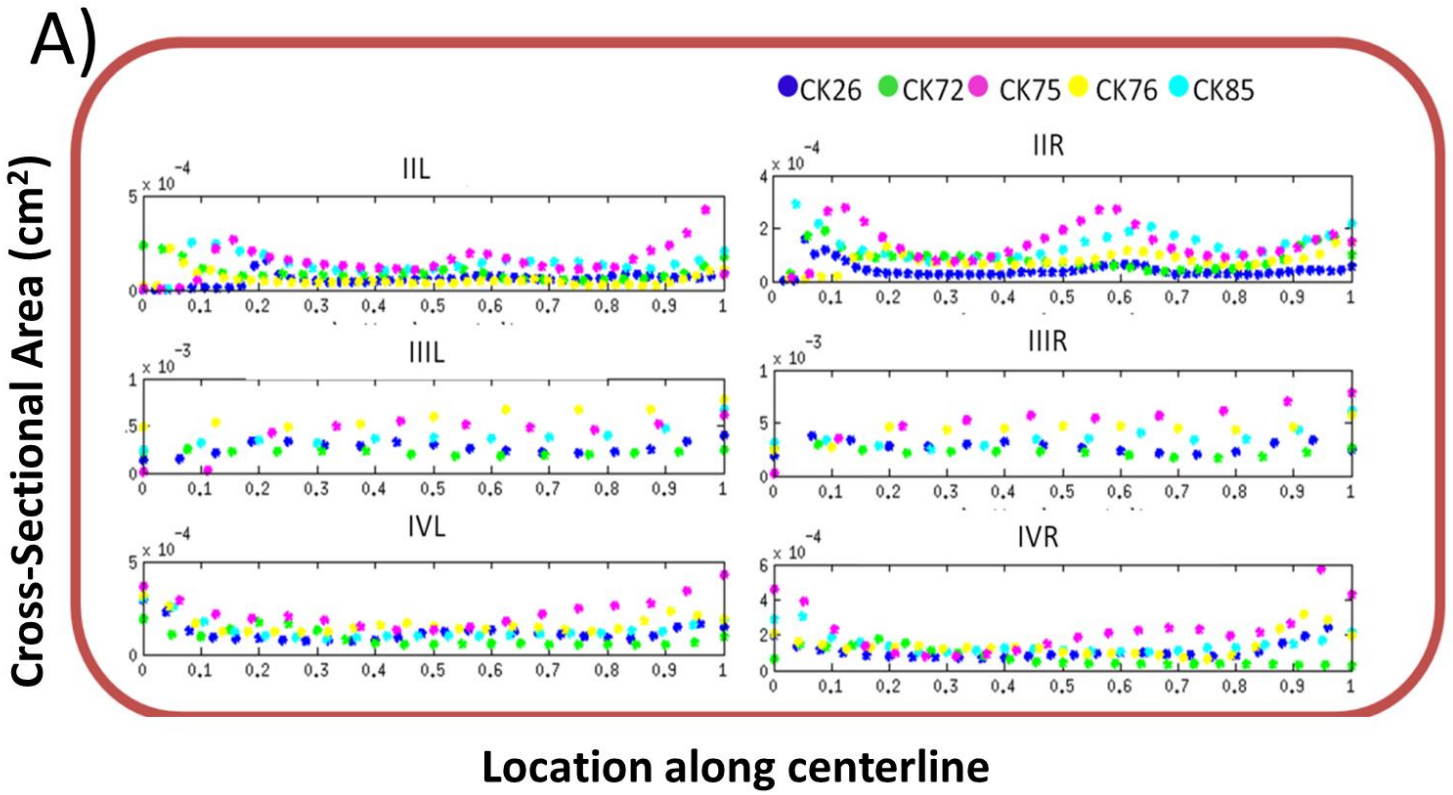
A)
CK26
CK72
CK75
CK76
CK85
IIL
IIR
IIIL
IIIR
IVL
IVR
Cross-Sectional Area (cm²)
Location along centerline

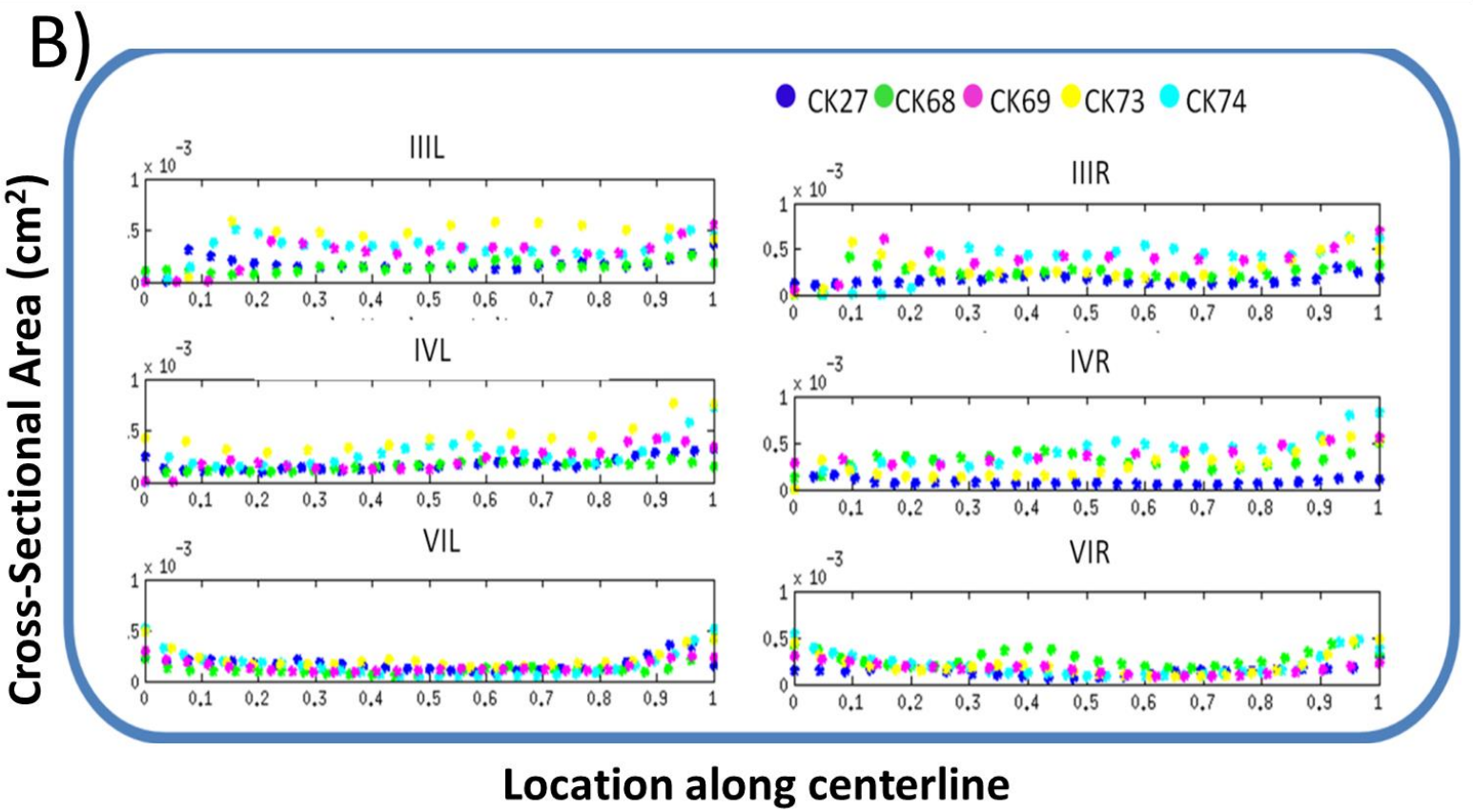
B)
CK27 CK68 CK69 CK73 CK74
IIIL
IIIR
IVL
IVR
VIL
VIR
x 10^-3
Cross-Sectional Area (cm²)
Location along centerline

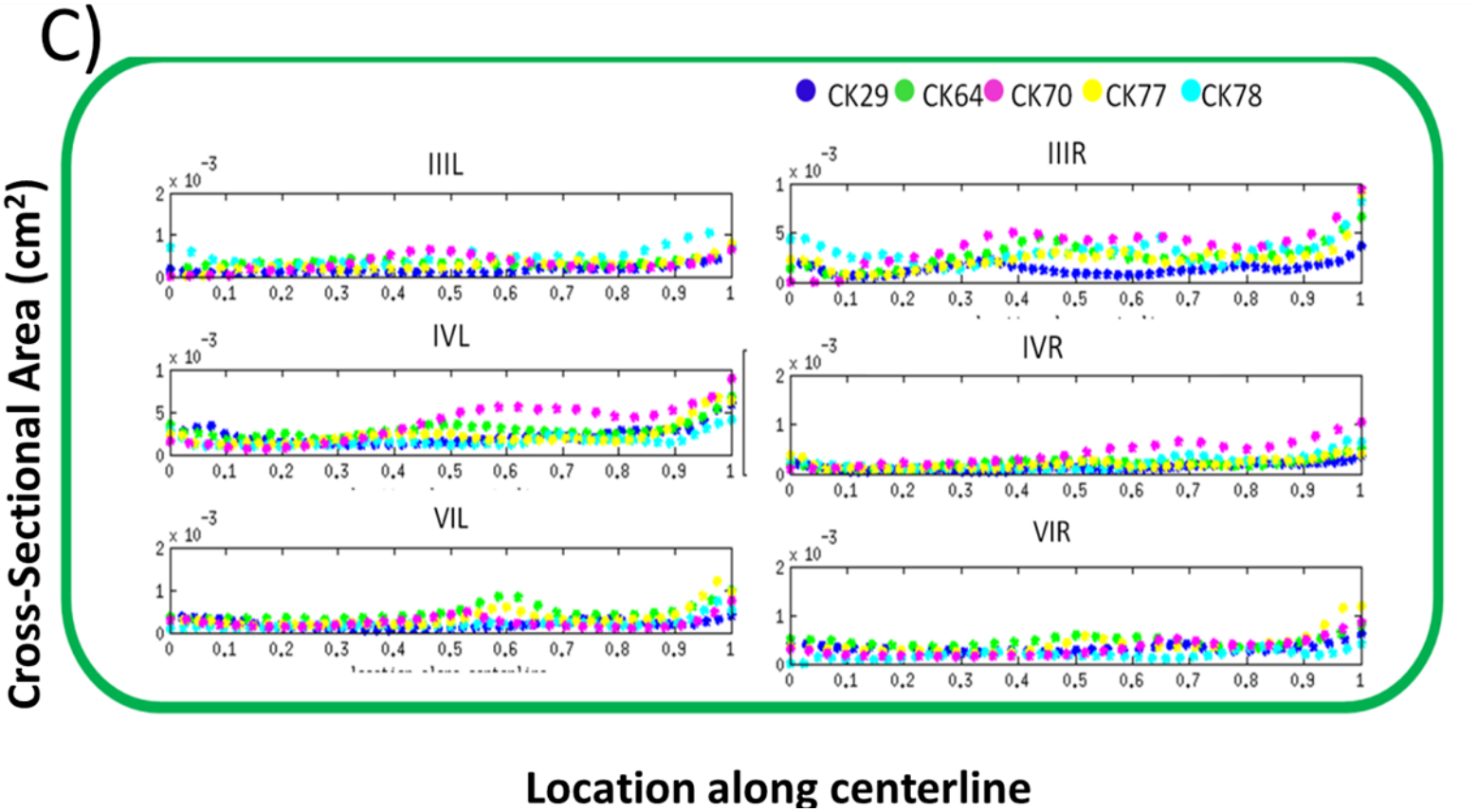

Figure 4.8. Cross-sectional Area Distributions for Day 3, Day 4, Day 5 Embryos

Cross-sectional area graphs shown over normalized arch lengths for day 3 (A) day 4 (B) and day 5 (C) embryos. Note how cross sectional areas vary greatly across the length of an arch, particularly day 3 and day 5 embryos

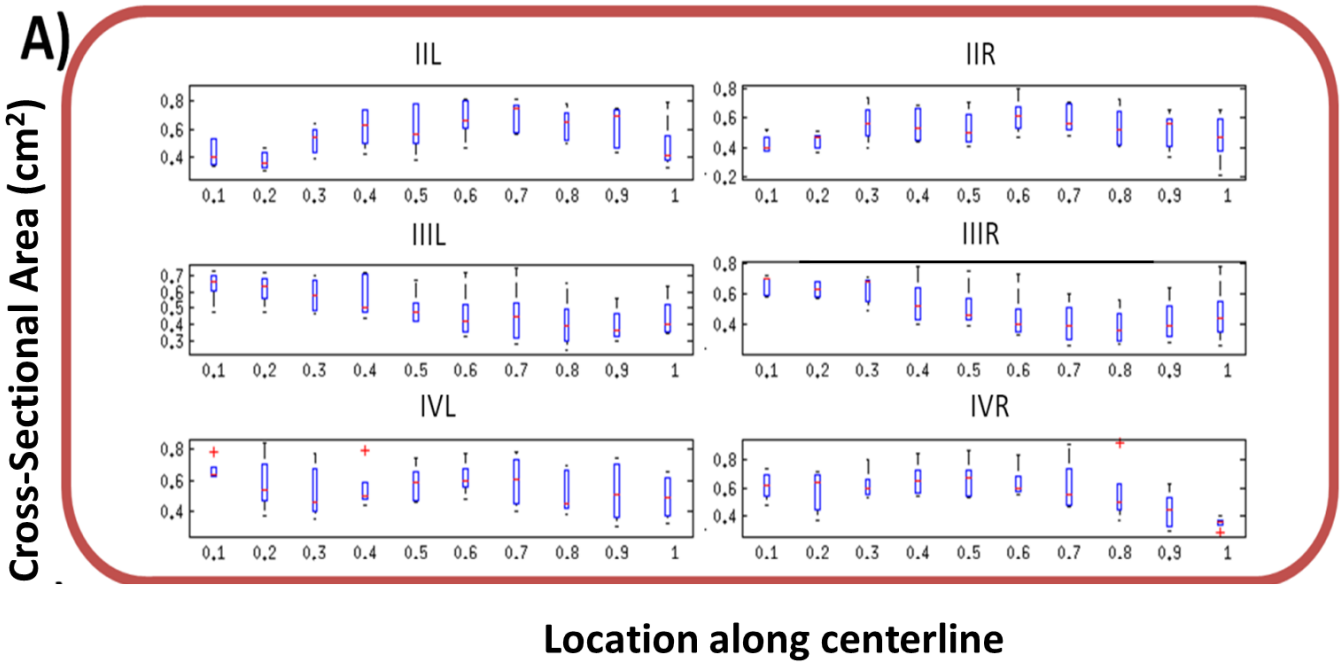
A)
Cross-Sectional Area (cm²)
IIL
IIR
IIIL
IIIR
IVL
IVR
Location along centerline

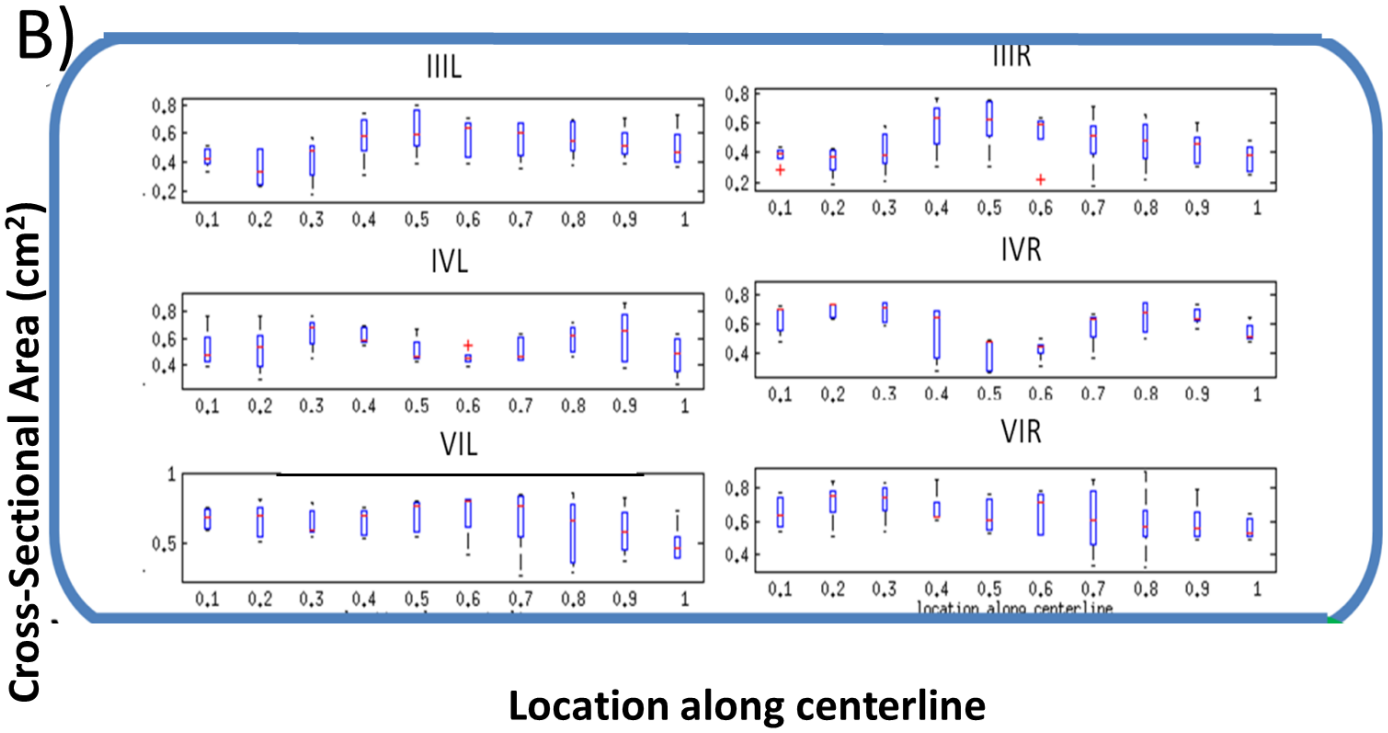
B)
IIIL
IIIR
IVL
IVR
VIL
VIR
Cross-Sectional Area (cm²)
Location along centerline

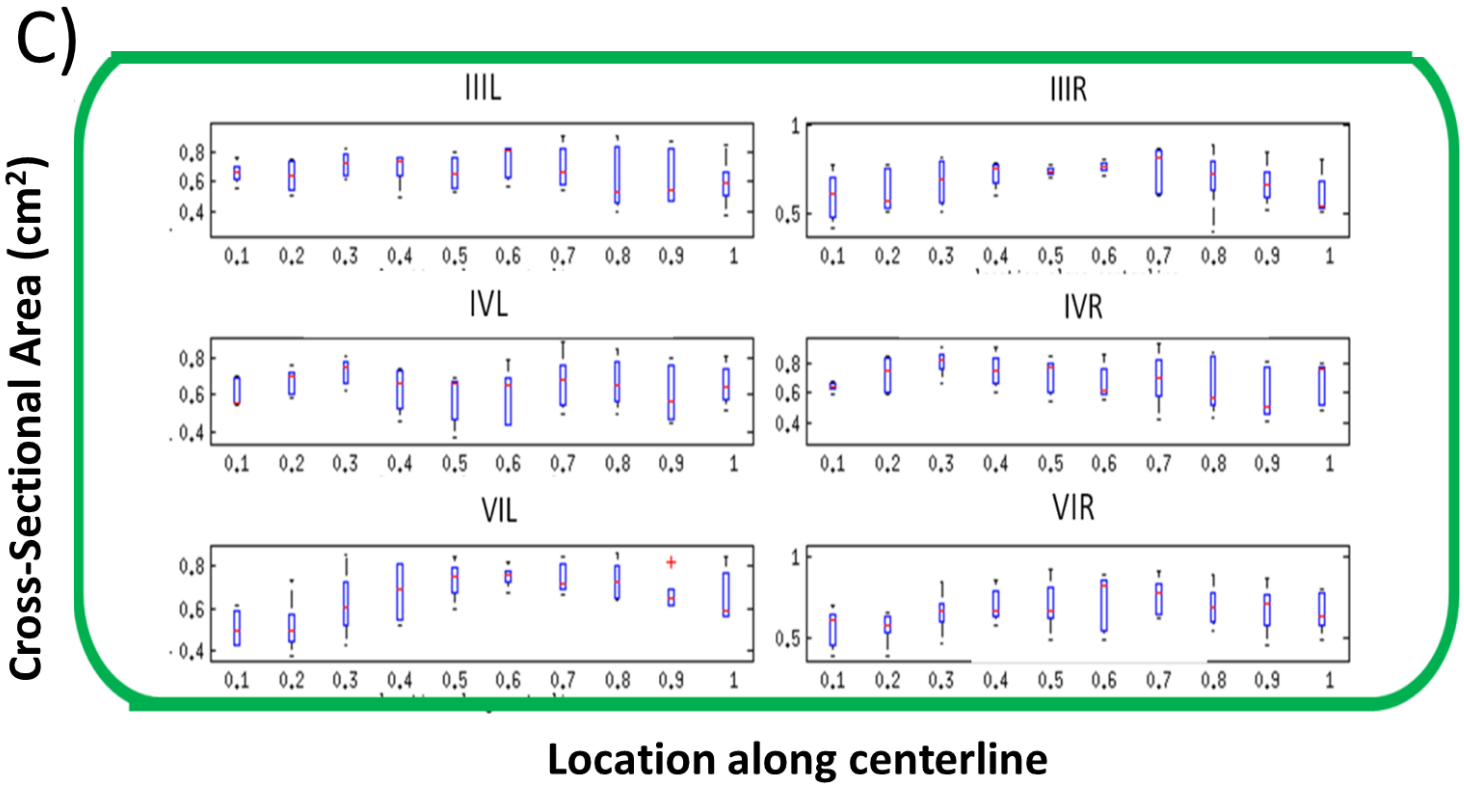

Figure 4.9. Shape Parameter Distributions for Day 3, Day4, Day 5 Embryos

Boxplots of shape parameter functions shown over normalized arch lengths for day3 (A) day 4 (B) and day 5 (C) embryos. Shape parameters range from zero to one, with one being a perfect circle and the parameter approaching zero as arch diameter in one direction largely skews arch diameter in the opposite directions. While distribution varies over the length of the arch, none of the cross-sectional areas are perfect circles.

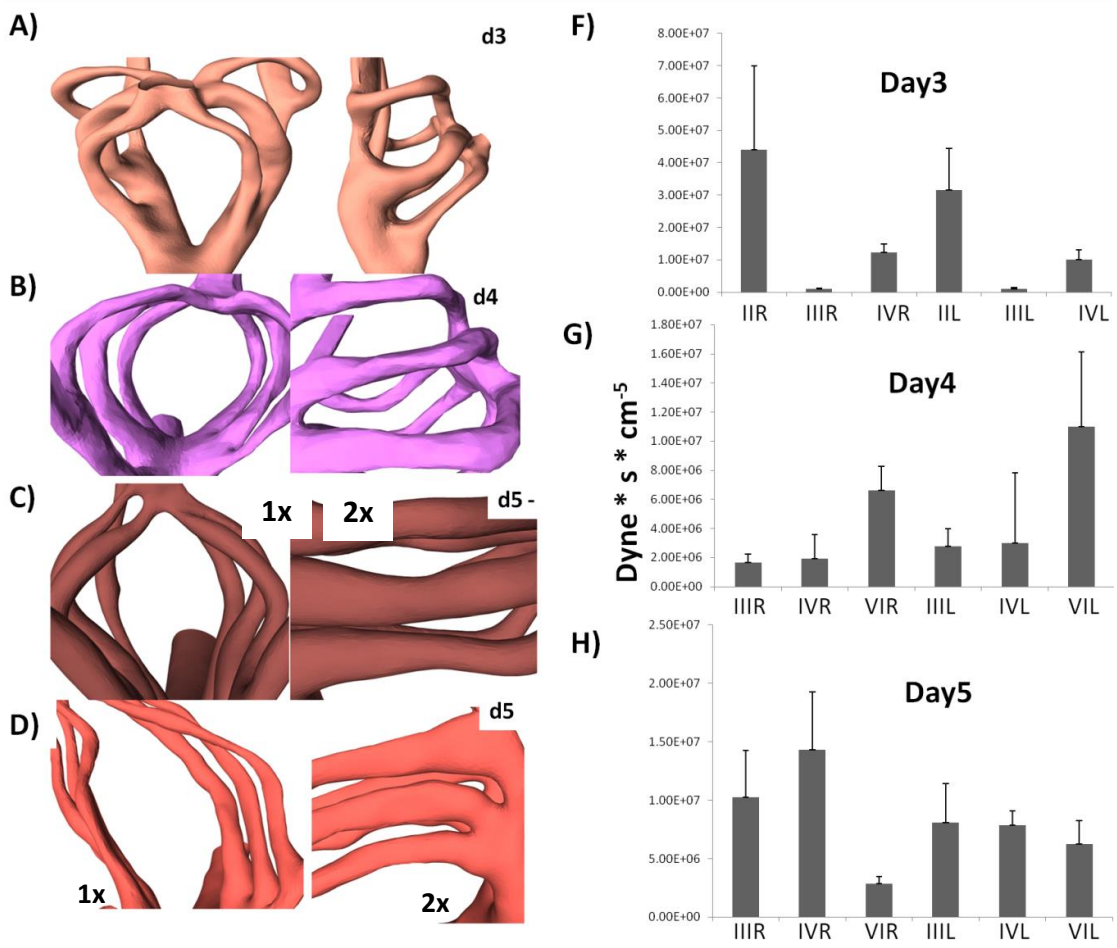

Figure 4.10. Characterization of Day 3, Day4, Day 5 Arch Artery Morphology Images of stage-specific arch artery morphology (A –D) and the corresponding electric circuit analogs (F-H). The elongated horizontal arch artery axis of day 3 embryos can be seen in (A). A still horizontally elongated, but tending toward a more circular shape can be seen in (B). An apparent perfect circle can be seen in the early day 5 embryo (C) and an elongated vertical axis becomes apparent in the mature day 5 (D).

Resistance area correlations are shown in Figure 4.11. As expected, the regressing PAA IIR and PAA IIL have the highest resistance and smallest mean cross-sectional area. PAA IVL, day 3, and PAA VIL day 4 have almost identical resistance area ratios. These caudal arches are both growing in on their respective days. For the

established arches (PAA IIIR and PAA IIIL) day 4 resistance values increase from day 3 to day 4, consistent with the narrowing of the vessel diameters and decrease in cross-sectional area. Day 3 and day 4 vessel resistance is roughly proportional to A^{-2}, while day 5 follows a trend of its own. By plotting functional versus geometric parameters we begin to quantify growth and underlying vessel trends in a way that fosters the development of accurate growth laws.

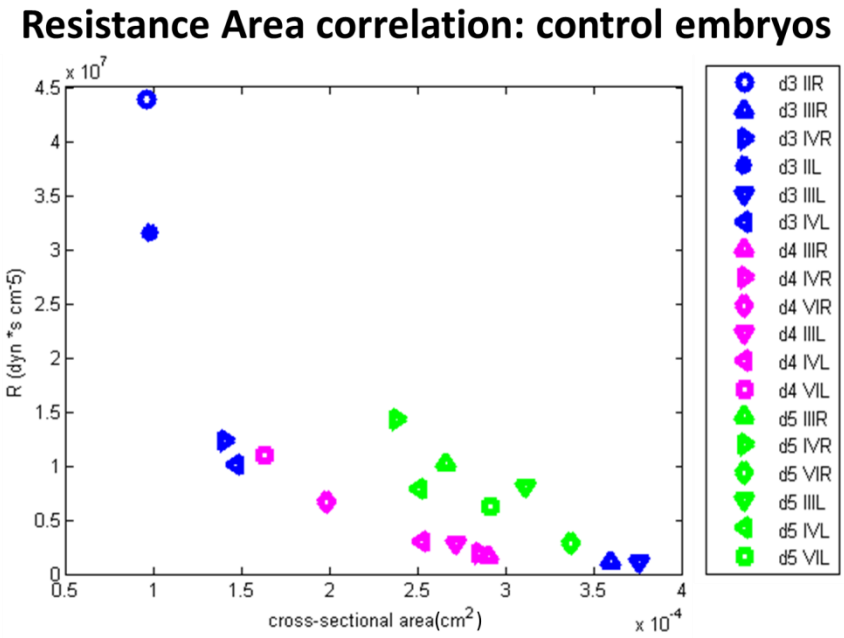

Figure 4.11. Resistance Area Graph of Day 3, Day4, Day 5 Control Embryos Graph showing how resistance, as measured as a function of pressure and flow correlates with mean vessel cross sectional area for the individual arch arteries across days. Markers are colored by day (blue, day 3; magenta, day 4; green, day 5) Marker shape corresponds to arch number, as outlined in legend.

4.5 Discussion

Right fourth arch dominance of the avian vascular system, as defined in the traditional sense of transporting the most flow, has been the premise of many existing pharyngeal arch artery studies (Wang et al. 2009; Hu et al. 2009; Kowalski et al. 2012). While the right fourth is certainly an important arch artery, as unscored by the detrimental effect of experimental lesions involving this artery (Lindsey et al., 2014), it does not always uptake the largest percentage of flow per cardiac cycle. The right fourth arch is assumed to uptake the largest amount of flow from the time that it has reached its full HH24 vessel diameter and possibly maintain this position through the maturation of the great vessels, as it takes its place among a major cardiovascular structure, the aortic arch. This flow dominance of the right fourth arch is not present in the HH26 (day 5) arch artery system. A major change is seen in the vascular structure of the more robust caudal PAA VI arches and that of the more intricate, narrow, upper PAA III and PAA IV structures. Not surprisingly PAA IIIR transports the most flow per cardiac cycle in the day 3 arch artery system, in which PAA II regresses and PAA IV is growing in. Together PAA IIIR and PAA IIIL carry between 78.5 ±0.4% and 92.5 ± .6% of flow through the arches per cardiac cycle. Peaks in wall shear stress were mostly found in the aortic sac, along the incline to PAA III, as well as along PAA III itself.

By day 4, now fully-formed PAA IVR is expected to dominate in terms of flow distribution and cross-sectional area across embryos. While the PAA IV fourth pair, receives a minimum of 32.9% of flow across day five embryos, PAA IVR does not always carry the largest flow distribution and can be seen bearing less than 10% in two of the five day 4 embryos. Because these embryos were preserved for nano-CT purposes, the viability of this particular subset could not be tracked over development.

Before preservation all embryos appeared normal and healthy, which raises the question of the importance of right IV arch artery flow dominance at different stages in development. By day 5, PAA VIR dominates all but one of the arch artery flow distributions. In the younger, day 5 minus, CK78 embryo, the right III is the dominate arch in terms of flow, followed closely by the fourth right. Right side flow dominance is preserved in all five control embryos.

We hypothesized that a combination of pressure and WSS maps could account for many of the structural changes seen between days over this critical window of development. Across days, the pressure magnitude was consistently greatest at the outflow tract junction before being dissipated both cranially through the aortic sac and dorsal -laterally over the arch arteries as they diverge from the aortic sac and reach their dorsal connection. In day three embryos, peak pressure extends farthest along the developing IV arches. Though the diameter of the IV arch approaches that of the second arch, the fourth arches' proximity to the ventricle and short vessel length render it more susceptible to pressure gradients over the course of the arch. Similarly to day 3, day 4 caudal arches experience the highest pressure magnitude over the length of the arch artery, as they have privileged access to outlet diameters. These caudal arches will experience the largest increases in vessel diameter within their subsets from one day to the next.

Resistance values were examined for the caudal most arches across days and compared to that of their stage specific side specific counterparts. For day 3, paired t-tests revealed significance when comparing arch IIIL to arch IV L ($P = 0.0274$). For Day 4, the significant differences were found when comparing PAA VI R to PAA IIIR ($P = 0.0453$) and PAA IVR ($P = 0.03625$). Figure 4.12 emphasizes the effects of

varying arch artery cross-sectional areas and shape on the velocity profile seen over the length of an arch

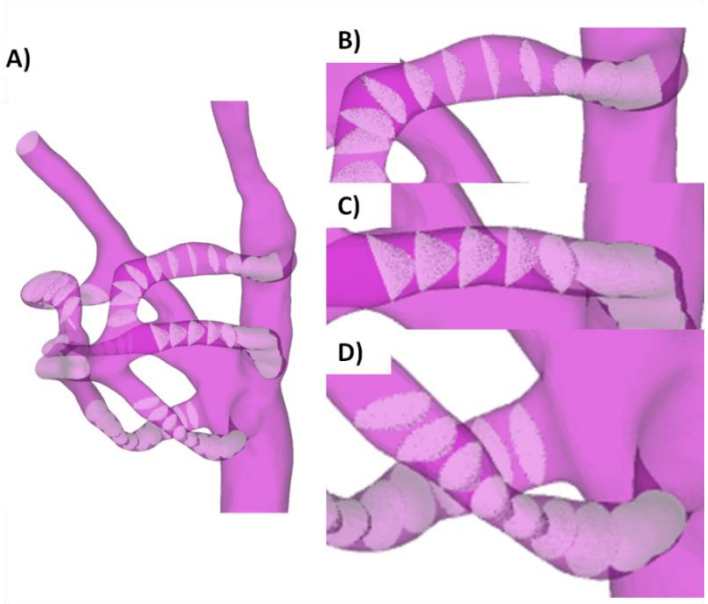

Figure 4.12. Variations in Arch Artery Velocity Profiles
The effect of changing area artery cross sectional area and shape on velocity profiles. A) Full scale image of day 4 arch artery flow. (B) Flow evolution over PAA IIIL (C) Flow evolution over PAA IVL (D) Flow evolution over PAAVIL.

Embryo-specific day 5 geometries offer a more detailed window into how arch artery growth proceeds at these stages. The five day 5 embryos presented can be grouped into three categories on the basis of vessel length and shape, day 5 – (CK78), day 5 (CK64 ,CK70,CK77), and day 5+ (CK29). Figure 4.12 illustrates lumped parameter values change for these day 5 subsets. PAA III and PAAIV values increase across day 5 development, while PAA VI decreases before increasing again.

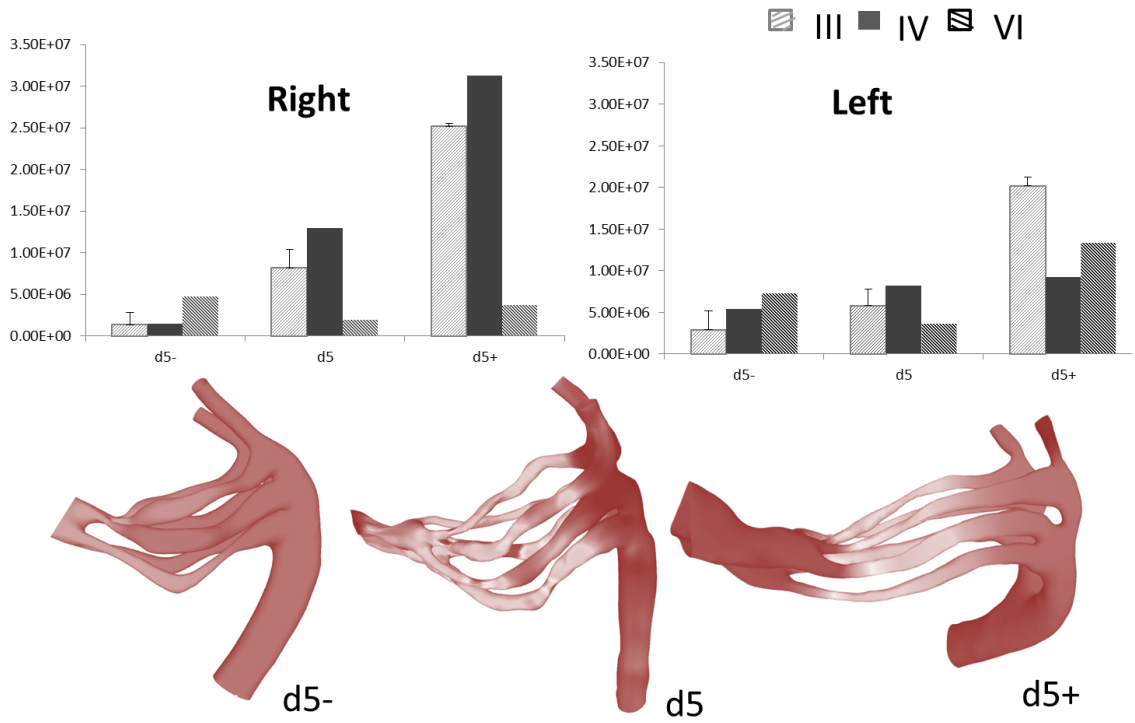

Figure 4.13: Lumped parameter resistance values for day 5 embryos broken up into subsets reflecting arch artery morphology.
A chick representing each subgroup is shown below in red.

From day 3 (HH18) to day 4 (HH24), the outflow tract that feeds into the pharyngeal arch arteries is undergoing conformational changes of its own. The proximal two-thirds of the primitive conus shift toward its definitive position ventral to the right atrium. The outflow tract structure itself loses its tubular character at HH24 (Manner 2000). Between day 4 and day 5, condensed mesenchyme of the aorticopulmonary septum projects into the aortic sac, beginning the division of pulmonary and aortic channels. By HH26 (day 5), the aorticopulmonary septum has lengthened toward the heart and entered the distal truncus (Waldo et al. 1998). The aorta and pulmonary trunk have lengthened and rotated 20° by stages HH 26–27 (Waldo et al., 1998). Day 5 also marks the period when condensed cardiac neural crest cells that surround the aortic arch arteries have begun to move into the walls of the distal aorta and

pulmonary trunk (Waldo et al., 1998). All of these movements are reflected in the shape changes of day 3 to day 5 pharyngeal arch artery geometries.

Advantage of multi-scale modeling approach

The use of multiscale modeling in providing clinically relevant boundary conditions have been extensively studied (Vignon-Clementel et al. 2006; Yang et al. 2012; Kung et al. 2013). Lump parameter models can be tuned to match patient specific flow and pressure curves. In the case of this study, lumped parameter bounds were tuned to maintain a 90-10 cranial caudal flow split over the course of one cardiac cycle as noted in (Hu & Clark, 1990, Wang et al., 2009). Caudal bounds were fixed to maintain stage-specific dorsal aorta pressure values. Cranial bounds were subsequently tuned though the 0D circuits shown in Figure 4.1 to achieve appropriate values for each embryo. Proximal resistance values represent those of large arteries and vessels, while distal resistance values represent that of downstream capillary beds. This information can prove to be particularly useful when assessing the effects of abnormal flow patterning and arch artery morphology on downstream circulation. In addition, lumped parameter representations of vessel morphology provide another means of quantifying the hemodynamic properties of the vessels themselves and understanding growth across the days. By comparing resistance values across days and arches a better understanding of how hemodynamic parameters translate into functionality is obtained.

Limitations.

As with all computational studies there are limitations to this study. Although pulsed wave Doppler ultrasound curves were gathered for day 3, day 4 and day5 outflow tracts, we choose to use the calculated inflow velocity displayed in equation 1.3 for the

following reasons: 1) The shape of the outflow curves was very different from that of the individual arch artery vessels, reflecting the influence of fluid structure interactions that could not be accounted for in this model. 2) The flow profile at the position of the Doppler probe was unknown. Poiseuille and Plug profile assumptions could therefore be a gross over or underestimate of flow. For this reason we also went with the natural boundary method when imposing the inlet flow profile. Though many inlet profiles for the geometries presented here assumed a Plug and Poiseuille like shape, profiles were specific to each geometry and its exact inlet shape/ angle. By using a combination of experimentally obtained velocity profiles, and in-silico derived flow and velocity profiles, we were able to obtain arch artery velocity profiles that mirror those seen experimentally. Mean flow values of calculated outflow inputs resembled mean arch artery inlet flow values reported by Yoshigi et al (Yoshigi, Knott, and Keller 2000).

4.6 Conclusion

This study examined embryo specific variations in pressure, wall shear stress, cross-sectional area, and shape variation, as well as their corresponding functional changes across the developing PAA vascular system. Right IV arch flow dominance was not conserved across embryos or days once the fully formed PAA IVR emerged. The transformation in PAA vessel morphology from day 3 to day 4 to day 5 was as if embryo were slowly being pulled from its outflow tract inlet in a slow manner that elongates the once highly elliptical vessels to that continuously more circular vessels (day 4 through day 5-), before simultaneously stretching the vessels along the cranial dorsal axis. Though rotation and elongation of the outflow tract are well documented, the corresponding arch artery shape changes have historically been ignored, as a

circular cross-sectional area is usually presumed. Changes in vessel shape and cross sectional area may influence the mechanical properties of the vessels themselves.

Acknowledgements:

Cornell Imaging facility, nano-CT; Jessica Ryvlin (ultrasound); Alex Chang (ultrasound); Charles-Olivier Artizzu (reconstructions); NSF GRFP, NSF GROW, NIH R01 HL110328.

REFERENCES

1. Banerjee, Indroneal, Katrina Carrion, Ricardo Serrano, Jeffrey Dyo, Roman Sasik, Sean Lund, Erik Willems, et al. 2015. “Cyclic Stretch of Embryonic Cardiomyocytes Increases Proliferation, Growth, and Expression While Repressing Tgf-β Signaling.” *Journal of Molecular and Cellular Cardiology* 79 (February 2): 133–44. doi:10.1016/j.yjmcc.2014.11.003.

2. Go, Alan S, Dariush Mozaffarian, Véronique L Roger, Emelia J Benjamin, Jarett D Berry, William B Borden, Dawn M Bravata, et al. 2013. “Executive Summary: Heart Disease and Stroke Statistics--2013 Update: a Report from the American Heart Association.” *Circulation* 127 (1) (January 1): 143–52. doi:10.1161/CIR.0b013e318282ab8f.

3. Hiruma, T, and R Hirakow. 1995. “Formation of the Pharyngeal Arch Arteries in the Chick Embryo. Observations of Corrosion Casts by Scanning Electron Microscopy.” *Anatomy and Embryology* 191 (5) (May): 415–23.

4. Hiruma, Tamiko, Yuji Nakajima, and Hiroaki Nakamura. 2002. “Development of Pharyngeal Arch Arteries in Early Mouse Embryo.” *Journal of Anatomy* 201 (1) (July): 15–29. doi:10.1046/j.1469-7580.2002.00071.x.

5. Hogers, B, M C DeRuiter, a C Gittenberger-de Groot, and R E Poelmann. 1999. “Extraembryonic Venous Obstructions Lead to Cardiovascular Malformations and Can Be Embryolethal.” *Cardiovascular Research* 41 (1) (January): 87–99.

6. Hogers, B., M.C. DeRuiter, A.C. Gittenberger-de Groot, and R.E. Poelmann. 1997. “Unilateral Vitelline Vein Ligation Alters Intracardiac Blood Flow Patterns and Morphogenesis in the Chick Embryo.” *Circ. Res.* 80 (4): 473–481.

7. Hu, Norman, Douglas a Christensen, Amit K Agrawal, Charity Beaumont, Edward B Clark, and John a Hawkins. 2009. “Dependence of Aortic Arch Morphogenesis on Intracardiac Blood Flow in the Left Atrial Ligated Chick Embryo.” *Anatomical Record (Hoboken, N.J. : 2007)* 292 (5) (May): 652–60. doi:10.1002/ar.20885.

8. Kowalski, William J, Kerem Pekkan, Joseph P Tinney, and Bradley B Keller. 2014. “Investigating Developmental Cardiovascular Biomechanics and the Origins of Congenital Heart Defects.” *Frontiers in Physiology* 5 (January): 408. doi:10.3389/fphys.2014.00408.

9. Kowalski, William J, Nikola C Teslovich, Onur Dur, Bradley B Keller, and Kerem Pekkan. 2012. “Computational Hemodynamic Optimization Predicts Dominant Aortic Arch Selection Is Driven by Embryonic Outflow Tract Orientation in the

Chick Embryo." *Biomechanics and Modeling in Mechanobiology* 11 (7) (September): 1057–73. doi:10.1007/s10237-012-0373-z.

10. Kowalski, William J., Onur Dur, Yajuan Wang, Michael J. Patrick, Joseph P. Tinney, Bradley B. Keller, and Kerem Pekkan. 2013. "Critical Transitions in Early Embryonic Aortic Arch Patterning and Hemodynamics." Edited by Leonard Eisenberg. *PLoS ONE* 8 (3) (March 21): e60271. doi:10.1371/journal.pone.0060271.

11. Kung, Ethan, Alessia Baretta, Catriona Baker, Gregory Arbia, Giovanni Biglino, Chiara Corsini, Silvia Schievano, et al. 2013. "Predictive Modeling of the Virtual Hemi-Fontan Operation for Second Stage Single Ventricle Palliation: Two Patient-specific Cases." *Journal of Biomechanics* 46 (2) (January 18): 423–429. doi:10.1016/j.jbiomech.2012.10.023.

12. Lindsey, Stephanie E, Prahlad G Menon, William J Kowalski, Akshay Shekhar, Huseyin C Yalcin, Nozomi Nishimura, Chris B Schaffer, Jonathan T Butcher, and Kerem Pekkan. 2014. "Growth and Hemodynamics after Early Embryonic Aortic Arch Occlusion." *Biomechanics and Modeling in Mechanobiology* (November 23). doi:10.1007/s10237-014-0633-1.

13. Lindsey, Stephanie E. 2014. "Mechanical Regulation of Cardiac Development." *Frontiers in Physiology* 5 (August): 1–15. doi:10.3389/fphys.2014.00318.

14. Liu, Aiping, Xin Yin, Liang Shi, Peng Li, Kent L Thornburg, Ruikang Wang, and Sandra Rugonyi. 2012. "Biomechanics of the Chick Embryonic Heart Outflow Tract at HH18 Using 4D Optical Coherence Tomography Imaging and Computational Modeling." *PloS One* 7 (7) (January): e40869. doi:10.1371/journal.pone.0040869.

15. Manner, Jorg. 2000. "Cardiac Looping in the Chick Embryo : A Morphological Review With Special Reference to Terminological and Biomechanical" 262 (March): 248–262.

16. Rychter, Z. 1962. "Experimental Morphology of the Aortic Arches and the Heart Loop in Chick Embryos." *Adv Morphog*.

17. Rychter, Z, and L Lemez. "Changes in Localization in Aortic Arches of Laminar Blood Streams of Main Venous Trunks to Heart after Exclusion of Vitelline Vessels on Second Day of Incubation." *Federation Proceedings. Translation Supplement; Selected Translations from Medical-related Science* 24 (5): 815–20.

18. Taber, Larry A. 1995. "Biomechanics of Growth, Remodeling, and Morphogenesis." *Applied Mechanics Reviews* 48 (8) (August 1): 487. doi:10.1115/1.3005109.

19. Vignon-Clementel, Irene E., C. Alberto Figueroa, Kenneth E. Jansen, and Charles A. Taylor. 2006. “Outflow Boundary Conditions for Three-dimensional Finite Element Modeling of Blood Flow and Pressure in Arteries.” *Computer Methods in Applied Mechanics and Engineering* 195 (29-32) (June): 3776–3796. doi:10.1016/j.cma.2005.04.014.

20. Waldo, K, S Miyagawa-Tomita, D Kumiski, and M L Kirby. 1998. “Cardiac Neural Crest Cells Provide New Insight into Septation of the Cardiac Outflow Tract: Aortic Sac to Ventricular Septal Closure.” *Developmental Biology* 196 (2) (April 15): 129–44. doi:10.1006/dbio.1998.8860.

21. Wang, Yajuan, Onur Dur, Michael J Patrick, Joseph P Tinney, Kimimasa Tobita, Bradley B Keller, and Kerem Pekkan. 2009. “Aortic Arch Morphogenesis and Flow Modeling in the Chick Embryo.” *Annals of Biomedical Engineering* 37 (6) (June): 1069–81. doi:10.1007/s10439-009-9682-5.

22. Yalcin, Huseyin C, Akshay Shekhar, Nozomi Nishimura, Ajinkya a Rane, Chris B Schaffer, and Jonathan T Butcher. 2010. “Two-photon Microscopy-guided Femtosecond-laser Photoablation of Avian Cardiogenesis: Noninvasive Creation of Localized Heart Defects.” *American Journal of Physiology. Heart and Circulatory Physiology* 299 (5) (November): H1728–35. doi:10.1152/ajpheart.00495.2010.

23. Yang, Weiguang, Jeffrey Feinstein, Shawn Shadden, Irene Vignon-Clementel, and Alison Marsden. 2012. “Optimization of a Y-graft Design for Improved Hepatic Flow Distribution in the Fontan Circulation.” *Journal of Biomechanical Engineering*.

24. Yoshigi, M, G D Knott, and B B Keller. 2000. “Lumped Parameter Estimation for the Embryonic Chick Vascular System: a Time-domain Approach Using MLAB.” *Computer Methods and Programs in Biomedicine* 63 (1) (August): 29–41.

CHAPTER 5

EFFECTS OF ABNORMAL PHARYNGEAL ARCH ARTERY MORPHOGENESIS IN THE DEVELOPING CHICK EMBRYO: A MULTI-SCALE APPROACH TO UNDERSTANDING RESULTING MORPHOLOGY AND FLUID-DYNAMIC CHANGES

5.1 Abstract

Abnormal pharyngeal arch artery morphogenesis is associated with a variety of cardiac outflow abnormalities and severe congenital heart defects. Exactly when and how these defects arise remains unknown. Contributing factors aside, hemodynamics is thought to play a critical role in abnormal cardiac morphogenesis. In this study we examine the effects of in-silico arch artery occlusion and partial occlusion on day 3 and day 4 control embryos. We compare in-silico results to that of experimentally obtained geometries. By examining morphological and functional parameters and comparing them to that of control embryos, we begin to assess how growth and hemodynamic trends are altered in times of need. Results indicate that geometrical changes work to lessen increases in pressure and wall shear stress upon vessel occlusion. Severity of right fourth arch artery occlusion may be due to disruptions in natural cranial pressure and shear forces.

5.2 Introduction

During cardiac morphogenesis, blood exits the developing heart through the pharyngeal arch artery system. These six bilateral paired vessels exist in various combinations as they sequentially emerge, remodel and disappear before forming the mature aortic arch, pulmonary artery, pulmonary veins and venae cavae. Hemodynamics plays a vital role in the maturation of the pharyngeal arch artery

system (Hu et al., 2009; Kowalski et al., 2013; Lindsey et al., 2014; Wang et al., 2009a). The role of abnormal hemodynamics in the creation of cardiac abnormalities has intrigued researchers for decades (deAlmeida, McQuinn, & Sedmera, 2007; Harh, Paul, Gallen, Friedberg, & Kaplan, 1973; Hogers, DeRuiter, Gittenberger-de Groot, & Poelmann, 1999, 1997; Hove et al., 2003; Hu et al., 2009; Rychter, 1962; Sedmera, Pexieder, Rychterova, Hu, & Clark, 1999; Tobita & Keller, 2000). Disruption of established flow patterns during critical windows of development produces a range of defects that drastically alter function of the mature heart. These defects may stem from improper cardiac looping, incomplete outflow tract rotation, incomplete outflow tract septation, abnormal maturation of the cardiac valves or yet to be determined factors. Cardiac morphogenesis is a complex interconnected process that is difficult to delineate. When development does not proceed according to plan, congenital heart defects arise. Malformations of the outflow tract account for over 50% of clinically relevant congenital heart defects (Go et al., 2013), yet the origin of such defects remains uncertain. Altered hemodynamic flow patterns in the heart following surgical manipulation of the atrium, has been shown to affect the ventricle, as well as the pharyngeal arch artery system. Surgical manipulation of the atria of HH21 (day 3.5) embryos immediately affected the arch arteries. By HH24 (day 4) the fourth aortic arch on the left and right were drastically reduced in dimensions, by HH27 (day 5) arches were skew and distorted. All embryos surviving to HH34 displayed hypoplastic ventricles; 70% of these also possessed a large array of abnormal aortic arch patterning that included interrupted aortic arch, hypoplastic aortic arch, and presence of vessels that should have disappeared (Hu et al., 2009).

A major limitation in determining the causality of clinically relevant cardiac abnormalities is the difficulty of studying the effects of hemodynamics alone in the

creation of cardiac abnormalities. In an effort to surgically manipulate flow patterns in experimental animal models, researchers have used a combination of ligations, clipping, and cauterizations, all of which disrupt flow patterns, as well as change the properties of the surrounding tissues and possibly triggering cell-signaling pathways. Alteration of mechanical stress and strains in the developing heart have been shown to regulate vascular growth and remodeling as well as trigger cell signaling and subsequent organization patterns(Fisher, Chien, Barakat, & Nerem, 2001; Hove et al., 2003; Van der Heiden et al., 2006). Recent advances in imaging technology have allowed for the minimally invasive occlusion of flow in the developing vascular system(Lindsey et al., 2014; Lindsey, Chapter 4). Studies such as these may prove to be important in delineating the sequence of events that leads to clinically relevant cardiac abnormalities. The coupling of computational modeling with such experimental studies can provide further insight into the mechanisms behind abnormal cardiac morphogenesis, correlating sites of altered wall shear stress (WSS) with commonly affected areas in the clinically associated disease model (Kowalski et al., 2013) or highlight driving forces in development (Lindsey et al., 2014; Wyczalkowski, Chen, Filas, Varner, & Taber, 2012)

In this study, we examine the effects of vessel occlusion on detailed 3D renderings of experimental occlusion geometries. Analysis of vessel morphology is performed on experimental occlusion geometries. We then compare the results to that of in-silico occlusions taken at the time of intervention in HH18 (day 3) control geometries, and in-silico occlusions taken in HH24 (day 4) control geometries, so as to see the effects on the 24 hour –post-experimental-occlusion time point. Coupling of the 3D geometry with 0D lumped parameter bounds, places the computational models back in the

context of the body, allowing for the effects of vessel occlusion on pressure and flow distributions to the rest of the body to be quantified.

5.3 Materials and Methods

Embryo culture and preparation

Fertile white Leghorn chicken eggs were incubated blunt-side up for three or four days of incubation in a continuous rocking incubator at 37.5^{o}C. Embryos were removed from the incubator at day 3 (HH18) if they were to undergo experimental micro-surgery for vessel occlusions. An embryo was allowed to develop to day 4 (HH24) without disruption so that an in-silico occlusion could be performed at that stage. Embryos being preserved were subsequently dissected away from their yolk sac. Injection micro-needles were fashioned from pulled capillary tubes (0.75 mm ID) cut to 20-35 µm inner diameter via a microforge (Glassworx, St. Louis, MO). A micromanipulator (model M3301L, World Precision Instruments, Sarasota FL) was used to position the needle into the apex of heart. The embryo's vascular system was flushed with phosphate buffer solution followed by 4% paraformaldehyde to preserve inner vascular volumetric integrity. The embryos were then left in 4% paraformaldehyde for 24-48 hours before being transferred to a 70% ethanol solution, and possibly stored for weeks. Before preparation for nano-CT scans ,embryos were brought up to a 30% ethanol solution. Embryos were then transferred to a diluted form of Lugol solution, aqueous potassium iodide and iodine, (Sigma-Aldrich, L6146). The embryos soaked in Lugol's and the solution was changed over several days until the embryos no longer took up any iodine. Embryos were then slowly dehydrated down to 100% ethanol placed in polymerase chain reaction tubes and sent to undergo 3-4µm nano-computed tomography scans (nano-CT).

Ultrasound Processing and generation of Inlet flow curves

Outflow tract (OFT) velocity and that of the three paired pharyngeal arch arteries were measured using B-mode guided Doppler Ultrasound (Vevo770 and Vevo 2100, Visualsonics, Inc.), as explained in (Lindsey, Chapter 3). A Poiseuille profile was assumed for day 4(HH24) embryos and Peak velocity converted to flow using equation 1.1.

$$Q = \frac{1}{2} Area * Vmax \qquad (1.1)$$

Plug flow was assumed for the day 5 embryos (HH26) and the peak velocity converted to flow using equation 1.2

$$Q = Area * Vmax \qquad (1.2)$$

The mean calculated flow was fed to each embryo via a steady-state simulation and the ratio between flow and velocity calculated in each of the individual arches. To compensate for the lack of fluid-structure interaction in our CFD inlet, a new inlet curve was calculated. Mean flow, calculated from Doppler ultrasound, was fed to each embryo via a steady-state simulation and the ratio between flow and velocity calculated in each of the individual arches. A new Qinlet was then calculated to be the sum of flow in each of the individual arches via the following equation:

$$Q_{inlet} = \sum_{i=0}^{6} Vi_{max}(t) * \frac{Q_i(ref)}{Vi_{max}} \quad (1.3)$$

where Vi_{max} is the Dopper pulse –wave velocity profile for that arch, ref refers to values measured in the steady state simulation with doppler imposed flow, and $Qi(ref)/Vi_{max}$ is an estimation of the profile contribution from each arch. (1.3)

Zero-dimensional lumped parameter estimation model

0D circuit representations of arch artery morphology were created for day 3, day 4, and day 5 geometries. Sundials initial value problem solver Implicit Differential-Algebraic solver, IDA, (Lawerence Livermore National Laboratory, Livermore, CA)

was used to obtain solutions to the 0-D circuit. Presented models (Figure 5.1) were adapted from Yoshigi et al's single compartment 0D model of HH18 and HH24 embryo circulation as seen from the PAAs (Yoshigi, Knott, and Keller 2000). Yoshigi's lumped parameter model, which was created to match the entirety of embryonic circulation outside the arch arteries, is split into three (Figure 5.1b) and scaled to represent cranial-caudal flow conditions. As a 90-10, cranial-caudal flow split is maintained over the course of a cardiac cycle, this is achieved by sending 5% of flow to the two cranial branches (respectively) and 90% to the caudal branch. After testing flow and pressure curves, the inductor was found to have a negligent value and removed from the circuits. The three compartment system was then placed back into the context of the arches by connecting it to 0D representations of the arches (Figure 5.1c and Figure 5.1d) as well as 3D arch artery reconstructions (Figure 5.2e). Each vessel that flow traveled through in order to reach the outlets was represented by a resistor, as pressure is dissipated across a vessel. Resistance values were updated after 3D simulations according to Ohms law. In the case of vascular structures this takes the form of equation 1.4.

$$P_{in} - P_{out} = Q * R \qquad (1.4)$$

Where Pin is pressure at the start of a vessel, Pout presents pressure at the end of a vessel and Q is taken midway along the arch diameter. In the event that a pressure drop was not accounted for in the lumped parameter model, a new resistor was added, as was the case with pressure drop seen in the aortic sac for the day3/day 4 circuit model. Final lumped parameter estimation of the day 3 and day 4 geometry is shown in Figure 5.1c. Figure 5.1d represents day 5 morphology. Lumped parameter abstraction of the 3D domain is represented in black; the Windkesssel boundary conditions are outlined with dotted lines.

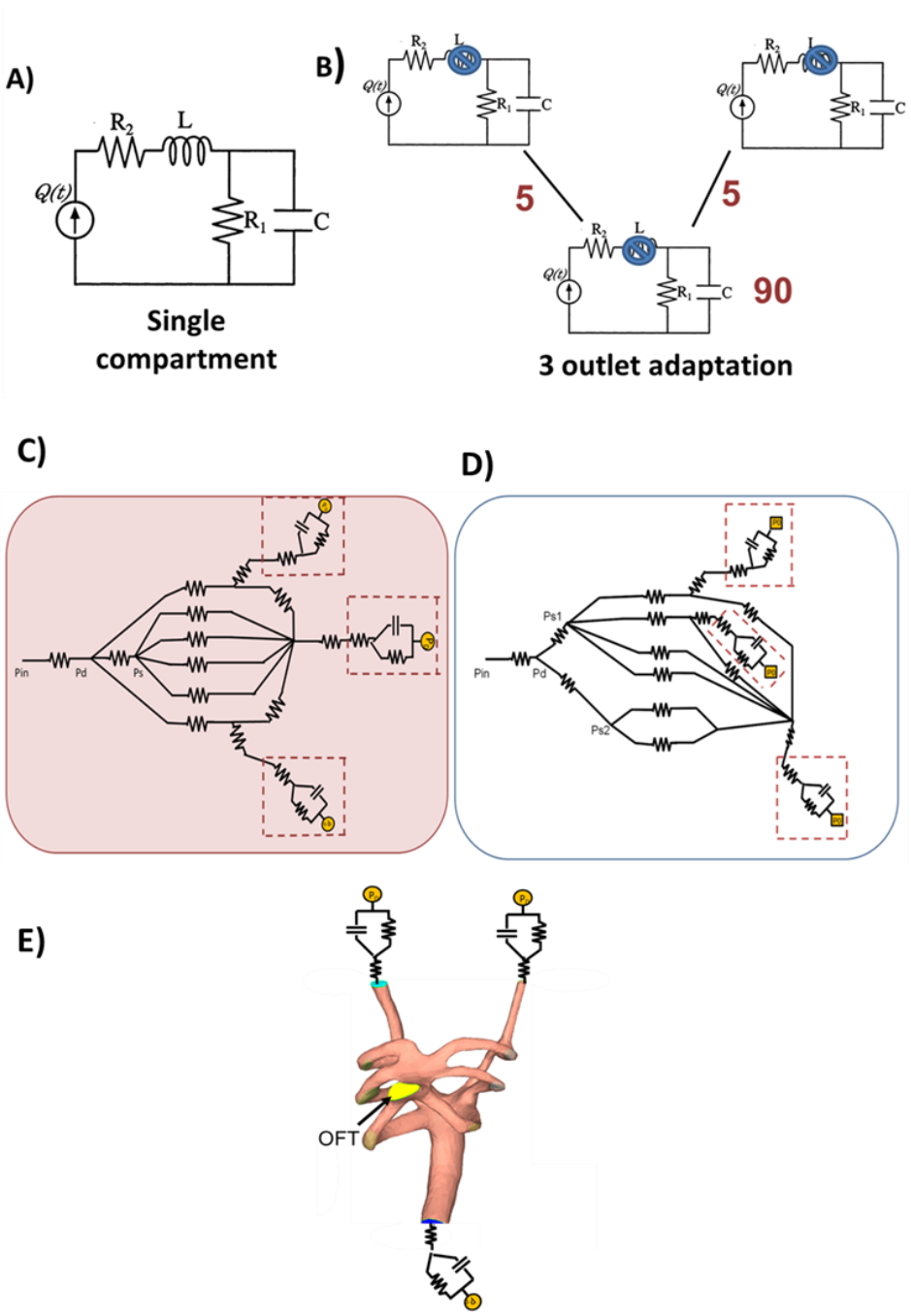

Figure 5.1. 0D Electric Analogs of Day3, Day4, and Day 5 PAA Systems
Yoshigi lumped parameter model as seen from arches (A), Modifications to account for 3 outlets and 90-10 cranial caudal flow split (B). Day3 and day 4 circuit geometries (C). Only the numbering of the arch arteries themselves will change between the days/stages. (D) Day 5 circuit. Notice how the arches are now split between two junctions. Dashes lines (red) outline 0D bounds.

In-silico geometry preparation and flow modeling

Embryo-specific 3D geometries of HH24 (day 4), and HH26 (day 5) pharyngeal arch artery (PAA) were generated for experimental occlusion geometries by importing nano-CT images into MIMICS (Materialise, Louvain, Belgium) and 3MATICs (Materialise, Louvain, Belgium), as outlined in Lindsey, Chaper 3. Geomagics Studio 10 (Geomagic Inc., Durham, NC) was also used for the preparation of 3D geometries for CFD. All embryos were scaled by a factor of three to account for the difference between dehydrated and native vessel size. India ink and Texas Red Dextran were used to obtain native vessel size across stages, results compared to that of 3D reconstructions and a scaling factor was generated.

For 3D mesh generation and adaptation, ghs3d and feflo (Loseille and Rainald 2010) were used. Grid sensitivity analysis was conducted on a control PAA model for each day in order to ensure consistency and reliability of the numerical solutions for all simulations presented in this study, beyond which resulting mass-flow redistributions were insensitive to further Cartesian grid refinements.

Boundary Conditions:

As outlined in Lindsey, Chapter 4, a natural flow profile was imposed at the inlet. To obtain this an auxiliary steady Stokes equation, with natural boundary conditions at the outlets, is solved first (Pant et al, 2013). The resulting outlet velocity profile subsequently scaled at each time-point to match the measured flow-rate. RCR Windkessel models are imposed at the outlets to assure the distribution of the total cardiac output to dorsal aorta and cranial vessels maintains a 90-10 flowsplit over the course of one cycle.

CFD simulations were conducted at INRIA Paris-Rocquencourt. Day 4 simulations cost an average of 20 hours at 16 core parallelism (2 nodes each) while day 5 simulations cost an average of 27 hours at 16 core parallelism. Pressure values from the 0D model were used as initial estimates of the caudual and cranial pressures, allowing one cycle to sufficiently represent.

Blood is considered to be an incompressible Newtonian fluid modelled by the incompressible Navier-Stokes equations (solved using the finite element library FELiSce). The following boundary conditions are imposed:

For the **outlet boundary conditions** RCR Windkessel models are imposed. These boundary conditions are non-homogeneous Neumann boundary conditions. The differential equation representing the RCR circuit is

$$P + R_5 C \frac{DP}{Dt} = (R_4 + R_5)Q + R_5 R_4 C \frac{dQ}{dt} \quad (1.5)$$

Where R_4 is the proximal resistance, R_5 is the distal resistance C represents capacitance P is pressure and Q is flow.

Morphology post- processing

The Vascular Modeling Toolkit (vmtk),supported by Orobix, sri, was used to obtain cross-sectional areas taken along the centerline of each geometry. Ensight (Computational Engineering International, Inc, Apex, NC), was used for all post-processing visualization and measurement of fluid properties.

Creation of In-Silico Occlusion Models

In silico occlusion models were made from two day 3 (CK26 and CK85) and one day 4 (CK73) pharyngeal arch artery systems (Lindsey, Chapter 4). The two day 3 control

references were chosen to represent the wide range of variability seen across day 3 embryos. CK 26 has a rapidly regressing right and left lateral second arches as well as a developing right and left lateral forth arch, while CK85 has the largest right and left lateral second arch, as well as the largest right and left lateral fourth arch, see in our day 3 control subset (Lindsey, Chapter 4). A full occlusion and a partial occlusion were made for each of the three reference geometries, bringing the number of in-silico occlusion geometries to six. Only one day 4 embryo was chosen for in-silico occlusion, as there is considerably less variability in arch artery diameters at this stage, when compared to day 3 embryos. Partial occlusions were made to mimic those seen in experimentally occluded embryos, either through two-photon microscopy (day 3 embryos) or their subsequent nano-CT reconstructions from images taken 24 hours post vessel occlusion.

Creation of In vivo-Occlusion Models

Embryos were experimentally occluded as previously described (Lindsey, Chapter 3; Lindsey Chapter 4). Briefly, HH18 embryos were open cultured and injected with Texas red dextran (70,000 MW, neutral Sigma-Aldrich D1830) diluted in Earle balanced salt solution (5% w/v) so that their vascular could be visualized by way of two-photon microscopy. Embryos with small fourth arch arteries were specifically chosen to facilitate ease of occlusion. Chosen embryos were pre-cooled in an ice-bath an ice bath to further facilitate ease of occlusion and slow heart rate.

A custom built two-photon excited fluorescence microscope with a separate femtosecond pulsed photoablation laser was used to perform targeted vessel disruption (Nishimura 2006, Lindsey 2014). The photoablation laser consisted of 1-kHz high-pulse-energy Ti:Sapphire amplified laser system with 50-fs pulse duration (Legend-USP, Coherent, Santa Clara, CA, 800-nm central wavelength). Photodisruption was

controlled and confined to the focal volume of the two-photon microscopy optics. To produce a vessel occlusion, laser pulse trains were used to grow and maintain a cavitation bubble that temporarily stopped flow in pharyngeal arch artery of choice. Nonlinear absorption of laser energy drives photodisruptive damage confined to the femto-liter volume focus of the two-photon microscopy optics (Vogel and Venugopalan 2003; Nishimura 2006). Following the creation of this cavitation bubble, laser energy was directed to the increasingly more stagnant flow directly behind the cavitation bubble, accumulating damage and cohesion in the lumen. This process was adjusted and/or repeated as needed until a stable occlusion was formed. Stable occlusions were taken to be those that persisted for 5 minutes without laser perturbation.

Following creation of the insult, embryos were returned to their incubator and allowed to develop for a minimum of 24 hours post-occlusion or until the embryo began to show signs of decreased vitality such as a slow labored heart beat and decrease in vitelline vein area and vessel size. Embryos were then preserved and prepared for nano-CT as mentioned above.

Statistical Analysis

Morphological and hemodynamic changes were compared qualitatively and quantified when possible. Results were summarized in the form of mean and standard deviation values over the course of one cardiac cycle. Paired T-tests were used where appropriate with $P < 0.05$ denoting significance.

5.4 Results

Experimental arch artery occlusion produced a range of defects as shown in Figure 5.2. The majority of embryos were preserved at day 4 (24 hours –post-occlusion), though CK1 and CK25 were preserved at day 5 (48 hours-post-occlusion). Observed malformations include the merging of arch arteries into a single vessel before separating into two distinct vessels, abnormal arch artery spacing, skewed right and left branches, enlarged arch arteries and outflow inlets, abnormal rotation of the outflow tract junction, abnormal bulging of the aortic sac and abnormal patterning of the cranial dorsal aorta branches. Flow remodeling over the 24 to 48 post occlusion period obscured the initial insult in the majority of day 4 and day 5 occlusion embryos, but is still visible in CK11, where it lesion resembles a bite taken out of a segment of the arch artery.

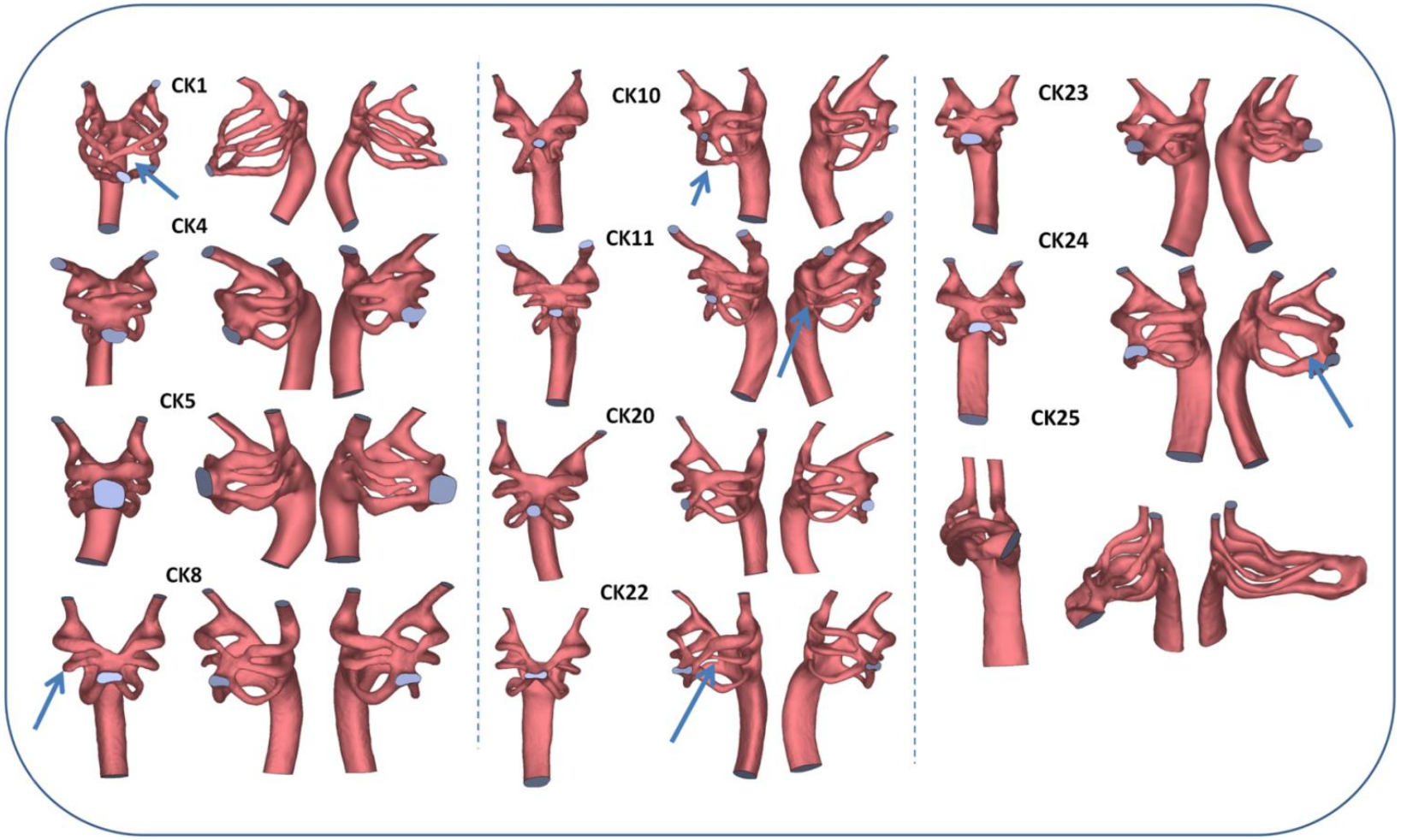

Figure 5.2. Experimental Arch Artery Occlusion and Partial Occlusion geometries.

Figure 5.2. 3D rendering of nano-CT calculate PAA geometries in d4 and d5 embryo following occlusion or partial occlusion of the right lateral IV arch at HH18. Arrows mark highlight specific defects: a single vessel before the start of the third and fourth left arch arteries in CK1, the close spacing of cranial arches in CK8 and the distance between those arches and that of the bottom VI pair, the assymmetry in CK10, the brief uniform segment for the left cranial arches in CK22 and the disappearance of the right IV arch in CK24.

Embryo-specific arch artery cross-sectional area and shape changes were followed over the course of individual vessels and compared to that of control means and standard deviations in the form of box plots for its respective day (Figures 5.3 and 5.4). Occluded embryos follow a similar trend to that of their control counterparts from their respective vessel midpoint onward. Prior to arch artery midpoint, the cross-sectional areas of a subset of vessels (CK4, CK6, CK23 and CK24), descend from relatively large cross-sectional areas before following the trends of other control and occlusion embryos. This same subset of embryos feature extremely enlarged left sixth arch arteries and slightly enlarged VI right arch arteries. Interestingly the occlusion shape parameters followed the same general increasing decreasing trend as the control embryos over the course of an arch. Occlusion arch arteries tended to be more circular (shape parameter closer to one) than their control counterparts.

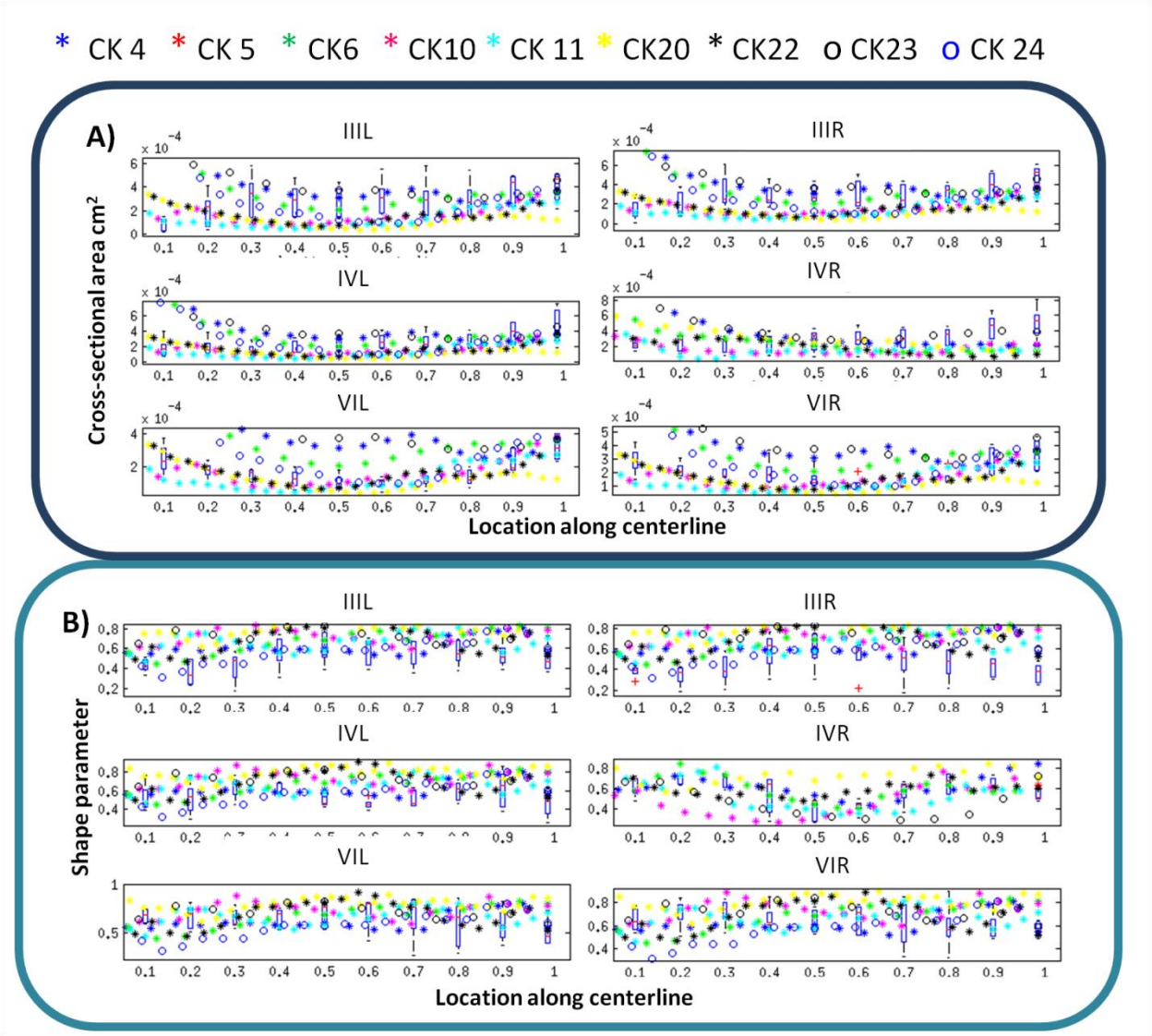

Figure 5.3. Cross Sectional Area and Shape Change for Day 4 experimental occlusion embryos.

Cross-sectional area changes along the centerline are shown for each of the day 4 occlusion arch arteries (A). Their corresponding shape parameters along the length of the arch are shown in (B). Box plots represent the mean and standard deviation of day 4 control embryos (n =5). The second half of PAA III R, IVR, IIIL IVL occlusion cross-sectional area curves follow a similar trend to that of controls. The beginning of the arch, where the highest pressure is received, deviates more from the control curves. The shape functions appear to be largely conserved, though vessels appear to have become more circular.

Experimental vessel occlusion geometries

Day 5 occlusion embryos differed greatly in stage specific characteristics with CK25 having already extended twisted and rotated and CK1 still in the process of fully extending and rotating. In both cases there is a clear distinction between the upper four cranial arches and the two caudal arches. Cross-sectional area plots (Figure 5.4a) highlight the vast differences in vessel morphology with CK1 resembling areas and trends similar to that of day 5 control embryos (shown in box plots, sample size of five) and CK25 featuring hyper enlarged aortic vessels. Interestingly, the shape parameter follows similar trends along the arches in PAA IIIL, IIIR and IVR. PAA IVL and VIL (middle), become increasingly circular in CK1 and more elliptical in CK25. This same trend occurs over two segments of CK25, with the embryos meeting and converging near the one third and two third mark along the normalized length.

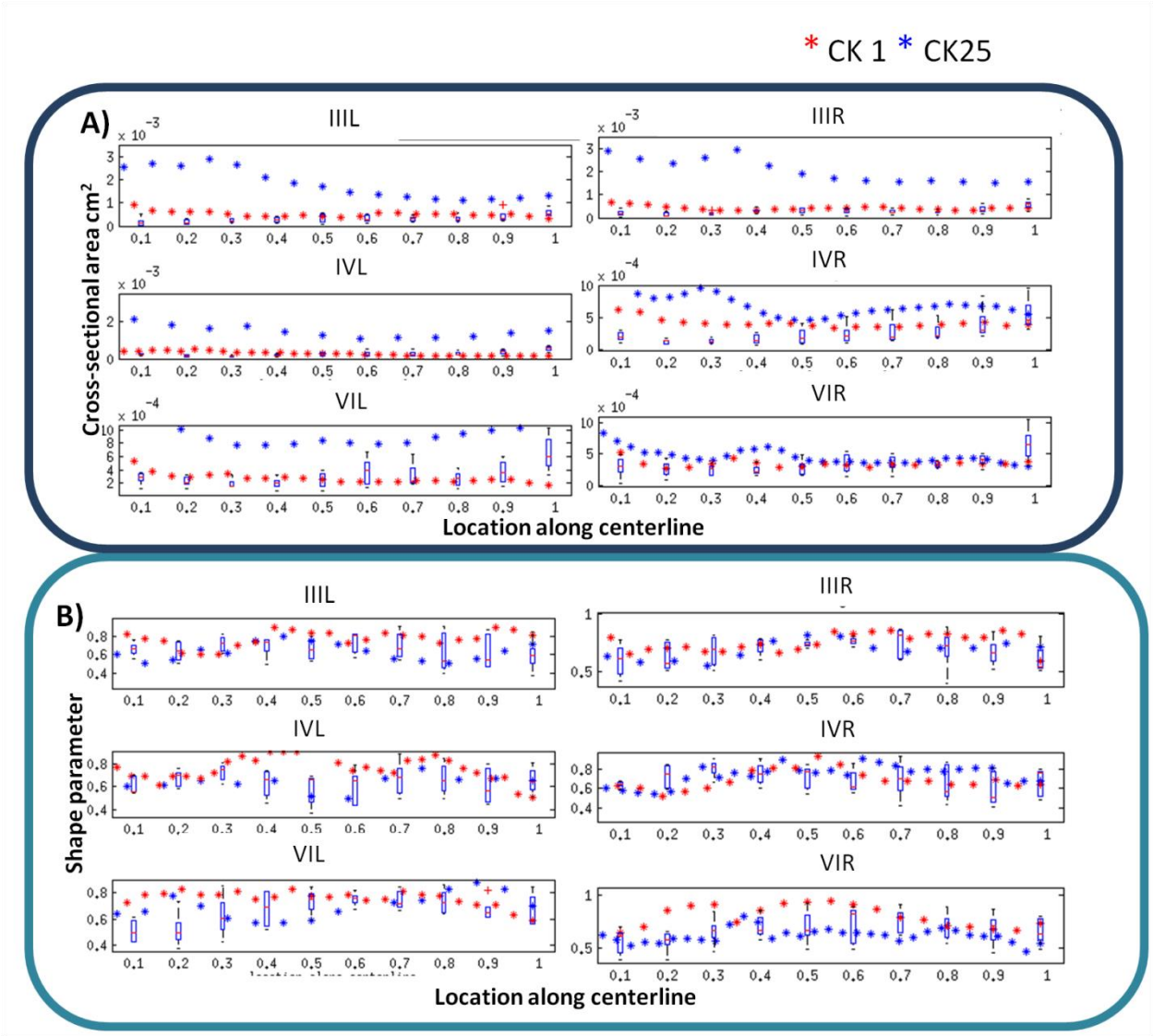

Figure 5.4. Cross-sectional Area and Shape Changes for Day 5 experimental occlusion embryos

Cross-sectional area changes along the centerline are shown for the two day 5 occlusion arch arteries (A). Their corresponding shape parameters along the length of the arch are shown in (B). Box plots represent the mean and standard deviation of day 5 control embryos (n =5). Of note are the similarities in shape parameter along the arch, after seeing such large differences in cross sectional area.

In-silico vessel occlusion

Day 3 in-silico occlusion/partial occlusion

CK26 and CK85 were occluded in-silico, in an effort to understand the immediate effects of arch artery occlusion. Each geometry was partially occluded as well as fully occluded. Table 1 shows the effects of vessel occlusion on flow distributions. With only 7% of flow being re-distributed in CK26 and 5% of the flow being re-distributed in CK85, changes in flow distribution are minimal. Upon PAA IVR vessel occlusion, more flow is re-distributed to the left side of the embryo than the right in the full occlusion case (59% of flow re-direction is channeled to the left), and is distributed equally in the case of the partial occlusion. Right side flow dominance is maintained in both cases. Similar trends can been seen for CK85 with the PAA III R and L taking up the bulk of flow redistribution. 58% of flow is distributed to the left side in the case of full vessel occlusion and equal distributions occurring with partial occlusion.

	CK26		CK26occl		CK26poccl		CK85		CK85occl		CK85poccl	
	Right	Left	Right	Left	Right	Left	Right	Left	Right	Left	Right	Left
II	0.6±0.1%	1.5±0.4%	1.0±1.0%	2.1±0.5%	0.6±0.04%	1.7±0.5%	3.4±0.7%	4.4±0.2%	3.5±0.7%	4.6±0.2%	3.4±0.7%	4.5±0.2%
III	47.0±1.4%	36.0±1.1%	49.3±1.8%	38.2±1.4%	50.6±1.7%	38.8±1.2%	35.1±0.2%	43.3±0.3%	37.2±0.3%	45.6±0.4%	36.5±0.2%	44.8±0.4%
IV	6.8±0.04%	8.1±0.1%	0.0%	9.3±0.04%	0.2±0.0%	8.2±0.06%	5.0±0.1%	8.7±0.2%	0.0%	9.2±0.2%	1.8%	9.0±0.2%

Table 5.1. Arch Artery Flow distributions for day 3 in-silico occlusion embryos.

Occl – occlusion; poccl – parital occlusion

The corresponding changes in pressure and wall shear stress (WSS) can be seen in Figure 5.5. Upon vessel occlusion there is an increase in magnitude of inlet pressure which is largely shouldered by the aortic sac and surgically altered IVR arch artery. Pressure in the left IV is slightly decreased upon vessel occlusion and slightly increased upon partial occlusion in both CK26 and Ck85 occlusion subsets. Similarly peak wall shear stress values are increased upon partial occlusion and decreased upon full occlusion.

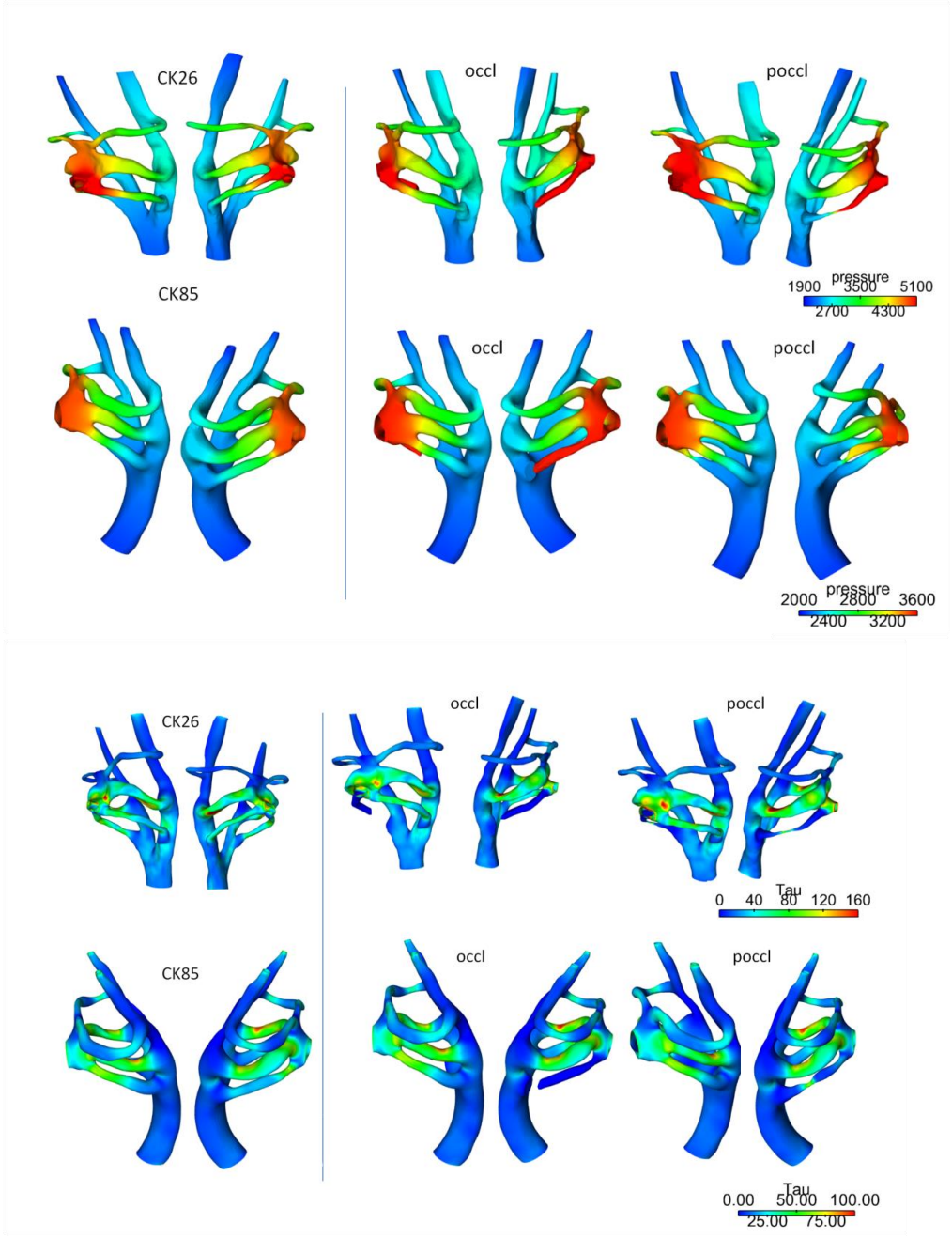

Figure 5.5. Pressure and Wall Shear Stress Distributions for Day 3

In-Silico Occlusion Embryos. Pressure and WSS values and measured in (dyne/cm^2).

90-10 cranial caudal flow distributions were maintained upon full and partial vessel occlusion of CK26 and CK85, though exact percentages deviated slightly (Table 2). The changes in downstream pressure and flow curves are displayed in Figure 5.6. Changes in the pressure and flow waveforms are seen in the lump parameter bounds upon vessel occlusion. While changes in the caudal pressure curves are slight, changes in cranial pressures are much larger particularly for CK26 full occlusion. Much smaller changes are seen in flow curves exiting through the 0D bounds.

CK26				CK85			
	Lcr	Rcr	CDL		Lcr	Rcr	CDL
cntrl	4.7%	5.2%	89.9%	cntrl	4.6%	4.9%	90.2%
occl	4.7%	5.2%	89.8%	occl	4.6%	4.9%	90.0%
poccl	4.7%	5.2%	89.9%	poccl	4.6%	4.9%	89.9%

Table 5.2 Cranial-caudal flow splits for CK26, CK85 control and occluded embryos.
Lcr = left cranial; Rcr – right cranial CDL –caudal; cntrl –control, poccl-partial occlusion; occl-occlusion.

	CK73		**CK73occl**		**CK73poccl**	
	Right	**Left**	**Right**	**Left**	**Right**	**Left**
III	**13.0±6.0%**	**38.8±6.4%**	**12.4±0.6%**	**43.8±1.6%**	**11.7±0.5%**	**41.4±1.7%**
IV	**8.8±5.7%**	**29.3±4.5%**	**0.0±0.0%**	**32.7±0.4%**	**5.4±0.4%**	**31.1±0.2%**
VI	**3.6±0.6%**	**6.5±1.5%**	**3.8±0.4%**	**7.3±0.5%**	**3.5±0.3%**	**7.0±0.5%**

Table 5.3. Flow distributions in Day 4 in-silico control and occlusion geometries.

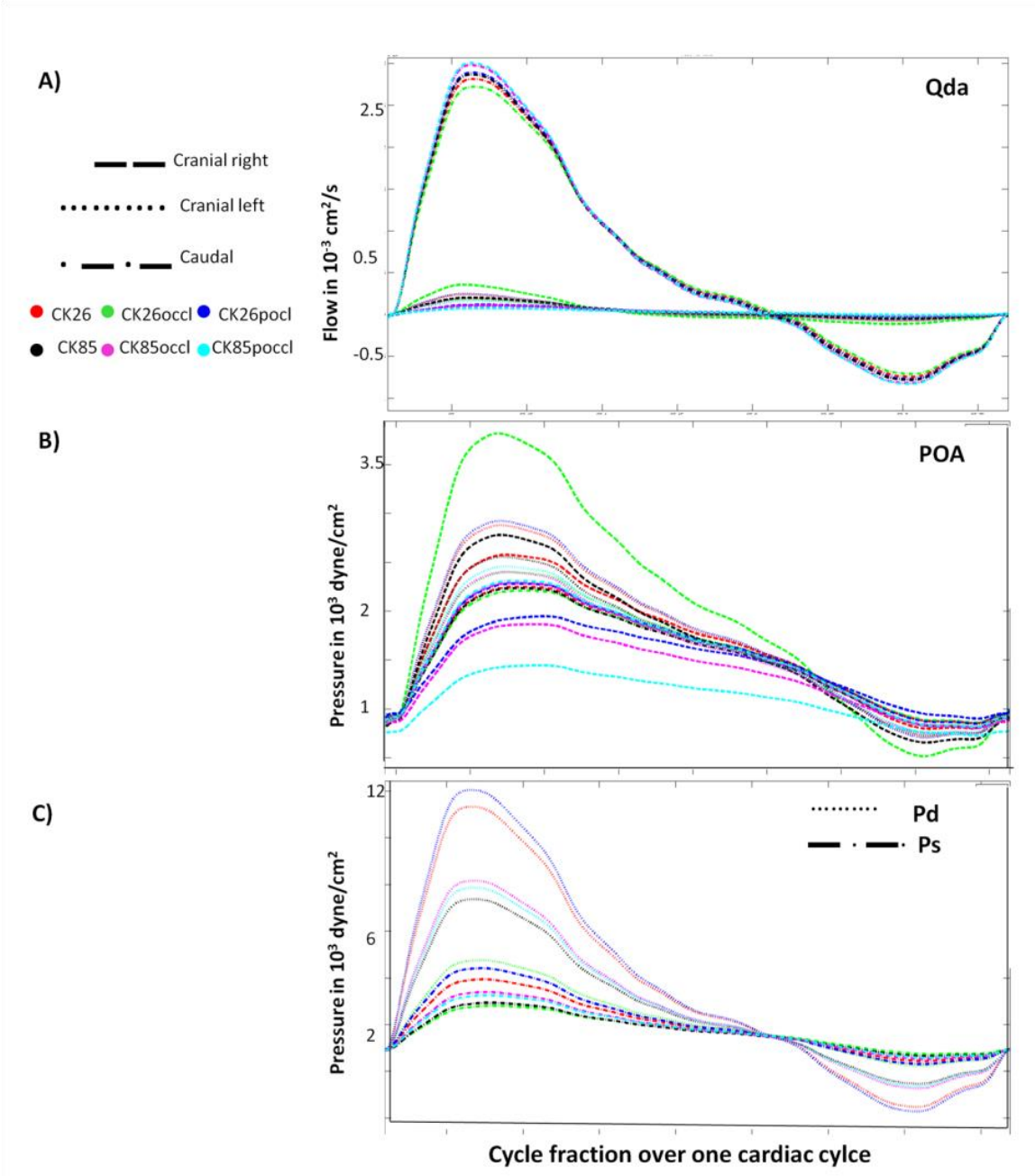

Figure 5.6. Changes in Downstream circulation upon day 3 in-silio occlusion. POA represents pressure at the 0D-3D junction. Qda represents flow entering the 0D bounds. Pd is the pressure at the base of the aortic sac before flow is distributed through the arches. Ps is the pressure in the aortic sac right before flow is distributed to the cranial four most arches (PAA III R, L and PAA IV R, L).

Day 4 in-silico occlusion/partial occlusion

A day 4 in-silico occlusion was performed to assess the immediate effects on the more stable day 4 arch artery form, where, unlike day 3, no arches are in the process of growing in or regressing. Table 3 shows effects of full and partial occlusion on CK73's vessel geometry. Occlusion of the right IV redistributed 9% of flow upon full vessel occlusion and 3.5% of the flow upon partial occlusion. 100% of the flow from PAA IVR was redistributed to the left, plus a little extra flow from the cranial IIIR arch. Similarly, partial occlusion of the right fourth caused 100% of the flow to be redistributes to the left side, including flow extra flow from PAA IIIR and a small amount of flow from PAA VIR.

Corresponding changes in pressure and wall shear stress maps are seen shown in Figure 5.7. Similarly to d3 In-silico occlusions, pressure magnitude increased at the outflow tract inlet. This increase in pressure was distributed cranially along the aortic sac, laterally along the IVR occluded or partially occluded arch as well as along the caudal VI arch arteries. Spikes in WSS increase in both the occlusion and the partial occlusion model.

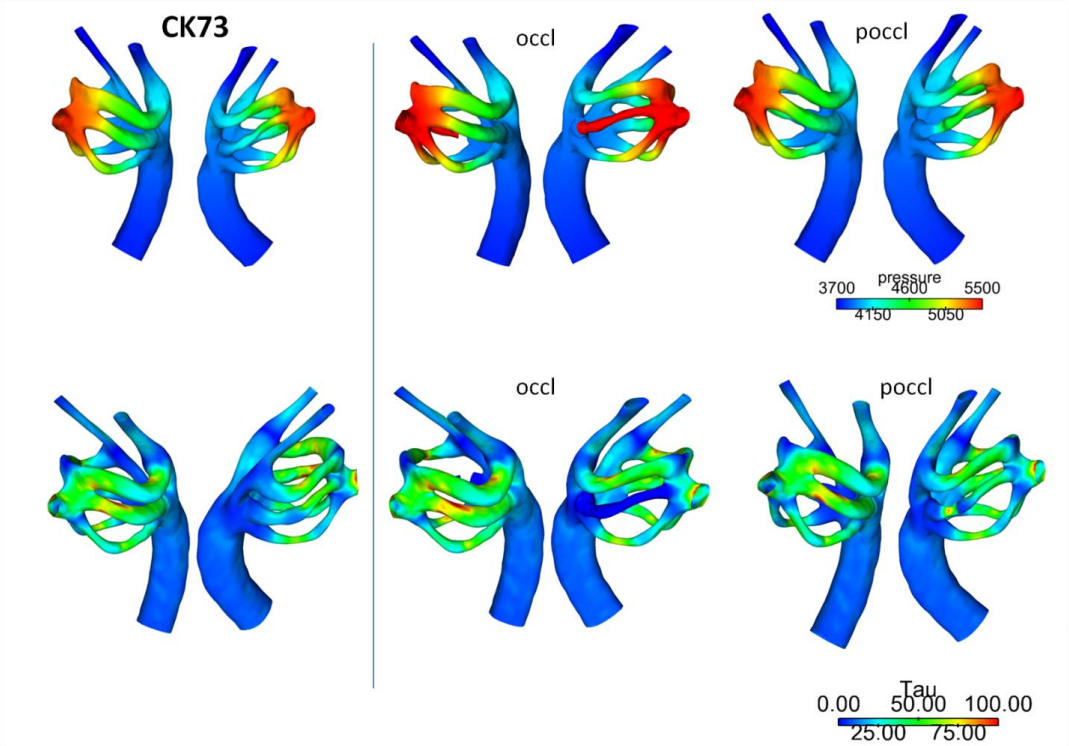

Figure 5.7 . Pressure and Wall Shear Stress Values for Day 4 In-silico occlusion. Pressure and WSS values and measured in (dyne/cm^2).

The 90-10 cranial- caudal flow split is conserved across control, occlusion and partial occlusion embryos. Deviations in branch specific percentages (Table 4) are even more slight than that of day 3 in-silico occlusion images.

CK73			
	Lcr	Rcr	CDL
cntrl	4.9%	4.9%	89.8%
occl	4.9%	4.9%	89.7%
poccl	4.9%	4.9%	89.8%

Table 5.4. Cranial-caudal flow splits for CK73 control and occluded embryos. Lcr = left cranial; Rcr – right cranial CDL –caudal; cntrl –control, poccl-partial occlusion; occl- occlusion.

Small changes in pressure and flow waveforms are seen in the lump parameter bounds upon vessel occlusion. Full and partial occlusion curves almost directly overlap for flow and pressure distribution curves associated with downstream circulation. There is a noticeable drop in the magnitude of right cranial pressure waveforms in occluded and partially occluded embryos when compared to that of the control (Figure 5.8B). Very slight changes are seen in flow curves distributed to the rest of the embryo upon vessel occlusion.

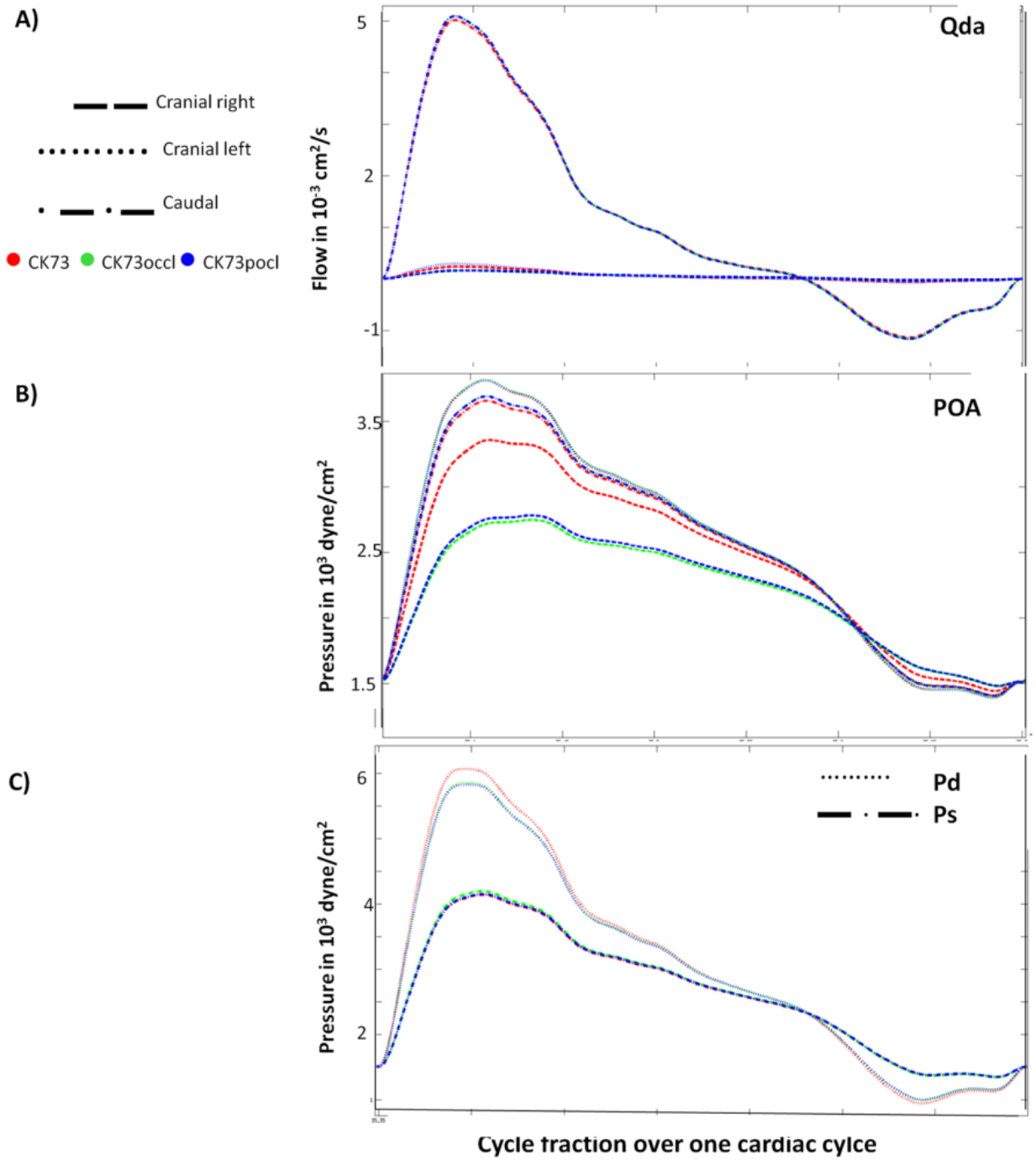

Figure 5.8. Changes in Pressure and Flow patterns with Day 4 In- Silico Occlusion POA represents pressure at the 0D-3D junction. Qda represents flow entering the 0D bounds. Pd is the pressure at the base of the aortic sac before flow is distributed through the arches. Ps is the pressure in the aortic sac right before flow is distributed to the cranial four most arches (PAA III R, L and PAA IV R, L).

Day 4 experimental occlusion CFD

Computational fluid dynamic simulations were performed on four of the eleven experimentally occluded embryo geometries. Flow distributions for these embryos are shown in Table 5. Flow dominance exists on the left for CK11 and CK22 occlusion images with 67% and 57% of flow being distributed to that side respectively. Dominance is found on the right in CK8 with 55% of flow being distributed to that side. Flow is split almost evenly between right and left arches in the fully occluded CK24 geometry. Arch artery dominance is seen in the right VI in CK8, the left third in CK11 and CK22, and is split almost evenly between the right III and left VI in CK24.

Pressure and wall shear stress maps in CK22 and CK24 embryos (Figure 5.9) are dramatically different from both those of day 4 control embryos, as seen in (Lindsey, Chapter 4), and In-silicoly occluded day 3 and day 4 embryos presented in this paper. The magnitude of pressure along the left arch arteries and the caudual R VI arch artery are so large in fully-occluded CK24 that pressure must be dissipated throughout the usually quiescent dorsal aorta. Pressure and WSS patterns in CK8 and CK11 resemble that of in-silicoly occluded and partially occluded day 3 and day 4 embryos, except that flow is dissipated more quickly cranially in the aortic sac. Aortic sac spikes in WSS occur over a slightly larger area in CK8 and CK11 than in insilicoly occluded embryos. A definite narrowing and horizontal axis elongation of the outflow tract junction can be seen in CK24 and CK22. A less severe narrowing and horizontal axis elongation of the outflow tract junction can also be seen in CK11, while CK8's outflow tract junction appears to be smaller and more circular.

	CK8		CK11		CK22		CK24	
	Right	**Left**	**Right**	**Left**	**Right**	**Left**	**Right**	**Left**
III	**14.9±0.2%**	**17.1±2.5%**	**27.6±0.2%**	**47.2±1.1%**	**15.1±0.3%**	**40.9±10.9%**	**31.8±2.5%**	**8.2±1.0%**
IV	**8.8±0.2%**	**17.2±2.7%**	**3.8±0.2%**	**15.2±0.3%**	**14.0±0.7%**	**3.8±2.3%**	**0**	**3.3±0.4%**
VI	**30.7±1.2%**	**11.8±5.3%**	**2.9±0.2%**	**3.3±0.2%**	**11.8±0.2%**	**11.8±0.2%**	**11.4±2.0%**	**31.0±7.2%**

Table 5.5. Mean Flow distributions in Day 4 occlusion geometries.

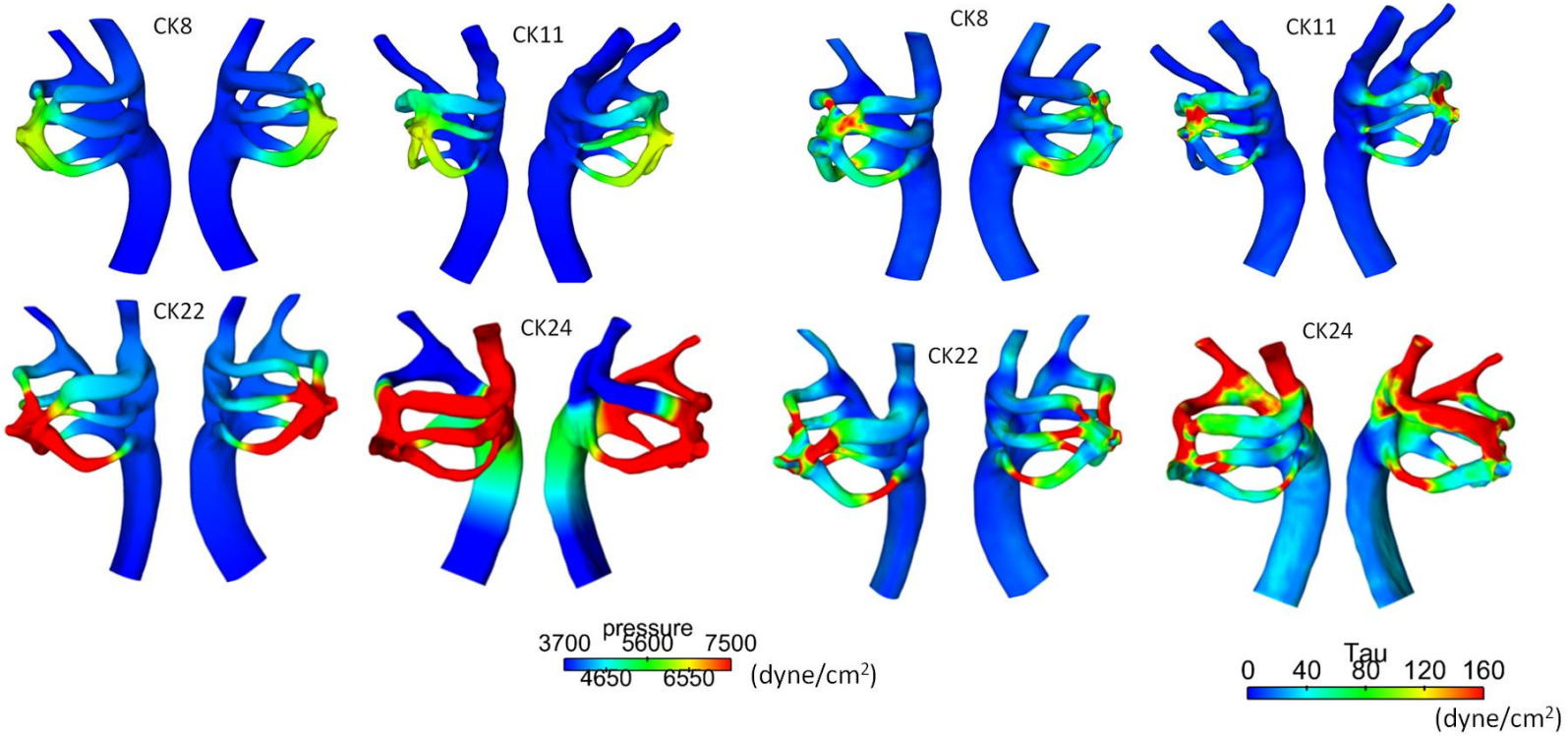

Figure 5.9. Pressure and Wall Shear Stress Variations for Day 4 Experimental Occlusion Embryos
Pressure and WSS were kept to be consistent with that of day 4 controls so that changes in pressure and WSS could be easily compared. Of note are the particularly high pressure and shear patterns seen in CK22 and CK24.

Figure 5.10 shows how vessel occlusion and subsequent remodeling affects day 4 resistance area correlation. Day 4 occlusion embryos no longer emulate the resistance proportionality to A^{-2} seen in day 3 and day 4 control embryos. PAA IIIL decreases in area and resistance from that of the day 4 control. PAA IVL has the same cross-sectional area (2.5 cm^2), but a different resistance for day 4 control, day 5 control and day 4 partial occlusion geometries. PAA VIR cross-sectional area dramatically increased from that of the day 4 control; its resistance slightly increased. PAA IVL partial occlusion embryo showed an even greater increase in cross-sectional area than that of PAA VIR, when compared to control, which resulted in a slight decrease in resistance. Functional –geometry correlations such as these begin to quantify the embryos complex growth adaptation process.

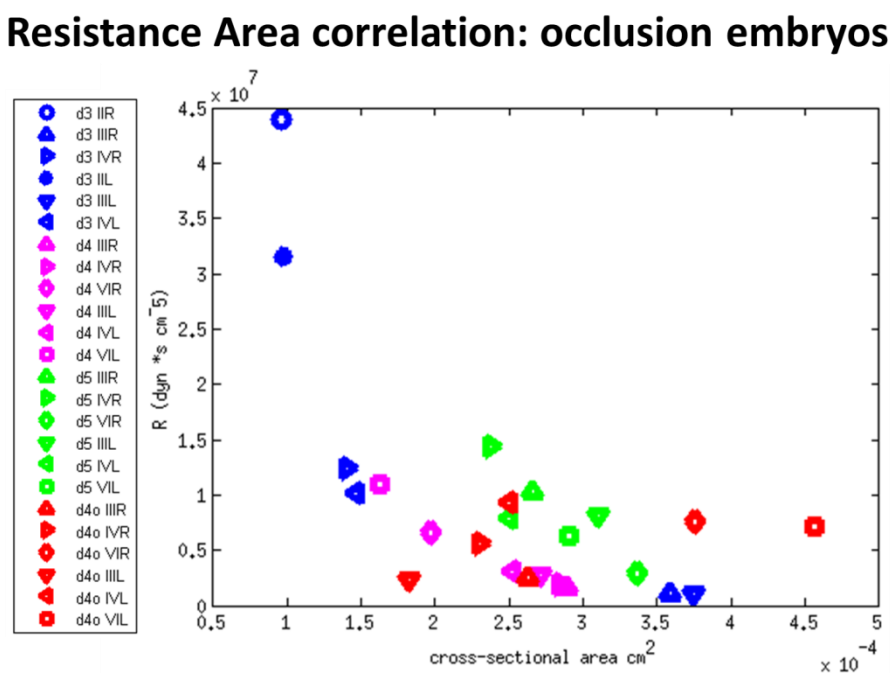

Figure 5.10 Resistance area correlation occluded embryos
Graph depicting resistance area correlation for experimentally obtained day 4 occlusion embryos (red) compared to that of day 3, day 4 and day 5 control embryos (presented in Chapter 4).

5.5 Discussion

Occlusion of the right IV arch artery at HH18 produces a large array of arch artery abnormalities. Remodeling of the arch artery vasculature is apparent within 24 hours of vessel occlusion and appears severe in two of the four computationally modeled experimental occlusion embryos. From HH18 – HH24, the arch arteries undergo many changes. These changes are the result of inlet flow stream distributions, 3D aortic sac and aortic arch geometries, and local vascular biologic responses to spatial variations in WSS (Wang et al., 2009b). Increase in arch artery flow over the course of development is thought to initiate maturation of their surrounding vessel walls (Silver & Hughes, 1973). The day 3 (HH18) time point is a particularly critical stage of

cardiovascular development as it precedes migration of neural crest cells down the pharyngeal arches. Cells of the cardiac neural crest migrate dorsolaterally and ventrolaterally. The circumpharyngeal crest, a consolidated group of neural crest cells, forms at the termis of the dorsolateral migration pathway (Kuratani & Kirby, 1991). It is there that dorsolaterally migrating cells arrest their movement temporarily while pharyngeal arches III, IV and VI form. The crest cells then seed the arch artereies, covering their endothelilal sheet and making up their ectomesenchyme. After the neural crest cells migrate down the caudal arch arteries, two prongs of crest cells, originating between the fourth and sixth arch arteries, extend dorsally into the aortic sac and initiate the formation of the aortic pulmonary septum (K. Waldo, Miyagawa-Tomita, Kumiski, & Kirby, 1998). Together with the shelf of tissue in the aortic sac, these prongs make up the aorticopulmonary septation complex. Occlusion of the right IV arch artery at HH18 and subsequent vessel remodeling may perturb this programmed sequence of events intensifying effects of arch artery occlusion.

The fate of the aortic arch arteries and the cardiac neural crest cells are inter-related. Neural crest cells form the smooth muscle tunics of the aortic arch artery derivatives. Disruption of even a small number of cardiac neural crest cells can result in a serious defect. Crest ablations are associated with failure of arch arteries three, four (right), and six to develop to the proper size (Bockman, Redmond, Waldo, Davis, & Kirby, 1987). There is a loss of bilateral symmetry, with uncommonly small or collapsed arch arteries on one side and unusually large arteries on the opposite side (K. L. Waldo, Kumiski, & Kirby, 1996). Many of these phenotypes can be seen in the experimental occlusion geometries found in Figure 5.2.

Effects of arch artery occlusion on downstream circulation were the most pronounced in the case of CK26, d3 arch artery occlusion, where despite having a more narrow right IV arch artery, more flow was re-distributed to the other arches than that of its "larger" d3 counterpart, CK85, who had larger PAA III and PAA IV vessels. These changes in pressure waveform distribution to the cranial arches may be triggering subsequent vessel remodeling in addition to the changes in flow and pressure changes in the arch arteries themselves. The use of lumped parameter bounds is particularly useful in contextualizing the effects insults to the region of interest have on the rest of the embryo.

Though our group has previously studied the effects of arch artery occlusion on HH18 and HH24 embryos (Lindsey et al., 2014), this study brings new light to our understanding of arch artery growth and adaptation in abnormal flow conditions. By examining embryo-specific geometries, placing them back in the context of the body, and comparing them to that of in-silio occlusion embryos, we are able to distinguish immediate changes from that of longer term adaptation to changing hemodynamic conditions. This study brings us closer to developing a detailed understanding of the factors involved in abnormal hemodynamics perturbations. Further characterization of these factors will prove to be a powerful tool in clinical diagnosis and intervention in abnormal cardiac development at their nascent stages.

Acknowledgements:

Cornell Imaging facility, nano-CT; Randolph Linderman (reconstructions); NSF GRFP, NSF GROW, NIH R01 HL 110328.

References

1. Bockman, D. E., Redmond, M. E., Waldo, K., Davis, H., & Kirby, M. L. (1987). Effect of neural crest ablation on development of the heart and arch arteries in the chick. *The American journal of anatomy*, *180*(4), 332–41. doi:10.1002/aja.1001800403

2. deAlmeida, A., McQuinn, T., & Sedmera, D. (2007). Increased ventricular preload is compensated by myocyte proliferation in normal and hypoplastic fetal chick left ventricle. *Circulation research*, *100*(9), 1363–70. doi:10.1161/01.RES.0000266606.88463.cb

3. Fisher, A. B., Chien, S., Barakat, A. I., & Nerem, R. M. (2001). Endothelial cellular response to altered shear stress. *American journal of physiology. Lung cellular and molecular physiology*, *281*(3), L529–33.

4. Go, A. S., Mozaffarian, D., Roger, V. L., Benjamin, E. J., Berry, J. D., Borden, W. B., … Turner, M. B. (2013). Executive summary: heart disease and stroke statistics--2013 update: a report from the American Heart Association. *Circulation*, *127*(1), 143–52. doi:10.1161/CIR.0b013e318282ab8f

5. Harh, J. Y., Paul, M. H., Gallen, W. J., Friedberg, D. Z., & Kaplan, S. (1973). Experimental production of hypoplastic left heart syndrome in the chick embryo. *The American journal of cardiology*, *31*(1), 51–6.

6. Hogers, B., DeRuiter, M. C., Gittenberger-de Groot, a C., & Poelmann, R. E. (1999). Extraembryonic venous obstructions lead to cardiovascular malformations and can be embryolethal. *Cardiovascular research*, *41*(1), 87–99.

7. Hogers, B., DeRuiter, M. C., Gittenberger-de Groot, A. C., & Poelmann, R. E. (1997). Unilateral Vitelline Vein Ligation Alters Intracardiac Blood Flow Patterns and Morphogenesis in the Chick Embryo. *Circ. Res.*, *80*(4), 473–481.

8. Hove, J. R., Köster, R. W., Forouhar, A. S., Acevedo-Bolton, G., Fraser, S. E., & Gharib, M. (2003). Intracardiac fluid forces are an essential epigenetic factor for embryonic cardiogenesis. *Nature*, *421*(6919), 172–7. doi:10.1038/nature01282

9. Hu, N., Christensen, D. a, Agrawal, A. K., Beaumont, C., Clark, E. B., & Hawkins, J. a. (2009). Dependence of aortic arch morphogenesis on intracardiac blood flow in the left atrial ligated chick embryo. *Anatomical record (Hoboken, N.J. : 2007)*, *292*(5), 652–60. doi:10.1002/ar.20885

10. Kowalski, W. J., Dur, O., Wang, Y., Patrick, M. J., Tinney, J. P., Keller, B. B., & Pekkan, K. (2013). Critical Transitions in Early Embryonic Aortic Arch

Patterning and Hemodynamics. (L. Eisenberg, Ed.)*PLoS ONE*, *8*(3), e60271. doi:10.1371/journal.pone.0060271

11. Kuratani, S. C., & Kirby, M. L. (1991). Initial migration and distribution of the cardiac neural crest in the avian embryo: an introduction to the concept of the circumpharyngeal crest. *The American journal of anatomy*, *191*(3), 215–27. doi:10.1002/aja.1001910302

12. Lindsey, S. E., Menon, P. G., Kowalski, W. J., Shekhar, A., Yalcin, H. C., Nishimura, N., … Pekkan, K. (2014). Growth and hemodynamics after early embryonic aortic arch occlusion. *Biomechanics and modeling in mechanobiology*. doi:10.1007/s10237-014-0633-1

13. Nishimura, N. et al., 2006. Targeted insult to subsurface cortical blood vessels using ultrashort laser pulses: three models of stroke. *Nature methods*, 3(2), pp.99–108.

14. Rychter, Z. (1962). Experimental morphology of the aortic arches and the heart loop in chick embryos. *Adv Morphog*.

15. Sedmera, D., Pexieder, T., Rychterova, V., Hu, N., & Clark, E. B. (1999). Remodeling of chick embryonic ventricular myoarchitecture under experimentally changed loading conditions. *The Anatomical record*, *254*(2), 238–52.

16. Silver, J., & Hughes, a F. (1973). The role of cell death during morphogenesis of the mammalian eye. *Journal of morphology*, *140*(2), 159–70. doi:10.1002/jmor.1051400204

17. Tobita, K., & Keller, B. B. (2000). Right and left ventricular wall deformation patterns in normal and left heart hypoplasia chick embryos. *American journal of physiology. Heart and circulatory physiology*, *279*(3), H959–69.

18. Van der Heiden, K., Groenendijk, B. C. W., Hierck, B. P., Hogers, B., Koerten, H. K., Mommaas, A. M., … Poelmann, R. E. (2006). Monocilia on chicken embryonic endocardium in low shear stress areas. *Developmental dynamics : an official publication of the American Association of Anatomists*, *235*(1), 19–28. doi:10.1002/dvdy.20557

19. Vogel, A. & Venugopalan, V., 2003. Mechanisms of pulsed laser ablation of biological tissues. *Chemical reviews*, 103(2), pp.577–644.

20. Waldo, K. L., Kumiski, D., & Kirby, M. L. (1996). Cardiac neural crest is essential for the persistence rather than the formation of an arch artery. *Developmental dynamics : an official publication of the American Association of Anatomists*, *205*(3), 281–92. doi:10.1002/(SICI)1097-0177(199603)205:3<281::AID-AJA8>3.0.CO;2-E

21. Waldo, K., Miyagawa-Tomita, S., Kumiski, D., & Kirby, M. L. (1998). Cardiac neural crest cells provide new insight into septation of the cardiac outflow tract: aortic sac to ventricular septal closure. *Developmental biology*, *196*(2), 129–44. doi:10.1006/dbio.1998.8860

22. Wang, Y., Dur, O., Patrick, M. J., Tinney, J. P., Tobita, K., Keller, B. B., & Pekkan, K. (2009a). Aortic arch morphogenesis and flow modeling in the chick embryo. *Annals of biomedical engineering*, *37*(6), 1069–81. doi:10.1007/s10439-009-9682-5

23. Wang, Y., Dur, O., Patrick, M. J., Tinney, J. P., Tobita, K., Keller, B. B., & Pekkan, K. (2009b). Aortic arch morphogenesis and flow modeling in the chick embryo. *Annals of biomedical engineering*, *37*(6), 1069–81. doi:10.1007/s10439-009-9682-5

24. Wyczalkowski, M. a, Chen, Z., Filas, B. a, Varner, V. D., & Taber, L. a. (2012). Computational models for mechanics of morphogenesis. *Birth defects research. Part C, Embryo today : reviews*, *96*(2), 132–52. doi:10.1002/bdrc.21013

25. Yoshigi, M., Knott, G. D., & Keller, B. B. (2000). Lumped parameter estimation for the embryonic chick vascular system: a time-domain approach using MLAB. *Computer methods and programs in biomedicine*, *63*(1), 29–41.

CONCLUSION

Pharyngeal arch artery morphogenesis involves a complex system of events that transform six bilateral arch pairs into the great vessels of the heart. Early patterning of the arch arteries can impact the shape, orientation, structure and function of the outflow tract, leading to a variety of cardiac abnormalities when events don't proceed as planned. At the heart of all of this is hemodynamics, the ultimate driver of morphogenesis, promoting growth and remodeling through changes in shear and pressure forces.

Though the importance of the outflow tract system in distributing oxygenated blood to the body has long been established, there remains much to be learned about arch artery morphogenesis in order to effect change and design possible interventions. With the advent of new imaging technology, studies aimed at addressing the root cause of problems have been made possible. Through non-linear optics, nano-CT and advanced ultrasound technologies, our group has begun to delineate the effects of hemodynamics alone in morphogenic patterning of the heart and its major vessels, a challenge that has plagued the field for years.

The presented studies lay the foundation for an advanced understanding of cardiac outflow morphogenesis. By combining computational and experimental techniques I've been able to establish a natural framework of hemodynamic and morphogenic indices, elucidating their role in both normal and abnormal development.

The combination of experimental and computational techniques has proven a powerful tool in explaining observed phenomenon. It is through this combination that the field

of cardiac development can ultimately obtain an understanding of underlying mechanisms of disease and abnormal patterning as well as optimize possible interventions.

Future directions for the work presented here should involve using information obtained from these models to grow the embryo between stages. Such a study would essentially validate information obtained from individual stages and solidify a working knowledge of early arch artery mechanics. The next step would be to correlate the changes seen on whole tissue level with changes observed on a molecular and cellular level. While hemodynamics may be the driving force behind structural stages, different processes are carrying the changes out on a molecular and cellular level. Uncovering them will add to the understanding of pharyngeal arch arteries and morphogenesis as a whole. Lastly, comparing the results of arch artery vessel occlusion to that of abnormalities originating from the outflow tract itself would help determine where the malformation is likely to have originated in clinically relevant congenital heart defects. Geometric changes resulting from outflow tract cushion ablation are presented in Appendix A.4.

APPENDIX A

A.1 Appendix to Chapter 4

Downstream Circulation (lumped parameter models)

		Mean ± Standard Error (Dyne*s*cm^{-5})		Caudal Bounds (Dyne*s*cm^{-5})
		Left	**Right**	
Day 3	**Proximal**	6.23E+006 ± 4.41E+005	5.82E+006 ± 6.02E+005	3.40E+005
	Distal	3.90E+007 ± 2.81E+006	3.42E+007 ± 2.16E+006	2.19E+006
Day 4	**Proximal**	5.02E+006 ± 6.61E+005	4.81E+006 ±5.99E+005	3.21E+005
	Distal	3.41E+007 ± 1.52E+006	3.68E+007 ± 1.63E+006	2.07E+006
Day 5	**Proximal**	3.35E+006 ± 6.62E+005	3.48E+006 ± 5.49E+005	2.32E+005
	Distal	2.65E+007 ± 1.67E+006	2.55E+007 ± 2.26E+006	1.61E+006

Table A.1. Lumped parameter bounds for day 3, 4 and 5 control images.

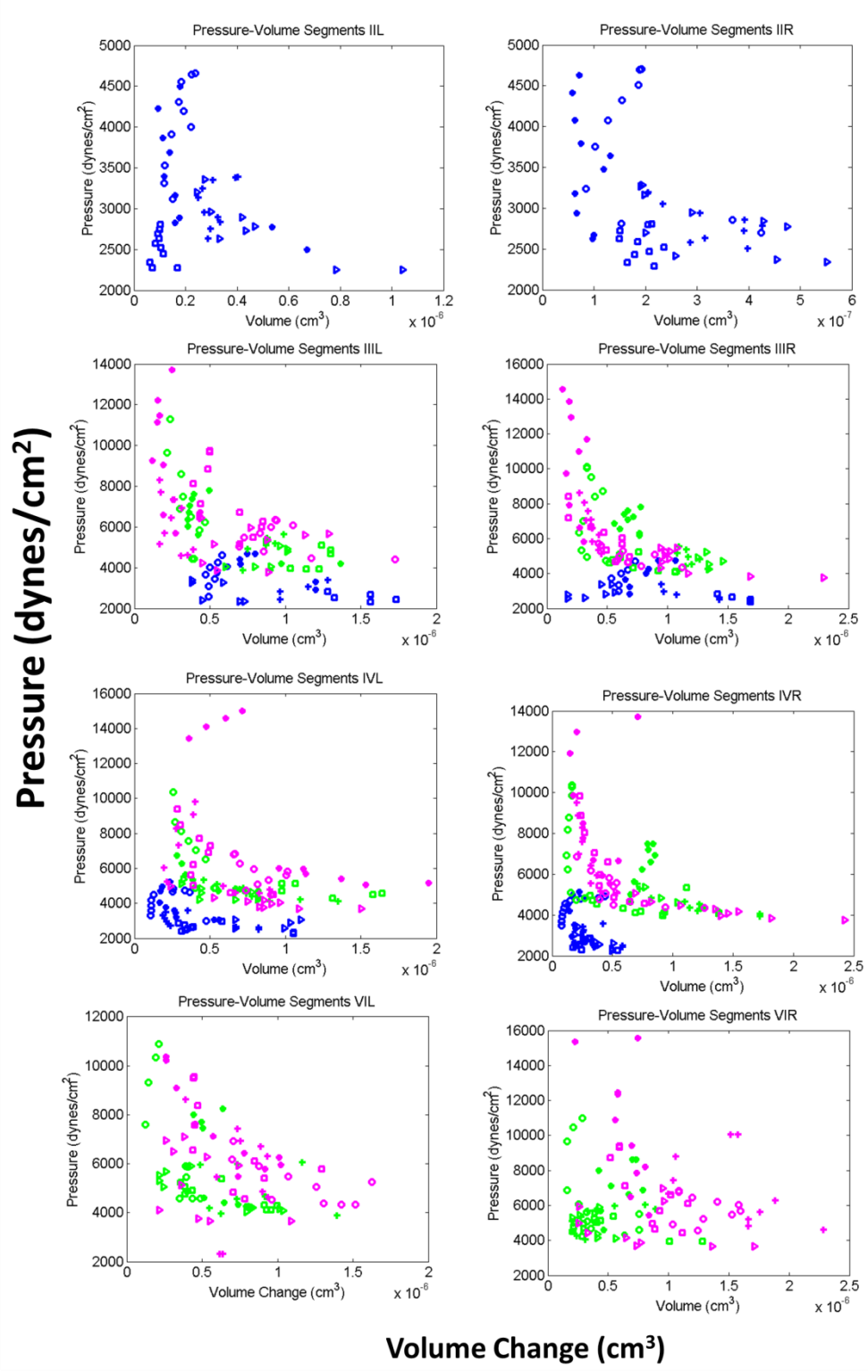

Figure A.1.1: Pressure-Volume Change curves for day 3 day 4 and day 5 control geometries plotted by day.

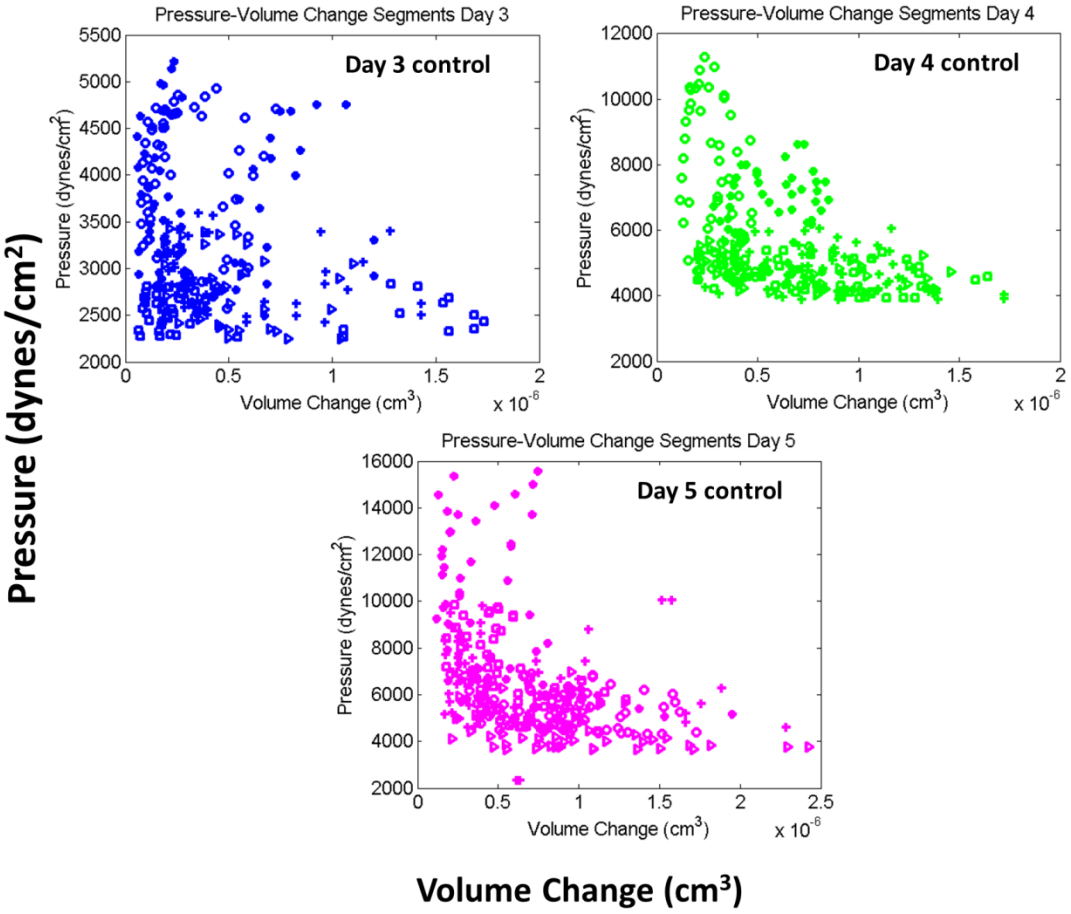

Figure A.1.2: Pressure-Volume Change curves for day 3, day 4, day 5 controls organized by day

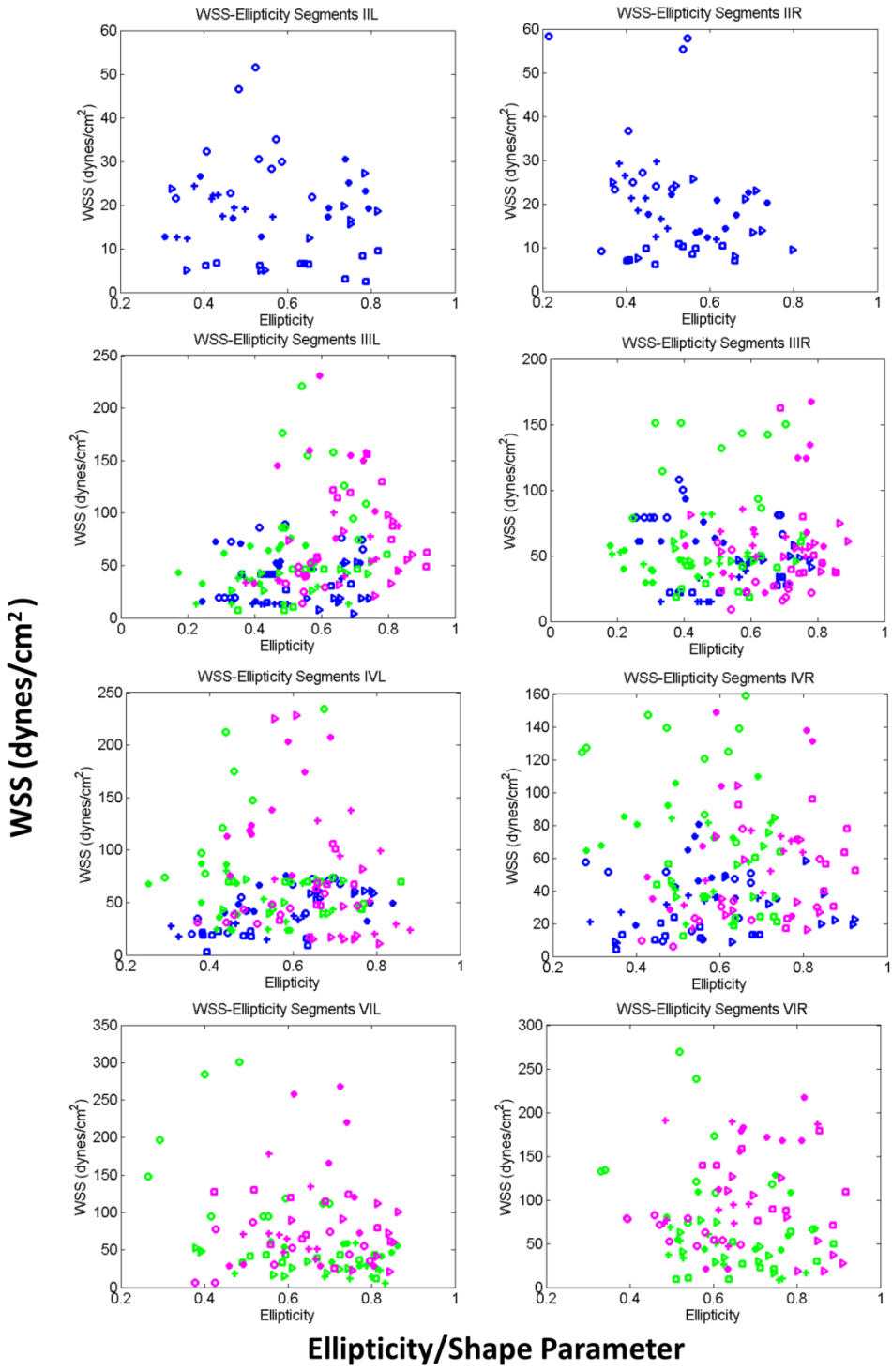

Figure A.1.5: Wall Shear Stress – Ellipticity curves by arch for day 3, day 4, day 5 controls

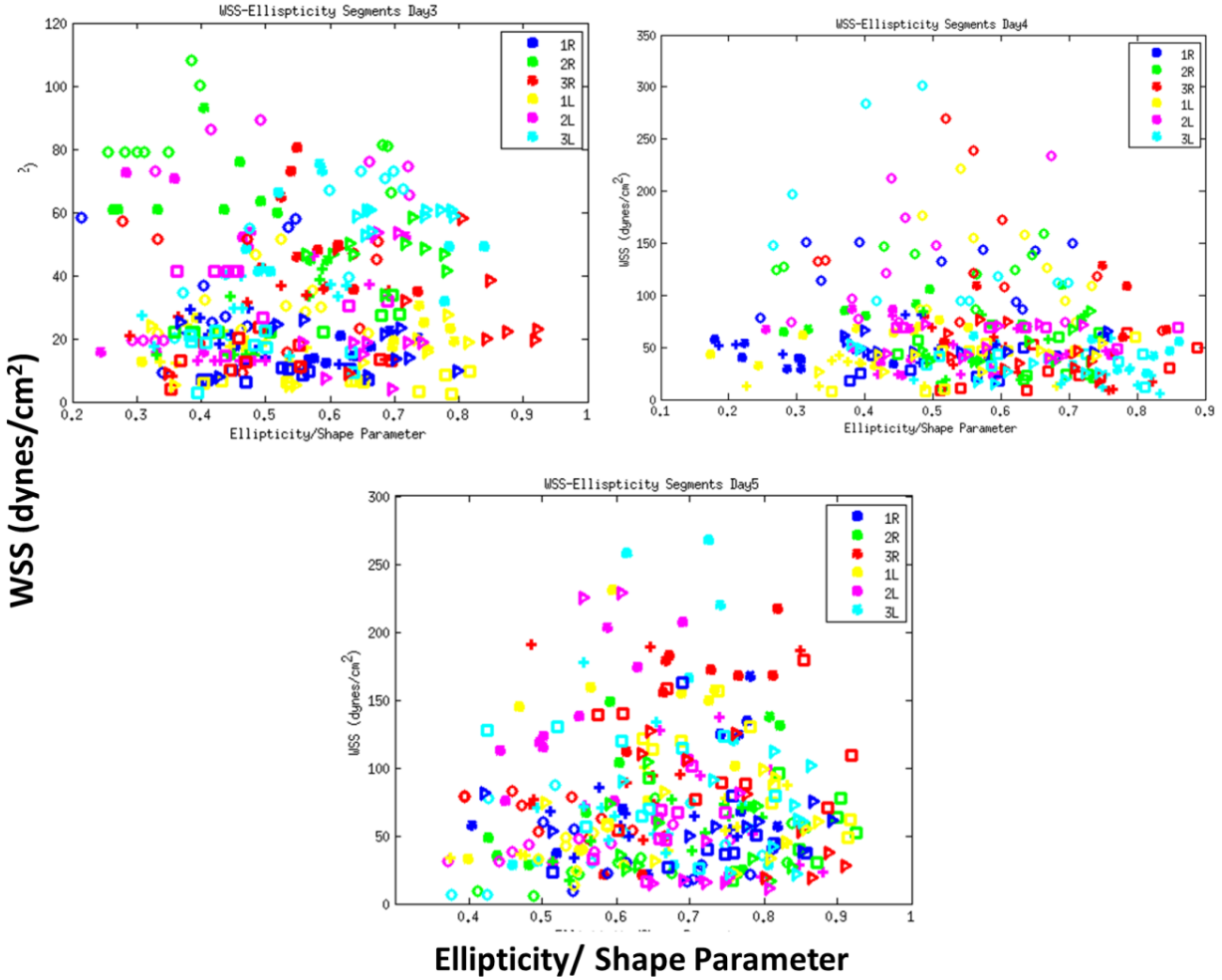

Figure A.1.5: Wall Shear Stress Ellipticity Values for Day 3, Day 4, Day 5 Control

A.2 Appendix for Chapter 5

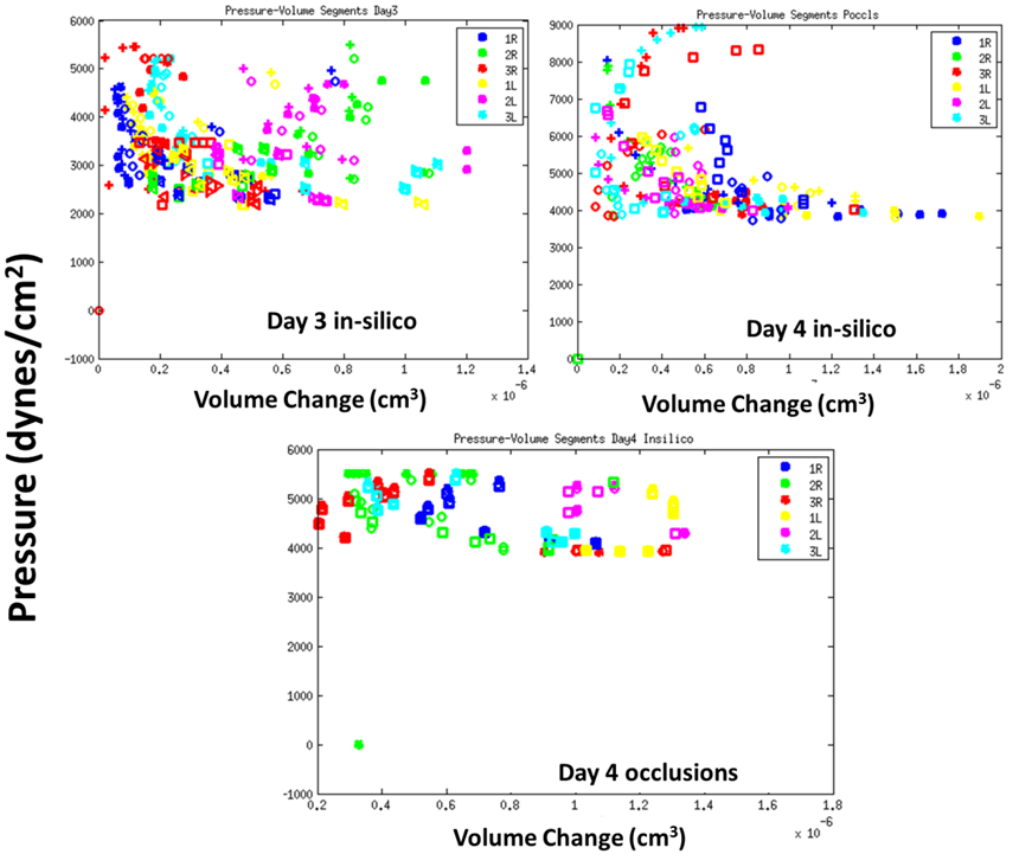

Figure A.2.2: Pressure-Volume Change Values for Occlusion Embryos

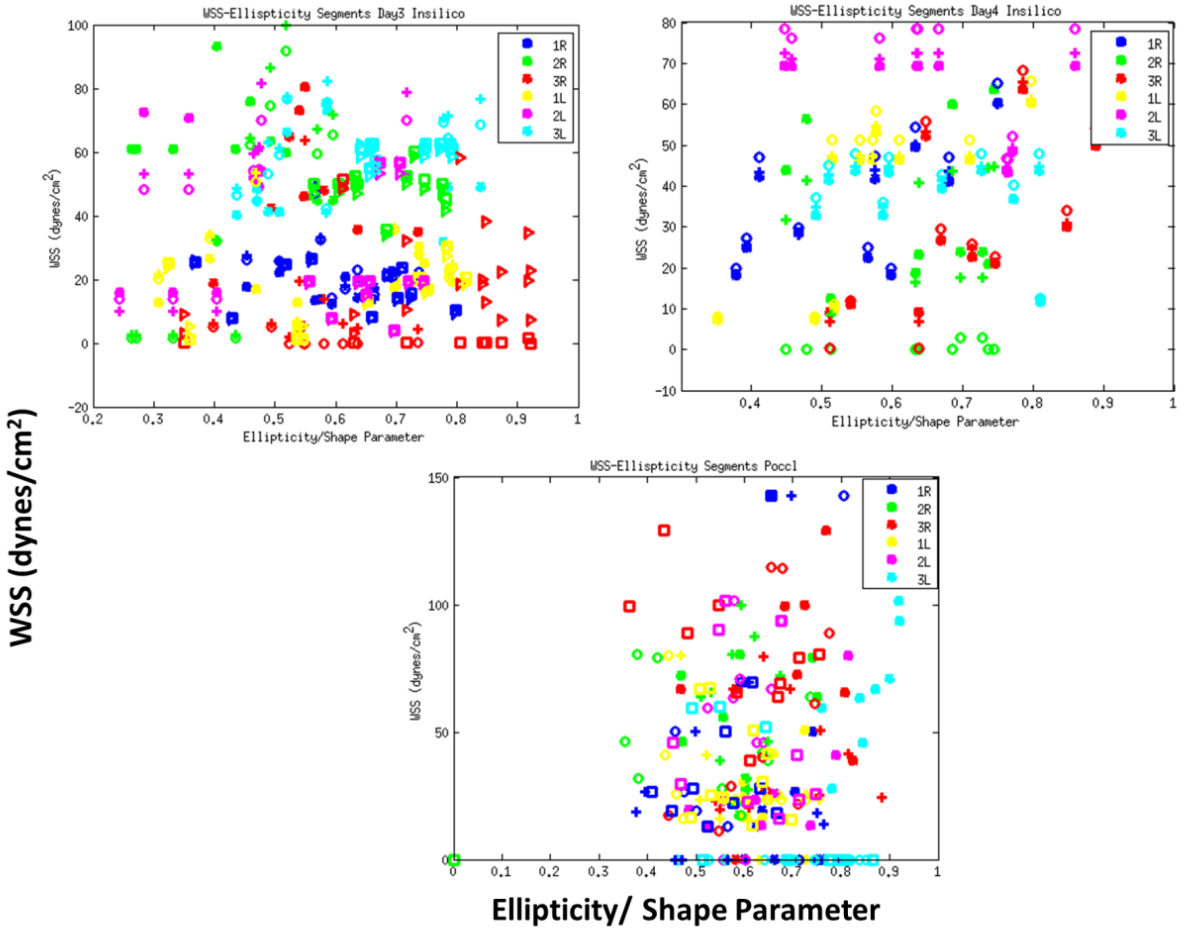

Figure A.2.2: Wall Shear Stress Ellipticity Values for Occlusion Embryos

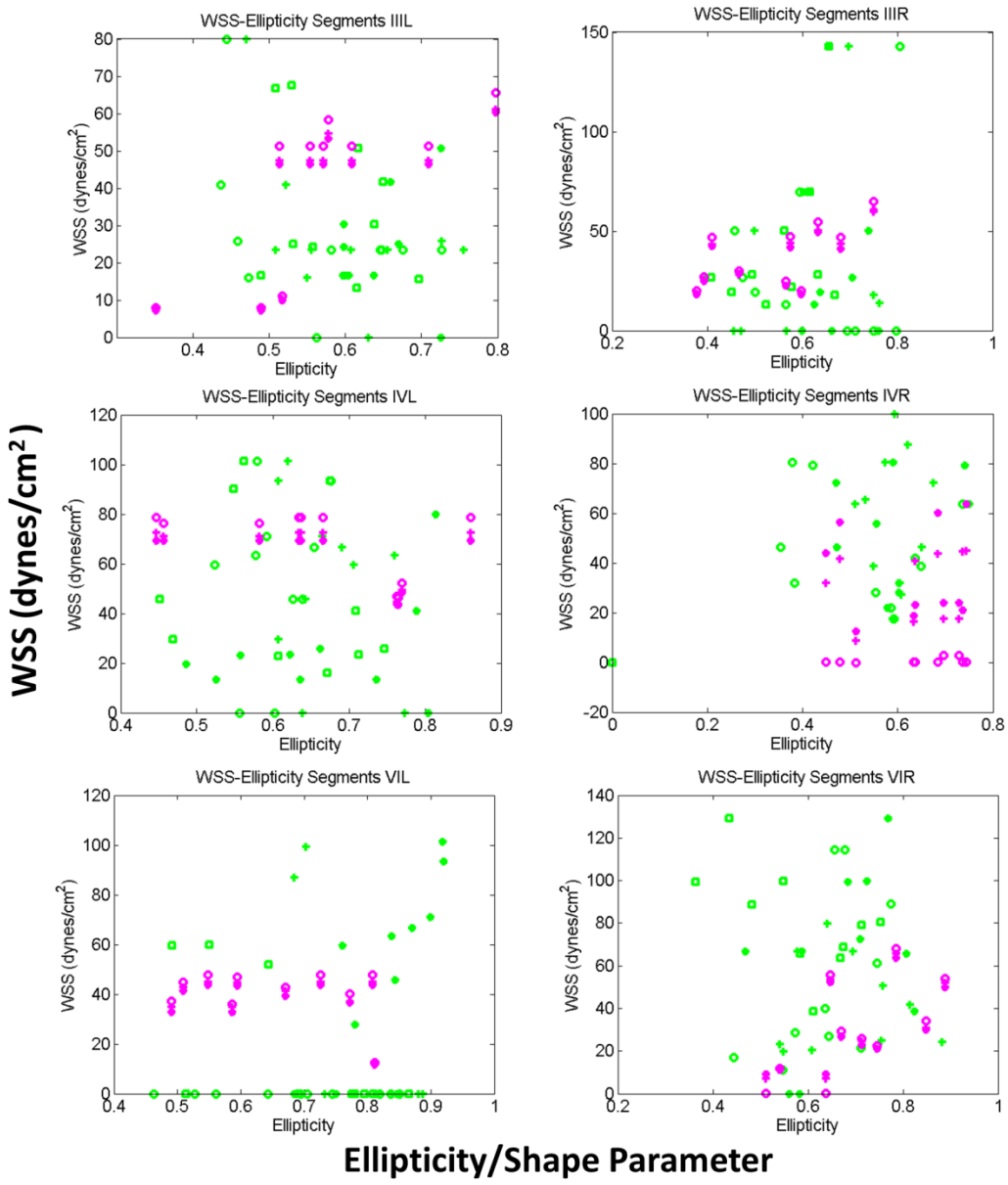

Figure A.2.2: Wall Shear Stress Ellipticity Values for experiment occlusion embryos (green) and day 4 in-silico occlusion embryos (magenta).

A.3 Supplemental Data from Cushion Ablation Studies

The following images and graphs are the result of two photon microscopy guided femtosecond laser ablation of HH18 (day 3) proximal distal outflow tract cushion ablations. Embryos survived through day 7.

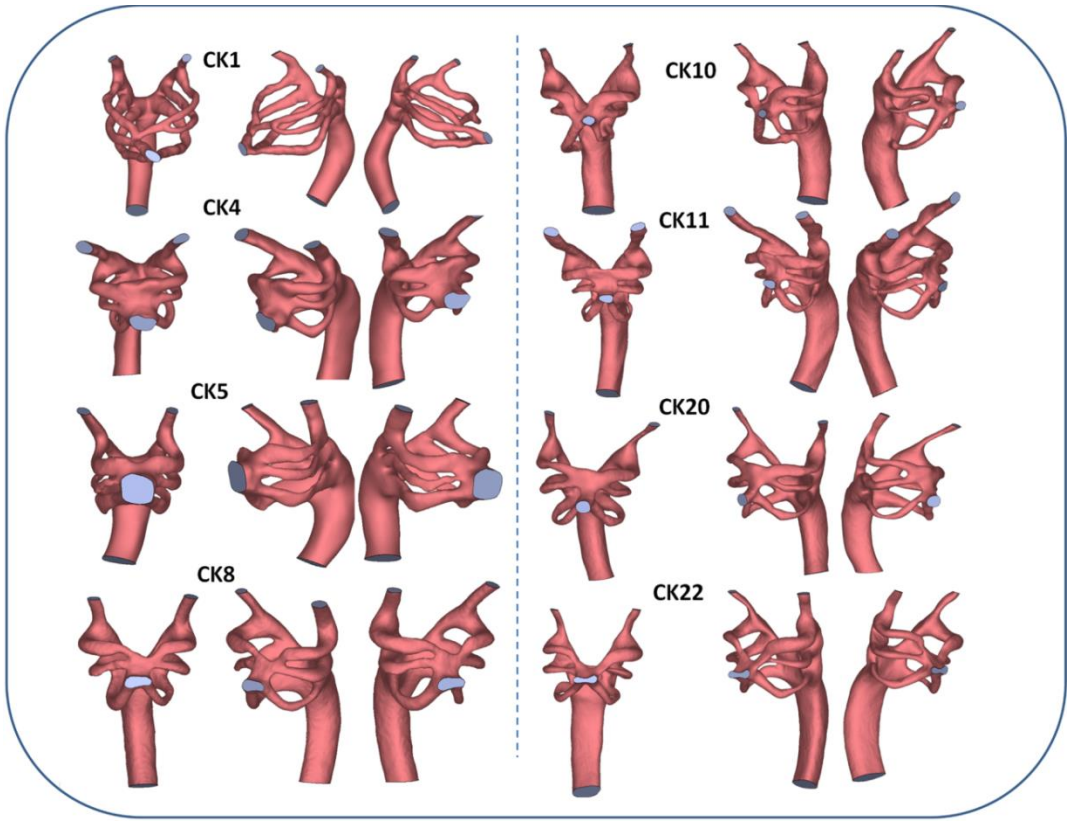

Figure A.3.1: Control images of late pharyngeal arch artery morphogenesis.

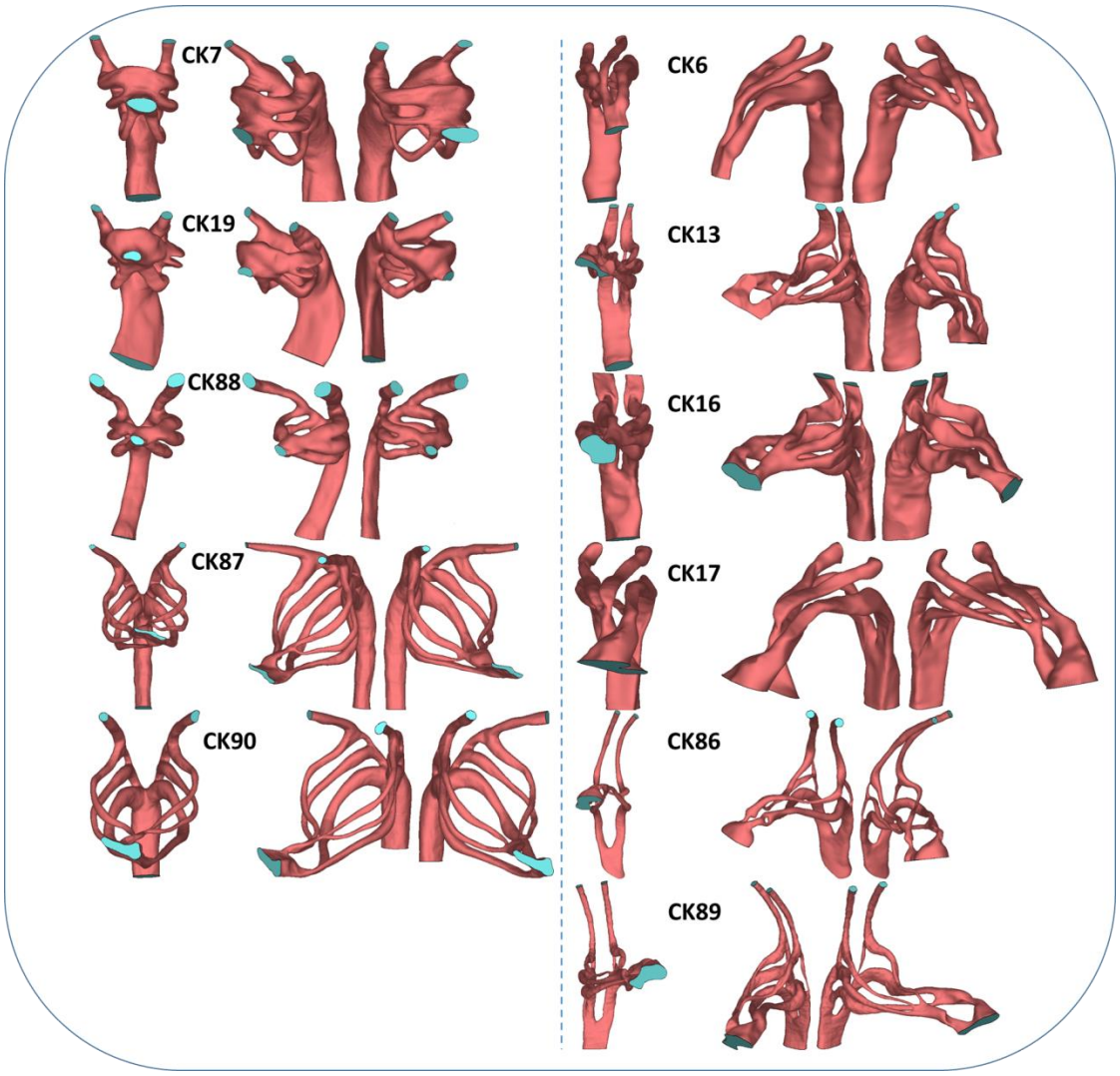

Figure A.3.2: Results of femto-second laser ablation of outflow tract cushions on pharyngeal arch artery morphogenesis.

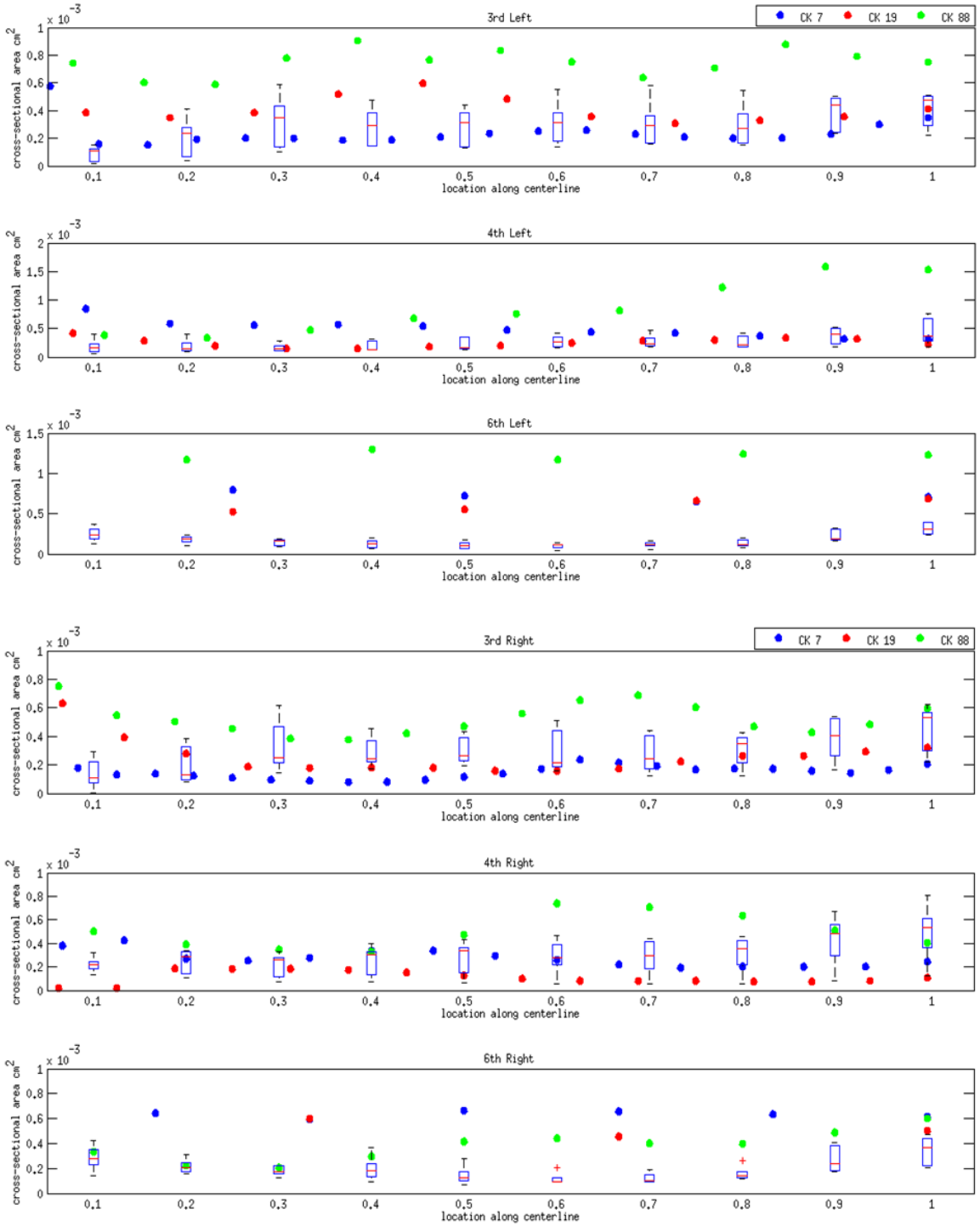

Figure A.3.3: Day 4 Cross-sectional area changes for cushion ablation embryos. Boxplots represent that of day 4 control embryos.

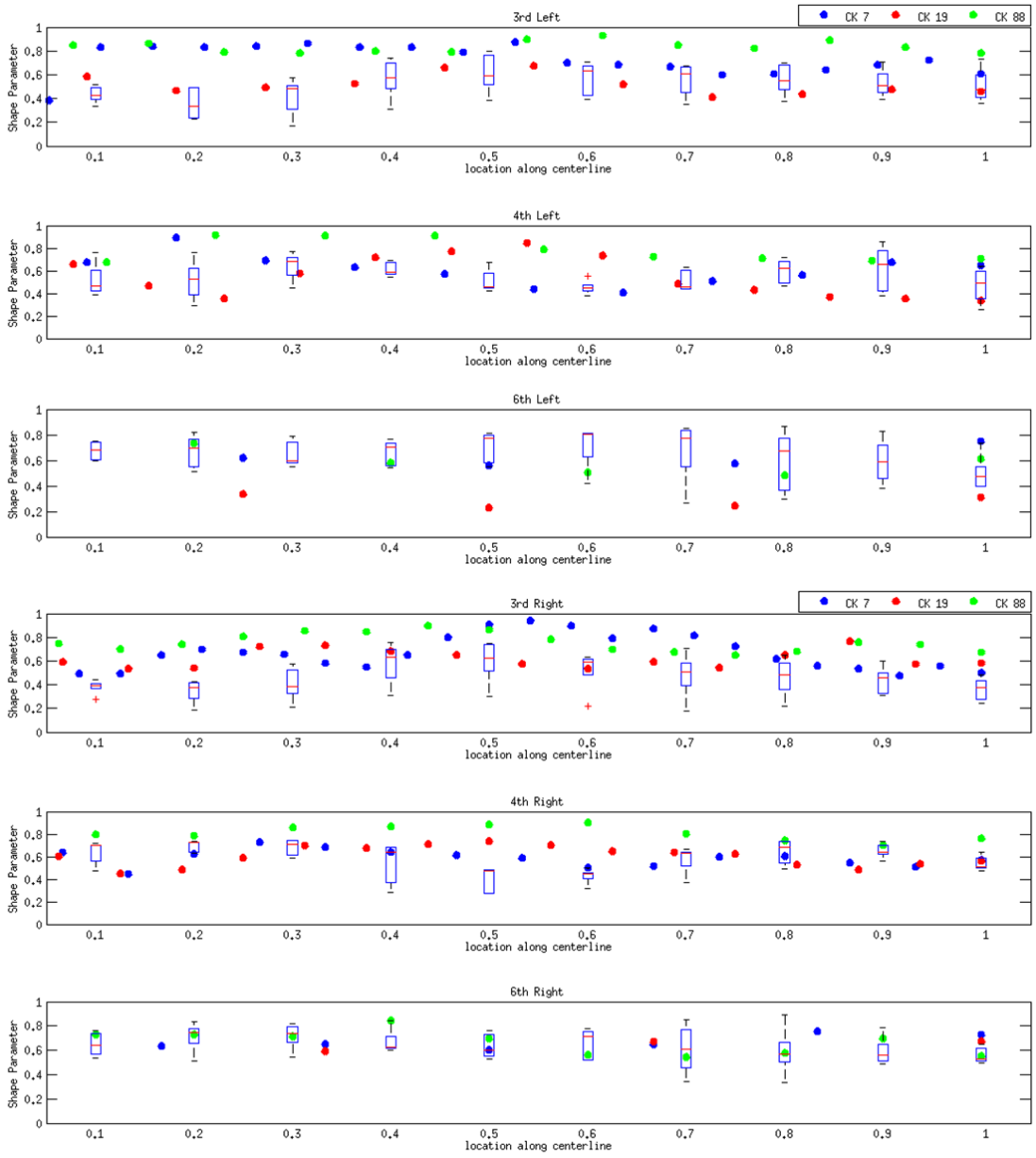

Figure A.3.4: Day 4 Shape parameter changes for cushion ablation embryos. Boxplots represent that of day 4 control embryos.

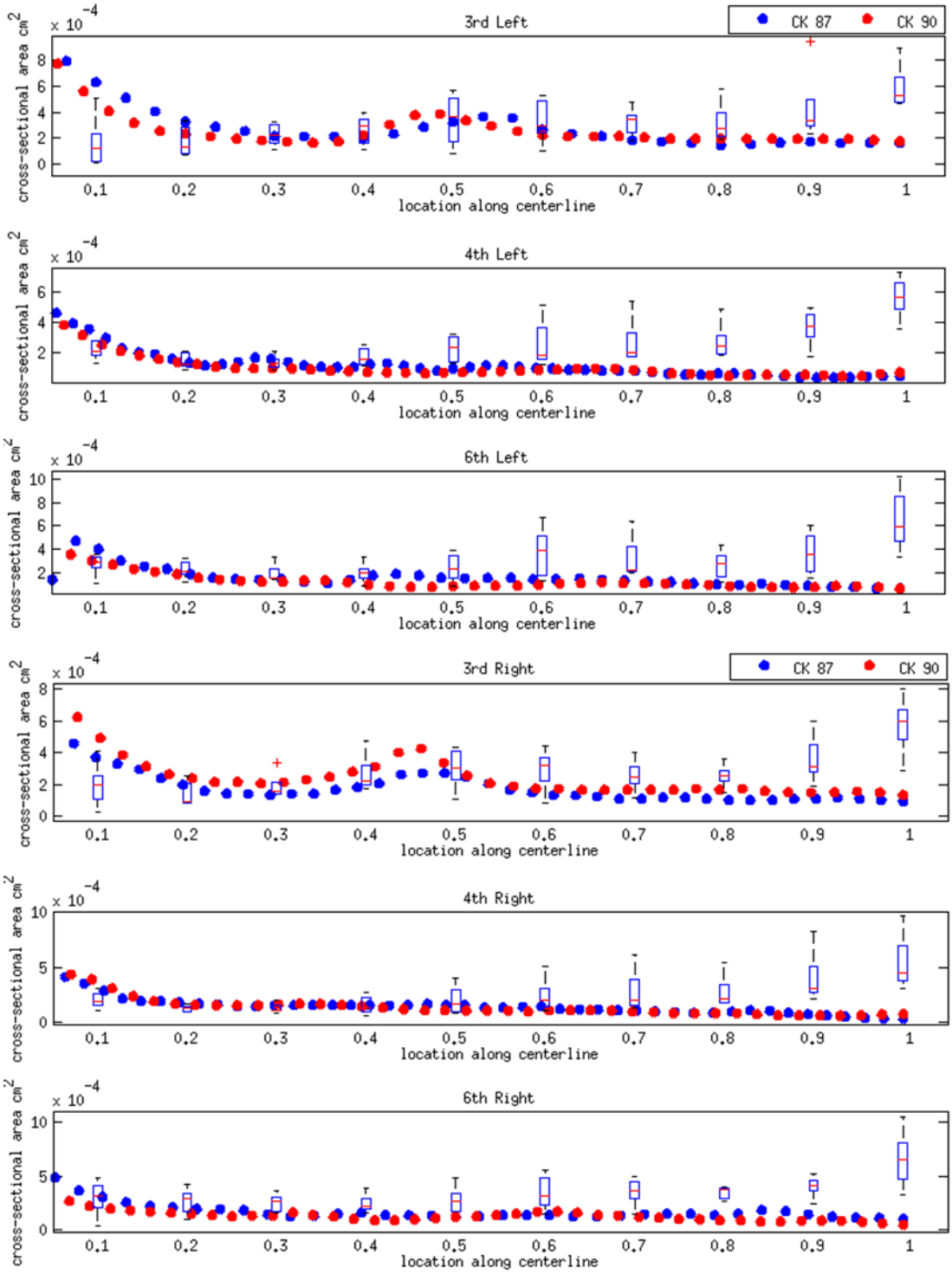

Figure A.3.5: Day 5 Cross-sectional area changes for day 4 cushion ablation embryos.

Boxplots represent that of day 5 control embryos.

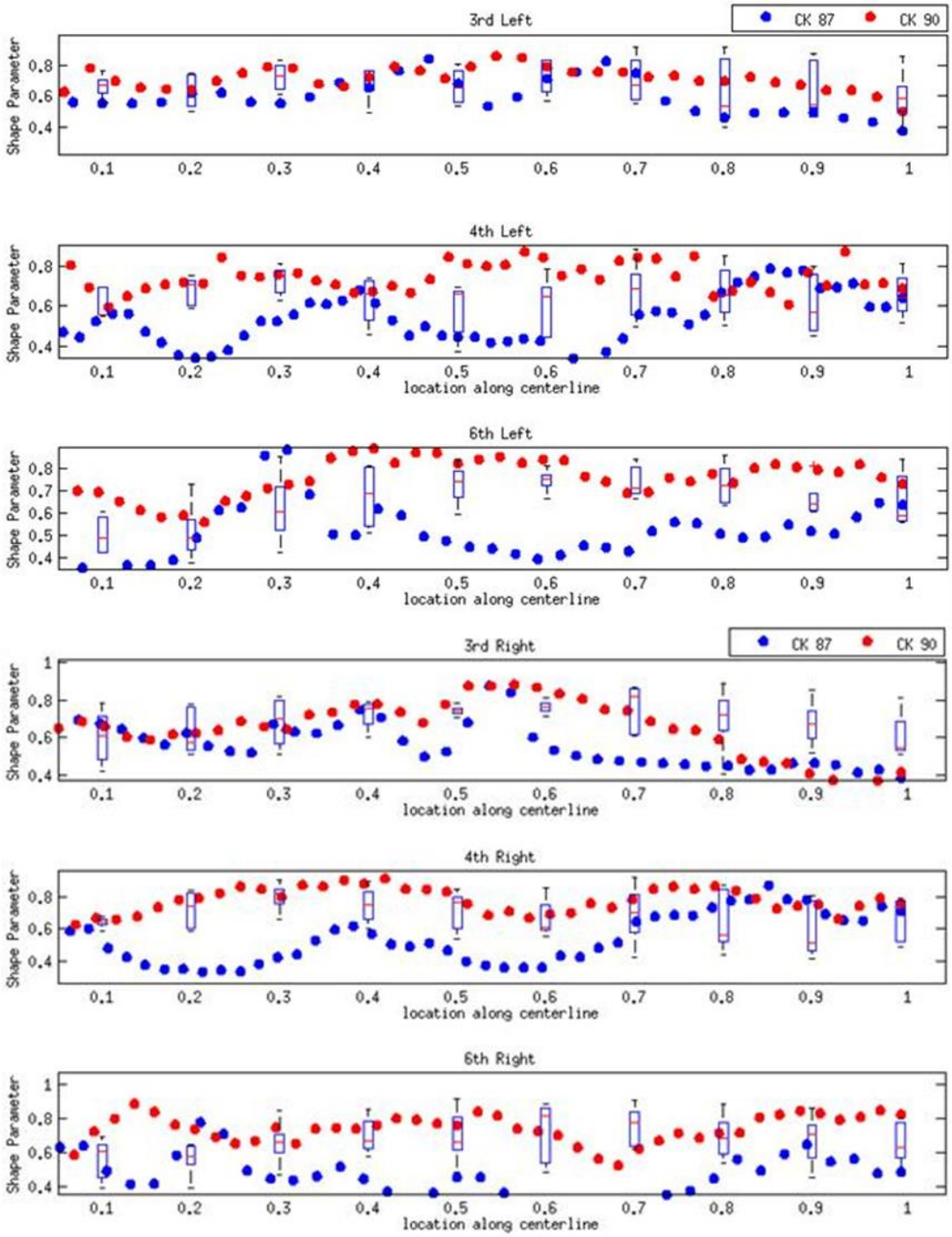

Figure A.3.6: Day 5 Shape Parameter changes for cushion ablation embryos. Boxplots represent that of day 5 control embryos.

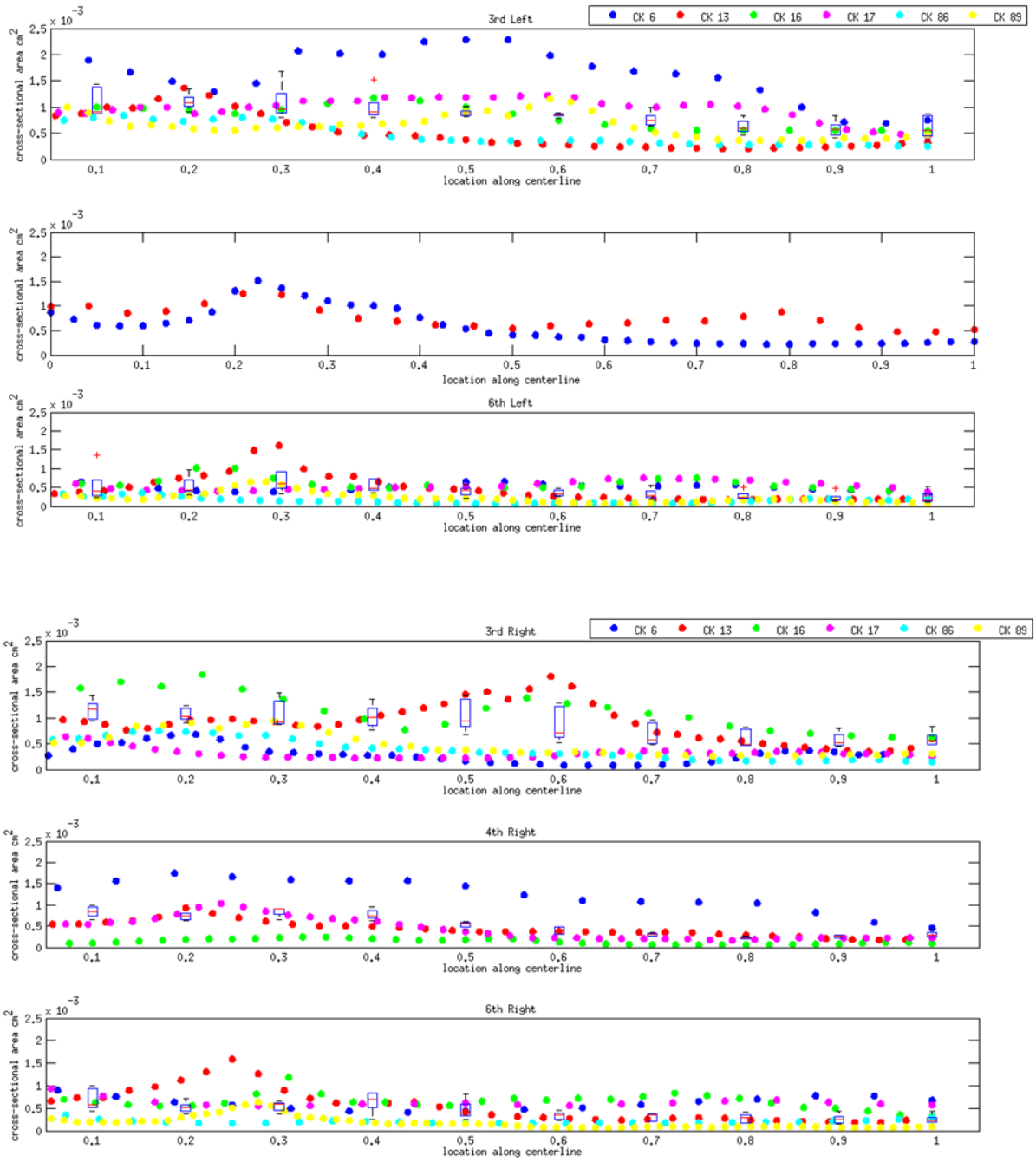

Figure A.3.7: Day 6 and Day 7 cross-sectional area changes for cushion ablation embryos.

Boxplots represent that of day 6 and day 7 control embryos.

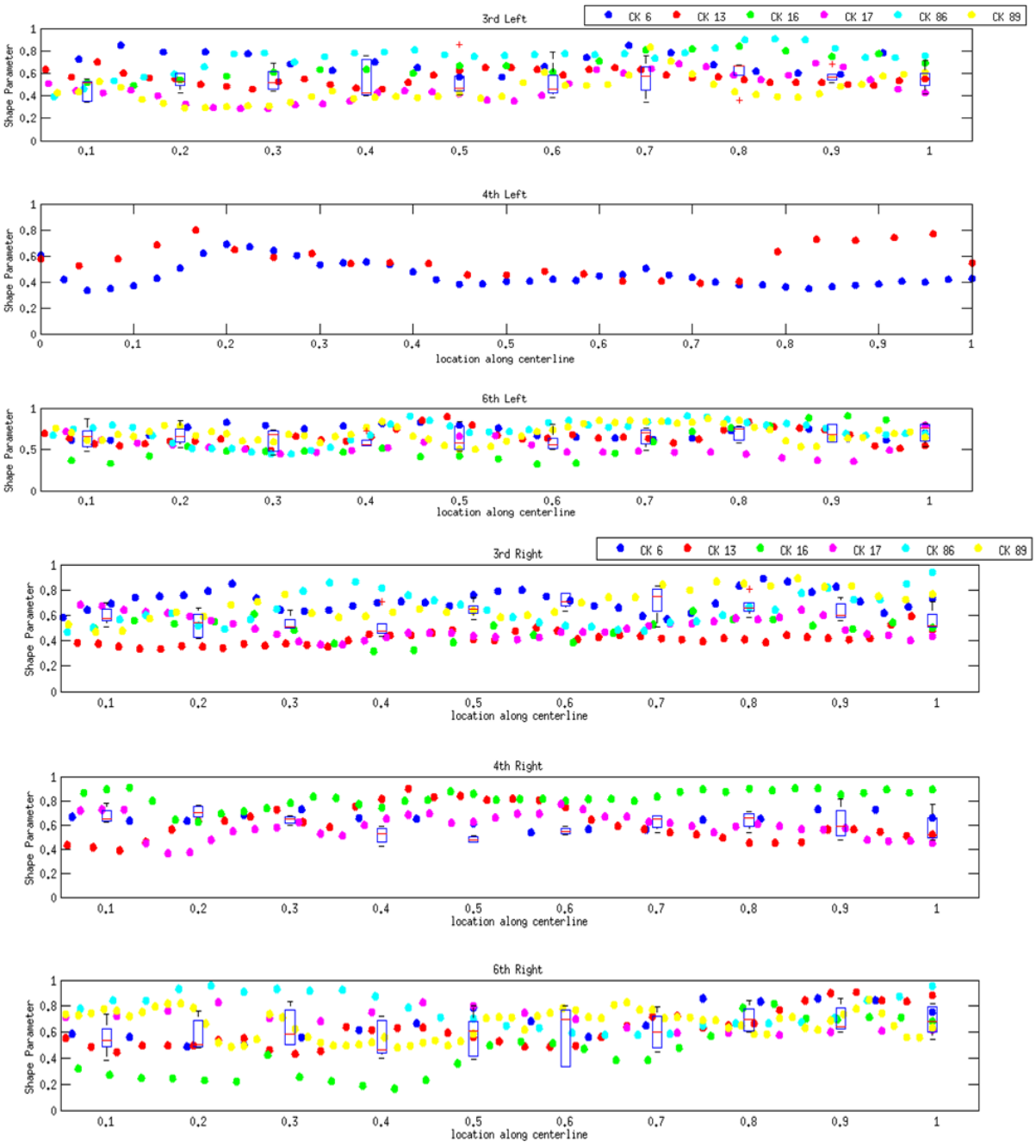

Figure A.4.8: Day 6 and Day 7 Shape Parameter changes for cushion ablation embryos.

Boxplots represent that of day 6 and day 7 control embryos.

APPENDIX B FOR PROTOCOLS AND SCRIPTS

B.1 Protocol for 3D reconstructions: MIMICS, 3MATIC, and Geomagic

MIMICS Protocol

1. Create new MIMICS file and input the image stack: File>New

Choose image stack file for import:

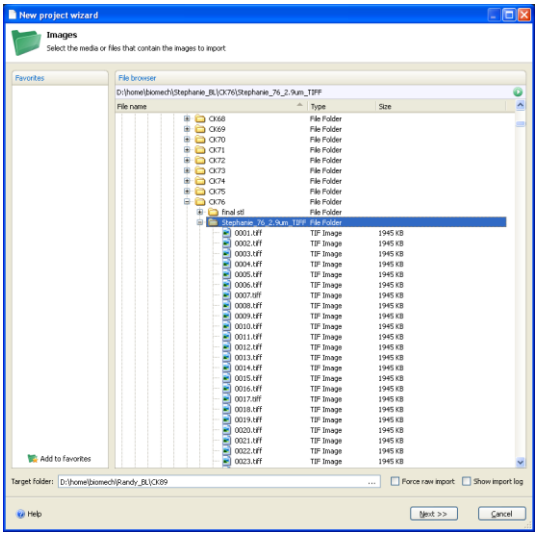

a. For DICOM images, you do not need to change the pixel dimensions.

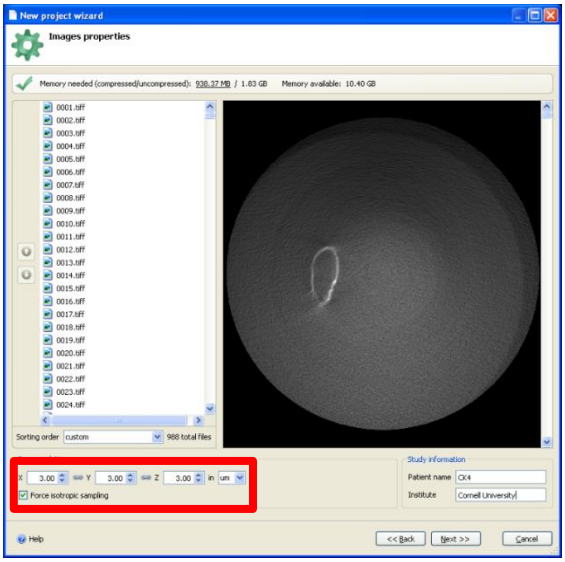

b. For TIFF image stacks, you need to input the correct pixel dimensions.

2. Create a new mask
    a. Since the mask needs to be manually created, the threshold used should

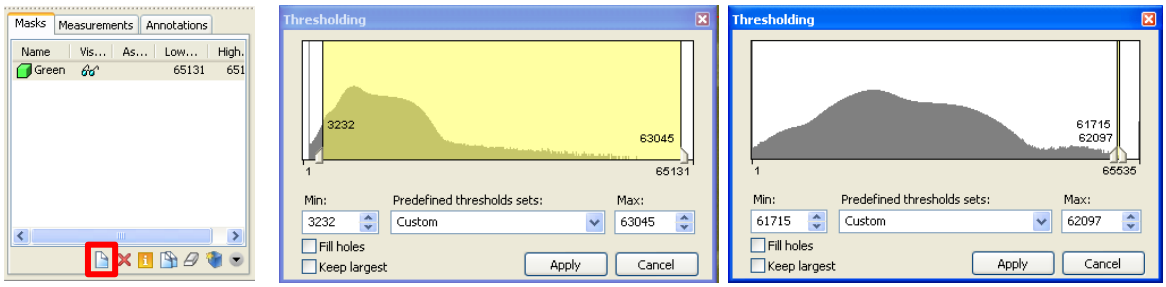

be high with a small width.

3. Edit mask
    a. Choose mask editing tool

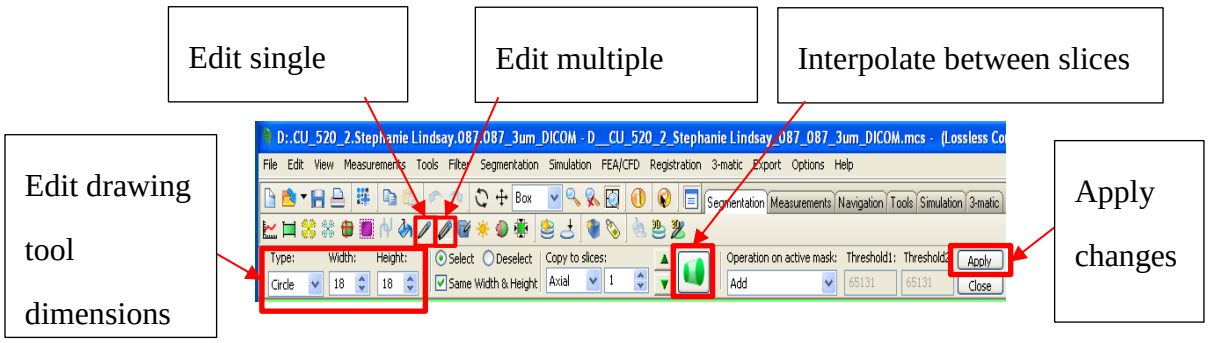

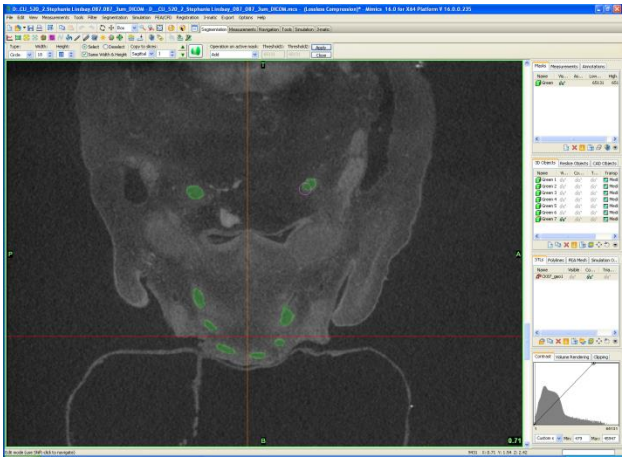

b. Use drawing tool to fill in areas to be included in the mask

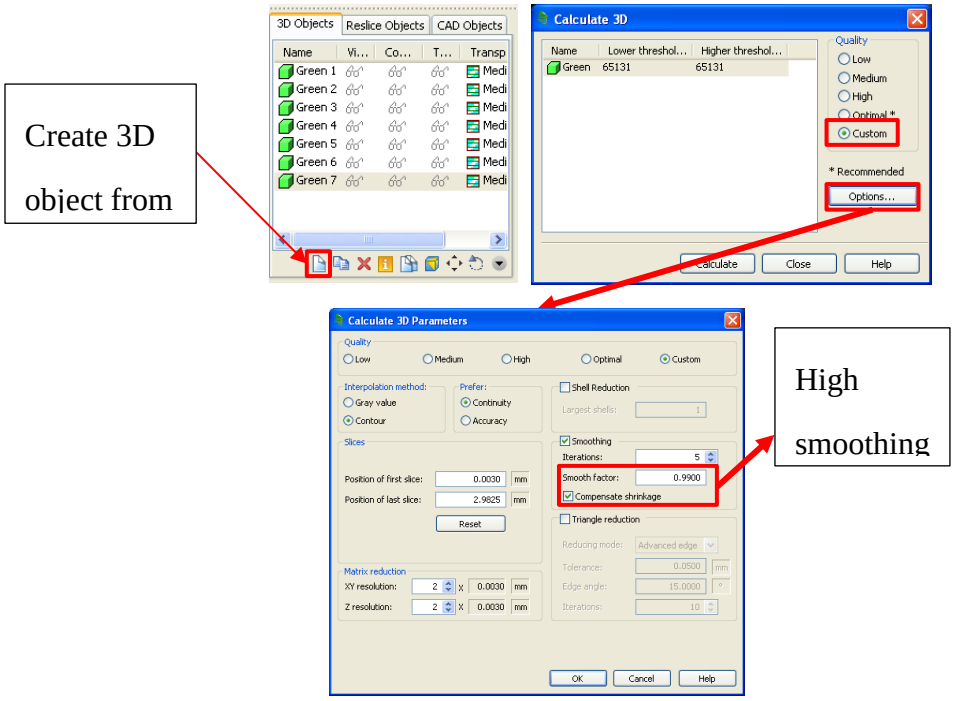

4. Convert mask to 3D object

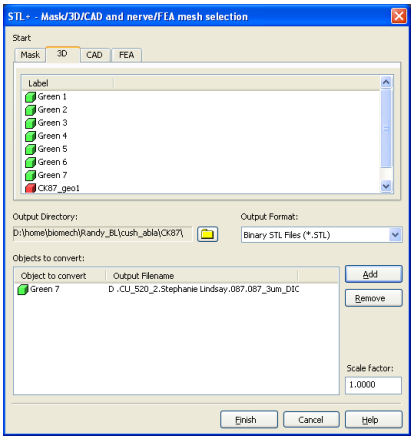

5. Output 3D geometry to .stl: File>STL+…

6. Import .stl to check sizing after smoothing in Geomagic: STLs tab> Load STL Button
    a. View .stl contours to compare against nanoCT scan: STLs tab> “Visible” and “Contour Visible” sunglasses

b. Create mask from .stl to alter it in Mimics: STLs tab> Actions Button>

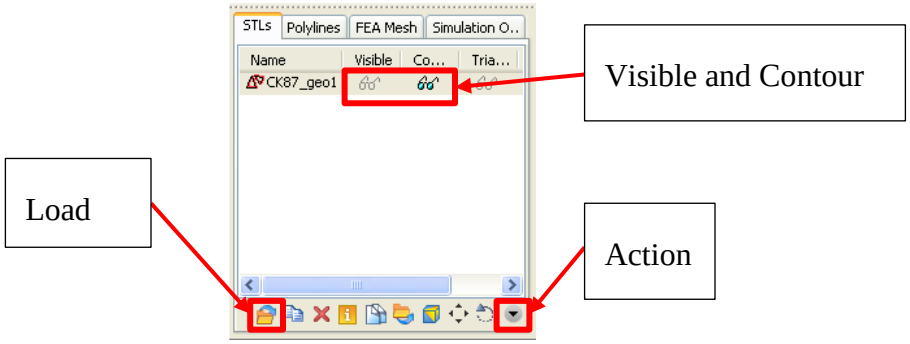

Calculate Mask from Object

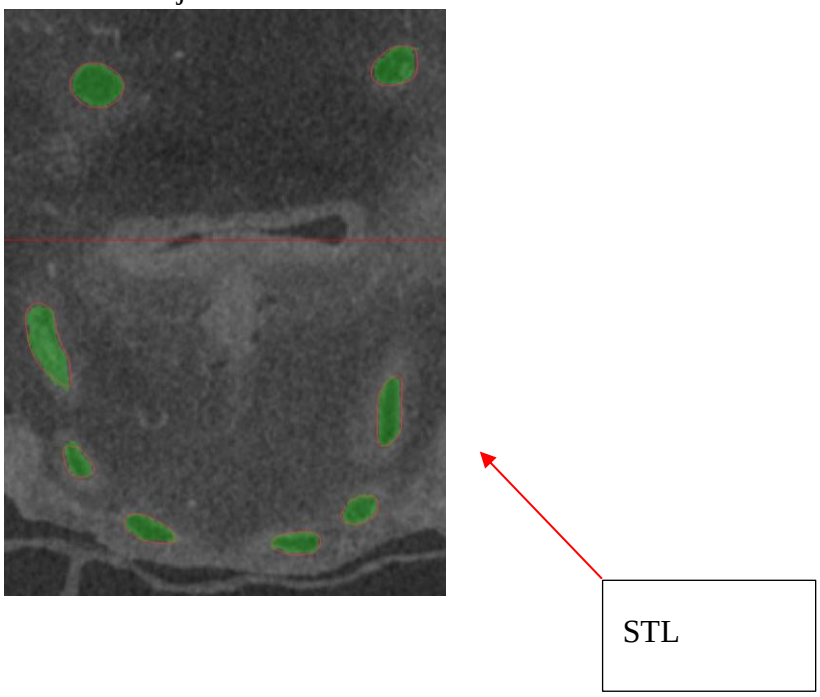

Geomagic Protocol

1. Import .stl file to be smoothed. Drag and drop or Home Button>Import
    a. Do not use Mesh Doctor
    b. Note: red areas are selected and blue areas are not selected

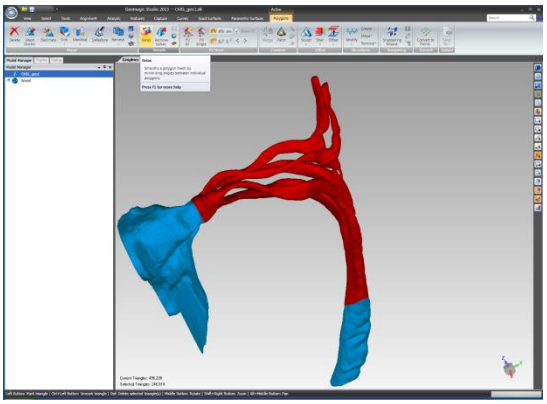

2. There are 2 main smoothing tools that were used
    a. Relax

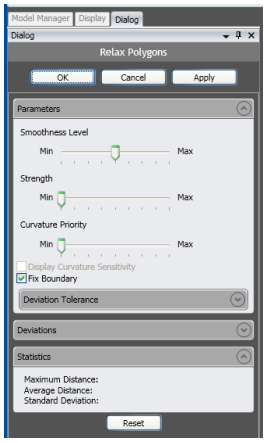

    b. Remove Spikes

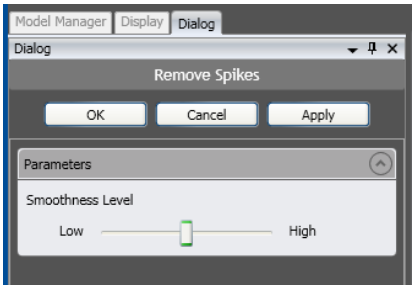

3. Filling tools fill holes in the surface that may exist

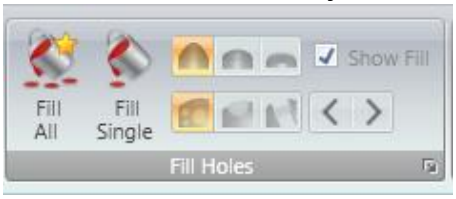

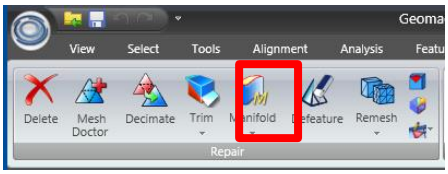

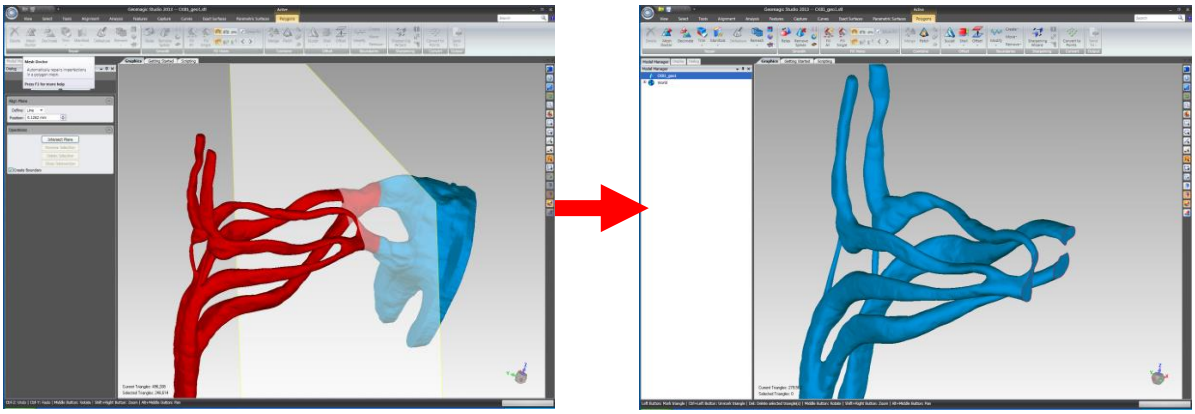

4. Trimming tool to cut geometry and form a flat surface

5. Export .stl after smoothing: Home Button>Save As (choose file type: stl)

3-MATIC Protocol

1. Import stl file to be "fixed" and scaled: Drag and Drop or File> Import Part
    a. Fix normals and split surfaces
    b. To see properties (e.g. # triangles, surface area, volume) select object

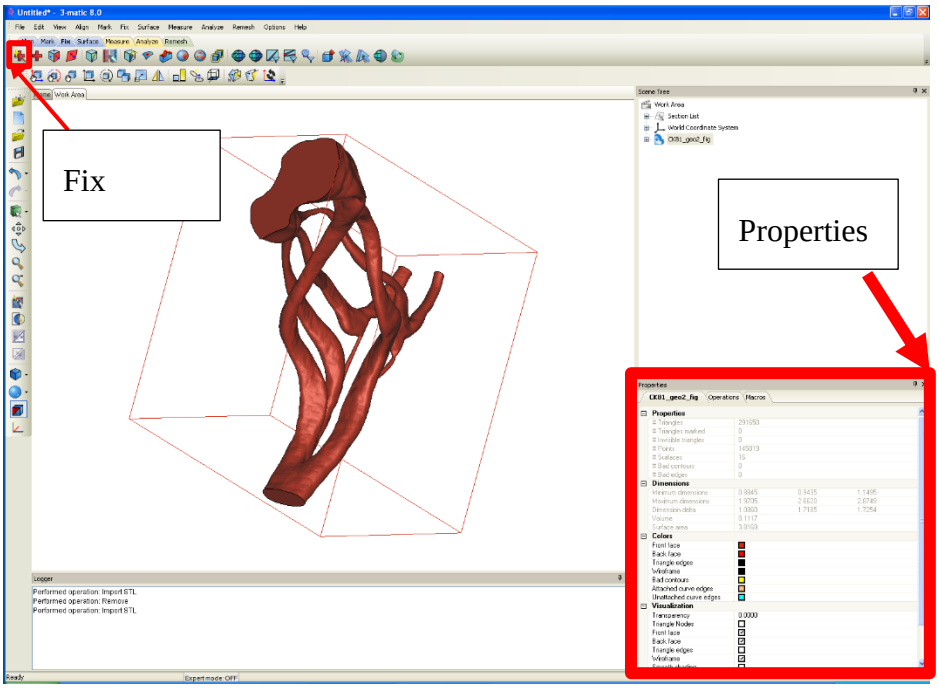

and view properties window.

2. Fix Wizard: go to fix tab and click on Fix Wizard icon (top leftmost icon, red cross with star)
    a. Follow advice given at the top of the Fix Wizard window for help

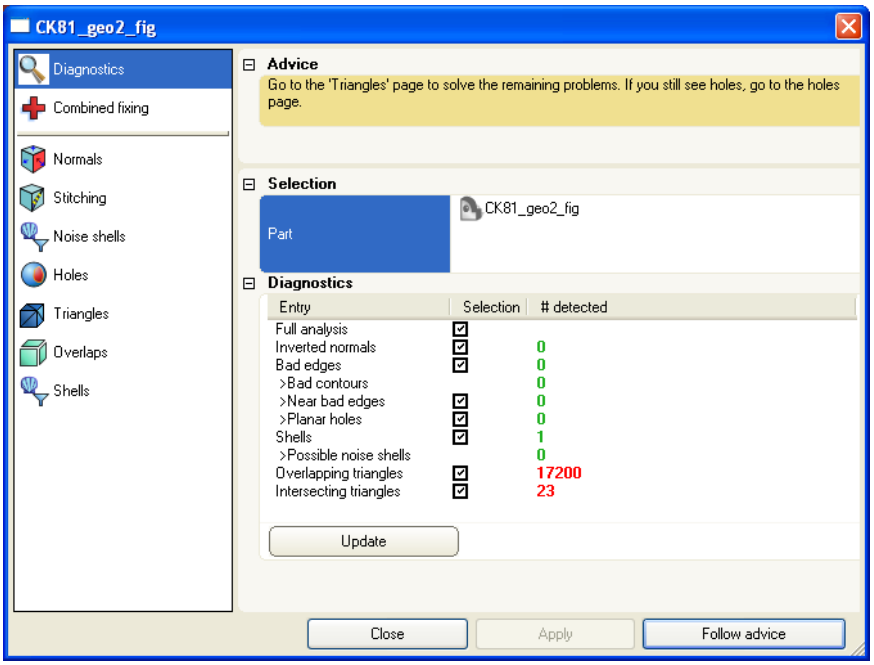

navigating the wizard

3. Export stl and do scaling: File> Export> STL
    a. Export options window

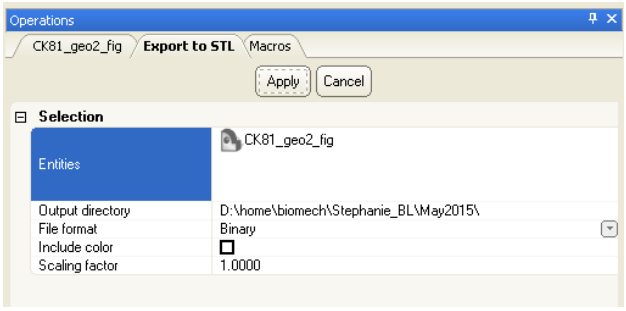

B.2 Protocol for VMTK (Vascular Modeling Tool Kit)

Because paired arch arteries are essentially loops, a clear exit for each arch must be created in order to run VMTK. Begin with the geometry below and use Geomagic to either cut the inlet (yellow) and aortic sac away from the arch entry ways or cut the dorsal aorta from the arch exits.

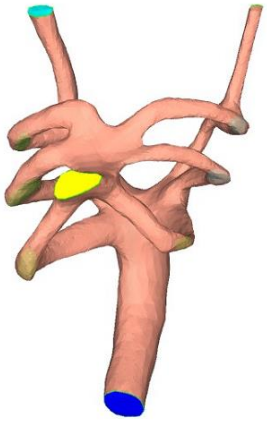

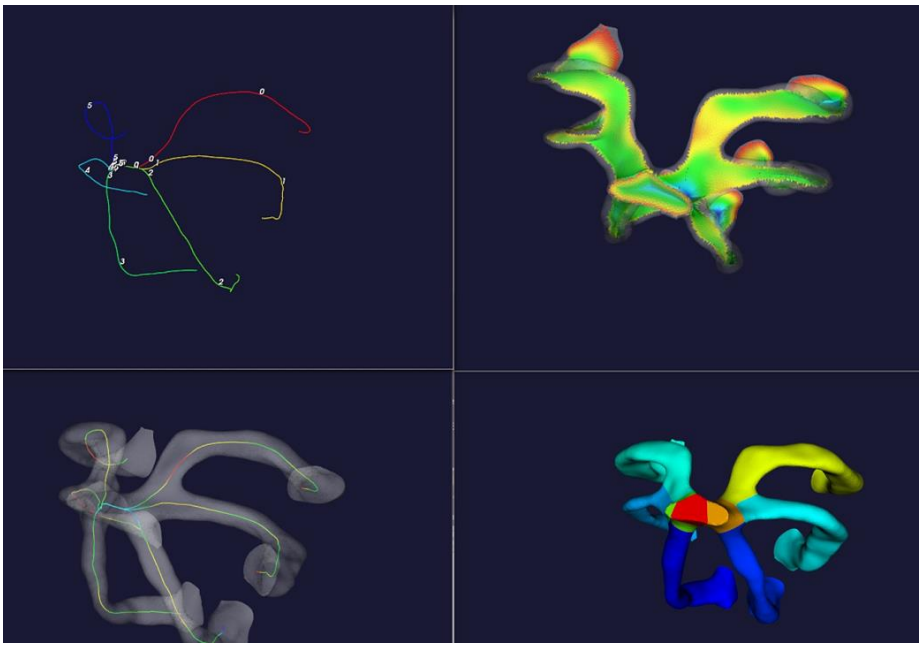

Dorsal aorta is cut above; aortic sac in example below.

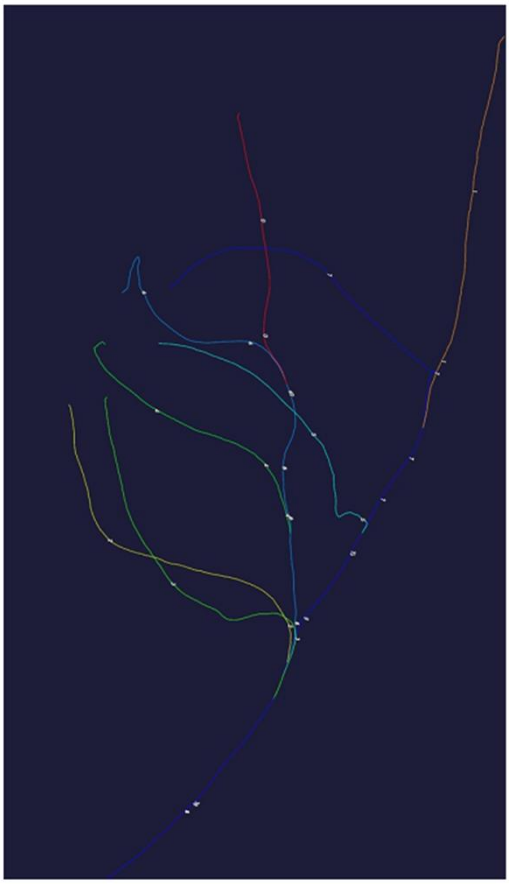

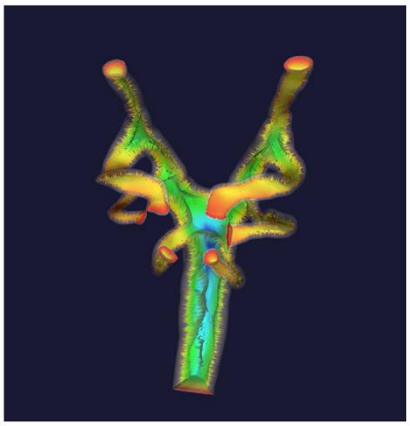

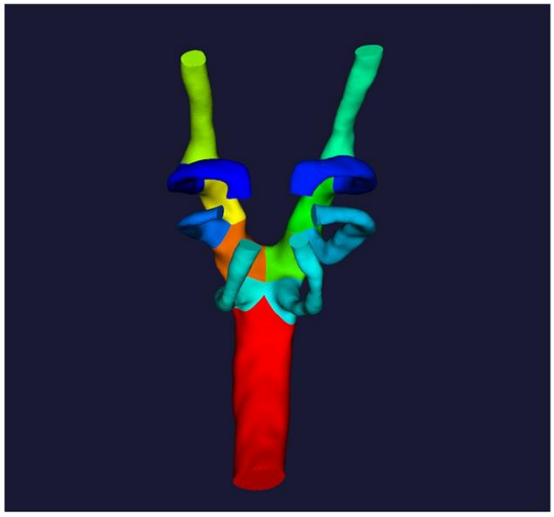

Remember to record the number of each vessel of interest. Using runvmtk.sh centerline cuts will be created along each of the arches

Runvmtk.sh:

```
# get the filenames
read -p "Enter input (.stl) filename" iName_stl
read -p "Enter vtp output filename" oName_vtp
read -p "Enter dat output filename" oName_dat
read -p "Enter txt output filename" oName_txt
read -p "Enter resampling length" rlen
# compute centerlines
vmtk vmtksurfacereader -ifile $iName_stl --pipe vmtkcenterlines --pipe
vmtkcenterlineresampling -length $rlen --pipe vmtkbranchextractor --pipe
vmtkbranchclipper --pipe vmtkbranchsections -ofile $oName_vtp --pipe
vmtksurfaceviewer -i @vmtkbranchsections.o --pipe vmtkcenterlineviewer -i
@vmtkbranchextractor.o -cellarray GroupIds
#convert to dat file
vmtk vmtksurfacewriter -ifile $oName_vtp -ofile $oName_dat -celldata 1
#convert to txt file
tail -n +2 $oName_dat > $oName_txt
```

B.3 Centerline Sections (MATLAB)

Use the following code to obtain the plain coordinates for centerline sections obtained from VMTK, so that they can be imported into Ensight.

```
close all;
clear all;

data = load('~/26b.txt');

X = data(:,1);
Y = data(:,2);
Z =  data(:,3);
GroupIds = data(:,4);
SectionMinSize = data(:,6);
SectionMaxSize = data(:,7);
c = [X,Y,Z];
l = length(c);


%%CK1  //CK26
oneR = 11;
twoR = 6;
threeR = 9;
oneL = 10;
twoL = 3;
threeL = 8;

%%
d =[X,Y,Z,GroupIds,SectionMinSize,SectionMaxSize];
[k1, k2, k3, k4, k5, k6] = deal(1);
 for p = 1:l;
    if d(p,4) == oneR
        X1(k1) = [d(p,1)];
        Y1(k1) = [d(p,2)];
        Z1(k1) = [d(p,3)];
        MinH1(k1) = [d(p,5)];
        MaxW1(k1) = [d(p,6)];
        k1 = k1 +1;
    end

    if d(p,4) == twoR
        X2(k2) = [d(p,1)];
        Y2(k2) = [d(p,2)];
        Z2(k2) = [d(p,3)];
        MinH2(k2) = [d(p,5)];
        MaxW2(k2) = [d(p,6)];
```

```
        k2 = k2 +1;
    end

    if d(p,4) == threeR
        X3(k3) = [d(p,1)];
        Y3(k3) = [d(p,2)];
        Z3(k3) = [d(p,3)];
        MinH3(k3) = [d(p,5)];
        MaxW3(k3) = [d(p,6)];
        k3 = k3 +1;
    end

    if d(p,4) == oneL
       X1b(k4) = [d(p,1)];
       Y1b(k4) = [d(p,2)];
       Z1b(k4) = [d(p,3)];
       MinH4(k4) = [d(p,5)];
       MaxW4(k4) = [d(p,6)];
        k4 = k4 +1;
    end


    if d(p,4) == twoL
        X2b(k5) = [d(p,1)];
        Y2b(k5) = [d(p,2)];
        Z2b(k5) = [d(p,3)];
        MinH5(k5) = [d(p,5)];
        MaxW5(k5) = [d(p,6)];
        k5 = k5 +1;
    end

    if d(p,4) == threeL
        X3b(k6) = [d(p,1)];
        Y3b(k6) = [d(p,2)];
        Z3b(k6) = [d(p,3)];
        MinH6(k6) = [d(p,5)];
        MaxW6(k6) = [d(p,6)];
        k6= k6 +1;
    end


 end
%% calculating length each arch


dR1 = (length(X1) -1) * 0.001;
dR2 = (length(X2) -1) * 0.001;
dR3 = (length(X3) -1 ) * 0.001;
dL1 = (length(X1b) -1 ) * 0.001;
dL2 =(length(X2b) -1 ) * 0.001;
```

```
dL3 =(length(X3b) -1 ) * 0.001;

archdimens = [dR1;dR2;dR3;dL1;dL2;dL3]

%% smoothing X,Y,Z
sx1 = fastsmooth(X1,3,3,1);
sy1 = fastsmooth(Y1,3,3,1);
sz1 = fastsmooth(Z1,3,3,1);

sx2 = fastsmooth(X2,3,3,1);
sy2 = fastsmooth(Y2,3,3,1);
sz2 = fastsmooth(Z2,3,3,1);

sx3 = fastsmooth(X3,3,3,1);
sy3 = fastsmooth(Y3,3,3,1);
sz3 = fastsmooth(Z3,3,3,1);

sx4 = fastsmooth(X1b,3,3,1);
sy4 = fastsmooth(Y1b,3,3,1);
sz4 = fastsmooth(Z1b,3,3,1);

sx5 = fastsmooth(X2b,3,3,1);
sy5 = fastsmooth(Y2b,3,3,1);
sz5 = fastsmooth(Z2b,3,3,1);

sx6 = fastsmooth(X3b,3,3,1);
sy6 = fastsmooth(Y3b,3,3,1);
sz6 = fastsmooth(Z3b,3,3,1);

sx = [sx1, sx2, sx3, sx4, sx5, sx6];
sy = [sy1, sy2, sy3, sy4, sy5, sy6];
sz = [sz1, sz2, sz3, sz4, sz5, sz6];

MinHa = [MinH1, MinH2, MinH3, MinH4, MinH5, MinH6];
MaxWb = [MaxW1, MaxW2, MaxW3, MaxW4, MaxW5, MaxW6];



%% condensing X,Y,Z

% taking everyother element of array
n =2;
rx = sx(1:n:end);
ry = sy(1:n:end);
rz = sz(1:n:end);
MinH = MinHa(1:n:end);
MaxW = MaxWb(1:n:end);
MinH = MinH'; MaxW = MaxW';
r = [rx; ry; rz];
```

```
r = r';
lr = length(r);

figure;
plot3(X,Y,Z,'*b')
hold on
plot3(sx,sy,sz,'*m')
hold on
plot3(rx,ry,rz,'*g')
hold on



%% calculating tangent slope & unit vector

p = 0;
i =2;
%ij = 1;

for p = 1:lr -1;
A1 = r(i,:);
A2 = r(i-1,:);

sD(i,:) = bsxfun(@minus,A1,A2).^2;

dx= sqrt(sD(:,1)); dy= sqrt(sD(:,2)); dz= sqrt(sD(:,3));
DS(i) = sqrt(sum(sD(:)));

xh(i)= (rx(i) - rx(i-1))/dx(i,1);
yh(i)= (ry(i) - ry(i-1))/dx(i,1);
zh(i)= (rz(i) - rz(i-1))/dx(i,1);

i = i +1;
%ij = ij +1;

end
rx = rx'; ry = ry'; rz = rz';
T = [xh;yh;zh];
T = T';
normT = sqrt(T(:,1).^2+T(:,2).^2+T(:,3).^2);
T(:,1) = T(:,1)./normT; T(:,2) = T(:,2)./normT; T(:,3) =
T(:,3)./normT;
T(1,1)= 0; T(1,2)= 0; T(1,3)= 0;

quiver3(rx,ry,rz,T(:,1),T(:,2),T(:,3))
hold on

%% calculating Normal N = dT/dS
```

```
s = 0;
tx = T(:,1); ty = T(:,2); tz = T(:,3);
i2 = 2;
for s = 1:lr -1

xn(i2)= (tx(i2) - tx(i2-1))./DS(i2);
yn(i2)= (ty(i2) - ty(i2-1))./DS(i2);
zn(i2)= (tz(i2) - tz(i2-1))./DS(i2);

i2 = i2 +1;

end
N = [xn;yn;zn];
N = N';
normN = sqrt(N(:,1).^2+N(:,2).^2+N(:,3).^2);
N(:,1) = N(:,1)./normN; N(:,2) = N(:,2)./normN; N(:,3) =
N(:,3)./normN;
N(1,1)= 0; N(1,2)= 0; N(1,3)= 0;

quiver3(rx,ry,rz,N(:,1),N(:,2),N(:,3))
hold off

%% radius of curvature: |ds/dT|
    %for subsequent calculations
 radiuscurvature = 1./normN;

 AreaCond = pi .* MaxW .* MinH;
 r_avCond = sqrt(AreaCond ./pi);
 dav = r_avCond ./radiuscurvature;

 dmin = MaxW ./radiuscurvature;
 dmax = MinH ./radiuscurvature;

R_filename = 'radiusofcurvature.txt';
R_fileID = fopen(R_filename, 'w');

fprintf(R_fileID,'%6s %12s\n','A','a/R');

 for i6=1:length(radiuscurvature)

        fprintf(R_fileID, '%1.8f  ',AreaCond(i6));
        fprintf(R_fileID, '%1.8f\n', radiuscurvature(i6));

 end


%% equations of planes
% i3 =1;
% syms x y z
```

```
% realdot = @(u, v) u*transpose(v); %% to get real of the
complex conjugates matlab calculates.
%
% for t=1:lr-1
% P0(i3,:) = T(i3+1,:);
% P = [x,y,z]; t =0;
% %PoP = bsxfun(@minus,P,P0);
% Planef(i3) = realdot(P-P0(i3),N(i3 +1,:))
% i3 = i3+1;
% end

%% extracting corner coordinates

vec2 = cross(N,T);
vec1 = N;
i4 =1;
sr =0;
d1 = 2.6 * max(MaxW); %2.6
d2 = 4.5 * max(MinH); %from 6
for sr =1:lr-1

C1(i4, :) = r(i4, :) + d1/(2) *vec1(i4, :);
C2(i4, :) = r(i4, :) - d2/(2) *vec2(i4, :);
C3(i4, :) = r(i4, :) - d1/(2) *vec1(i4, :);
%C3(i4, :) = r(i4, :) + d2/(2) *vec2(i4, :);

% C1(i4, :) = r(i4, :) + (d1/2) *vec2(i4, :) + (d2/2) *
vec1(i4, :);
% C2(i4, :) = r(i4, :) - (d1/2) *vec2(i4, :) - (d2/2) *
vec1(i4, :);
% C3(i4, :) = r(i4, :) - (d1/2) *vec2(i4, :) + (d2/2) *
vec1(i4, :);

i4 = i4 +1;

end

%% printing planes corners to file (ensight format)
    % part: select_begin
    % 2
    % part: select_end
    % clip: begin
    % clip: tool plane
    % clip: plane_extents finite
    % clip: plane 1 -1 -1 0
    % clip: plane 2 1 -1 0
    % clip: plane 3 1 1 0
    % clip: end
    % clip: create
```

```
filename = 'planecoordinates.txt';
fileID = fopen(filename, 'w');



 for i6=1:length(C1)

     formatSpec1 = ' clip: plane 1 %5.4f %5.4f %5.4f \n';
     formatSpec2 = ' clip: plane 2 %5.4f %5.4f %5.4f \n';
     formatSpec3 = ' clip: plane 3 %5.4f %5.4f %5.4f \n';

     fprintf(fileID,'part: select_begin \n 1 \n part:
select_end \n clip: begin \n clip: tool plane \n clip:
plane_extents finite \n');
     fprintf(fileID,formatSpec1,C1(i6,:));
     fprintf(fileID,formatSpec2,C2(i6,:));
     fprintf(fileID,formatSpec3,C3(i6,:));
     fprintf(fileID,' clip: end \n clip: create \n');
     fprintf(fileID,'\n');

     i6 = i6 + 1;

end
```

%%Matlab will output a graph that shows the normal and tangents

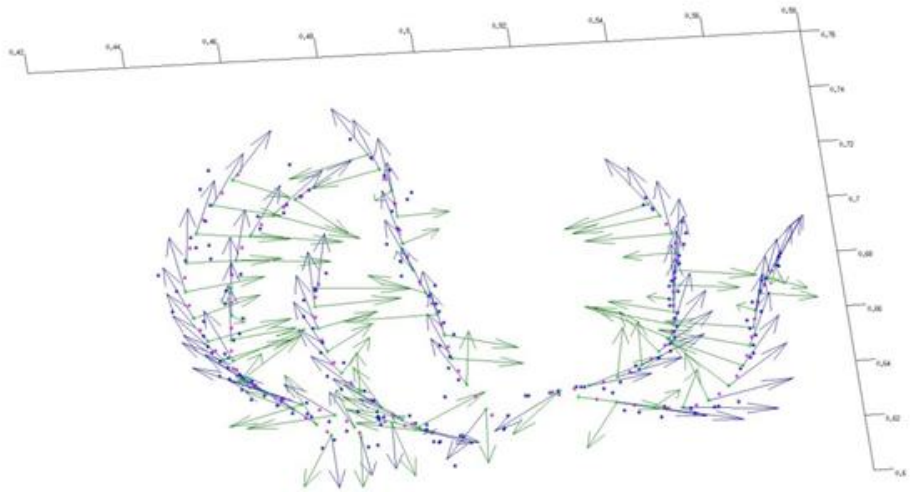

B.4 Pressure-Volume Code (MATLAB)

```
close all;

clear all;

data = load('/home/steph/Documents/FluidProps/d3_RePVelD.txt');
data2 =
load('/home/steph/Documents/FluidProps/d3_RePVelD2.txt');
data3 =
load('/home/steph/Documents/FluidProps/d3_RePVelD3.txt');
data4 =
load('/home/steph/Documents/FluidProps/d3_RePVelD4.txt');
data5 =
load('/home/steph/Documents/FluidProps/d3_RePVelD5.txt');

c26Re = data(:,1);
c26P = data(:,2);
c26MaxVel =  data(:,3);
c26DeanN = data(:,4);
c26A = data(:,5); %Area
c72Re = data2(:,1);
c72P = data2(:,2);
c72MaxVel =  data2(:,3);
c72DeanN = data2(:,4);
c72A = data2(:,5); %Area
c75Re = data3(:,1);
c75P = data3(:,2);
c75MaxVel =  data3(:,3);
c75DeanN = data3(:,4);
c75A = data3(:,5); %Area
c76Re = data4(:,1);
c76P = data4(:,2);
c76MaxVel =  data4(:,3);
c76DeanN = data4(:,4);
c76A = data4(:,5); %Area
c85Re = data5(:,1);
c85P = data5(:,2);
c85MaxVel =  data5(:,3);
c85DeanN = data5(:,4);
c85A = data5(:,5); %Area
%%

L26 = [0.0560    0.0150    0.0250    0.0470    0.0160
0.0250];
L72 = [0.0340    0.0130    0.0220    0.0290    0.0130
0.0200];
L75 = [0.0260    0.0110    0.0200    0.0240    0.0100
0.0190];
```

```
L76 = [0.0360    0.0100    0.0240    0.0430    0.0080
0.0220];
L85 = [0.0320    0.0090    0.0190    0.0320    0.0090
0.0160];

%%
c261R_A = c26A(3:27);
c262R_A = c26A(28:34);
c263R_A = c26A(35:48);
c261L_A = c26A(49:72);
c262L_A = [c26A(73:79);c26A(1);];
c263L_A = [c26A(80:90);c26A(2);];

c261R_P = c26P(3:27);
c262R_P = c26P(28:34);
c263R_P = c26P(35:48);
c261L_P = c26P(49:72);
c262L_P = [c26P(73:79);c26P(1);];
c263L_P = [c26P(80:90);c26P(2);];


dx261R = L26(1)/(length(c261R_P) -1 );
dx262R = L26(2)/(length(c262R_P) -1 );
dx263R = L26(3)/(length(c263R_P) -1 );
dx261L = L26(4)/(length(c261L_P) -1 );
dx262L = L26(5)/(length(c262L_P) -1 );
dx263L = L26(6)/(length(c263L_P) -1 );

%%

c721R_A = [c72A(1:16);c72A(35);c72A(51)];
c722R_A = [c72A(17);c72A(19:23)];
c723R_A = c72A(25:34);
c721L_A = c72A(36:49);
c722L_A = [c72A(50);c72A(52:56);c72A(67)];
c723L_A = [c72A(57:66);c72A(68)];

c721R_P = [c72P(1:16);c72P(35);c72P(51)];
c722R_P = [c72P(17);c72P(19:23)];
c723R_P = c72P(25:34);
c721L_P = c72P(36:49);
c722L_P = [c72P(50);c72P(52:56);c72P(67)];
c723L_P = [c72P(57:66);c72P(68)];

dx721R = L72(1)/(length(c721R_P) -1 );
dx722R = L72(2)/(length(c722R_P) -1 );
dx723R = L72(3)/(length(c723R_P) -1 );
dx721L = L72(4)/(length(c721L_P) -1 );
dx722L = L72(5)/(length(c722L_P) -1 );
dx723L = L72(6)/(length(c723L_P) -1 );
```

```
%%

c751R_A = [c75A(2:12);c75A(20)];
c752R_A = [c75A(13);c75A(15:18)];
c753R_A = [c75A(19);c75A(21:28);c75A(14)];
c751L_A = c75A(30:41);
c752L_A = [c75A(42);c75A(44:45);c75A(56)];
c753L_A = [c75A(47:55);c75A(57)];

c751R_P = [c75P(2:12);c75P(20)];
c752R_P = [c75P(13);c75P(15:18)];
c753R_P = [c75P(19);c75P(21:28);c75P(14)];
c751L_P = c75P(30:41);
c752L_P = [c75P(42);c75P(44:45);c75P(56)];
c753L_P = [c75P(47:55);c75P(57)];

dx751R = L75(1)/(length(c751R_P) -1 );
dx752R = L75(2)/(length(c752R_P) -1 );
dx753R = L75(3)/(length(c753R_P) -1 );
dx751L = L75(4)/(length(c751L_P) -1 );
dx752L = L75(5)/(length(c752L_P) -1 );
dx753L = L75(6)/(length(c753L_P) -1 );


%%

c761R_A = c76A(2:17);
c762R_A = [c76A(18);c76A(20:22)];
c763R_A = c76A(24:35);
c761L_A = c76A(39:57);
c762L_A = [c76A(1);c76A(60:61);c76A(73);c76A(74)];
c763L_A = c76A(63:72);

c761R_P = c76P(2:17);
c762R_P = [c76P(18);c76P(20:22)];
c763R_P = c76P(24:35);
c761L_P = c76P(39:57);
c762L_P = [c76P(1);c76P(60:61);c76P(73);c76P(74)];
c763L_P = c76P(63:72);

dx761R = L76(1)/(length(c761R_P) -1 );
dx762R = L76(2)/(length(c762R_P) -1 );
dx763R = L76(3)/(length(c763R_P) -1 );
dx761L = L76(4)/(length(c761L_P) -1 );
dx762L = L76(5)/(length(c762L_P) -1 );
dx763L = L76(6)/(length(c763L_P) -1 );
```

```
%%

c851R_A = c85A(2:15);
c852R_A = [c85A(16:20);c85A(55);c85A(56)];
c853R_A = c85A(21:29);
c851L_A = c85A(30:43);
c852L_A = [c85A(44:48);c85A(2)];
c853L_A = c85A(49:54);

c851R_P = c85P(2:15);
c852R_P = [c85P(16:20);c85P(55);c85P(56)];
c853R_P = c85P(21:29);
c851L_P = c85P(30:43);
c852L_P = [c85P(44:48);c85P(2)];
c853L_P = c85P(49:54);

dx851R = L85(1)/(length(c851R_P) -1 );
dx852R = L85(2)/(length(c852R_P) -1 );
dx853R = L85(3)/(length(c853R_P) -1 );
dx851L = L85(4)/(length(c851L_P) -1 );
dx852L = L85(5)/(length(c852L_P) -1 );
dx853L = L85(6)/(length(c853L_P) -1 );


%% CK26


%%Volume Calculation
i = 2;
for i = 2:length(c261R_P)
V1R_c26(i-1) = ((c261R_A(i) + c261R_A(i-1)))/2 * dx261R;
i = i +1;
end
i = 2;
for i = 2:length(c262R_P)
V2R_c26(i-1) = ((c262R_A(i) + c262R_A(i-1)))/2 * dx262R;
i = i +1;
end
i = 2;
for i = 2:length(c263R_P)
V3R_c26(i-1) = ((c263R_A(i) + c263R_A(i-1)))/2 * dx263R;
i = i +1;
end
i = 2;
for i = 2:length(c261L_P)
V1L_c26(i-1) = ((c261L_A(i) + c261L_A(i-1)))/2 * dx261L;
i = i +1;
end
```

```
i = 2;
for i = 2:length(c262L_P)
V2L_c26(i-1) = ((c262L_A(i) + c262L_A(i-1)))/2 * dx262L;
i = i +1;
end
i = 2;
for i = 2:length(c263L_P)
V3L_c26(i-1) = ((c263L_A(i) + c263L_A(i-1)))/2 * dx263L;

i = i +1;
end


%%ten sections along arch

%%Pressure

c261R_P =c261R_P';

if length(c261R_P) <= 10
        i = length(c261R_P);
        c261R_Pav10 = c261R_P;
        while i < 10
            c261R_Pav10 = [c261R_Pav10
c261R_P(length(c261R_P))];
            i = i + 1;
        end
        c261R_Pav10 = c261R_Pav10';
    else
        c261R_PavD = floor(linspace(1, length(c261R_P), 10));
        c261R_Pfs = fastsmooth(c261R_P', (c261R_PavD(2) - 1),
3, 1);
        c261R_Pav10 = c261R_Pfs(c261R_PavD);
end

c262R_P =c262R_P';

if length(c262R_P) <= 10
        i = length(c262R_P);
        c262R_Pav10 = c262R_P;
        while i < 10
            c262R_Pav10 = [c262R_Pav10
c262R_P(length(c262R_P))];
            i = i + 1;
        end
        c262R_Pav10 = c262R_Pav10';
    else
        c262R_PavD = floor(linspace(1, length(c262R_P), 10));
        c262R_Pfs = fastsmooth(c262R_P', (c262R_PavD(2) - 1),
3, 1);
```

```
        c262R_Pav10 = c262R_Pfs(c262R_PavD);
end

c263R_P =c263R_P';

if length(c263R_P) <= 10
        i = length(c263R_P);
        c263R_Pav10 = c263R_P;
        while i < 10
            c263R_Pav10 = [c263R_Pav10
c263R_P(length(c263R_P))];
            i = i + 1;
        end
        c263R_Pav10 = c263R_Pav10';
    else
        c263R_PavD = floor(linspace(1, length(c263R_P), 10));
        c263R_Pfs = fastsmooth(c263R_P', (c263R_PavD(2) - 1),
3, 1);
        c263R_Pav10 = c263R_Pfs(c263R_PavD);
end

c261L_P =c261L_P';

if length(c261L_P) <= 10
        i = length(c261L_P);
        c261L_Pav10 = c261L_P;
        while i < 10
            c261L_Pav10 = [c261L_Pav10
c261L_P(length(c261L_P))];
            i = i + 1;
        end
        c261L_Pav10 = c261L_Pav10';
    else
        c261L_PavD = floor(linspace(1, length(c261L_P), 10));
        c261L_Pfs = fastsmooth(c261L_P', (c261L_PavD(2) - 1),
3, 1);
        c261L_Pav10 = c261L_Pfs(c261L_PavD);
end

c262L_P =c262L_P';

if length(c262L_P) <= 10
        i = length(c262L_P);
        c262L_Pav10 = c262L_P;
        while i < 10
            c262L_Pav10 = [c262L_Pav10
c262L_P(length(c262L_P))];
            i = i + 1;
        end
        c262L_Pav10 = c262L_Pav10';
```

```
    else
        c262L_PavD = floor(linspace(1, length(c262L_P), 10));
        c262L_Pfs = fastsmooth(c262L_P', (c262L_PavD(2) - 1),
3, 1);
        c262L_Pav10 = c262L_Pfs(c262L_PavD);
end

c263L_P =c263L_P';

if length(c263L_P) <= 10
        i = length(c263L_P);
        c263L_Pav10 = c263L_P;
        while i < 10
            c263L_Pav10 = [c263L_Pav10
c263L_P(length(c263L_P))];
            i = i + 1;
        end
        c263L_Pav10 = c263L_Pav10';
    else
        c263L_PavD = floor(linspace(1, length(c263L_P), 10));
        c263L_Pfs = fastsmooth(c263L_P', (c263L_PavD(2) - 1),
3, 1);
        c263L_Pav10 = c263L_Pfs(c263L_PavD);
end

%%Volume

if length(V1R_c26) <= 10
        i = length(V1R_c26);
        V1R_c26av10 = V1R_c26;
        while i < 10
            V1R_c26av10 = [V1R_c26av10
V1R_c26(length(V1R_c26))];
            i = i + 1;
        end
        V1R_c26av10 = V1R_c26av10';
    else
        V1R_c26avD = floor(linspace(1, length(V1R_c26), 10));
        V1R_c26fs = fastsmooth(V1R_c26', (V1R_c26avD(2) - 1),
3, 1);
        V1R_c26av10 = V1R_c26fs(V1R_c26avD);
end

if length(V2R_c26) <= 10
        i = length(V2R_c26);
        V2R_c26av10 = V2R_c26;
        while i < 10
            V2R_c26av10 = [V2R_c26av10
V2R_c26(length(V2R_c26))];
            i = i + 1;
```

```
        end
        V2R_c26av10 = V2R_c26av10';
    else
        V2R_c26avD = floor(linspace(1, length(V2R_c26), 10));
        V2R_c26fs = fastsmooth(V2R_c26', (V2R_c26avD(2) - 1),
3, 1);
        V2R_c26av10 = V2R_c26fs(V2R_c26avD);
end

if length(V3R_c26) <= 10
        i = length(V3R_c26);
        V3R_c26av10 = V3R_c26;
        while i < 10
            V3R_c26av10 = [V3R_c26av10
V3R_c26(length(V3R_c26))];
            i = i + 1;
        end
        V3R_c26av10 = V3R_c26av10';
    else
        V3R_c26avD = floor(linspace(1, length(V3R_c26), 10));
        V3R_c26fs = fastsmooth(V3R_c26', (V3R_c26avD(2) - 1),
3, 1);
        V3R_c26av10 = V3R_c26fs(V3R_c26avD);
end

if length(V1L_c26) <= 10
        i = length(V1L_c26);
        V1L_c26av10 = V1L_c26;
        while i < 10
            V1L_c26av10 = [V1L_c26av10
V1L_c26(length(V1L_c26))];
            i = i + 1;
        end
        V1L_c26av10 = V1L_c26av10';
    else
        V1L_c26avD = floor(linspace(1, length(V1L_c26), 10));
        V1L_c26fs = fastsmooth(V1L_c26', (V1L_c26avD(2) - 1),
3, 1);
        V1L_c26av10 = V1L_c26fs(V1L_c26avD);
end

if length(V2L_c26) <= 10
        i = length(V2L_c26);
        V2L_c26av10 = V2L_c26;
        while i < 10
            V2L_c26av10 = [V2L_c26av10
V2L_c26(length(V2L_c26))];
            i = i + 1;
        end
        V2L_c26av10 = V2L_c26av10';
```

```
    else
        V2L_c26avD = floor(linspace(1, length(V2L_c26), 10));
        V2L_c26fs = fastsmooth(V2L_c26', (V2L_c26avD(2) - 1),
3, 1);
        V2L_c26av10 = V2L_c26fs(V2L_c26avD);
end

if length(V3L_c26) <= 10
        i = length(V3L_c26);
        V3L_c26av10 = V3L_c26;
        while i < 10
            V3L_c26av10 = [V3L_c26av10
V3L_c26(length(V3L_c26))];
            i = i + 1;
        end
        V3L_c26av10 = V3L_c26av10';
    else
        V3L_c26avD = floor(linspace(1, length(V3L_c26), 10));
        V3L_c26fs = fastsmooth(V3L_c26', (V3L_c26avD(2) - 1),
3, 1);
        V3L_c26av10 = V3L_c26fs(V3L_c26avD);
end



%%The same pressure volume calculations that were made for CK26
are subsequently repeated for the remaining four embryos, with
only 'c26' changing.
```

B.5 IDA Lumped Parameter Code

Below is the main source file for a day 3 or day 4 circuit.

```
/*
 * -----------------------------------------------------------------
-----
 *
  Author:SEL
  Early Chick Circulaiton: A simplified model
 * -----------------------------------------------------------------
-----

       P_OA - P_DA = Q_da * R_4
       P_DA - P_C= L* dQ_da/dt
          P_C- P_OUT= R5 * Q_R5

       dP_C/dt - dP_OUT/dt = Q_C * (1/C)

       Q_da = Q_C + Q_R5


 with initial conditions: Q_A; P_OUT


 */

#include <stdio.h>
#include <math.h>
#include <ida/ida.h>
#include <ida/ida_dense.h>
#include <nvector/nvector_serial.h>
#include <sundials/sundials_math.h>
#include <sundials/sundials_types.h>

#include "Interp_ArchA.h"
#include "spline.h"
#include "constants.h"

/* Prototypes of functions called by IDA */

int resrob(realtype tres, N_Vector yy, N_Vector yp,
           N_Vector resval, void *user_data);

static int grob(realtype t, N_Vector yy, N_Vector yp,
                realtype *gout, void *user_data);

int jacrob(long int Neq, realtype tt,  realtype cj,
           N_Vector yy, N_Vector yp, N_Vector resvec,
```

```
           DlsMat JJ, void *user_data,
           N_Vector tempv1, N_Vector tempv2, N_Vector tempv3);

/* Prototypes of private functions */
static void PrintHeader(FILE* dataOutput,realtype rtol,
N_Vector avtol, N_Vector y);
static void PrintOutput(void *mem,FILE* dataOutput, realtype t,
N_Vector y);
static void PrintRootInfo(int root_f1, int root_f2);
static void PrintFinalStats(void *mem);
static int check_flag(void *flagvalue, char *funcname, int
opt);

/*
 *-------------------------------------------------------------------
-------
 * Main Program
 *-------------------------------------------------------------------
-------
 */

extern double Get_Q_A_at_t(double current_time);
//extern double Get_P_OUT_at_t(double current_time);
extern double Get_Q_A_prime_at_t(double current_time);
//extern double Get_P_OUT_prime_at_t(double current_time);
//extern double Get_P_OUT_pp_at_t(double current_time);

int main(void)
{

  create_Q_A();
  //create_P_OUT() ;
  create_spline_Q_A ();
  //create_spline_P_OUT ();

  void *mem;
  N_Vector yy, yp, avtol;
  realtype rtol, *yval, *ypval, *atval;
  realtype t0, tout1, tout, tret;
  int iout, retval, retvalr;
  int rootsfound[2];

  FILE* dataOutput = NULL;
  mem = NULL;
  yy = yp = avtol = NULL;
  yval = ypval = atval = NULL;

  //itest=0; // debug
  dataOutput = fopen("data.txt", "w+");
```

```
  /* Allocate N-vectors. */
  yy = N_VNew_Serial(NEQ);
  if(check_flag((void *)yy, "N_VNew_Serial", 0)) return(1);
  yp = N_VNew_Serial(NEQ);
  if(check_flag((void *)yp, "N_VNew_Serial", 0)) return(1);
  avtol = N_VNew_Serial(NEQ);
  if(check_flag((void *)avtol, "N_VNew_Serial", 0)) return(1);

  /* Create and initialize  y, y', and absolute tolerance
vectors. */

  realtype Q_A;
  //realtype P_OUT;
  realtype Q_A_p;
  //realtype P_OUT_p;
  realtype time;

//printf(" time = %4.6f\n" , time);

  /* Variable known at time*/
     Q_A= Get_Q_A_at_t(time);
     //P_OUT= Get_P_OUT_at_t(time);

     Q_A_p= Get_Q_A_prime_at_t(time);
     //P_OUT_p= Get_P_OUT_prime_at_t(time);

  yval = ypval = NULL;
  ypval = NV_DATA_S(yp);
  yval = NV_DATA_S(yy);

/*
     printf(" &&&&&&&&&&&&&&&&&&&&&&\n");
  for(i=0;i<28;i++)
     printf(" res %d = %4.6f\n" , i, ypval[i]);
  return(0);
*/

  rtol = RCONST(1.0e-4);
  atval = NV_DATA_S(avtol);

  atval[0] = RCONST(1.0e-6);
  atval[1] = RCONST(1.0e-6);
  atval[2] = RCONST(1.0e-6);
  atval[3] = RCONST(1.0e-6);
  atval[4] = RCONST(1.0e-6);
  atval[5] = RCONST(1.0e-6);
  atval[6] = RCONST(1.0e-6);
  atval[7] = RCONST(1.0e-6);
  atval[8] = RCONST(1.0e-6);
  atval[9] = RCONST(1.0e-6);
```

```
  atval[10] = RCONST(1.0e-6);
  atval[11] = RCONST(1.0e-6);
  atval[12] = RCONST(1.0e-6);
  atval[13] = RCONST(1.0e-6);
  atval[14] = RCONST(1.0e-6);
  atval[15] = RCONST(1.0e-6);
  atval[16] = RCONST(1.0e-6);
  atval[17] = RCONST(1.0e-6);
  atval[18] = RCONST(1.0e-6);
  atval[19] = RCONST(1.0e-6);
  atval[20] = RCONST(1.0e-6);
  atval[21] = RCONST(1.0e-6);
  atval[22] = RCONST(1.0e-6);
  atval[23] = RCONST(1.0e-6);
  atval[24] = RCONST(1.0e-6);
  atval[25] = RCONST(1.0e-6);
  atval[26] = RCONST(1.0e-6);
  atval[27] = RCONST(1.0e-6);
  atval[28] = RCONST(1.0e-6);
  atval[29] = RCONST(1.0e-6);
  atval[30] = RCONST(1.0e-6);
  atval[31] = RCONST(1.0e-6);
  atval[32] = RCONST(1.0e-6);
  /* Integration limits */
  t0 = ZERO;
  tout1 = dT;

  PrintHeader(dataOutput,rtol, avtol, yy);

  /* Call IDACreate and IDAInit to initialize IDA memory */
  mem = IDACreate();
  if(check_flag((void *)mem, "IDACreate", 0)) return(1);
  retval = IDAInit(mem, resrob, t0, yy, yp);
  if(check_flag(&retval, "IDAInit", 1)) return(1);
  /* Call IDASVtolerances to set tolerances */
  retval = IDASVtolerances(mem, rtol, avtol);
  if(check_flag(&retval, "IDASVtolerances", 1)) return(1);

  /* Free avtol */
  N_VDestroy_Serial(avtol);

    /* Call IDADense and set up the linear solver. */
  retval = IDADense(mem, NEQ);
  if(check_flag(&retval, "IDADense", 1)) return(1);
  retval = IDADlsSetDenseJacFn(mem, jacrob);
  if(check_flag(&retval, "IDADlsSetDenseJacFn", 1)) return(1);

  /* In loop, call IDASolve, print results, and test for
errorf. */
```

```
  iout = 0; tout = tout1;
  while(1) {

    retval = IDASolve(mem, tout, &tret, yy, yp, IDA_NORMAL);

    PrintOutput(mem,dataOutput,tret,yy);


    if(check_flag(&retval, "IDASolve", 1)) return(1);

    if (retval == IDA_SUCCESS) {
      iout++;
      tout += dT; //incrementoutput time by DT
    }


     if (iout ==NOUT) break;
  }

  PrintFinalStats(mem);

  /* Free memory */

  IDAFree(&mem);
  N_VDestroy_Serial(yy);
  N_VDestroy_Serial(yp);
  fclose(dataOutput);

  return(0);

}

/*da0
 *--------------------------------------------------------------------
-------
 * Functions called by IDA
 *--------------------------------------------------------------------
-------
 */

/*
 * Define the system residual function.
 */


int resrob(realtype tres, N_Vector yy, N_Vector yp, N_Vector
rr, void *user_data)
{
  realtype *yval, *ypval, *rval;
  int i;
```

```
  yval = NV_DATA_S(yy);
  ypval = NV_DATA_S(yp);

  rval = NV_DATA_S(rr);

/* updating time inputs for P, Q curves */
      realtype Q_A = Get_Q_A_at_t(tres);
      //realtype P_OUT = Get_P_OUT_at_t(tres);
      //realtype P_OUT_p = Get_P_OUT_prime_at_t(tres);
      realtype Q_A_p = Get_Q_A_prime_at_t(tres);
      fprintf(stderr," tres %lf Q_A %lf P_OUT %f P_OUT_p
%10.10e\n",tres, Q_A,P_OUT,P_OUT_p);
//

  rval[0]  = P_OA_C1 - P_DA_C1 - Q_da_C1 * R_4_C1;
  rval[1]  = P_C_C1 - P_DA_C1 +  L_C1* Q_da_C1_p;
  rval[2]  = P_C_C1- P_OUT - R_5_C1 * Q_R5_C1;
  rval[3]  = (P_C_C1_p - P_OUT_p) * C_C1 - Q_C_C1;
  rval[4]  = Q_da_C1 - Q_C_C1 - Q_R5_C1;

  rval[5]  = P_OA_C2 - P_DA_C2 - Q_da_C2 * R_4_C2;
  rval[6]  = P_C_C2 - P_DA_C2 +  L_C2* Q_da_C2_p;
  rval[7]  = P_C_C2- P_OUT - R_5_C2 * Q_R5_C2;
  rval[8]  = (P_C_C2_p - P_OUT_p) * C_C2 - Q_C_C2;
  rval[9]  = Q_da_C2 - Q_C_C2 - Q_R5_C2;

  rval[10]  = P_OA_CDL - P_DA_CDL - Q_da_CDL * R_4_CDL;
  rval[11]  = P_C_CDL - P_DA_CDL +  L_CDL* Q_da_CDL_p;
  rval[12]  = P_C_CDL - P_OUT - R_5_CDL * Q_R5_CDL;
  rval[13]  = (P_C_CDL_p - P_OUT_p) * C_CDL - Q_C_CDL;
  rval[14]  = Q_da_CDL - Q_C_CDL - Q_R5_CDL;

  rval[15] = P_AP1 - P_OA_C1 - Q_da_C1 * R_BR;
  rval[16] = P_AP1 - P_AP3 - Q_ER * R_ER;
  rval[17] = P_AP3 - P_OA_CDL - Q_da_CDL * R_DO;
  rval[18] = P_AP2 - P_AP3 - Q_EL * R_EL;
  rval[19] = P_AP2 - P_OA_C2 - Q_da_C2 * R_BL;

  rval[20] = Q_A - QA_1 - QA_2 - QA_3;
  rval[21] = QA_1 - Q_da_C1 - Q_ER;
  rval[22] = Q_da_CDL - QA_3 - Q_ER - Q_EL;
  rval[23] = QA_2 - Q_EL - Q_da_C2;

  rval[24] = QA_3_p - Q_IIIR_p - Q_IIR_p - Q_IIIL_p - Q_IIL_p;

  rval[25] = Pd_p - P_AP1_p - QA_1_p * RA_4R;
  rval[26] = Pd_p - Ps_p - QA_3_p * R_JNC;
  rval[27] = Pd_p - P_AP2_p - QA_2_p * RA_4L;
  rval[28] = Pin_p - Pd_p -  Q_A_p * R_OFT;
```

```
  rval[29] = Ps_p - P_AP3_p -  Q_IIIR_p * RA_3R;
  rval[30] = Ps_p - P_AP3_p - Q_IIR_p * RA_2R;
  rval[31] = Ps_p - P_AP3_p - Q_IIIL_p * RA_3L;
  rval[32] = Ps_p - P_AP3_p - Q_IIL_p * RA_2L;

//if(itest == 0){
//  printf(" &&&&&&&&&&&&&&&&&&&&&\n");
//  for(i=0;i<28;i++)
//   printf(" res %d = %4.6f\n" , i, rval[i]);
  return(0);
/*
 printf(" &MyInitValues&&&&&&&&\n");
printf(" Q_A, Q_A_p = %4.6f %4.6f\n" , Q_A, Q_A_p);
  for(i=0;i<28;i++){
      printf(" yy %d = %4.6f\n" , i, yval[i]);
      printf(" yp %d = %4.6f\n" , i, ypval[i]);
      if(i==27) printf(" &&endy&&\n");
      }
      itest=1;
      return(0);
}*/

}

 /* Define the Jacobian function.
 */

int jacrob(long int Neq, realtype tt,  realtype cj,
           N_Vector yy, N_Vector yp, N_Vector resvec,
           DlsMat JJ, void *user_data,
           N_Vector tempv1, N_Vector tempv2, N_Vector tempv3)
{
 //realtype *yval;

 //yval = NV_DATA_S(yy);
///copy and paste from matlab
return(0);
}

/*
 *-----------------------------------------------------------------
-------
 * Private functions
 *-----------------------------------------------------------------
-------
 */

/*
 * Print first lines of output (problem description)
 */
```

```
static void PrintHeader(FILE* dataOutput, realtype rtol,
N_Vector avtol, N_Vector y)
{
  realtype *atval, *yval;

  atval  = NV_DATA_S(avtol);
  yval  = NV_DATA_S(y);

  printf("Early chick circultion");

#if defined(SUNDIALS_EXTENDED_PRECISION)
  printf("Tolerance parameters:  rtol = %Lg   atol = %Lg %Lg
%Lg %Lg %Lg %Lg %Lg %Lg %Lg %Lg %Lg %Lg %Lg %Lg %Lg %Lg %Lg %Lg
%Lg %Lg %Lg %Lg %Lg %Lg %Lg %Lg %Lg %Lg %Lg %Lg %Lg %Lg %Lg
\n",
         rtol, atval[0],atval[1],atval[2], atval[3], atval[4],
atval[5],atval[6],atval[7], atval[8], atval[9],
atval[10],atval[11],atval[12], atval[13], atval[14]
atval[15],atval[16],atval[17], atval[18], atval[19], atval[20],
atval[21], atval[22], atval[23], atval[24], atval[25],
atval[26], atval[27], atval[28], atval[29], atval[30],
atval[31], atval[32]);
  printf("Initial conditions y0 = (%Lg %Lg %Lg %Lg %Lg %Lg %Lg
%Lg %Lg %Lg %Lg %Lg %Lg %Lg %Lg %Lg %Lg %Lg %Lg %Lg %Lg %Lg %Lg
%Lg %Lg %Lg %Lg %Lg %Lg %Lg %Lg %Lg %Lg %Lg %Lg %Lg %Lg %Lg)\n",
         yval[0], yval[1], yval[2], yval[3], yval[4], yval[5],
yval[6], yval[7], yval[8], yval[9], yval[10], yval[11],
yval[12], yval[13], yval[14], yval[15], yval[16], yval[17],
yval[18], yval[19], yval[20], yval[21], yval[22], yval[23],
yval[24], yval[25], yval[26], yval[27], yval[28], yval[29],
yval[30], yval[31], yval[32]);
#elif defined(SUNDIALS_DOUBLE_PRECISION)
  printf("Tolerance parameters:  rtol = %lg   atol = %lg %lg
%lg %lg %lg %lg %lg %lg %lg %lg %lg %lg %lg %lg %lg %lg %lg %lg
%lg %lg %lg %lg %lg %lg %lg %lg %lg %lg %lg %lg %lg %lg %lg %lg
\n",
         rtol, atval[0],atval[1],atval[2], atval[3], atval[4],
atval[5],atval[6],atval[7], atval[8], atval[9],
atval[10],atval[11],atval[12], atval[13], atval[14],
atval[15],atval[16],atval[17], atval[18], atval[19], atval[20],
atval[21], atval[22], atval[23], atval[24], atval[25],
atval[26], atval[27], atval[28], atval[29], atval[30],
atval[31], atval[32]);
  printf("Initial conditions y0 = (%lg %lg %lg %lg %lg %lg %lg
%lg %lg %lg %lg %lg %lg %lg %lg %lg %lg %lg %lg %lg %lg %lg %lg
%lg %lg %lg %lg %lg %lg %lg %lg %lg %lg %lg %lg %lg %lg %lg)\n",
         yval[0], yval[1], yval[2], yval[3], yval[4], yval[5],
yval[6], yval[7], yval[8], yval[9], yval[10], yval[11],
yval[12], yval[13], yval[14], yval[15], yval[16], yval[17],
```

```
yval[18], yval[19], yval[20], yval[21], yval[22], yval[23],
yval[24], yval[25], yval[26], yval[27], yval[28], yval[29],
yval[30], yval[31], yval[32]);
#else
  printf("Tolerance parameters:  rtol = %g   atol = %g %g %g %g
%g %g %g %g %g %g %g %g %g %g %g %g %g %g %g %g %g %g %g %g %g %g
%g %g %g %g %g %g %g %g \n",
         rtol, atval[0],atval[1],atval[2], atval[3], atval[4],
atval[5],atval[6],atval[7], atval[8], atval[9],
atval[10],atval[11],atval[12], atval[13], atval[14]
atval[15],atval[16],atval[17], atval[18], atval[19], atval[20],
atval[21], atval[22], atval[23], atval[24], atval[25],
atval[26], atval[27], atval[28], atval[29], atval[30],
atval[31], atval[32]);
  printf("Initial conditions y0 = (%g %g %g %g %g)\n",
        yval[0], yval[1], yval[2], yval[3], yval[4], yval[5],
yval[6], yval[7], yval[8], yval[9], yval[10], yval[11],
yval[12], yval[13], yval[14], yval[15], yval[16], yval[17],
yval[18], yval[19], yval[20], yval[21], yval[22], yval[23],
yval[24], yval[25], yval[26], yval[27], yval[28], yval[29],
yval[30], yval[31], yval[32]);
#endif

/*
  printf("Constraints and id not used.\n\n");
  printf("-------------------------------------------------------
------------------\n");
  printf("  t   Q_4A    POA_C1    PDA_C1    PC_C1    Qda_C1
QR5_C1     QC_C1   POA_C2    PDA_C2    PC_C2    Qda_C2
QR5_C2    QC_C2  POA_CDL    PDA_CDL    PC_CDL    Qda_CDL
QR5_CDL     QC_CDL ");
  printf("      | nst  k      h\n");
  printf("-------------------------------------------------------
------------------\n");
/*
  fprintf(dataOutput,"/* ---------------------------------------
---------------------------------\n");
  fprintf(dataOutput,"  t   Q_4A    POA_C1    PDA_C1    PC_C1
Qda_C1      QR5_C1     QC_C1   POA_C2    PDA_C2    PC_C2
Qda_C2     QR5_C2    QC_C2  POA_CDL    PDA_CDL    PC_CDL
Qda_CDL     QR5_CDL     QC_CDL");
  fprintf(dataOutput,"      | nst  k      h\n");
  fprintf(dataOutput,"-------------------------------------------
-----------------------------\n */// ");


}

/*
 * Print Output
```

```
 */
extern double Get_Q_A_at_t(double current_time);
static void PrintOutput(void *mem,FILE* dataOutput, realtype t,
N_Vector y)
{
  realtype *yval;
  int retval, kused;
  long int nst;
  realtype hused;

  yval  = NV_DATA_S(y);

  retval = IDAGetLastOrder(mem, &kused);
  check_flag(&retval, "IDAGetLastOrder", 1);
  retval = IDAGetNumSteps(mem, &nst);
  check_flag(&retval, "IDAGetNumSteps", 1);
  retval = IDAGetLastStep(mem, &hused);
  check_flag(&retval, "IDAGetLastStep", 1);

/*
 printf("%10.4e %12.4e %12.4e %12.4e %12.4e %12.4e %12.4e
%12.4e %12.4e %12.4e %12.4e %12.4e %12.4e %12.4e %12.4e %12.4e
%12.4e %12.4e %12.4e| %3ld  %1d %12.4e\n",
         t, yval[0], yval[1], yval[2], yval[3], yval[4],
yval[5], yval[6], yval[7], yval[8], yval[9], yval[10],
yval[11], yval[12], yval[13], yval[14], yval[15], yval[16],
yval[17],  nst, kused, hused);
*/
/*
 printf("%10.4e %12.4e %12.4e %12.4e %12.4e %12.4e %12.4e
%12.4e %12.4e %12.4e %12.4e %12.4e %12.4e %12.4e %12.4e %12.4e
%12.4e %12.4e %12.4e| %3ld  %1d %12.4e\n",
         t, yval[0], yval[1], yval[2], yval[3], yval[4],
yval[5], yval[6], yval[7], yval[8], yval[9], yval[10],
yval[11], yval[12], yval[13], yval[14], yval[15], yval[16],
yval[17],  nst, kused, hused);*/
  fprintf(dataOutput,"%10.4e %12.4e %12.4e %12.4e %12.4e %12.4e
%12.4e %12.4e %12.4e %12.4e %12.4e %12.4e %12.4e %12.4e %12.4e
%12.4e %12.4e %12.4e %12.4e %12.4e %12.4e %12.4e %12.4e %12.4e
%12.4e %12.4e %12.4e %12.4e %12.4e %12.4e %12.4e %12.4e %12.4e
%12.4e %12.4e| %3ld  %1d %12.4e\n",
         t, Get_Q_A_at_t(t), yval[0], yval[1], yval[2],
yval[3], yval[4], yval[5], yval[6], yval[7], yval[8], yval[9],
yval[10], yval[11], yval[12], yval[13], yval[14], yval[15],
yval[16], yval[17], yval[18], yval[19], yval[20], yval[21],
yval[22], yval[23], yval[24], yval[25], yval[26], yval[27],
yval[28], yval[29], yval[30], yval[31], yval[32], nst, kused,
hused);
}
/*
```

```
 * Print final integrator statistics
 */

static void PrintFinalStats(void *mem)
{
  int retval;
  long int nst, nni, nje, nre, nreLS, netf, ncfn, nge;

  retval = IDAGetNumSteps(mem, &nst);
  check_flag(&retval, "IDAGetNumSteps", 1);
  retval = IDAGetNumResEvals(mem, &nre);
  check_flag(&retval, "IDAGetNumResEvals", 1);
  retval = IDADlsGetNumJacEvals(mem, &nje);
  check_flag(&retval, "IDADlsGetNumJacEvals", 1);
  retval = IDAGetNumNonlinSolvIters(mem, &nni);
  check_flag(&retval, "IDAGetNumNonlinSolvIters", 1);
  retval = IDAGetNumErrTestFails(mem, &netf);
  check_flag(&retval, "IDAGetNumErrTestFails", 1);
  retval = IDAGetNumNonlinSolvConvFails(mem, &ncfn);
  check_flag(&retval, "IDAGetNumNonlinSolvConvFails", 1);
  retval = IDADlsGetNumResEvals(mem, &nreLS);
  check_flag(&retval, "IDADlsGetNumResEvals", 1);
  retval = IDAGetNumGEvals(mem, &nge);
  check_flag(&retval, "IDAGetNumGEvals", 1);

  printf("\nFinal Run Statistics: \n\n");
  printf("Number of steps                    = %ld\n", nst);
  printf("Number of residual evaluations     = %ld\n",
nre+nreLS);
  printf("Number of Jacobian evaluations     = %ld\n", nje);
  printf("Number of nonlinear iterations     = %ld\n", nni);
  printf("Number of error test failures      = %ld\n", netf);
  printf("Number of nonlinear conv. failures = %ld\n", ncfn);

}

static int check_flag(void *flagvalue, char *funcname, int opt)
{
  int *errflag;
  /* Check if SUNDIALS function returned NULL pointer - no
memory allocated */
  if (opt == 0 && flagvalue == NULL) {
    fprintf(stderr,
            "\nSUNDIALS_ERROR: %s() failed - returned NULL
pointer\n\n",
            funcname);
    return(1);
  } else if (opt == 1) {
    /* Check if flag < 0 */
    errflag = (int *) flagvalue;
```

```
    if (*errflag < 0) {
      fprintf(stderr,
              "\nSUNDIALS_ERROR: %s() failed with flag =
%d\n\n",
              funcname, *errflag);
      return(1);
    }
  } else if (opt == 2 && flagvalue == NULL) {
    /* Check if function returned NULL pointer - no memory
allocated */
    fprintf(stderr,
            "\nMEMORY_ERROR: %s() failed - returned NULL
pointer\n\n",
            funcname);
    return(1);
  }

  return(0);
}
```